GALLIUM ARSENIDE FIELD EFFECT TRANSISTORS MICROSTRIP INTEGRATED CIRCUIT DIELECTRIC RESONATOR OSCILLATORS

DAVID ANDREW CROUCH

B.Sc(Eng) University of Cape Town

Thesis submitted to the Department of Electrical and Electronic Engineering of the University of Cape Town in partial fulfillment of the requirements for the degree M.Sc(Eng).

September 1988

DECLARATION

I declare that this dissertation is my own unaided work. It is being submitted in partial fulfillment of the requirements for the degree of Master of Science in Engineering at the University of Cape Town. It has not been submitted before for any degree or examination at any other university.

Signed by candidate

(Signature of Candidate)

6th day October 1988

SYNOPSIS

This thesis is concerned with Gallium Arsenide Metal Semiconductor Field Effect Transistor Microstrip Integrated Circuit Dielectric Resonator Oscillators (GaAs MESFET MIC DROs) - the different types, their design and their performance compared to other high Q factor (ie narrowband) microwave oscillators. The thesis has three major objectives. The first is to collate the information required to build microwave DROs. The second is to present the practical results obtained from Dielectric Resonator Bandreject and Bandpass filters (DR BRFs and DR BPFs). The last is to present and compare results from a DR stabilised microstrip oscillator and three types of series feedback DROs.

Narrowband oscillators are usually evaluated in terms of their frequency stability, reliability, size, cost, efficiency and output power characteristics. In terms of these parameters DROs outperform Gunn cavity oscillators and are only bettered by crystal locked sources in terms of frequency temperature stability and long-term stability. The components of a GaAs MESFET MIC DRO possess ideal properties for the construction of a narrowband source with the exception of the long term stability of the GaAs MESFET. GaAs MESFET DROs have the best published DRO results for efficiency, output power, power temperature stability and external Q factor.

Basic oscillator theory derived by Kurokawa can be applied to both negative resistance and feedback oscillators. Impedance locus, device-line and operating point concepts provide a convenient framework for understanding hysteresis in microwave oscillators. The work by Kurokawa can also be translated into the S-parameter domain which has proved convenient for the design of microwave oscillators.

A DR can be used in two ways to produce a DRO - as a passive stabilisation element for a free-running oscillator, or, as part of the intrinsic oscillator feedback circuit. Design of a DRO is best done using S-parameters since these are easily measurable for the active device and DR resonant circuit. Mathematical models exist for DR BRFs and DR BPFs and the equivalent circuit elements can be determined from scalar measurement on the network analyser. This allows computer models of DR BRFs and

equally coupled DR BPFs to be entered on TOUCHSTONE which already has suitable models for the active device and microstrip feedback/output elements. To the Author's knowledge, the theory required to determine the equivalent circuit elements of an equally coupled DR BPF from scalar measurements on a network analyser has not been reported on before.

Once a particular oscillator topology has been chosen, the three basic parameters available for optimisation are - selection of the active device, the matching of the device and the coupling of the resonant system into the microwave circuit. An investigation into the optimisation of these parameters for best noise, best frequency temperature stability, best long term stability, maximum output power and maximum efficiency showed that optimisation for a particular characteristic proceeds, in general, at the expense of the others.

Suitable DR BRFs for use in DROs were constructed on both 10mil and 31mil dielectric RT DUROID 5880 at 5.75 GHz. The 10mil dielectric DR BRFs were found to have a far narrower coupling range (0.1 to 1.5) than the 31mil dielectric DR BRFs (0.2 to 13) but higher Quality factors over that range. For the 31mil DR BRFs tested a second DR mode was found to exist close to the TE_{01} frequency.

Practical results showed that, whilst DR BRFs are best characterised from reflection measurements, transmission measurements are best for DR BPFs. Practical transmission coefficient measurements of equally coupled DR BPFs were used to derive equivalent circuit models. The TOUCHSTONE results from these models agreed very closely with the initial measurements indicating that the equivalent circuits calculated from scalar network analyser measurements were correct. This result also validated the theory derived.

A Three-port microstrip topology was found to be suitable for the construction of an unstabilised microstrip oscillator at a specific frequency with high output power and a poor pulling factor. To design such an oscillator on a frequency domain computer package such as TOUCHSTONE requires that $|S_{21}|$ be reduced to allow for saturation of the transistor under large signal steady — state conditions. The required reduction in $|S_{21}|$ was determined using a convergent numerical method. Under small

signal start up conditions there are two possible source load reactances which give a particular gate reflection coefficient; this results in two possible oscillator configurations. Both configurations were evaluated on TOUCHSTONE and the oscillator with the best characteristics was then constructed. This oscillator was found to meet all the criteria specified for an unstabilised source.

To produce a stabilised DRO, a DR was placed on the output of the constructed microstrip oscillator. Adding the DR had the effect of dramatically improving the stability of the oscillator over the stabilisation range. The actual stabilisation performance did not, however, agree well with theory and stabilised oscillation did not occur at the design frequency of 5.75 GHz.

Three basic configurations exist for a series feedback DRO - common source, common drain and common gate. All three types of oscillator were constructed and their performance evaluated.

The common source oscillator was found to have the best tuning range, frequency temperature stability and pushing and pulling characteristics. Highest output power and efficiency results at 5.75 GHz were recorded for the common source and common gate oscillators respectively. Four conclusions can be drawn from the results obtained. Firstly, the small signal S-parameters supplied by the device manufacturer are useful for calculating the required reactance of the common stub, but not the placement of the DR. Secondly, the placement of the DR is best performed practically. Thirdly, the oscillator configuration which gives the best frequency stability results cannot be accurately predicted from the manufacturer's small signal data - but only from actual construction of the oscillators. Finally, frequency stability can be traded off against output power and efficiency.

Future research work on DR filters should investigate further the parameters involved in the construction of DR BRFs and BPFs such as dielectric thickness as well as the elimination of undesirable DR modes. It is envisaged that more accurate design methods for series feedback STDROs will involve large signal measurements although little practical advantage may result. The construction of parallel feedback oscillators,

although not pursued, offers several areas for future research. These include ascertaining the most practical design method and deriving an equivalent model for a DR BPF with coupling lines at right angles.

ACKNOWLEDGEMENTS

I would like to express my appreciation to my supervisor Professor B.J. Downing for his guidance and support during the course of this thesis.

I would also like to thank Paul Daniels, Andy Vinnecombe and Neville Wright for their technical assistance and Mrs Anne Grant for word processing the main body of this dissertation.

Financial assistance from the Council for Scientific and Industrial Research is gratefully acknowledged.

TABLE OF CONTENTS

TABLE OF CONTENTS (Contd)

TABLE OF CONTENTS (Contd)

TABLE OF CONTENTS (Contd)

TABLE OF CONTENTS (Contd) PAGE

TABLE OF CONTENTS (Contd)

TABLE OF CONTENTS (Contd)

LIST OF ILLUSTRATIONS

PAGE

FIGURES

LIST OF ILLUSTRATIONS (Contd)

LIST OF ILLUSTRATIONS (Contd)

LIST OF ABBREVIATIONS

AM	Amplitude Modulation
BPF	Bandpass Filter
BRF	Bandreject Filter
dB	decibel
dBc	decibels relative to carrier
dBm	decibels relative to 1 mW
dc	direct current
DR	Dielectric Resonator
DRO	Dielectric Resonator Oscillator
FET	Field Effect Transistor
FM	Frequency Modulation
GaAs	Gallium Arsenide
GHz	GigaHertz
HBT	Heterojunction Bipolar Transistor
HEMPT	High Electron Mobility Transistor
Hz	Hertz
IMPATT	IMPact ionisation Avalanche Transit Time
kHz	kiloHertz
LO	Local Oscillator
MCC	Miniature Ceramic Circuit
MESFET	Metal Semiconductor Field Effect Transistor
MHz	MegaHertz
MIC	Microstrip Integrated Circuit
mw	microwave
mW	milliWatt
ppm/K	parts per million per Kelvin
Q factor	Quality factor
RF	Radio Frequency
STDRO	Stable Transistor Dielectric Resonator Oscillator
TE	Transverse Electric
TEM	Transverse Electromagnetic
TS	TOUCHSTONE
VSWR	Voltage Standing Wave Ratio
W	Watt
YIG	Yttrium Iron Garnet

CHAPTER 1

INTRODUCTION

This thesis is concerned with Gallium Arsenide Metal Semiconductor Field Effect Transistor Microstrip Integrated Circuit Dielectric Resonator Oscillators (GaAs MESFET MIC DROs) - the different types, their design and their performance compared to other microwave oscillators. To this end the aims of this thesis can be stated as follows:

(1) to examine the GaAs MESFET MIC DRO as a fixed frequency highly stable microwave (mw) source in terms of its components

(2) to present the results of an extensive literature survey on DROs

(3) to compare GaAs MESFET MIC DROs with other types of DROs and other highly stable mw oscillators

(4) to collate the basic oscillator theory required to understand and design new oscillators

(5) to present the theory required to characterise the components of a GaAs MESFET MIC DRO in terms of S-parameters and to present suitable S-parameter design techniques for different types of DROs

(6) to discuss the different criteria which are important in oscillator design and the tradeoffs involved

(7) to characterise DR Bandreject Filters (BRFs) and DR Bandpass Filters (BPFs) from practical measurements

(8) to investigate practically DR stabilised mw oscillators and series feedback DROs

(9) from the practical results to come to conclusions as to which type of DRO considered (stabilised or series feedback) offers the best design option

(10) to make recommendations as to the possible direction of further work

The scope of the practical research work which could be accomplished was severely limited by the fact that only a single DR was available and the FETs were expensive. Practical oscillator construction was limited to oscillators with DR BRFs - parallel feedback oscillators are not considered in this thesis. The lack of equipment to measure noise performance ruled out noise measurements which provide an important indication of frequency stability.

It is shown that it is not possible to optimise for all criteria simultaneously, so that oscillator design becomes a matter of compromise.

This thesis can be divided into four sections. The first section, comprising Chapters 2 to 6, describes the research completed to satisfy aims (1) to (6). This forms the literature survey section of the thesis. The second section, which consists of Chapters 7 and 8, outlines practical measurements taken on DR BRFs and DR BPFs to characterise the filters in terms of their equivalent circuits (aim 7). Chapters 9 to 11, which make up the third section, describe the practical work done in designing, building and evaluating DR stabilised oscillators and series feedback DROs (aims (8) and (9)). The final section, Chapter 12 and Chapter 13, summarises the main results and conclusions and makes recommendations for future work (aim 10)).

A breakdown of the different chapters is now given.

Chapter 2 serves as an introduction to mw oscillators.

Chapter 3 introduces DROs and compares them with two other types of narrowband mW sources. GaAs MESFET MIC DROs are examined in terms of the properties required by a stable mw frequency source. The chapter presents the results of an extensive literature survey of DROs and using these results GaAs MESFET MIC DROs are compared with other types of DROs.

Chapter 4 presents the basic oscillator theory required to understand the design of mw oscillators. This theory is used in Chapter 5 to describe the basic design concepts for the different types of transistor DROs. At

microwave frequencies S-parameters provide the best practical method of characterising oscillator components so the relevant S-parameter theory is described.

Chapter 6 considers the criteria for best noise performance, best frequency temperature stability, best long-term stability, maximum output power and maximum efficiency.

Chapter 7 describes practical measurements taken on DR Band Reject Filters to allow calculation of R, L and C for the equivalent model as a function of distance of the DR from the microstripline and airgap height. Chapter 8 follows with the corresponding practical measurements taken on DR Bandpass Filters.

Chapter 9 describes the design, construction and evaluation of a DR BRF stabilised oscillator. The design of a 3-port MIC oscillator is presented along with the theory required to stabilise it with a DR BRF. The results from the stabilised oscillator are compared with theory.

Chapter 10 presents the practical Common Drain (CD), Common Source (CS) and Common Gate (CG) series feedback oscillators constructed. The results for the three configurations are compared and discussed. Conclusions are drawn as to the success which can be attributed to designing with the small signal S-parameters supplied by the manufacturer.

Chapter 11 evaluates the results from the DR stabilised oscillator and series feedback DROs to come to a conclusions as to which type of oscillator provides the best design choice.

The penultimate chapter, Chapter 12, summarises the important results and conclusions, leaving the last chapter, Chapter 13, to make recommendations for future research.

CHAPTER 2

MICROWAVE OSCILLATORS

2.1 Introduction

Microwave oscillators form an integral part of most microwave systems. Such systems include radar, navigation systems, satellite communication links and systems for military applications such as electronic warfare.

The first microwave sources used bulky klystron or magnetron tubes which require large power supplies. During the 1960s the first solid-state microwave devices became available in the form of Gunn diodes and impatt avalanche transit time (IMPATT) diodes. Gunn diodes and IMPATT diodes are examples of two terminal negative resistance devices.

The 1970s saw a major advance in microwave solid state technology with the development of the bipolar silicon transistor and the Gallium Arsenide (GaAs) metal semiconductor field effect transistor (MESFET). These devices have three terminals.

Solid-state technology has resulted in microwave sources which are highly cost effective, reliable, low noise, efficient, physically small and which require low voltage power supplies.

2.2 Wideband, Narrowband and Fixed Frequency Microwave Oscillators

Microwave oscillators can be split into three basic categories -wideband, narrowband and fixed frequency oscillators.

2.2.1 Wideband Oscillators

Wideband oscillators are designed to be electronically tunable over a bandwidth of an octave or more. There are two basic types using solid-state devices - YIG tuned and varactor tuned oscillators.

Yttrium iron garnet (YIG) is a material which provides a high Q resonance in a magnetic field. The frequency of resonance is determined by the

magnetic field and greater than octave band tuning is possible (Papp, 1980). Since the resonant circuit is high Q, YIG tuned oscillators have good spectral purity but their frequency agility is poor.

Varactor tuned oscillators differ fundamentally from YIG tuned oscillators in that they are essentially low Q voltage controlled oscillators. In this case the reverse voltage across the varactor diode determines the resonant frequency while the low Q circuit results in excellent frequency agility but poor noise performance.

2.2.2 Narrowband and Fixed Frequency Oscillators

Fixed frequency oscillators are used to provide a reference signal. Frequency stability and spectral purity are therefore of paramount importance. Narrowband oscillators are usually designed as fixed frequency oscillators with the facility to perturb the frequency over a narrow bandwidth. This allows the source to be either frequency modulated or locked to another signal.

Producing a solid-state stable microwave source requires a resonant system with high frequency stability and an active device. Fixed frequency or narrowband solid state microwave sources can be classified according to the type of resonant system employed. The three most common are quartz crystal locked, resonant cavity and dielectric resonator oscillators.

CHAPTER 3

THE GaAs MESFET MIC DRO AS A NARROWBAND FREQUENCY SOURCE

3.1 Introduction

This chapter begins by introducing DROs and defining their scope as microwave sources. It then outlines factors which are important to narrowband frequency sources. Using these factors DROs are compared with two other solid-state narrowband sources - namely Gunn diode Cavity Resonator oscillators and quartz crystal phase locked oscillators.

By examining the properties of the components of a GaAs MESFET MIC DRO it is shown that these oscillators have the inherent potential to be excellent narrowband frequency sources. A table is presented as an appendix reviewing the DRO results found after an extensive literature review. The best results for GaAs MESFET DROs and other types of DROs are summarised in a table in the main text.

The chapter is concluded with a summary of the main results.

3.2 Dielectric Resonator Oscillators

Dielectric resonator oscillators consist of three basic components:

(1) a solid-state active device - DROs have been constructed using Gunn diodes, IMPATT diodes, bipolar transistors, GaAs MESFETS and HEMPTs (high electron mobility transistors)

(2) a dielectric resonator - in 1939 R.D. Richtmyer showed that unmetalised dielectric objects can function as electrical resonators. Their advantages over other microwave resonators are discussed in the next section

(3) a circuit connecting the dielectric resonator system with the active device and feeding power out

Dielectric resonator oscillators have been constructed at frequencies from 1 GHz (Loboda, 1987) to 35 GHz (Dow, 1986). The lower frequency limit is determined by resonator size (>2 inches in diameter for $\xi \sim 40$) while the upper frequency limit is established by the minimum Q which can be tolerated as the intrinsic Q falls off with increasing frequency (Plourde, 1981).

DROs can be divided into two basic categories - negative resistance DR oscillators and feedback DR oscillators.

If the active device used is a two terminal device then the class of oscillator which can be constructed is limited to that of a negative resistance DR oscillator. A three terminal device (i.e. a transistor) can be used to produce either class of DR oscillator.

3.3 Factors Important to a Narrowband Oscillator

When evaluating a narrowband solid-state frequency source the following factors need to be considered - frequency stability, reliability, size, cost, efficiency and output power characteristics.

(a) Frequency stability

The primary requirement for a reference signal is that it be frequency stable. The frequency stability of an oscillator is characterised in terms of noise, temperature stability, pushing and pulling factors, mechanical stability and long-term stability (aging). Most narrowband oscillators are used as local oscillators (LOs) where a very clean signal is required. Thus both AM and FM (phase) noise need to be kept to a minimum. This is especially ture for digital mw communication systems where a low bit error rate is essential (Varian, 1986: 87) Frequency temperature stability is important since many military and commercial communication applications of mw oscillators demand reliable operation, within a narrow tolerance, over a temperature range of typically -20°C to +65°C

(b) Reliability

Oscillators are usually fundamental building blocks in the systems in which they are used. As a result failure of the oscillator will invariably cause the whole system to fail. Reliability thus becomes a very important criterion and this is especially true for oscillators in systems which cannot be easily serviced. Satellites and missiles are examples of systems where reliability is crucial. The reliability of an oscillator is a function of the number of components, the reliability of each individual component and the operating conditions of the oscillator

(c) Size

Besides the obvious space advantages, reducing the size of an oscillator also results in decreased weight and advantages in cost and reliability

(d) Cost

To be economically viable the cost of an oscillator should be kept as low as possible. Thus oscillators which have low component counts and use the cheapest technology possible will have an economic edge

(e) Efficiency

Oscillators used in applications such as satellites, missiles and portable communication equipment must be highly efficient if power supplies are to be kept small and light

(f) Output power characteristics

The output power characteristics of an oscillator are specified in terms of the output power and its temperature stability

Many narrowband applications such as transmitter carrier generation require high power oscillators. There are two possible approaches to producing a high power oscillator - either a single high power device can be used or a low power oscillator can be followed by a high power amplifier. The first approach has advantages in cost, reliability, compactness and efficiency - the second gives better frequency stability.

3.4 Comparison of DROs with Other Narrowband Sources

Table 3.1 compares Cavity Gunn oscillators and phase locked oscillators with DROs.

Table 3.1 Comparison of DROs with Gunn Cavity Resonator Oscillators and Quartz Crystal Locked Microwave Souurces

	Gunn Cavity Oscillator	Crystal Multiplier Chain	DROs
(A) FREQUENCY STABILITY			
(1) noise	excellent	Very good - traded against long term stab (Hamilton,1978)	excellent
(2) temperature	good +/-20 to 30 ppm	excellent 0.03ppm/K for ovenised (Hamilton,1978)	excellent 0.04ppm/K ovenised (Lan,1986)
(3) long term	>5ppm/year	excellent < 5ppm/year	>5ppm/year
(4) environmental	fair	fair	excellent
(B) EFFICIENCY	low < 4%	very low	high (15-20%)
(C) RELIABILITY	fair	good	excellent
(D) POWER VARIATION	high	high	low
(E) SIZE	small	large	smallest

The main disadvantage of Gunn Cavity oscillators as narrowband frequency sources are their low efficiency, their average environmental stability (20 times worse than that of a DRO (Mizumura, 1982: 178)) and their high power variation. They have been largely superceded by FET DROs.

Microwave oscillators locked to a crystal oscillator provide the ultimate in frequency stability in terms of variation with temperature and long-term stability. At present they are the only oscillators capable of a long-term stability of less than 5ppm/year and, as a result, have to be used for applications such as digital microwave telecommunications. Varian (Varian, 1986: 88) has demonstrated that, for frequencies above 10 KHz from the carrier, GaAs MIC DROS can outperform phase locked sources in terms of FM noise.

The main disadvantages of phase locked oscillators are that they are complex with a large number of ports. This results in a reduction in system reliability and high cost (Agarwal, 1986: 177).

3.4.1 Conclusions

It has been seen that DROs now have the potential to totally outperform Gunn Cavity Stabilised oscillators. They outperform quartz crystal phase-locked oscillators on all criteria except frequency temperature stability and long-term frequency stability. Quartz crystal phase locked microwave sources still have to be used in applications where very high frequency stability is required such as digital microwave telecommunication links.

3.5 Inherent Suitability of a GaAs MESFET DRO as a Narrowband Source

GaAs MESFET MIC DROs have the inherent potential to be low noise, highly temperature stable, mechanically stable, very reliable, compact, low cost and highly efficient. These properties are the result of the components from which they are constructed. A GaAs MESFET DRO consists of:

(1) a GaAs MESFET solid-state device
(2) a dielectric resonator
(3) a microstrip integrated circuit

This section discusses each component of a GaAs MESFET MIC DRO comparing it with alternative technology and then isolating the factors which make it particularly suitable for use in a narrowband source. Disadvantages are also discussed.

3.5.1 The Suitability of a GaAs MESFET as the Active Device

The first DROs were constructed using Gunn diodes or IMPATT diodes since these were the first solid-state devices to be developed at microwave frequencies.

Three terminal active devices such as GaAs FETs and silicon bipolar transistors (at frequencies below X-band) have now largely replaced Gunn and IMPATT diodes in solid-state microwave oscillators since they are more efficient than Gunn diodes and have better noise characteristics than IMPATT diodes (Abe, 1978: 65).

3.5.1.1 GaAs vs Silicon Technology

For frequencies below 6 GHz silicon bipolar transistors have an advantage over GaAs FETs in that they typically have 6 to 10 dB less FM noise close to the carrier (Kajfez, 1986: 490). However, the fact that GaAs has an electron mobility six times that of silicon means that it can be used to produce microwave oscillators up to 100 GHz (Niehenke, 1985: 28) whilst silicon oscillators have only been reported up to X-band. GaAs FET devices can be used over the entire MIC DRO range of 1 to 35 GHz.

GaAs has many intrinsic properties which make it a better material than silicon for use in a microwave oscillator (Niehenke, 1985: 25). Of all the semiconductors GaAs has the largest band gap between the valence and conduction bands. This higher band gap translates into fewer intrinsic conduction carriers, especially at high temperatures. This fact makes GaAs suitable for high temperature operation and a good semi-insulating substrate material. The higher mobility of electrons in GaAs leads to a lower resistivity and consequently a lower loss. Besides resulting in a higher frequency of operation it also means that GaAs is more efficient than silicon at the same frequency. GaAs is also inherently ten times more

radiation resistant than silicon which is an important factor for consideration in military and satellite applications.

One disadvantage of GaAs relative to other semiconductors is its lower thermal conductivity. As a result the length of the heat conduction path in the semiconductor must be minimised to keep the junction cool. Another disadvantage is that GaAs technology is not yet as reproducible as silicon technology leading to variations in device parameters.

3.5.1.2 Summary of Factors Which Make GaAs MESFETs Suitable for Use in a Narrowband Source

The following factors make a GaAs MESFET a good active device:

(1) linear phase change with temperature - the phase change with temperature of the reflection coefficient looking into a port of a GaAs MESFET is linear. This aids the design of oscillators with high temperature stability (Tsironis, 1982)

(2) low noise - GaAs FETs inherently have a low noise figure with exceptional noise figures such as 1.35 dB at 12 GHz quoted in the literature (Niehenke, 1985: 27). Because of their construction FET devices produce greater flicker noise near the carrier than do bipolar transistors (Vendelin, 1982: 157). Current development of GaAs microwave heterojunction bipolar transistors (HBTs) has resulted in three terminal devices with low noise characteristics on a par with silicon bipolars and superior to GaAs FETs (Agarwal, 1986, 180)

(3) efficiency - GaAs MESFET oscillators are capable of excellent efficiencies. Figures of 35% by Gilmore (Niehenke, 1985: 36) and 38% by Abe for an unstabilised oscillator (Abe, 1978: 156) have been reported. The typical efficiency for low noise, highly temperature stable GaAs FET DRO units is 15% through X-band (Niehenke, 1985: 38)

(4) output power - GaAs FET devices capable of producing oscillators with output powers of 1W (30 dBm) at 8 GHz have been reported (Niehenke, 1985: 36). This is more than adequate for most narrowband oscillator

application; for example, most LO applications require only 5-20 mW of output power (Purnell, 1981: 104)

3.5.1.3 Problem of Long-term Stability of GaAs MESFET Devices

With all their advantages GaAs MESFET DROs have yet to be successfully used in digital telecommunication systems because of their lack of long-term stability (Varian, 1987: 583).

The problem with producing highly stabilised DROs is that the stability of the oscillator is not solely dependent on the resonator but also on the active device. In a recent paper (Varian, 1987) Varian concludes that units with long-term frequency stabilities approaching those of crystal oscillators can be built provided special care is taken with the selection, insertion and operating conditions of the FET active device.

Varian isolates the integrity of the FET gate as being the main cause of long-term drift. The changing of surface states in the device in the long-term produces an apparent change in gate capacitance. By screening FETs for small gate capacitance change with time Varian was able to product DROs with stabilities of about 10ppm/year.

3.5.2 The Suitability of a Dielectric Resonator as the Resonant System

The advantages of dielectric resonators result from the combination of properties they possess. They fill a gap between waveguide and stripline technologies by providing Qs and temperature stabilities approaching those of invar cavity resonators along with integrability approaching that of stripline resonators (Plourde, 1981: 754).

The dielectric properties of most importance for dielectric resonator applications are:

(1) the Q factor which is approximately equal to the inverse loss tangent $\tan \delta$

(2) the temperature coefficient of resonant frequency τ_f

(3) the dielectric constant ε

Dielectric resonators provide performance comparable to TE_{01} mode waveguide filters if the following values are available: $Q \sim 8000$ and $\tau_f \sim$ 20ppm/°C or τ_f 1-2ppm/°C to compete with copper or invar respectively.

DRs with unloaded Q values of 10 000 at 10 GHz and precise linear temperature coefficients are now available (Niehenke, 1985: 36).

DRs usually have a high value of $\varepsilon \sim 40$ since the resulting resonators are small and have good energy confinement within the resonator thereby reducing extraneous circuit effects. This makes the DR system easier to model mathematically.

3.5.2.1 Advantages of Using a DR as the Resonant System in a Narrowband Oscillator

The following factors make DRs excellent for use in narrowband oscillators:

(1) excellent frequency stability and purity

(a) low phase noise - tests by Loboda et al. (Loboda, 1987: 862) showed that the DR contributes negligible phase noise compared with the active device in a DRO

(b) high temperature stability - DRs are now commercially available with temperature coefficients between -9ppm/°C and +9ppm/°C with a linear variation with temperature (Kajfez, 1986: 507). This allows a DR to be selected which will compensate for the linear frequency change with temperature produced by the active device. High DR temperature stability ($\pm$1ppm) is achieved by compensating thermal expansion of the resonator α_L with a corresponding change in the dielectric constant temperature coefficient τ_k according to the formula:

$$\tau_f = -(\tau_k/2 + \alpha_L) \qquad (3.1)$$

where τ_f is the resonant frequency temperature coefficient (Purnell, 1981: 103)

(c) mechanical stability - tests on DROs designed for missile transponder applications at vibration levels of up to 50 Gs at 50–200 Hz yielded less than 5 KHz peak to peak FM (Purnell, 81: 108)

(2) size - the high permittivity of dielectric materials used results in a DR of small size for frequencies above about 4 GHz. Small resonator size allows the DRO to be easily mounted in an oven to reduce temperature effects where desired and also permits many circuit configurations to be used

(3) cost - DRs are made from ceramics and can be produced in large quantities at low cost

(4) efficiency - new dielectric materials are low loss (Tsironis, 1983: 741) allowing efficient oscillators to be built

(5) power capabilities - the low loss tangent of the dielectric material allows high power operation

3.5.3 The Suitability of Microstrip Technology in the Construction of DROs

Microstrip offers the following advantages for use in a narrowband source:

(1) frequency range - microstrip has been used to construct DROs over the entire DR range
(2) manufacturing tolerances - microstrip can be manufactured to very tight tolerance values
(3) integrability with DR - DRs can easily be magnetically coupled to a microstripline to form a resonant circuit. Usually the resonator is used in the TE_{0i} mode and magnetically coupled to the TEM mode of the microstripline. Higher Q resonant circuits are obtained by raising the resonator above the ground plane using rigid low-loss dielectric supports of quartz, beryllia or forsterite (Plourde, 1981: 763)
(4) integrability with active device - microstripline board facilitates the insertion of the active device in a compact form (Niehenke, 1985: 24)

(5) reliability - microstrip boards are highly reliable (Hagihara, 1982: 235)

(6) size - microstrip allows compact oscillators to be built (Hagihara, 1982: 235)

(7) cost - microstrip provides a low cost circuit (Imai, 1985: 242)

(8) efficiency - microstrip boards provide a low loss microwave circuit below 20 GHz. They have, however, been used to make MIC DROs up to frequencies of 35 GHz (Dow, 1986)

3.6 Literature Review of DROs

Table A.1 in Appendix A presents the results of a literature review of different types of DROs.

Table 3.2 summarises the best results found for different types of DROs.

Table 3.2 Summary of best results for different types of DROs

	Criterion	GaAs MESFET MIC DROs	Lan's DRO	Gunn Diode DROs	IMPATT Diode DROs	Bipolar DROs
Frequency Stability	(1) noise (refered to 4 GHz)	−117 dBc/Hz @10kHz (Varian,1986)	−130dBc/Hz @10kHz			−108dBc/Hz @10kH (Agarwal,1986)
	(2) temperature	0.12ppm/K (Tsironis,1985)	0.04ppm/K	0.2ppm/K (Makino,1979)	1ppm/K (Imai,1985)	
	(3) long term	10ppm/year (Varian,1987)				5ppm/year (Plourde,1981)
Efficiency		28% (Jaques,1985)	6%			27% (Podcameni,1985)
Output Characteristics	(1) power output	27bDm (Mizumura,1982)	11.5dBm	16 dBm (Hagihara,1982)	26dBm (Hagihara,1982)	14.9dBm (Plourde,1981)
	(2) output temp stability	0.008dB/K (Abe,1977)	0.012db/K	0.036dB/K (Hagihara,1982)	0.036dB/K (Hagihara,1982)	
	(3) pushing factor	0.2MHz (Khanna,1981)	0.02MHz/V	0.6MHz/V (Makino,1979)		
	(4) pulling factor	Ext Q = 56500 (Khanna,1981)				Ext Q = 4000 (Plourde,1981)

Five types are considered:

(1) GaAs MIC DROs
(2) A GaAs DRO built by Lan et al. (Lan, 1986) using a temperature compensated two-stage FET amp, a temperature controlled invar cavity containing a DR and utilising miniature ceramic circuit (MCC) technology
(3) Gunn diode DROs
(4) IMPATT diode DROs
(5) Bipolar device DROs

3.6.1 Comparison of Results for Different Types of DROs

Table 3.2 shows that GaAs MESFET MIC DROs have recorded the best DRO results for efficiency, power output, power temperature stability and external Q factor.

The only criteria on which other DROs have recorded better results are frequency stability and pushing factor. Of these best noise performance, temperature stability and pushing factor were obtained with a FET DRO designed by Lan. This DRO features a separate temperature controlled invar cavity containing a DR and a temperature compensated two-stage FET amplifier.

Tsironis (Tsironis, 1985) obtained a temperature stability of 0.12ppm/°C over a range of -50°C to +100°C without ovenising the MIC GaAs DRO. It is, therefore, expected that putting this DRO in a controlled oven should produce temperature stability results comparable with those of Lan.

Varian's phase noise result of -117 dBc/Hz at 10 KHz off carrier (referred to 4 GHZ) is 13 dB higher than that obtained by Lan. However, this result is obtained without using a special invar cavity for the resonator and a two-stage amplifier.

Lan's excellent pushing figure of 0.02 MHz/V is the result of using a two-stage amplifier and keeping the loaded Q of the DR above 8000 with the invar cavity design.

As pointed out in Section 3.5.1.3, the biggest problem concerning the application of GaAs MIC DROs is found in their long-term frequency stability. Most authors choose to ignore this specification. Work by Varian indicates that careful screening of FET devices can be used to improve the long-term stability of GaAs MIC DROs. The best long-term DRO stability to date, however, would appear to be 5ppm/year for a bipolar DRO.

3.7 Chapter Summary

An ideal narrowband frequency source should be highly frequency stable, reliable, compact, low cost, efficient and have good output characteristics.

The discussion in this chapter has shown that DROs make excellent frequency sources. They outperform other narrowband solid-state sources on all criteria with the exception of the high stability characteristics of quartz crystal phase locked microwave sources.

GaAs MESFET MIC DROs consist of a GaAs MESFET transistor embedded in a microwave integrated circuit with a dielectric resonator as a resonant element. Each of the components has ideal characteristics for use in a narrowband source with the exception of the long-term characteristics of the FET.

A literature review has shown that GaAs MIC DROs have the best published results for efficiency, power output, power temperature stability and external Q factor. The best noise performance, temperature stability and pushing factor results for a DRO were those for a FET DRO featuring a DR in a separate temperature stabilisied invar cavity and a two-stage FET amplifier. The best long-term frequency stability characteristics have been recorded for a bipolar DRO.

CHAPTER 4

BASIC MICROWAVE OSCILLATOR THEORY

4.1 Introduction

This chapter discusses basic oscillator theory. Oscillator theory developed by Kurokawa can be applied to both negative resistance oscillators and feedback oscillators and is first used to derive the oscillation conditions for a microwave oscillator. Impedance locus, device-line and operating point are introduced and series and parallel resonance discussed. These concepts are then used to explain how frequency and power hysteresis occur in microwave oscillators.

The components of a GaAs MESFET MIC DRO are best described in terms of their S-parameters. To this end N-port microwave oscillator analysis is discussed using scattering matrices. The analysis is shown to be consistent in the case of a two-port active device with Kurokawa's results.

4.2 Analysis of Microwave Oscillators by Kurokawa's Method

4.2.1 Modelling of Microwave Oscillators for Analysis by Kurokawa's Method

From a practical perspective it is convenient to split microwave solid state oscillators into two categories - negative resistance oscillators and feedback oscillators. These are illustrated in Figure 4.1 (Hamilton, 1978: 63).

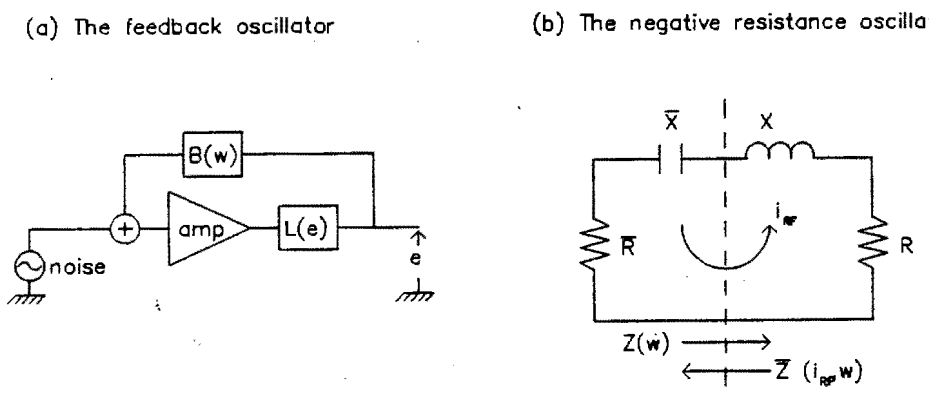

Fig 4.1 The two types of solid-state oscillator

In 1969 Kurokawa (Kurokawa, 1969) published a general analysis of negative resistance oscillators. His ideas have formed the basis for most subsequent microwave oscillator work.

Kurokawa proposed that a free running negative resistance microwave oscillator could be modelled as shown in Figure 4.2.

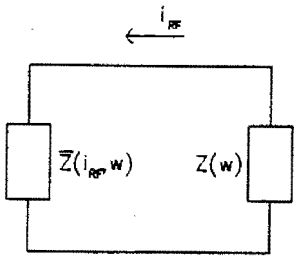

Fig 4.2 Equivalent circuit of a free-running microwave oscillator

$Z(\omega)$ is the circuit impedance seen from the device and $\bar{Z}(i_{RF}, \omega)$ is the device impedance. The important point to note is that the circuit impedance is amplitude independent whilst the device impedance is a function of the RF signal amplitude i_{RF}.

For a negative resistance oscillator the reference plane is chosen at the device terminals since this allows the active and passive parts of the circuit to be nicely separated.

Khana (Kajfez, 1986: 484) points out that this analysis can be applied to any microwave oscillator. This is because any oscillator can be represented in an arbitrary plane on the output line by a nonlinear impedance $\bar{Z}$, having a negative real part, in series with a load impedance Z.

4.2.2 Oscillation Conditions (Kajfez, 1986: 484)

If we assume that a current $i_{RF}(t) = I_o \cos\omega_o t$ exists in the circuit and that the circuit has a high enough Q factor to suppress any harmonies then, by Kirchoff's law:

$$[Z(w_0) + \bar{Z}(I_0,w_0)].I_0 = 0 \qquad (4.1a)$$

Let $Z + \bar{Z} = (R + \bar{R}) + j(X + \bar{X}) = Z_T = R_R + jX_T$

Since I_0 is not = 0, $[Z + \bar{Z}] = 0$ ie $Z = -\bar{Z}$ (4.1b)

Thus and $R_T + jX_T = 0$ (4.1c)

$$R_T(I_0,w_0) = 0 \qquad (4.2a)$$

$$X_T(I_0,w_0) = 0 \qquad (4.2b)$$

Since $Re(Z) > 0$, (4.1b) implies $Re(-\bar{Z}) > 0$
and thus $Re(\bar{Z}) < 0$ ie for oscillation the device must present a negative resistance.

The frequency of oscillation is determined by the requirement that the load reactance be equal and opposite to the device reactance i.e. equation (4.2b). This is known as the frequency resonance condition (Vendelin, 1982: 135) since it determines the frequency of oscillation. Equations (4.2a) and (4.2b) together imply what is known as the oscillator resonance condition i.e. both the circuit imaginary term and the circuit real term are zero for oscillation.

At microwave frequencies it is often more convenient to express oscillation conditions (4.2a) and (4.2b) in terms of the corresponding reflection coefficients Γ and $\bar{\Gamma}$. The oscillation condition becomes:

$\Gamma\,\bar{\Gamma} = 1$ (4.3a) where $\bar{\Gamma}$ = reflection coefficient looking into device
Γ = reflection coefficient looking into load

which is really two separate conditions

$$|\Gamma|.|\bar{\Gamma}| = 1 \qquad (4.3b)$$

$$\text{and } \angle\Gamma + \angle\bar{\Gamma} = 2\pi n, \text{ n is an integer} \qquad (4.3c)$$

These conditions correspond to the well known Barkhausen criteria for oscillation, namely:

(1) loop gain equal to unity
(2) net zero phase shift around the loop

The Barkhausen criteria are particularly useful for visualising the conditions for oscillation in a parallel feedback oscillation.

The equivalence of (4.3a) to (4.2a) and (4.2b) is derived in Appendix B.

4.2.3 Impedance Locus, Device Line and Operating Point (Kurokawa, 1973: 1387)

To appreciate the meaning of (4.1a) the locus of the circuit impedance and that of the device impedance are drawn on the complex plane by varying ω and i_{RF} as shown in Figure 4.3.

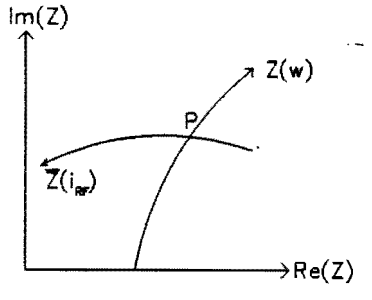

Fig 4.3 Impedance locus , device-line and operating point

The impedance line is defined as the locus of $Z(\omega)$ whilst the device line is defined as the locus of $\bar{Z}\ (i_{RF}, \omega)$. The arrowheads attached to the impedance line and device line indicate direction of increasing ω and i_{RF} respectively.

For steady state oscillation at frequency $Z(\omega_o)$ must be equal to $\bar{Z}(I_o, \omega_o)$. This corresponds to the intersection of the two loci and is known as the operating point.

4.2.4 Series and Parallel Resonance (Vendelin, 1982: 137)

When designing oscillators it is often useful to use a compressed Smith Chart whch allows reflection coefficients greater than one to be plotted. Since $\Gamma < 1$, $\bar{\Gamma} > 1$ for the oscillation condition (4.3a) to be satisfied. Figure 4.4 shows values of $\bar{\Gamma} > 1$ plotted on a compressed Smith Chart.

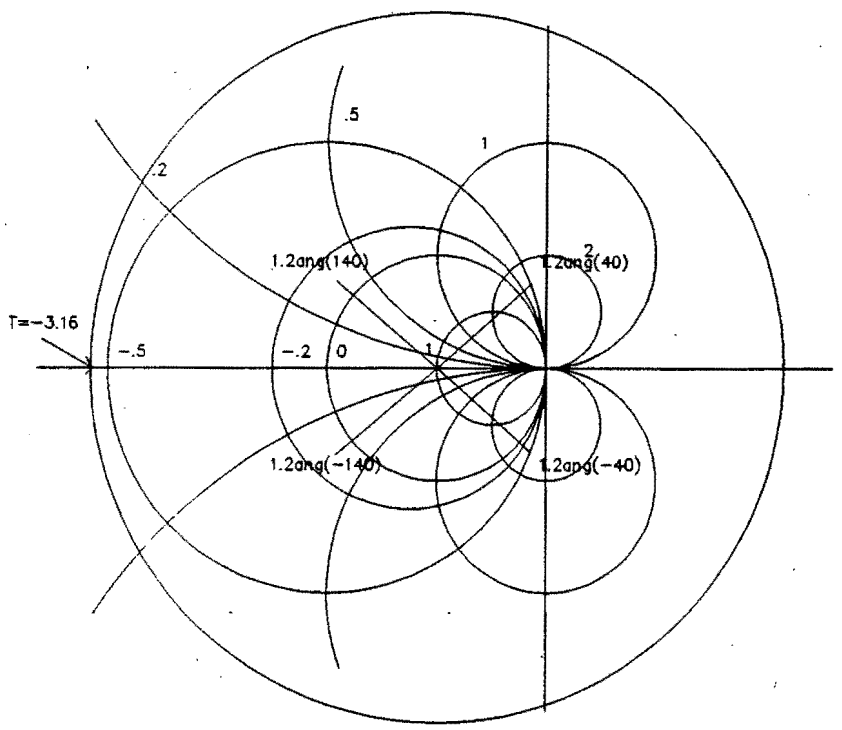

Fig 4.4 Reflection coefficients > 1 plotted on a compressed Smith Chart

As indicated a frequency resonance condition requires that the circuit imaginary term be zero. If the impedance resonance is on the left-hand real axis, this is a series resonance, i.e. at frequencies above resonance the impedance is inductive and below resonance the impedance is capacitive. If the impedance is on the right hand real axis the resonance is a parallel resonance. Oscillators can be divided into two types, series resonant or parallel resonant as shown in Figure 4.5.

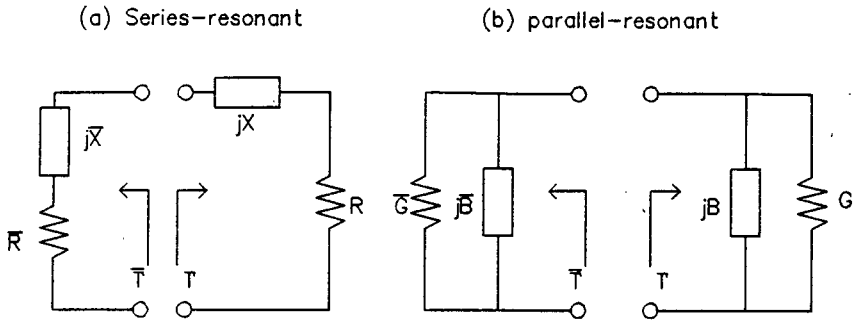

Fig 4.5 Series and parallel oscillator equivalent circuits

The equivalent circuit of the active device is chosen from the frequency response of the output port. Devices which are stable when terminated in an open circuit should be modelled as series circuits; those which are stable with a short circuit termination should be modelled as a shunt circuit (Hamilton, 1978: 65).

For the series-resonant condition the negative resistance of the active device should exceed the load resistance at the start up of oscillation by about 20 percent (Vendelin, 1982: 138). As the oscillation builds up the magnitude of the negative resistance of the active device drops due to large signal limiting effects until the steady state oscillation condition is reached.

A clear picture of how the operating point establishes itself can be seen in Figure 4.6 where the locus of $-\bar{Z}^{*}$ (i_{RF}) is shown together with the locus of $Z^{*}(\omega)$. These two quantities must be equal to each other for oscillation to occur and i_{RF} adjusts itself until this condition is met. This sets both the amplitude and frequency of oscillation. The conjugates of $-\bar{Z}(i_{RF})$ and $Z(\omega)$ have been used for convenience in plotting so that the two loci occur in the same quadrant of the R, jX plane.

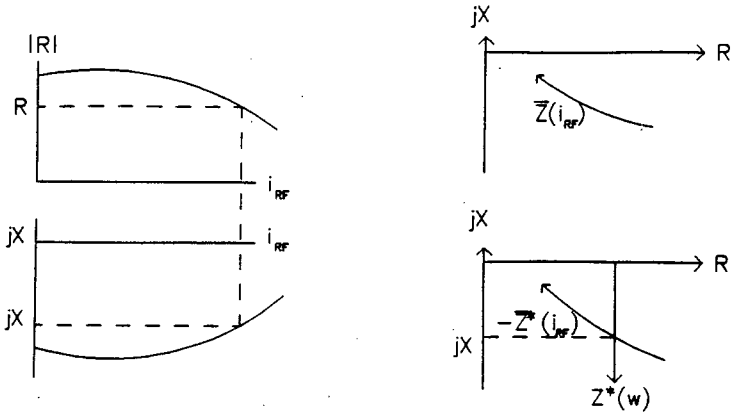

Fig 4.6 Series negative resistance circuit

4.2.5 Frequency and Power Hysteresis (Hamilton, 1978: 65) (Kurokawa, 1973: 1389)

To avoid hysteresis effects during tuning it is important that the active device be modelled correctly and then resonated with the appropriate type of resonant circuit. A series resonant device should be resonated by a series resonator.

Figure 4.7 shows a normally series connected device being resonated by a parallel resonant circuit. L_1C_1 represents a series resonant circuit due to package parasitics whilst L_2C_2 is the incorrectly added parallel circuit.

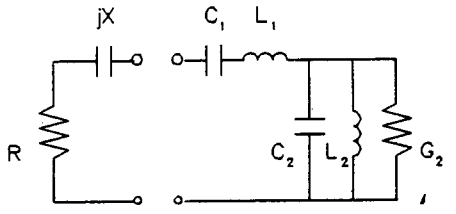

Fig 4.7 Series resonant circuit tuned by parallel circuit

The parallel resonant circuit has a negative reactance slope at ω_o given by:

$$\left.\frac{dX_2}{dw}\right|_{w=w_0} = -\frac{2C_2}{G_2^2} \qquad (4.4a)$$

and the positive slope of the reactance of the series network is:

$$\left.\frac{dX_1}{dw}\right|_{w=w_0} = 2L_1 \qquad (4.4b)$$

Three different situations now arise depending on the relative values of the slopes as shown in Figure 4.8.

(1) For $Q_1 > Q_2$, i.e. the positive series slope dominates, the circuit is undercoupled (Figure 4.8a). In this case there is a single well-determined operating point and no circuit tuning problems are encountered.

(2) For $Q_1 = Q_2$, i.e. the two slopes are equal, there is a cusp in the locus as shown in Figure 4.8b. Near the cusp the operating point becomes quite indeterminate and very noisy operation results.

(3) For $Q_1 < Q_2$, the negative slope of the parallel circuit dominates, resulting in a loop locus. A loop in the impedance locus produces the conditions required for frequency and power hysteresis. This phenomenon has been investigated by Kurokawa (Kurokawa, 1973: 1388).

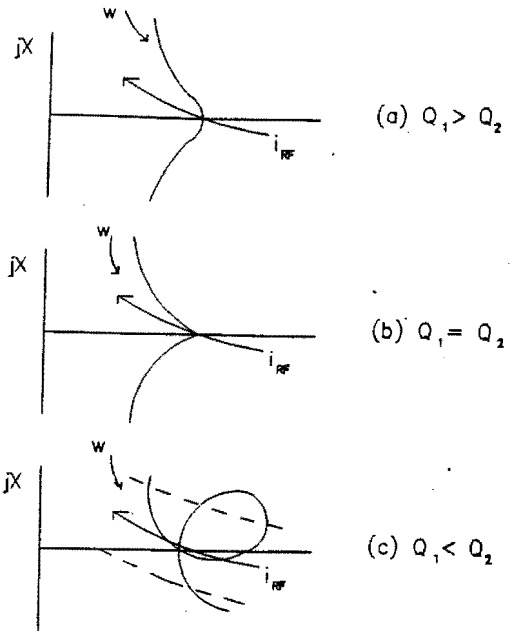

Fig 4.8 The impedance loci presented for different Q-values

Consider the case where the location of impedance locus with a loop is moved downwards by tuning the oscillator as shown in Figure 4.9.

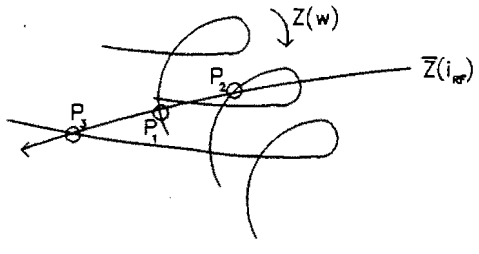

Fig 4.9 Variation of the operating point as the impedance locus changes it's position

The operating point P_1 moves first to the right as indicated by P_2 but as soon as the upper edge of the loop separates from the device line, the operation point jumps to the left.

Figure 4.10 shows the situation near the upper edge of the loop.

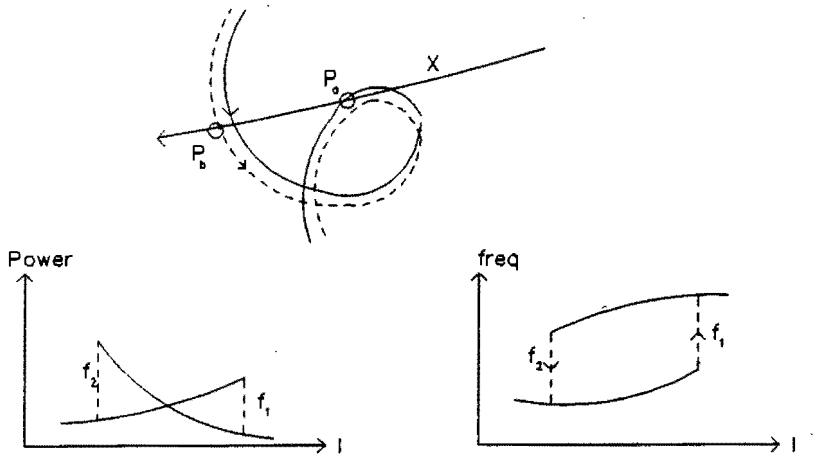

Fig 4.10 Typical frequency and power hysteresis as a result of a jump in the operating point

As the operating point P_a approaches the upper edge of the loop, the intersecting angle becomes small and oscillation becomes noisy. As the impedance locus moves downwards to the dotted position, the loop no longer intersects the device line - no steady state oscillation is therefore possible near the top of the loop. Consequently the operating point jumps to the point P_b. If the maximum power is located at a position indicated by X, the power initially increases as the locus moves downwards, since the operating point approaches the maximum power point. When the operating point jumps to P_b the power suddenly decreases and the frequency increases as indicated in Figure 4.10. If the adjustment is reversed, the locus moves upwards, the operating point moves to the right, and the frequency, as well as the power, follows a different path; and when the lower edge of the loop separates from the device line, the frequency and power suddenly jump again. In this particular case both frequency and power decrease.

4.3 N-port Microwave Oscillator Analysis Using Scattering Matrices (Kajfez, 1986: 485)

For the analysis of GaAs MIC DROS the best way to characterise the different components is in terms of their S-parameters as these are either supplied or easily measurable.

An oscillator can be considered as a combination of an active multiport and a passive multiport as shown below in Figure 4.11.

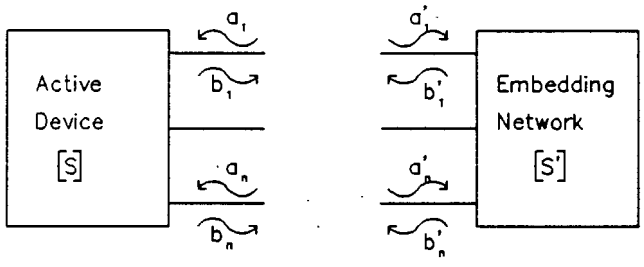

Fig 4.11 Oscillator as a combination of an active multiport and a passive multiport

For the active device we have $|\, b \,> \;=\; \underline{S} \;|\, a \,>$ (4.5a)

and for the embedding circuit $|\, b' \,> \;=\; \underline{S}' \,|\, a' \,>$ (4.5b)

When the active device and embedding network are connected together we have, for the oscillation conditions:

$$|\, b' \,> \;=\; |\, a \,> \qquad (4.6a)$$

and $|\, a' \,> \;=\; |\, b \,>$ (4.6b)

Thus $|\, a' \,> \;=\; |\, b \,> \;=\; \underline{S} \,|\, a \,> \;=\; \underline{S} \,|\, b' \,> \;=\; \underline{S}\underline{S}' \,|\, a' \,>$

or $(\underline{S}\underline{S}' - \underline{1}) \,|\, a \,> \;=\; |\, 0 \,>$ (4.7)

where $\underline{1}$ is the identity matrix. Since $|a' > \neq |0>$ it follows that $\underline{M} \equiv \underline{S}\,\underline{S} - \underline{1}$ is a singular matrix.

i.e. $\det \underline{M} = 0$ (4.8a)

This equation represents the generalised large signal oscillation condition for an n-port oscillator.

Equation (4.8a) can be split into two oscillation conditions namely:

$$|\det(\underline{S}\underline{S}' - \underline{1})| = 0 \quad (4.8b)$$

and $\text{Arg}\ \det(\underline{S}\underline{S}' - \underline{1}) = 0$ (4.8c)

4.3.1 Verification for a Two-port Loaded by Two Impedances (Kajfez, 1980: 487)

Figure 4.12 shows a two-port device loaded by two impedances.

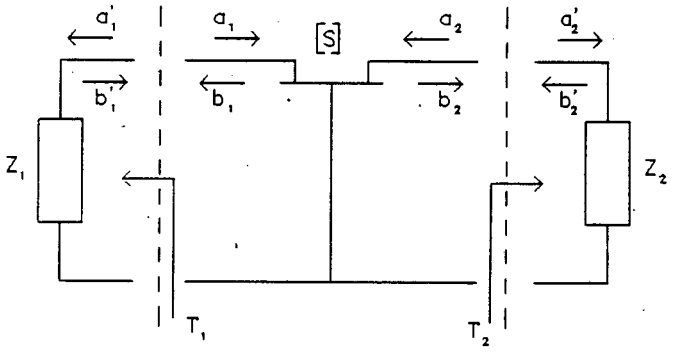

Fig 4.12 Two-port FET oscillator circuit

For the active device $\underline{S} = \begin{bmatrix} S_{11} & S_{12} \\ S_{21} & S_{22} \end{bmatrix}$ (4.9a)

and for the embedding circuit $\underline{S}' = \begin{bmatrix} \Gamma_1 & 0 \\ 0 & \Gamma_2 \end{bmatrix}$ (4.9b)

From (4.8a) oscillation condition is det $\underline{M} = 0$

$$|\underline{M}| = |\underline{SS}' - \underline{1}| = \begin{vmatrix} S_{11}\Gamma_1 - 1 & S_{12}\Gamma_2 \\ S_{21}\Gamma_1 & S_{22}\Gamma_2 - 1 \end{vmatrix} = 0$$

giving $(S_{11}\Gamma_1 - 1)(S_{22}\Gamma_2 - 1) - S_{12}S_{21}\Gamma_1\Gamma_2 = 0$ (4.10a)

This equation gives the well-known results first obtained by Baswapatna (Basawapatna, 1979):

$$S_{11} + \frac{S_{12}S_{21}\Gamma_2}{1 - S_{22}\Gamma_2} = \frac{1}{\Gamma_1} \quad (4.10b)$$

$$S_{22} + \frac{S_{12}S_{21}\Gamma_1}{1 - S_{11}\Gamma_1} = \frac{1}{\Gamma_2} \quad (4.10c)$$

These results can be written as $S_{11}'.\Gamma_1 = 1$ (4.11a)

and $S_{22}'.\Gamma_2 = 1$ (4.11b)

where S_{11}' is the modified reflection coefficient at port 1 with port 2 loaded by an impedance corresponding to a reflection coefficient Γ_2 as shown in Figure 4.13 below.

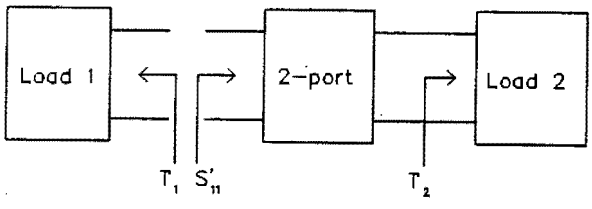

Fig 4.13 Modified reflection coefficient for a 2-port connected to a load

This result is essentially the same as equation (4.3a) derived earlier.

CHAPTER 5

BASIC SYNTHESIS OF TRANSISTOR DROs

5.1 Introduction

A dielectric resonator can be used in two different ways to produce a stable MIC transistor oscillator: (Kajfez, 1986: 490)

(1) as a passive stabilisation element used to stabilise a free-running transistor oscillator. Such an oscillator has been termed a "dielectrically stabilised oscillator"

(2) as an integral circuit element in the oscillator circuit where it is employed to determine the oscillator frequency. Such an oscillator has been termed a "stable transistor dielectric oscillator (STDRO)"

Synthesis involves constructing an oscillator using basic components whose characteristics need to be known accurately. At microwave frequencies S-parameter measurements are usually the most accurate way to characterise components since a good open or short circuit is difficult to obtain. The first section of this chapter, therefore, analyses dielectric resonators coupled to microstriplines and 3-port transistors in terms of their S-parameters.

The second section deals with the basic synthesis of "dielectrically stabilised oscillators" and the last with "stable DR transistor oscillators".

5.2 S-parameter Characterisation of Oscillator Components

A DR can be coupled to a single microstripline to produce a bandstop filter or to two lines simultaneously to give a bandpass filter.

5.2.1 S-parameter Characterisation of a Dielectric Resonator Coupled to a Microstripline as a Bandstop Filter

5.2.1.1 S-parameter Matrix of a DR Bandstop Filter

The most commonly used configuration for coupling a dielectric resonator to a microstripline is shown in Figure 5.1.

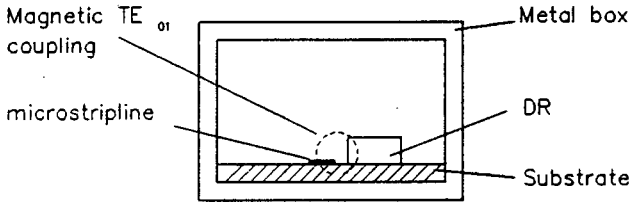

Fig 5.1 DR in a typical MIC configuration

The TE_{01} mode of the resonator is magnetically coupled to the TEM mode of the microstripline. The shielding conditions provided by the metallic shielding box and the turning screw affect the frequency and Q factor of the resonator as described later in Chapter 7.

Guillon et al. (Guillon, 1981) were among the first to realise that a dielectric resonator coupled to a microstripline can be modelled as a parallel resonant circuit in series with the line as shown in Figure 5.2.

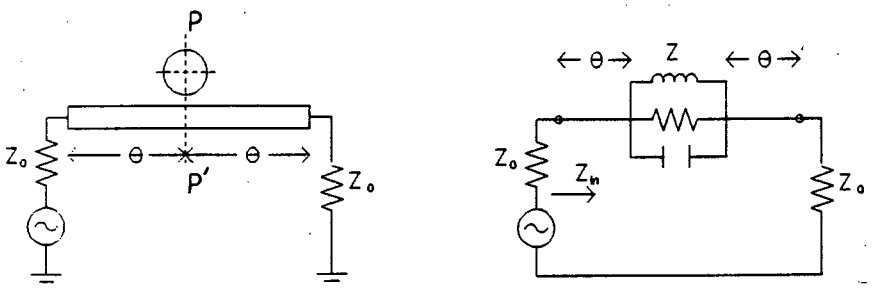

Fig 5.2 DP coupled to a microstripline and it's equivalent circuit

The coupling coefficient between the resonator and the line is defined as:

$$K = \frac{R}{R_{ext}} = \frac{R}{2Z_0} = \frac{S_{110}}{1 - S_{110}} = \frac{1 - S_{210}}{S_{210}} = \frac{S_{110}}{S_{210}} \qquad (5.1)$$

where S_{110} and S_{210} are the real quantities representing the reflection and transmission coefficients respectively in the symmetry plane PP'.

The normalised induced input impedance z_{in} is given by:

$$z_{in} = \frac{2K}{1 + j2Q_U\delta} + 1 \qquad (5.2)$$

where $$\delta = \frac{f - f_0}{f_0} \qquad (5.3)$$

This result is derived in Appendix C.

S_{11} can now be derived using the formula $$S_{11} = \frac{z_{in} - 1}{z_{in} + 1} \qquad (5.4)$$

giving $$S_{11} = \frac{K}{K + 1 + j2Q_U\delta} \qquad (5.5)$$

S_{21} is found using the relationship $S_{21} = 1-S_{11}$ which holds since $S_{11} = S_{22}$.

This gives
$$S_{21} = \frac{1 + j2Q_U\delta}{K + 1 + j2Q_U\delta} \tag{5.6}$$

The complete S-parameter matrix of the DR coupled to a microstripline line in the resonator plane is thus given by:

$$\underline{S}_R = \begin{bmatrix} \frac{K}{K + 1 + j2Q_U\delta} & \frac{1 + j2Q_U\delta}{K + 1 + j2Q_U\delta} \\ \frac{1 + j2Q_U\delta}{K + 1 + j2Q_U\delta} & \frac{K}{K + 1 + j2Q_U\delta} \end{bmatrix} \tag{5.7}$$

This reduces at resonance (δ=0) to

$$\underline{S}_{R0} = \begin{bmatrix} \frac{K}{K + 1} & \frac{1}{K + 1} \\ \frac{1}{K + 1} & \frac{K}{K + 1} \end{bmatrix} \tag{5.8}$$

The effect of the transmission line length (in the input and output planes) on the S-parameters can be included by simply adding a phase adjustment term giving finally:

$$S_{ij} = S_{ij}e^{-j2\theta} \tag{5.9}$$

The coupling factor K is a function of the distance between the dielectric resonator and the microstripline under fixed shielding conditions, it also relates the various quality factors by the equation:

$$Q_u = Q_L(1 + K) = KQ_{ex} \qquad (5.10)$$

where Q_U, Q_L and Q_{ex} represent the unloaded, loaded and external quality factor respectively.

5.2.1.2 Determining Q_U, Q_L and Kappa From Scalar Measurement of the Network Analyser Display of S_{11} or S_{22} for a DR Bandstop Filter

In a paper in 1983 (Khanna, 1983) Khanna and Garault described a method of determining the quality factors as well as the coupling coefficient Kappa from the network analyser display of S_{11} or S_{22}.

K is determined directly from equation (5.1) whilst using the equations derived in Appendix D it becomes possible to determine the quality x needed for the measurement of Q_U and Q_L from the transmission coefficient magnitude plane as shown in Figure 5.3(a).

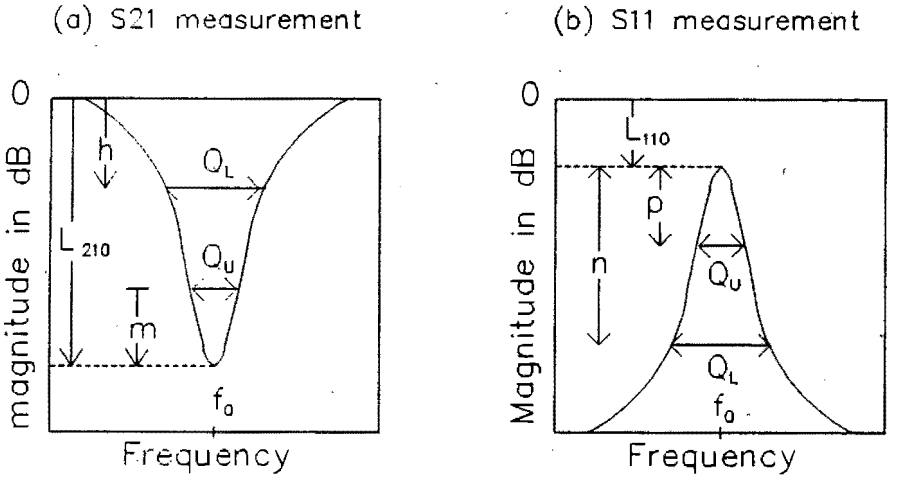

Fig 5.3 Determination of Qu and Ql for a BRF from scalar measurement of S21 and S11

$$x(dB) = h = m = 3 - 10\log_{10}(1 + 10^{-0.1L_{210}}) \qquad (5.11)$$

where the insertion loss L_{210} is given by

$$L_{210}(dB) = -20\log_{10}S_{210} \qquad (5.12)$$

Similar calculations apply to the reflection coefficient magnitude plane producing quantities n and p required for the measurement of Q_L and Q_U respectively as shown in Figure 5.3(b).

$$n = \text{a constant } 3 \text{ dB} \tag{5.13}$$

$$p = 10\log_{10}(10^{0.1L_{110}} - 2.10^{0.05L_{110}} + 2) \tag{5.14}$$

Thus Khanna and Garault's method allows simple magnitude measurements of either the reflection coefficient or transmission coefficient displays to determine the coupling coefficient κ, Q_U and Q_L. These empirical values can then be substituted in the S-parameter matrix to fully characterise the dielectric resonator coupled to a microstripline under given shielding conditions.

5.2.1.3 Determination of R, L and C from Kappa and Q_U

For CAD design the bandstop filter is best modelled using the equivalent circuit shown in Figure 5.2.

From (5.1) $$R = 2Z_0\kappa \tag{5.15}$$

For a parallel LRC circuit $$Q_U = \frac{R}{w_0 L} = w_0 RC \tag{5.16}$$

Thus $$L = \frac{R}{w_0 Q_U} \tag{5.17}$$

$$C = \frac{Q_U}{w_0 R} \tag{5.18}$$

5.2.2 S-parameter Characterisation of a Dielectric Resonator Simultaneously Coupled to Two Microstriplines to Form a Bandpass Filter

5.2.2.1 S-parameter Matrix of a DR Bandpass Filter

A model for a dielectric resonator coupled between two microstriplines as a bandpass filter was presented by Galwas in 1983 (Galwas, 1983). The arrangement to be modelled is shown in Figure 5.4 and the equivalent circuit in Figure 5.5.

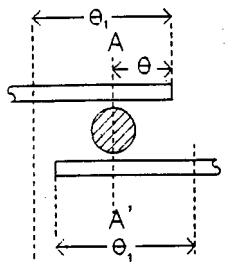

Fig 5.4 DR coupled simultaneously to two microstriplines

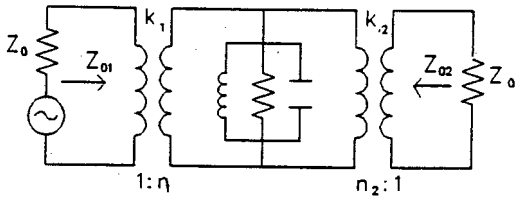

Fig 5.5 Equivalent circuit of a DR coupled to two microstriplines

This model is limited to the case where $\theta = \theta_1 = \pi/2$ at the resonant frequency. This results in an effective short circuit at the plane AA' and optimal magnetic coupling of the resonator to the microstriplines in the TE_{01} mode.

The S-parameter matrix of this configuration at the resonant plane can be presented by:

$$\underline{S}_R = \begin{bmatrix} \dfrac{K_1 - K_2 - 1 - j2Q_U\delta}{1 + K_1 + K_2 + j2Q_U\delta} & \dfrac{2\sqrt{(K_1K_2)}}{1 + K_1 + K_2 + j2Q_U\delta} \\ \dfrac{2\sqrt{(K_1K_2)}}{1 + K_1 + K_2 + j2Q_U} & \dfrac{K_2 - K_1 - 1 - j2Q_U\delta}{1 + K_1 + K_2 + j2Q_U\delta} \end{bmatrix} \quad (5.19)$$

where K_1 and K_2 are the coupling coefficients of the DR with the input and output microstriplines defined as:

$$K_1 = \frac{R}{n_1^2 z_{01}} \quad (5.20)$$

$$K_2 = \frac{R}{n_2^2 z_{02}} \quad (5.21)$$

Appendix E sets out the derivation of the S-parameters from the equivalent model.

Podcameni and Conrado in a paper in 1985 (Podcameni, 1985) took this work further to analyse the configurations of Figure 5.6(a) and Figure 5.6(b) where θ was allowed to vary.

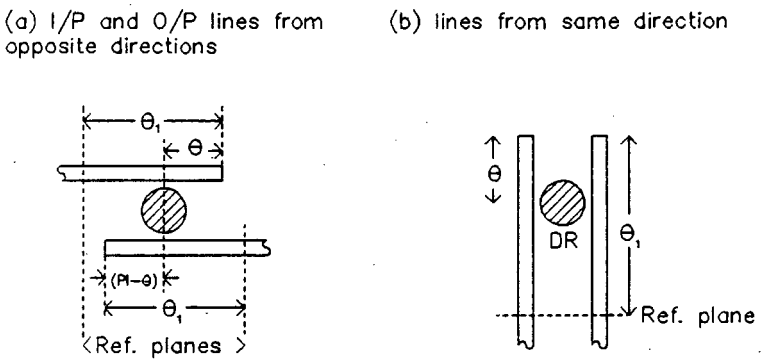

Fig 5.6 Two configurations possible for a transmission mode DR coupled between two microstriplines

They proposed the equivalent circuits shown in Figure 5.7 to model these configurations.

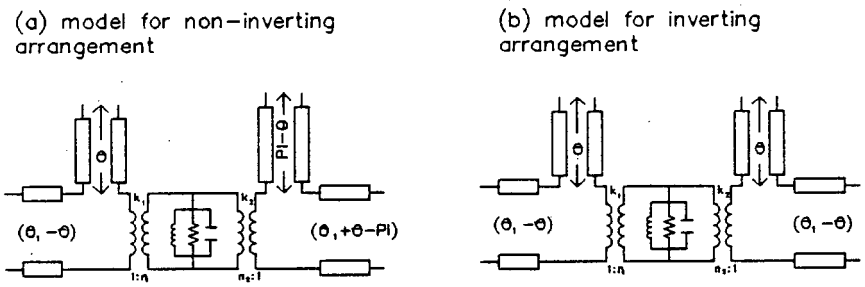

Fig 5.7 Equivalent circuits using open circuit stubs

These two models differ fundamentally in that there exists a phase inversion as far as transmission is concerned. In addition, whilst the resonant frequency of the circuit in Figure 5.6 (a) is that of the DR, this is not true for the circuit of Figure 5.6(b). In this case the resonant frequency is near, but not equal to, that of the DR.

Furthermore, the frequency of this circuit depends on θ, i.e. the position of the DR relative to the ends of the microstriplines.

The important point concerning θ is that it can be used to alter the magnitude response of the bandpass filter without affecting its phase provided the resonant frequency is kept constant (constant retuning required for the circuit in Figure 5.6(b)). The amplitude response as a function of θ is depicted in Figure 5.8. This is identical for both circuits.

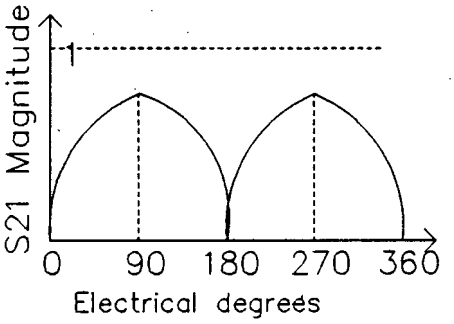

Fig 5.8 Transmission coefficient magnitude as a function of the DR position

The maximum transmission value, obtained at $\theta = \pi/2$, depends on the coupling factors κ_1 and κ_2.

For the symmetrical case $\kappa_1 = \kappa_2 = \kappa$ the S-parameter matrices obtained can be written as: (Podcameni, 1985: 1330)

(1) For the circuit in Figure 5.7(a)

$$S_{R(1)} = e^{-j2\theta_1} \begin{bmatrix} 1 - \dfrac{2\kappa\sin^2\theta}{D_1} & \dfrac{-2\kappa\sin^2\theta}{D_1} \\ \dfrac{-2\kappa\sin^2\theta}{D_1} & 1 - \dfrac{2\kappa\sin^2\theta}{D_1} \end{bmatrix} \qquad (5.22)$$

where $D_1 = 2\kappa\sin^2\theta + 1 + j2Q_U\delta$

(2) For the circuit in Figure 5.7(b)

$$S_{R(2)} = e^{-j2\theta_1} \begin{vmatrix} 1 - \dfrac{2K\sin^2\theta}{D_2} & \dfrac{2K\sin^2\theta}{D_2} \\ \dfrac{2K\sin^2\theta}{D_2} & 1 - \dfrac{2K\sin^2\theta}{D_2} \end{vmatrix} \qquad (5.23)$$

where $D_2 = 2K\sin^2\theta + 1 + j(2Q_U\delta + 2K\cot\theta\sin^2\theta)$

For the case $\theta_1 = \theta_2 = \pi/2$ these matrices reduce to

$$S_{R(1)} = \begin{bmatrix} \dfrac{-1 - j2Q_U\delta}{1 + 2K + j2Q_U\delta} & \dfrac{2K}{1 + 2K + j2Q_U\delta} \\ \dfrac{2K}{1 + 2K + j2Q_U\delta} & \dfrac{-1 - j2Q_U\delta}{1 + 2K + j2Q_U\delta} \end{bmatrix} \qquad (5.24)$$

and

$$S_{R(2)} = \begin{bmatrix} -1 + \dfrac{2K}{1 + 2K + j2Q_U\delta} & \dfrac{-2K}{1 + 2K + j2Q_U\delta} \\ \dfrac{-2K}{1 + 2K + j2Q_U\delta} & -1 + \dfrac{2K}{1 + 2K + j2Q_U\delta} \end{bmatrix} \qquad (5.25)$$

Comparing (5.4) with (5.19) we see that the models of Galwas and Podcameni are consistent at least for the case $K_1 = K_2 = K$.

5.2.2.2 Determining Q_U, Q_L and Kappa from Scalar Measurement of the Network Analyser Display of S_{11} or S_{21} for a DR Bandpass Filter with Equal Coupling

The results required to determine Kappa, Q_U and Q_L from scalar measurements in the reflection and transmittance planes are presented here. As far as the author knows they have not been reported elsewhere in the literature, although they follow on directly from the work of Guillon et al. on bandstop filters. The results are derived in Appendix F.

Transmittance measurements

Figure 5.9(a) shows the measurement points for a transmission magnitude display.

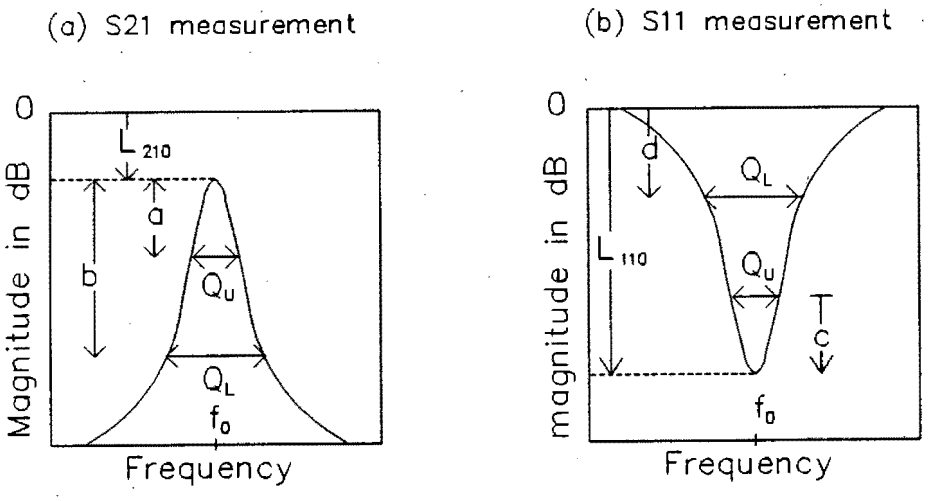

Fig 5.9 Determination of Qu and Ql for a BPF from scalar measurement of S21 and S11

L_{210} is measured on the display and used to calculate S_{210}, Kappa, a and b, using the equations below. Knowing a and b, Q_U and Q_L can be read off the display.

$$S_{210} = 10^{-0.05L_{210}} \tag{5.26}$$

$$K = \frac{S_{210}}{2(1 - S_{210})} \tag{5.27}$$

$$a = -20\text{Log}_{10}\left| \frac{1}{\sqrt{(S_{210}^2 - 2S_{210} + 2)}} \right| \tag{5.28}$$

$$b = \text{a constant 3dB} \tag{5.29}$$

Reflection measurements

Figure 5.9(b) shows the measurement points for a reflection magnitude display.

L_{110} is measured on the display and used to calculate S_{110}, Kappa, c and d. Knowing c and d, Q_U and Q_L can be read off the display.

$$S_{110} = 10^{-0.05L_{110}} \tag{5.30}$$

$$K = -\frac{(1 + S_{110})}{2S_{110}} \tag{5.31}$$

$$c = d = 20\log_{10}\left[\frac{\sqrt{(S_{110}^2 + 1)}}{\sqrt{2}} \right] \text{ dB} \tag{5.32}$$

5.2.2.3 Determination of R', L' and C' from Kappa and Q_U

For the case of equal coupling the circuit of Figure 5.5 can be simplified to that of Figure 5.10 where

$$R' = \frac{R}{n^2} \quad (5.33) \qquad L' = \frac{L}{n^2} \quad (5.34) \qquad C' = n^2C \quad (5.35)$$

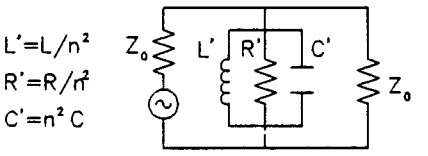

Fig 5.10 Equivalent circuit of DR BPF for equal coupling

For equal coupling $K = K_1 = K_2 = \frac{R}{n^2 Z_0} = \frac{R'}{Z_0}$ (5.36)

giving $R' = KZ_0$ (5.37)

$$Q_U = \frac{R}{w_0 L} = \frac{\frac{R}{n^2}}{w_0 \frac{L}{n^2}} = \frac{R'}{w_0 L'} \quad (5.38)$$

Thus

$$L' = \frac{R'}{w_0 Q_U} = \frac{KZ_0}{w_0 Q_U} \quad (5.39)$$

also $Q_U = w_0 RC = w_0 (R/n^2)(n^2 C) = w_0 R'C'$ (5.40)

giving

$$C' = \frac{Q_U}{R' w_0} = \frac{Q_U}{KZ_0 w_0} \quad (5.41)$$

5.2.3 3-Port S-Parameter Characterisation of Transistors (Kajfez, 1986: 481)

Althougth a transistor is a three part device it is invariably characterised by its two port S-parameters with one of its parts grounded. The three different configurations possible are shown below in Figure 5.11.

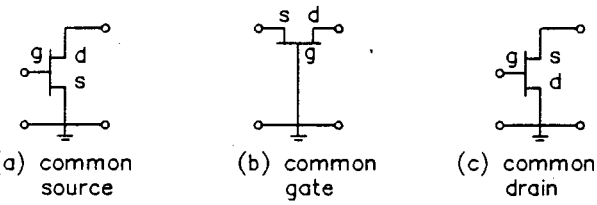

Fig 5.11 Three configurations of the transistor

Most manufacturers provide the common source S-parameters when specifying GaAs FET.

For the design work on oscillators to follow it is useful to be able to convert the 2-port common source S-parameters to 3-port parameters which can then be used to provide common gate and common drain S-parameters.

The transistor as a 3-port device is shown in Figure 5.12.

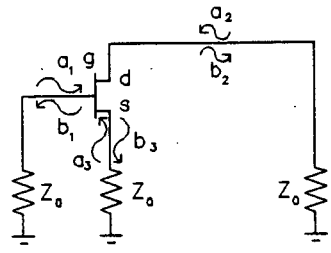

Fig 5.12 The transistor as a 3-port device

The S-parameter matrix for such a characterisation is given by:

$$\begin{bmatrix} b_1 \\ b_2 \\ b_3 \end{bmatrix} = \begin{bmatrix} S_{11} & S_{12} & S_{13} \\ S_{21} & S_{22} & S_{23} \\ S_{31} & S_{32} & S_{33} \end{bmatrix} \begin{bmatrix} a_1 \\ a_2 \\ a_3 \end{bmatrix} \qquad (5.42)$$

Appendix G derives the relations necessary to obtain analytically the 3-port S-parameters from the 2-port common source S-parameters.

5.3 Dielectrically Stabilised Oscillators (Kajfez, 1986: 491-493)

The use of a DR as a passive stabilisation element to stabilise a FET oscillator was the first method used to produce highly stable DROs (Abe, 1977). Passive stabilisation is only possible for free-running oscillators with a poor pulling figure, i.e. their frequency is sensitive to the variation in load impedance. The dielectic resonator is positioned with respect to the oscillator plane in such a way that the effective Q of the oscillator is increased. This results in better frequency stability at the expense of output power. For best frequency stability the loaded Q, Q_L, of the resonator should be as high as possible. Q_L is related to the unloaded Q, Q_U, by $Q_L = Q_U/(1+\kappa)$ (5.43), i.e. for best stability the DR should be lightly coupled.

Any of the classical cavity stabilisation modes can be used (i.e. reaction, reflection or transmission) but the reaction mode is the one generally used to realise a stabilised TDRO. This is shown in Figure 5.13.

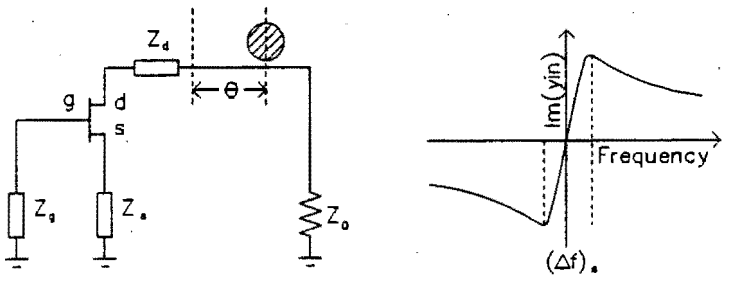

Fig5.13 Reactive mode DR stabilisation of a transistor oscillator

For the reactive mode stabilisation the DR is placed either a quarter (Makino, 1979: 634) or a half wavelength (Abe, 1978: 159) from the oscillator plane depending on whether the output requirements of the device require dX/dw positive or dB/dw positive respectively.

5.3.1 Stabilisation Range

In this section the stabilisation range is considered to be solely determined by the reaction mode DR filter - an approximation which gives useful information about the effects of factors such as the coupling coefficient on the stabilisation range. In point of fact the stabilisation range is determined by both the unstabilised oscillator resonant circuit and the reaction mode DR filter. Since two resonant circuits are involved, there is the possibility of hysteresis and two stabilisation ranges can be identified - one in which the stabilisation is free from hysteresis and one in which hysteresis occurs. The two stabilisation ranges are considered in more detail in Chapter 9.

5.3.1.1 Stabilisation Range of a Reaction Mode DR Circuit

The half wavelength case giving positive dB/dw is considered here. The quarter wavelength case (dX/dw positive) can be derived in a similar manner.

From (5.2) the normalised input admittance of the stabilisation circuit is given by:

$$Y_{in} = \frac{1}{1 + \dfrac{2K}{(1 + j\Delta)}} \qquad \Delta = 2Q_U\delta \qquad (5.44)$$

This has real and imaginary parts

$$Re(Y_{in}) = \frac{1 + 2K + \Delta^2}{(1 + 2K)^2 + \Delta^2} \qquad (5.45)$$

$$Im(Y_{in}) = \frac{2K\Delta}{(1 + 2K)^2 + \Delta^2} \qquad (5.46)$$

$Im(y_{in})$ is shown plotted in Figure 5.13 as a function of frequency.

The stabilised frequency range $(\Delta f)_s$ over which dB/df is positive is calculated by differentiating (5.46) and equating to zero. i.e.,

$$\frac{dB}{df} = 0 = \frac{4Q_U K[(1 + 2K)^2 - \Delta^2]}{f_0[(1 + 2K)^2 + \Delta^2]^2} \qquad (5.47)$$

This gives $|\Delta| = \left| \frac{f - f_0}{f_0} \right| 2Q_U = \frac{(\Delta f)_s}{f_0} Q_U = (1 + 2K)$ (5.48)

$$\text{i.e. } (\Delta f)_s = \frac{f_0}{Q_U}(1 + 2K) \qquad (5.49)$$

From the equation above (5.49) it is seen that the stabilisation range is a function of the coupling coefficient. Increasing the coupling of the DR to the line increases the stabilisation range.

5.3.2 Output Power Reduction

This stabilisation method reduces the useful RF output power in two ways. The first results from the fact that the unstabilised oscillator no longer sees a load impedance of 50Ω and the second is due to the insertion loss of the resonator.

From (5.45) the load admittance presented by the stabilisation circuit at resonance is given by:

$$Y_s = \frac{Y_0}{(1 + 2K)} \qquad (5.50)$$

This results in a reduction in output power L_1 given by:

L_1 = power output of oscillator with load impedance presented by DR / power output of oscillator when matched to 50Ω

$$L_1 = \frac{P_0 \left[\frac{Y_0}{(1 + 2K)} \right]}{P_0(Y_0)} \qquad (5.51)$$

The power loss due to the insertion loss of the resonator is given by:

$$L_2 = \frac{1}{(1 + K)^2} \qquad (5.52)$$

The total insertion loss of the stabilisation system is given by the sum of L_1 and L_2.

Equations (5.51) and (5.52) show that increasing the coupling results in a larger insertion loss.

5.3.3 Trade-offs Involving the Coupling Coefficient

The frequency stability, stabilisation range and output power have all been shown to be functions of the coupling coefficient.

In practice the stability range is usually the parameter which determines the coupling coefficient. The unstabilised oscillator usually has a fairly large temperature coefficient requiring a large stabilisation range to ensure stabilisation of the oscillator over the designed temperature range. Increasing the coupling coefficient to achieve adequate stability range results in decreased frequency stability and may result in an excessive insertion loss.

5.3.4 Mode Hopping and Hysteresis

Besides the disadvantage of inherent power loss, stabilised DROs also suffer from mode-hopping and hysteresis. As described in Chapter 4, these effects are the result of having two resonant circuits present - the free running oscillator tuned circuit and the DR stabilisation circuit. Chapter 9 describes hysteresis in dielectrically stabilised oscillators in more detail.

5.4 Stable Transistor DRO (STDRO) Design (Kajfez, 1986: 494)

A stable transistor DRO uses the dielectric resonator as a circuit element directly responsible for producing the conditions required for oscillation at a particular frequency. It is used as the matching element in a negative resistance oscillator and the feedback element in a feedback oscillator.

STDROs have the following advantages over stabilised DROs:

(1) no mode hopping or hysteresis

(2) reduced size and cost

(3) higher efficiency and therefore higher output with the same transistor

(4) simpler construction

They have, therefore, largely replaced stabilised TDROs.

5.4.1 STDRO Topology

As oscillator circuit can be represented as either a series or parallel feedback circuit as shown in Figure 5.14. In STDROs the DR is used to provide one or more of the immittances shown.

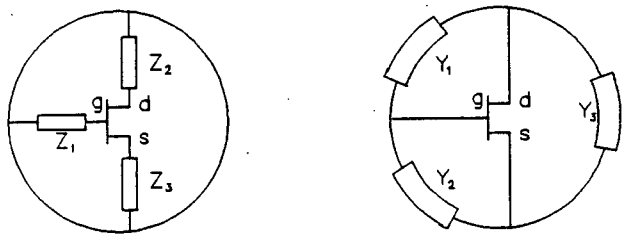

(a) Series (b) Parallel

Fig 5.14 Series and Parallel feedback oscillator configurations

Depending on whether the DR is used as a series or parallel feedback element, STDROs can be divided into series feedback STDROs and parallel feedback STDROs respectively.

5.4.2 Series Feedback STDROs

Figure 5.15 shows the basic configurations which have been used to produce series feedback STDROs.

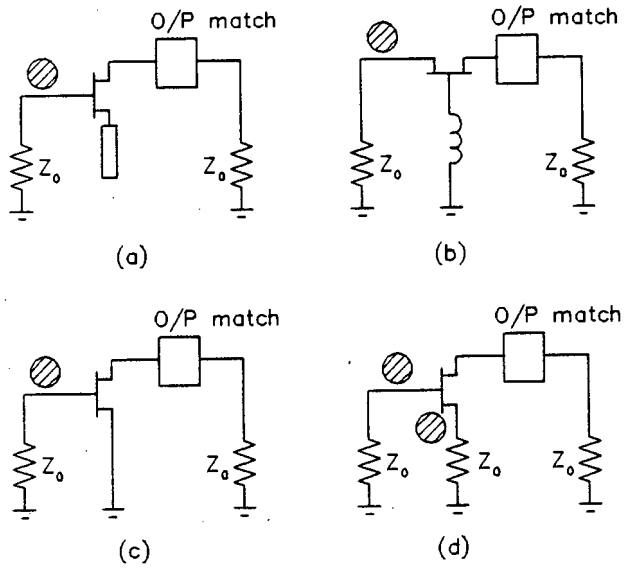

Fig 5.15 Different configurations for series feedback STDROs

Traditionally the series feedback STDRO with the form shown in Figure 5.16 has been termed a reflection DRO (Khanna, 1981). In this circuit the DR can be regarded as the matching element of a negative resistance oscillator.

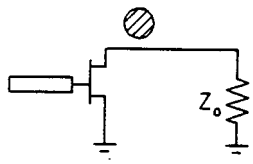

Fig 5.16 Reflection DRO

5.4.2.1 Basic Design of a Series Feedback STDRO (Kajfez, 1986: 495-500)

This section outlines the concepts involved in designing a series feedback oscillator with the configuration of Figure 5.15(a). Chapter 10 on series feedback STDROs contains a detailed step-by-step design example of such an oscillator with the relevant theory.

The conceptual design steps involved in the design of a common source series feedback oscillator are outlined in Figure 5.17. The transistor is characterised by its 3-port S-parameters for such a design.

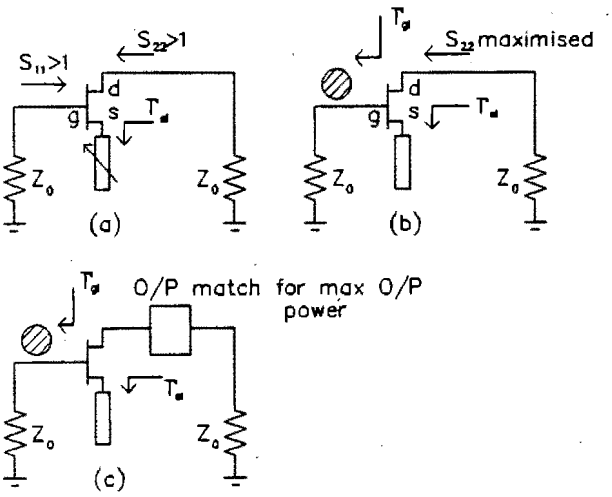

Fig 5.17 Conceptual steps in designing a common source series feedback STDRO

STEP 1: Determining a value of Z_s which gives $\Gamma_g > 1$ and $\Gamma_d > 1$

The first step in the design (Figure 5.17(a)) is to find a value of Z_s which results in values of both Γ_g and Γ_d greater than one for a 50 Ω measuring system. This provides the negative resistance conditions looking into the input and output ports required for oscillation.

STEP 2: Determining the optimal resonator position for maximum drain reflection coefficient.

The second step in the design (Figure 5.17(b)) is to determine the value of gate load reflection coefficient Γ_{gl} which maximises the magnitude of the drain (output) reflection coefficient. The magnitude of the required

load reflection coefficient determines the coupling of the DR to the microstripline whilst the phase angle determines the distance of the DR from the gate of the FET.

STEP 3: Determining the drain output match required for maximum oscillator output power.

The final step in the design of a common source feedback oscillator (Figure 5.17(c)) is to find the drain output match which results in maximum output power into 50 Ohms.

5.5 Parallel Feedback STDROs (Kajfez, 1986: 502)

The most commonly used configuration for a parallel feedback STDRO is shown in Figure 5.18.

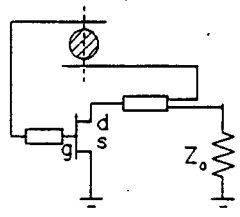

Fig 5.18 Parallel feedback STDRO using transistor as a 2-port device

This configuration basically consists of the transistor used as an amplifier with some of the output power being coupled back through a DR bandpass filter to sustain oscillations.

Thus, for instance, the transistor can be matched for best noise performance or for maximum transducer gain to achieve good frequency stability.

For oscillation to occur two criteria need to be satisfied:

(1) the total phase shift round the feedback loop must be a multiple of 2π radians

(2) the open loop small signal gain must exceed unity at f_o

The first condition can be written as:

$$\phi_A + \phi_R + \phi_C = 2\pi n \quad n = 0,1,2 \ldots \tag{5.53}$$

where ϕ_A, ϕ_R and ϕ_C are the respective insertion phases of the amplifier, the DR bandpass filter and the remaining feedback circuitry at f_o.

The second condition can be written as:

$$G_A - L_R - L_C > 0dB \tag{5.54}$$

where G_A, L_R and L_C are the amplifier gain, the DR bandpass filter insertion loss and the loss in the other feedback components in dB respectively.

Under steady-state oscillation conditions the total gain around the feedback loop is equal to unity. Since the open loop gain is designed for a value larger than unity to ensure reliable startup - amplifier gain compression occurs under steady state conditions.

For maximum oscillation output power the device is operating under large signal conditions and hence is already into gain compression.

Excessive gain compression can adversely affect the oscillator noise performance due to increased amplified noise figure and AM to FM conversion.

Thus achievement of high oscillation output power levels in parallel feedback oscillators has to be traded off against good noise performance and frequency stability.

CHAPTER SIX

OPTIMAL DESIGN OF MICROWAVE OSCILLATORS AND DROs

6.1 Introduction

Chapter 3 has shown that GaAs MCI DROs inherently have the potential to make ideal narrowband sources provided long-term stability is not a stringent requirement.

It is obvious that a MIC DRO cannot be built which optimises all the factors required of a narrowband source simultaneously. Most of the factors can only be optimised at the expense of one or more of the others. For example, designing for best noise performance requires large amounts of feedback power. This is at cross purposes with extracting the maximum possible output power from the oscillator.

This chapter begins by considering the oscillator design criteria required to achieve:

(1) best noise performance
(2) best frequency temperature stability
(3) best long-term stability
(4) maximum output power
(5) maximum efficiency

In the case of a GaAs MIC DRO, once a particular topology has been decided upon, there are three basic parameters which can be used to optimise performance:

(1) the specficiation of an active device
(2) the matching of the active device to the circuit
(3) the coupling of the dielectric resonator into the circuit

Using these parameters it is demonstrated that it is not possible to optimise all five performance criteria simultaneously. Oscillator design is thus usually a matter of compromise.

6.2 Oscillator Design for Different Performance Criteria

6.2.1 Designing for Optimum Low Noise Performance (Scherer, 1979) (Muat, 1984)

This section investigates the factors influencing the noise performance of an oscillator as described by Leeson's equation. F, f_C, P_{avail} and Q_L are isolated as parameters which can be optimised to give low noise performance. The optimisation of these parameters is discussed and used to produce a summary of important design criteria for low noise oscillators.

6.2.1.1 Optimising the Factors Influencing the Low Noise Performance of an Oscillator as Described by Leeson's Equation

A simple first order approximation describing the phase noise performance of an oscillator is given by Leeson's equation (Scherer, 1979: 120)

$$L(f_m) = \frac{FkT}{P_{avail}} \cdot \left[1 + \left[\frac{1}{f_m} \cdot \frac{f_0}{2Q_L} \right]^2 \right] \cdot \frac{1}{2} \left[1 + \frac{f_c}{f_m} \right] \qquad (6.1)$$

where $L(f_m)$ = the ratio of the noise power due to phase modulation in a 1 Hz bandwidth (centred f_m Hz off the carrier) to the total signal power.

F = the noise factor of the active device
k = Boltzman's constant
T = temperature in Kelvin
P_{avail} = the power available from the source in Watts
f_c = corner frequency for flicker noise of the device

$\frac{f_0}{2Q_L}$ represents the half bandwidth of the resonator

For $L(f_m)$ within the half-bandwidth of the resonator, i.e. $f_m < \frac{f_0}{2Q_L}$

then $(\frac{1}{f_m} \frac{f_0}{2Q_L})^2 > 1$

and Leeson's equation can be simplified to

$$L(f_m) = \frac{1}{2} \cdot \frac{1}{f_m^2} \left[\frac{f_0}{2Q_L} \right]^2 \cdot \frac{FkT}{P_{avail}} \left[1 + \frac{f_c}{f_m} \right] \qquad (6.2)$$

From this equation it follows that, for a particular oscillation frequency f_o, spectral purity close to the carrier will depend on f_c, F, P_{avail} and Q_L. For best noise performance f_c and F should be minimised whilst P_{avail} and Q_L should be maximised.

(a) Minimising f_c

To minimise f_c the active device should have low flicker noise. As already discussed, silicon bipolar transistors have better flicker noise characteristics than GaAs FETs but can only be used at low microwave frequencies. The effect of flicker noise should also be minimised by employing low frequency feedback and effective biasing of the active device.

Camiade et al. (Camiade, 1983) have investigated the solid state mechanisms in a FET responsible for producing low frequency flicker noise which becomes phase noise around the carrier under oscillation conditions.

They have derived the following simplified equation for the low frequency noise in terms of physical FET parameters:

$$S_{en}(f) = \frac{4V_p^2}{N_D Z a L}\left[X(X - X)^2 . \frac{\alpha c}{f}\right] \qquad (6.3)$$

where S_{en} is the spectral density function of the low frequency noise
V_P is the pinch off voltage
N_D is the doping density
Z is the gate width
L is the gate length
a is the epi-layer thickness

and

$$X = 1 - \sqrt{\frac{V_{bi} - V_{gs}}{V_p}}$$

V_{bi} is the built in voltage and
V_{gs} is the gate source voltage

$$10^{-5} < \alpha c < 10^{-3}$$

From this relationship it appears that an efficient way of ensuring minimum low frequency noise is to select devices with large gate widths and large gate lengths. There is a limitation to this choice since as Z and L increase the negative resistance available from the device decreases. To compensate for this higher coupling between the DR and the microstrip circuit is necessary resulting in a lower Q_L. The relationship does show, however, that power devices which have large Z should be considered for low noise design.

(b) Minimising F

To minimise F an active device should be chosen which has an intrinsically low noise figure. In addition the FET must be matched to the circuit with input and output reflection coefficients corresponding to those required for minimum noise figure. For good noise performance P_{avail} also needs to be maximised. Thus a compromise may result between matching for best noise figure and matching to improve P_{avail}.

(c) Maximising Q_L

The loaded Q, Q_L, depends on the unloaded Q of the resonator, Q_U and the coupling of the circuit to it. For maximum loaded Q the resonator should have as high an unloaded Q as possible and be lightly coupled to the rest of the circuit, i.e. also have a high external Q. This is summarised by the equation

$$\frac{1}{Q_L} = \frac{1}{Q_{ex}} + \frac{1}{Q_U} \qquad (6.4)$$

Q_L can also be expressed as $Q_L = \dfrac{w_0 W_e}{\text{Total dissipated power}}$ (6.5)

where W_e is the reactive energy in the resonator at frequency w_0

The resonator can be modelled as a parallel RLC circuit (see Chapters 7 and 8) so that the reactive energy can be expressed as:

$$W_e = \frac{1}{2} CV^2 \qquad (6.6)$$

Thus, for best Q_L the reactive energy should be maximised by means of a high r.f. voltage across the resonator. The maximum limit for this is set by the breakdown voltage of the active device. An active device with good voltage breakdown characteristics should thus be selected for low noise design (Scherer, 1979: 122).

It should be noted that increasing Q_L by decreasing the coupling in a feedback oscillator increases the resonator insertion loss thus reducing P_{avail}. There is therefore a compromise between maximising Q_L and P_{avail} for best noise performance.

To maximise the loaded Q one also needs to understand how it is related to the loop gain phase slope $\frac{\partial(\text{ang(loop gain)})}{\partial f}\Big|_{f = f_o}$

The relation is $$Q_L = \frac{f_0}{2} \cdot \frac{\partial(\text{ang(loop gain)})}{\partial f}\Big|_{f = f_0} \qquad (6.7)$$

Thus for best phase noise performance oscillation should occur at the maximum phase slope where Q_L is a maximum. This can be achieved by adjusting the coupling network.

(d) Maximising the available power

To maximise the available power the signal power taken out should be minimised without going below the limits set by additive noise. Thus most of the power is available to the feedback loop.

Maximum P_{avail} is also achieved by selecting a high power FET.

6.2.1.2 Summary of Design Criteria for a Low Noise Oscillator

From the foregoing discussion the following points can be made concerning the design of low noise GaAs FETs oscillators:

(a) Active device characteristics

For low noise performance a device should be selected which:

(1) is a high power device
(2) has good flicker noise characteristics
(3) has a low noise figure
(4) has large voltage breakdown characteristics

The device should also be properly heatsunk

(b) Matching of the active device

The device should be matched for best noise figure. This may, however, have to be compromised with power matching considerations which also affect the noise performance of the oscillator.

(c) Quality factor of the resonator

The unloaded Q of the resonator should be as high as possible to achieve a high value of Q_L.

(d) Circuit considerations

The following circuit considerations should be implemented in a low noise design:

(1) low frequency feedback and effective biasing should be employed to minimise flicker noise

(2) coupling to the resonator should be light to achieve high Q_{ex} and hence a high Q_L. However this may have to be compromised with considerations of coupling back P_{avail}.

6.2.2 Designing for Best Frequency Temperature Stability

The design of a highly temperature stable DRO depends on whether the DR is used to stabilise a free-running oscillator or as a series feedback

element in a STDRO. In both cases it is found that the temperature performance can be optimised by adjusting the temperature coefficient of the DR system or the coupling of the DR to the microstrip circuit.

6.2.2.1 Designing a DR Stabilitied Oscillator for Best Frequency Temperature Performance

The temperature behaviour of oscillators stabilised by a DR coupled to the output port as a bandreject filter was first analysed for a Gunn oscillator by Makino et al. (Makino, 1979) and for a FET oscillator by Abe et al. (Abe, 1978).

The temperature coefficient of a stabilised FET DR oscillator (see Chapter 9) is given by:

$$p = \frac{1}{f_r}.\frac{\Delta f_r}{\Delta T} + \frac{1}{1 + \frac{2K}{(1+2K)^2}.\frac{Q_U}{Q_{oex}}}.\frac{1}{f_0}.\frac{\Delta f_0}{\Delta T} \qquad (6.8)$$

It is seen that the stabilised oscillator temperature coefficient (p) depends on the temperature coefficient of the unstabilised oscillator ($\frac{1}{f_o}\frac{\Delta f_o}{\Delta T}$), the external Q of the unstabilised oscillator (Q_{oex}), the temperature coefficient of the DR and shield ($\frac{1}{f_r}\frac{\Delta f_r}{\Delta T}$), the unloaded Q of the DR (Q_U) and the coupling between the DR and the output line (K). Usually the properties of the unstabilised oscillator are fixed. This leaves the coupling coefficient and the temperature coefficient of the DR as parameters which can be used to provide temperature compensation. Usually the coupling coefficient is set and a DR chosen with appropriate positive temperature coefficient to cancel the negative temperature coefficient according to equation (6.8).

6.2.2.2 Designing a Series Feedback STDRO for Best Frequency Temperature Performance

The best DRO temperature stability has been reported for a series feedback STDRO (Tsironis, 1982). Tsironis has derived the following simplified equation to describe the frequency temperature behaviour of a series feedback STDRO:

$$\frac{df}{fdT} \approx \frac{1}{f_r}.\frac{df_r}{dT} + \frac{K + 1}{2Q_U}.\frac{\partial \phi_G}{\partial T} \qquad (6.9)$$

It is seen that STDRO temperature coefficient ($\frac{df}{fdT}$) is dependent on the temperature coefficient of the DR ($\frac{df_r}{f_r dT}$), the phase shift with temperature of the active device ($\frac{\partial \phi_G}{\partial T}$) and the coupling coefficient (K).

Tsironis found ϕ_G to vary linearly with temperature, i.e. $\frac{\partial \phi_G}{\partial T}$ = a constant = -2600ppm/K° for his device. For best temperature stability at a particular frequency we require $\frac{1}{f}\frac{df}{dT} = 0$. Since $\frac{\partial \phi_G}{\partial T}$ is constant it forms a proportionality factor between the DR temperature coefficient ($\frac{df_r}{f_r dT}$) and the stabilisation factor $\frac{K + 1}{2Q_U}$

$$\text{i.e.} \quad \frac{1}{f_r}.\frac{df_r}{dT} = -\left[\frac{\partial \phi_G}{\partial T}\right].\frac{K + 1}{2Q_U} \qquad (6.10)$$

$\frac{\partial \phi_G}{\partial T}$ is set for a particular device and Q_U for a particular resonant system so, as for the DR stabilised oscillator, two parameters remain to adjust the temperature stability - the temperature coefficient of the DR and the coupling coefficient.

A complete temperature compensation of the frequency drift of a GaAs FET oscillator is possible for a certain range of temperature coefficients of the dielectric material. Restrictions on the range are set mainly by the obtainable output power at different temperatures. This can be seen from Figure 6.1 (Tsironis, 1982: 186) where the resonator stability ($\frac{df_r}{f_r dT}$) needed for complete compensation of temperature drift ($\frac{df}{fdT} = 0$) is given, together with the stabilisation factor ($\frac{K+1}{2Q_U}$), on the left axis, as a function of the coupling between the resonator and the microstripline. The oscillation power is indicated on the right axis.

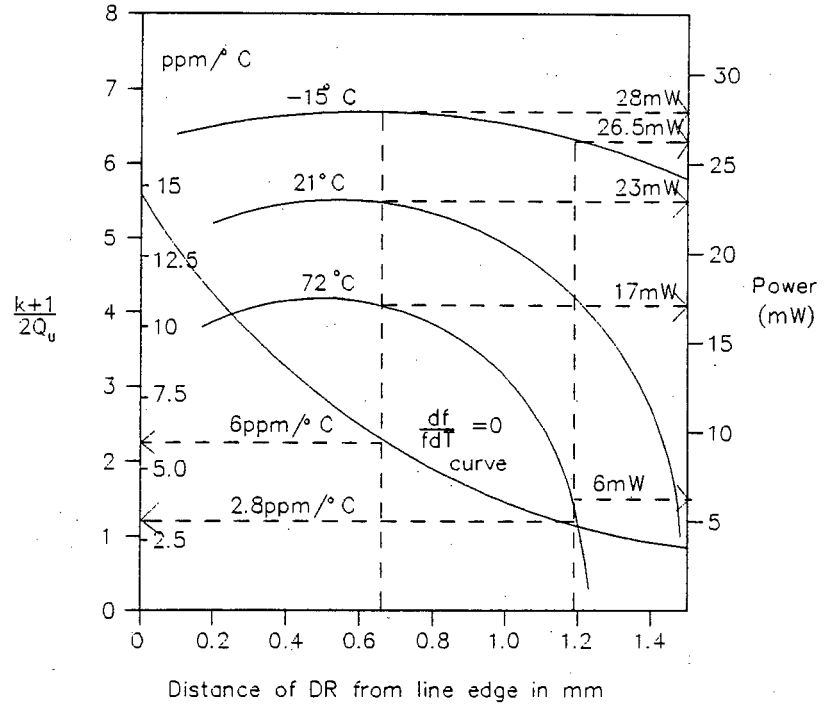

Fig 6.1 Coupling-stabilisation-power diagram of GaAs FET STDRO

Consider d = 0.63mm (resonator just touching line). Here $\frac{df_r}{f_r dT}$ = +6ppm/K, P(-15°) = 28mw; P(21°C) = 23mw, P(72°C) = 17mw i.e. an overall power variation from -15°C to +72°C of 2.2 dB results.

Consider d = 1.2mm then $\frac{df_r}{f_r dT}$ = 2.8ppm/K but the power variation between -15°C and 72°C is 4.5 dB with P(72°C) = 6mw. It is doubtful that the oscillator will start up reliably at higher temperatures.

Thus, in general, decreasing the coupling (by increasing d) increases the possibility of using a low $\frac{df_r}{f_r dT}$ material to compensate but increases the power drop at high temperatures.

It is seen from equation (6.10) that the larger the unloaded Q value of the DR the smaller will be the resonator temperature coefficient $(\frac{df_r}{f_r dT})$ required for stabilisation. Since it is easier to make DRs with small temperature coefficients the Q_U of the resonant system should be maximised for good temperature stabilisation.

6.2.3 Designing for Best Long-Term Frequency Stability

As already discussed in Chapter 3, the inadequate long-term frequency stability of FET DROs is the major factor preventing them from replacing phase locked oscillators in many applications.

Varian has isolated the integrity of the FET gate as being a significant factor in long-term drift (Varian, 1987).

From his paper the following points can be made concerning the design of oscillators with long-term stability:

(a) operating conditions of the FET

(1) FETs should not be subjected to electrical stresses greater than 50% of their rated maximum values. This may require a compromise with biasing conditions for optimal output power, noise figure etc

(2) the channel temperature of the FET should be kept below 150°C. Thus good heatsinking is essential. Power devices are usually better designed with regard to good heatsinking

(b) screening of the FET

The FET should be screened to minimise the change of gate capacitance with time. This may involve designing with a FET which has shown consistently high gate integrity from one device to another

6.2.4 Designing for Maximum Oscillator Power

This section describes how maximum FET oscillator power and the conditions required to obtain it can be determined using an empirical relation involving only P_{sat} and the small signal gain G. The problems involved with large signal design are briefly discussed. Finally a summary of design criteria for high power oscillators is presented.

6.2.4.1 Maximum FET Oscillator Output Power

Various empirical relationships have been derived to describe the power gain characteristics of a FET power amplifier.

Purcel et al. (Purcel, 1975: 219) approximated the characteristics with the expression:

$$P_{out} = \frac{GP_{in}}{1 + G.\frac{P_{in}}{P_{sat}}} \qquad (6.11)$$

where P_{sat} is the saturated output power
G is the small signal gain which varies as $G = \left[\frac{f_u}{f}\right]^2$
where f is the oscillator frequency and
f_u is the frequency at which the device gain becomes unity

Johnson (Johnson, 1979: 222) provided a better approximation which has an exponential form:

$$P_{out} = P_{sat}\left[1 - \exp\left[-\frac{GP_{in}}{P_{sat}}\right]\right] \qquad (6.12)$$

This expression can be used to calculate the maximum oscillator output power. For oscillators the objective is to maximise $(P_{out} - P_{in})$ of the amplifier which is the useful power to the load. For maximum oscillator output power:

$$\frac{\partial P_{out}}{\partial P_{in}} = 1 \qquad (6.13)$$

$$\frac{\partial P_{out}}{\partial P_{in}} = G.\exp\left[-\frac{GP_{in}}{P_{sat}}\right] = 1$$

$$\exp\left[\frac{GP_{in}}{P_{sat}}\right] = G \quad \text{or} \quad \frac{P_{in}}{P_{sat}} = \frac{\ln G}{G}$$

$$P_{in} = P_{sat}\left[\frac{\ln G}{G}\right] \qquad (6.14)$$

At the maximum value of $P_{out} - P_{in}$ the amplifier output is:

$$P_{out} = P_{sat}\left[1 - \exp\left[-\frac{G\ln G}{G}\right]\right]$$

$$= P_{sat}\left[1 - \exp\left[\frac{1}{\ln G}\right]\right] = P_{sat}\left[1 - \frac{1}{G}\right] \qquad (6.15)$$

Hence maximum oscillator output power is given by:

$$P_{osc(max)} = P_{out} - P_{in} = P_{sat}\left[1 - \frac{1}{G}\right] - P_{sat}\left[\frac{\ln G}{G}\right]$$

$$= P_{sat}\left[1 - \frac{1}{G} - \frac{\ln G}{G}\right] \qquad (6.16)$$

Figure 6.2 shows a plot of $\frac{P_{osc}}{P_{sat}}$ versus small signal common source gain G.

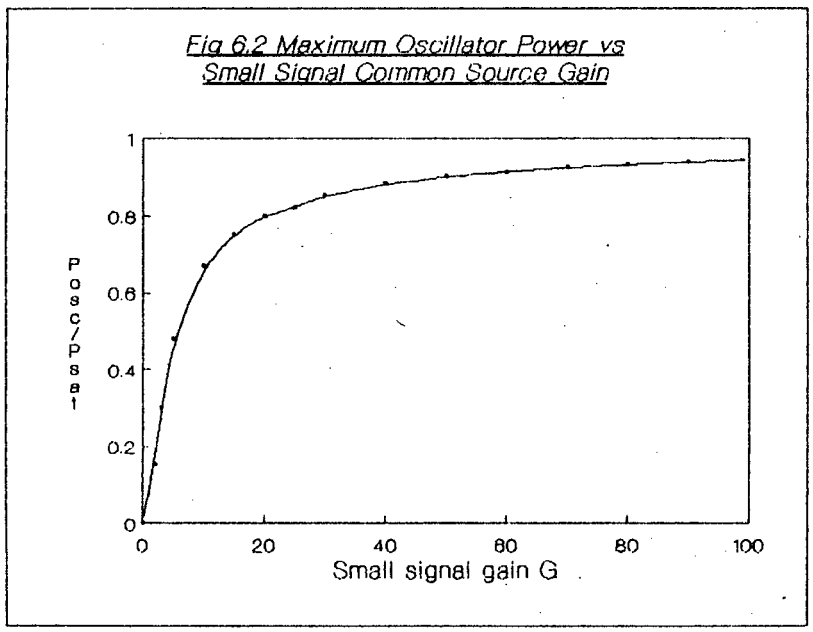

This illustrates the importance of high device gain for a high oscillator output power.

Maximum efficient gain is defined by Kotzebue (Johnson, 1979: 222) as the power gain which maximises the two-port added power, i.e. results in maximum oscillator output power. Thus the maximum efficient gain is given by:

$$G_{ME(max)} = \left[\frac{P_{out}}{P_{in}}\right]_{max} = \frac{P_{sat}\left[\frac{G-1}{G}\right]}{P_{sat}\left[\frac{\ln G}{G}\right]} = \left[\frac{G-1}{\ln G}\right] \quad (6.17)$$

6.2.4.2 Problems Involved with Large Signal Design

The problem with designing oscillators for maximum output power it that the S-parameters are a function of the device input and output power-levels. Thus the S-parameters used in such a design should be those which the device presents when operating under maximum oscillator power conditions.

Measuring large signal S-parameters is not an easy task since most network analysers are not capable of large signal operation. As a result work has been done to try and derive large-signal S-parameters from those measured for small signals using computer models, e.g. the work done by Johnson (Johnson, 1979).

Another approach is to do load pull measurements to determine the input and output match required for maximum power gain at a specific input power.

6.2.4.3 Summary of Design Criteria for High Power Oscillators

From the preceding discussion, the following points can be made concerning high power oscillator design:

(a) Active device characteristics

For a high power oscillator design a device should be selected which has

(1) P_{sat} as high as possible (i.e. a high power device)

(2) the maximum available small signal gain at the frequency of interest should be as large as possible

(b) matching of the active device

The device should be matched for maximum oscillator power. To do this load-pull measurements should be undertaken under power conditions determined from the expressions derived using P_{sat} and the small signal gain.

(c) coupling back power

For maximum oscillator output power it has been shown that there are optimal device input and output powers. To attain these values it is important that the right amount of power is fed back to the input of the device. In the case of a DRO feedback oscillator, for instance, this will depend on the coupling of the DRO to the MIC lines.

6.2.5 Designing for Maximum Efficiency

This section examines the relationship between GaAs MESFET oscillator efficiency and power. It is shown that they have the same dependence on f and G provided certain conditions are met. This being the case, it follows that, for a particular device, high efficiency design will follow the same criteria as a high power oscillator design except P_{sat} is no longer a direct factor.

Evans in a letter in 1985 (Evans, 1985: 254) has proposed that to a first approximation the efficiency of an oscillator is directly proportional to the output power. Thus maximising the output power results in an optimal DC to RF efficiency. It also follows that the efficiency of an oscillator has the same frequency dependence as the output power.

Evans argues that the FET device in a typical oscillator is operating as a class A amplifier. This being the case, and neglecting parasitics, then it can be shown that this amplifier has a maximum DC input to RF output

efficiency of 50%. Since the device's maximum output power is P_{sat} then the DC input must be $2P_{sat}$. Defining the oscillator's efficiency as:

$$n = \left[\frac{P_{osc}}{2P_{sat}}\right] * 100\% \qquad (6.18)$$

and assuming the DC power consumed is invariant with frequency, then it follows from (6.16) that:

$$n = \frac{1}{2}\left[1 - \frac{1}{G} - \frac{\ln G}{G}\right] * 100\% \qquad (6.19)$$

i.e. the conversion efficiency is directly proportional to the output power and has the same frequency dependence.

Since the conversion efficiency of an oscillator has the same dependence as the output power, it follows that designing for maximum output power will also result in an oscillator with the best efficiency possible.

The criteria for designing for maximum efficiency are therefore the same as those employed for maximum power design, with one exception. Equation (6.19) is independent of P_{sat} since it does not automatically follow that a high power device is required for high efficiency. Thus a low power device can produce good efficiency provided it is operating under maximum oscillator power conditions.

6.3 Impossibility of Simultaneously Meeting Optimal Performance Criteria using the Parameters Available for Optimisation in a GaAs MIC DRO

In the case of a GaAs MIC DRO, once a particular topology has been decided upon there are three basic parameters which can be used to optimise performance:

(a) specification of an active device
(b) matching of the active device to the circuit
(c) coupling the dielectric resonator into the circuit

This section shows how the different performance optimisations compete with each other over these parameters.

(a) active device characteristics

For best oscillator performance the device chosen should:

(1) be a high power device since this allows optimisation for low noise, long-term stability and maximum output power

(2) have the best possible small signal gain for best frequency stability, maximum output power and efficiency

Power devices usually have smaller gain than low power devices

(b) matching of the active device

Here there is active competition. The possible matching conditions are for

(1) low noise figure - for best noise performance

(2) maximum gain - for best frequency and temperature stability

(3) G_{ME} under large signal conditions - for best oscillator output power and efficiency

(c) coupling of the resonator into the circuit

Here again there are competing requirements. We would like the resonator to be:

(1) lightly coupled to provide high loaded Q for best noise and temperature performance

(2) coupled for the power feedback conditions required to produce G_{ME} - this for best power and efficiency

(3) coupled so as to balance the opposite temperature coefficients of the active device and the dielectric resonator to produce a high temperature stability

From the above it can be seen that oscillator design is usually a compromise between many different factors. Some factors, such as power and efficiency, can be optimised together whilst others, such as temperature stability and output power, have to be traded off against each other.

CHAPTER 7

7. MEASUREMENT OF DR BANDREJECT FILTERS

7.1 Introduction

This chapter describes measurements taken to characterise DR bandstop filters constructed on both 10mil and 31mil RT DUROID 5880.

The dependence of κ, Q_U, and Q_L on the distance of the DR from the microstripline is investigated for both types of filter at 5.75 GHz. This is followed by investigations into the dependence of f, κ, Q_U and Q_L on the airgap height x for a d = 1.38mm 31mil BRF and for a d = 0.60mm 10mil BRF. These filters correspond to the BRFs used in oscillators described in Chapter 10 and Chapter 9 respectively.

The chapter ends with an investigation into the variation of resonant frequency with temperature for the d = 1.38mm 31mil BRF.

7.2 DR Bandstop Filters Constructed with 32mil and 10mil Dielectric RT DUROID 5880

RT DUROID 5880 with ε_r = 2.2 was available in two dielectric thicknesses, h = 10mil (0.254mm) and h = 31mil (0.7874mm). Tests were performed with the DR available coupled to 50 Ohm lines etched on both types of board. For h = 10mil the width of the microstripline was 0.76mm and for h = 31mil the width was 2.34mm.

7.2.1 Construction

The test boards and brass cavities constructed had the dimensions shown in Figure 7.1. Figure 7.2 is a photograph of a 31mil DR bandstop filter with the cavity lid removed.

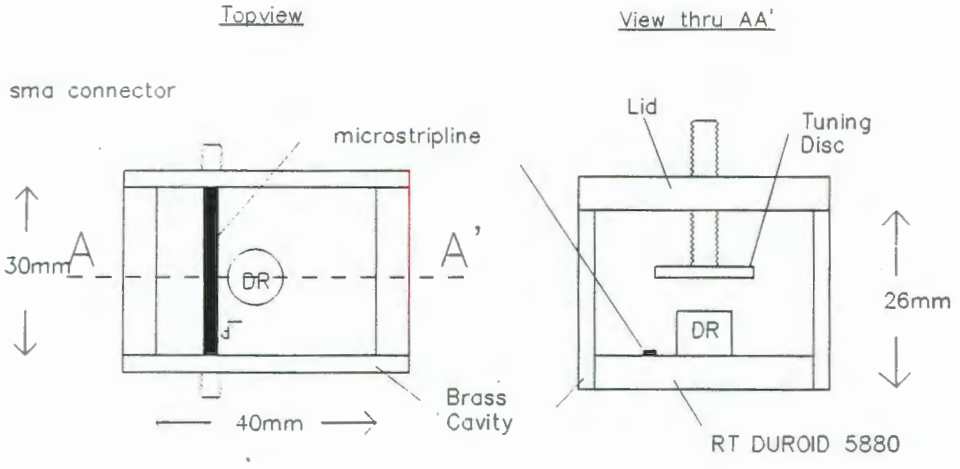

Fig 7.1 Dimensions of test board and brass cavity

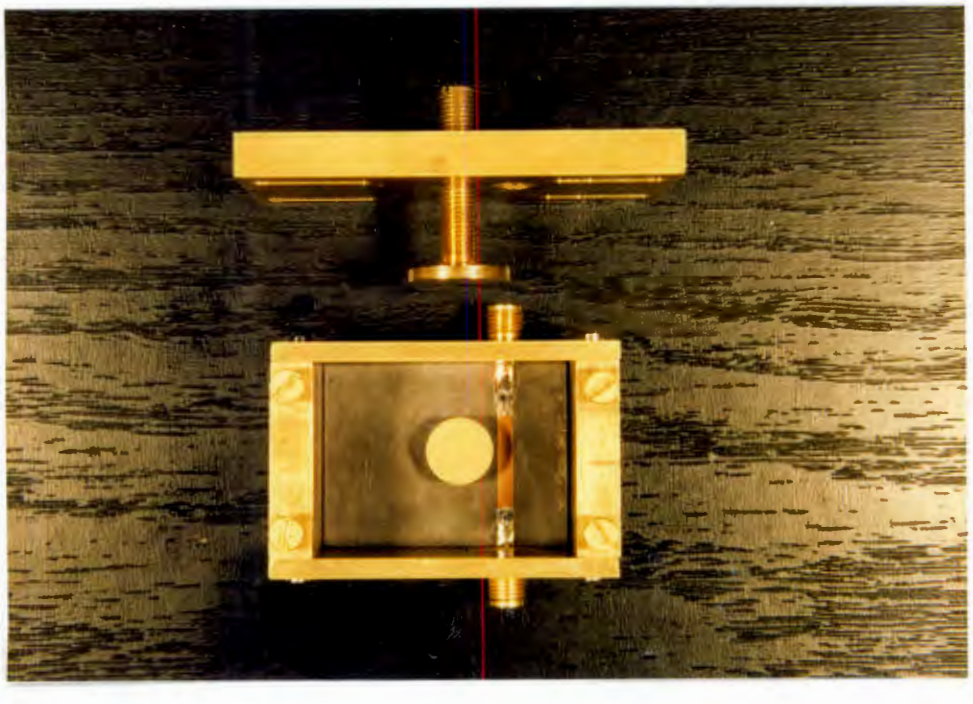

Fig 7.2 Photograph of 31mil DR bandstop filter

7.2.2 Measurement Procedure

Chapter 5 explains how the network analyser display can be used to determine the coupling coefficient, the unloaded Q factor and the loaded Q factor of a DR bandstop filter.

The equations derived in Section 5.2.1 were used to calculate κ, Q_U and Q_L from the network analyser display of S_{11} and S_{21}.

7.3 Measured Dependence of the Coupling Coefficient κ, Unloaded Quality Factor (Q_U) and Loaded Quality Factor (Q_L) on the Distance d Between the DR and the Edge of the Microstripline

Tests were performed at 5.75 GHz on DR filters constructed on 10mil and 31mil substrates to determine the dependence of κ, Q_U and Q_L on the distance d between the edge of the DR and the edge of the microstripline.

7.3.1 Results

Figure 7.3, Figure 7.4 and Figure 7.5 show, respectively, the results of plotting κ vs d, Q_U vs d and Q_L vs d for DR bandstop filters constructed on the two substrates. In general results for both S_{11} and S_{21} measurements are shown.

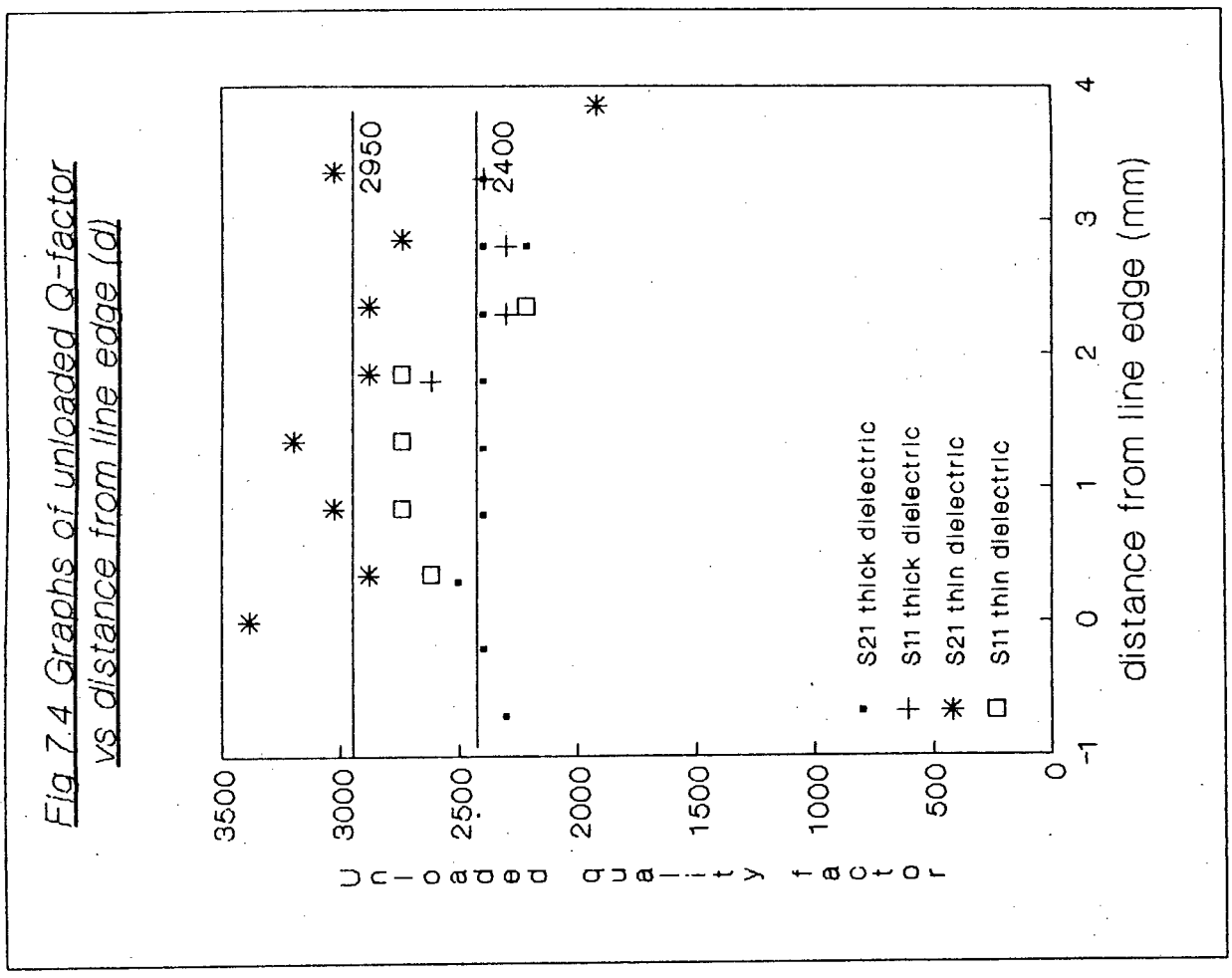
Fig 7.4 Graphs of unloaded Q-factor vs distance from line edge (d)
Unloaded quality factor
3500
3000
2500
2000
1500
1000
500
0
2950
2400
S21 thick dielectric
S11 thick dielectric
S21 thin dielectric
S11 thin dielectric
-1
0
1
2
3
4
distance from line edge (mm)

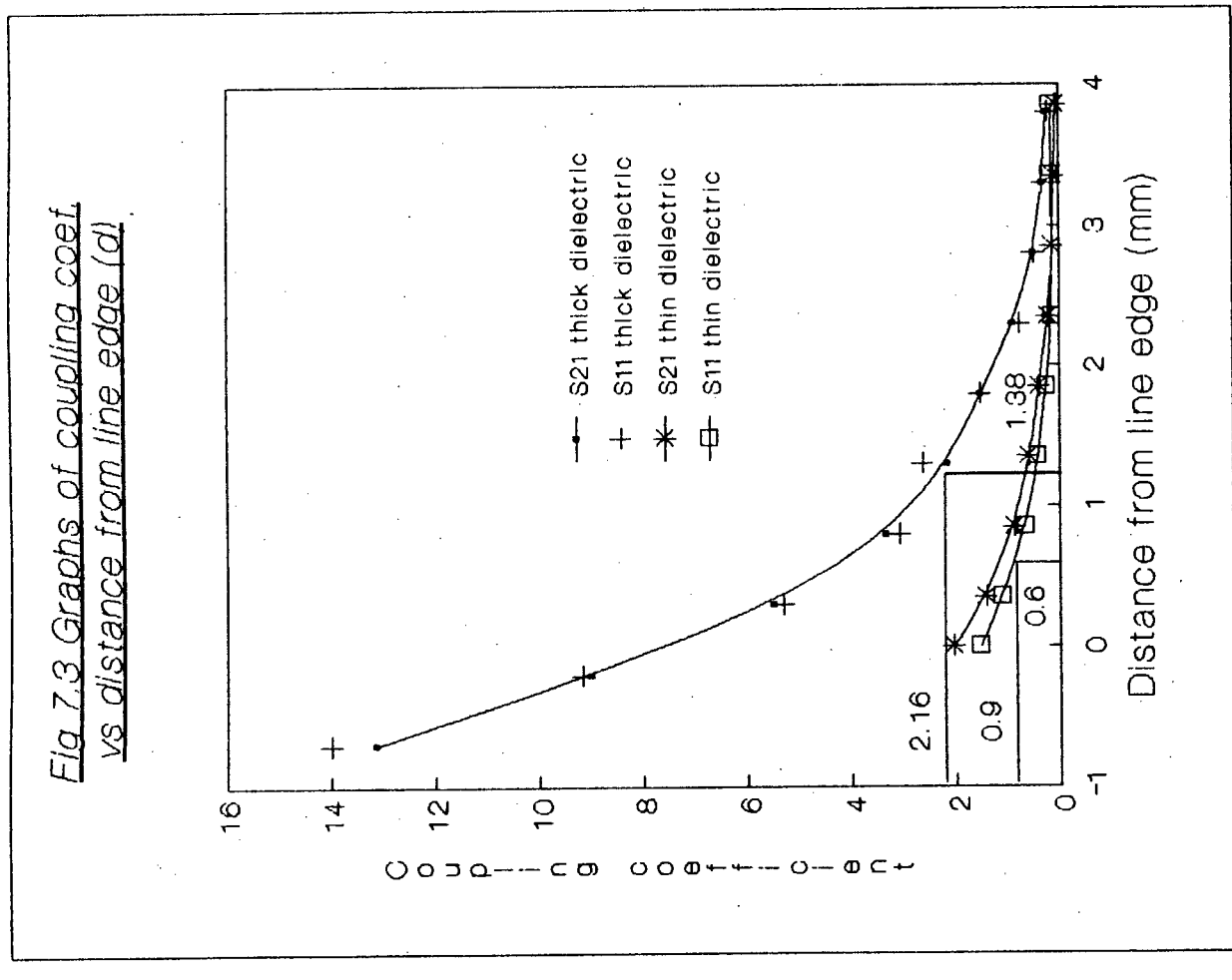
Fig 7.3 Graphs of coupling coef. vs distance from line edge (d)
Coupling coefficient
16
14
12
10
8
6
4
2
0
S21 thick dielectric
S11 thick dielectric
S21 thin dielectric
S11 thin dielectric
2.16
0.9
0.6
1.38
-1
0
1
2
3
4
Distance from line edge (mm)

Fig7.5 Graphs of loaded Q vs distance from line edge (d)

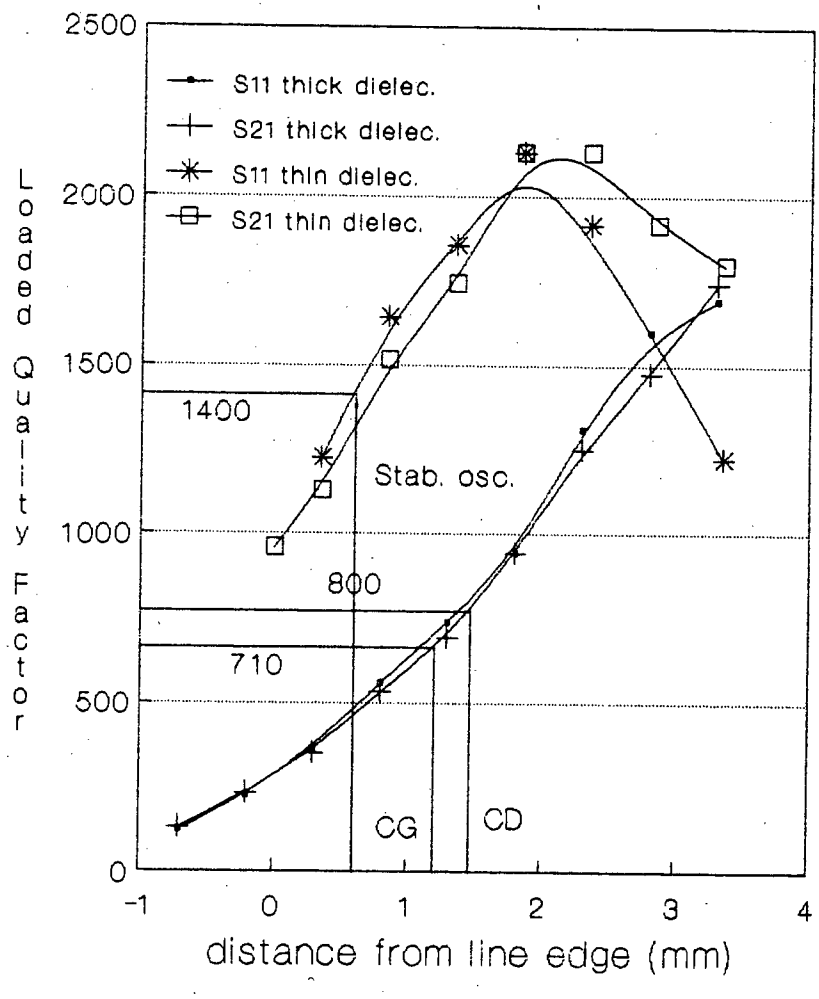

7.3.2 Discussion of Results

(1) κ vs d

Figure 7.3 shows that for the 31mil DR filter the S_{21} results give a very smooth curve with the S_{11} results scattered on either side. For the 10mil filter, however, the results obtained from S_{11} measurements are consistently lower than those obtained from measurements taken in the S_{21} plane. This results in two distinct curves. Since oscillators are to be constructed using the power reflected from bandstop filters S_{11} results should be used for design purposes. For the 31mil DR filter the S_{21} curve can be used since the S_{11} results are scattered on either side.

As expected, the graphs show that the coupling between the DR and a 50Ω microstripline increases as the DR is moved closer to the line. Both the thin (10mil) and thick (31mil) dieletric graphs have the same shape but the coupling between DR and 50Ω line is much greater for the thick dieletric filter than the thin one at the same distance from the line.

(2) Q_U vs d

For large values of κ, S_{11} measurements cannot be used to produce accurate values of Q_U. Thus for the thick dieletric filter S_{11} results for Q_U are only shown for $d > 1.5$mm. Q_U appears to be fairly constant with d for both the thick and thin dielectric filters with values of 2300 and 2950 respectively.

(3) Q_L vs d

Figure 7.5 shows that, for both types of bandstop filter, the S_{11} results for Q_L are higher than the S_{21} results. This is consistent with lower values of κ over the measured range. The Q_L of the thick dieletric filter increases steadily as the coupling decreases due to increased d. For the thin dielectric filter, however, the value of Q_L peaks for $d \sim 2$mm and then begins to fall. The Q_L values of the thin dielectric filter are greater than those of the thick dielectric filter for values of $d < 2.7$mm. The difference in Q_L is most noticeable for small values of d. For example, for $d = 0$mm, $Q_L \sim 300$ for the 31mil DR filter and $Q_L \sim 950$ for the 10mil DR filter - a factor of three difference.

7.3.3 Comparison of Results from the Two Types of DR Bandstop Filter

Figure 7.3 shows that the thin dielectric filter has a useful range of coupling values between 0.1 and 1.5. Table 7.1 compares Q_L and Q_U values of the 2 types of filter for κ values of 1.5, 1.0 and 0.5 (S_{11} results used).

Table 7.1 Comparison of Qu and Ql at given k for thin and thick dielectric DR BRFs

k	d_{thin}	d_{thick}	$Q_{U\ thin}$	$Q_{U\ thick}$	$Q_{L\ thin}$	$Q_{L\ thick}$
1.5	0.0	1.8	2950	2400	1090	1020
1.0	0.45	2.2	2950	2400	1380	1250
0.5	1.1	2.8	2950	2400	1740	1600

These results show that the thin dielectric DR bandstop filter has higher Q_U and Q_L values over its useful range of coupling values. However, much higher coupling values can be obtained with the thick dielectric DR bandstop filter which has a useful range of coupling values from about 0.2 to 13. This range is nine times that of the thin dielectric filter at a frequency of 5.75 GHz.

7.4 Measured Dependence of f, K, Q_U and Q_L as a Function of Airgap Distance x for a d = 1.38mm 31mil DR BRF

Chapter 10 describes the construction of a common drain series feedback STDRO on 31mil RT DUROID 5880. For this oscillator the DR was positioned 1.38mm from the edge of the microstripline. Tests were carried out to investigate the properties of the frequency determining DR BRF as a function of the airgap height x. Figure 7.6 and Figure 7.7 show the S_{21} and S_{11} averaged results of these tests. In both Figures there are two sets of curves, the first for the TE_{01} DR resonant mode and the second for a DR resonant mode whose resonant frequency increased with increasing x. Figure 7.6 shows the results of f vs x and K vs x, Figure 7.7 the results of Q_U vs x and Q_L vs x.

Fig 7.6 Graphs of k vs x and f vs x for 2 DR resonant modes (31 mil,d=1.38)

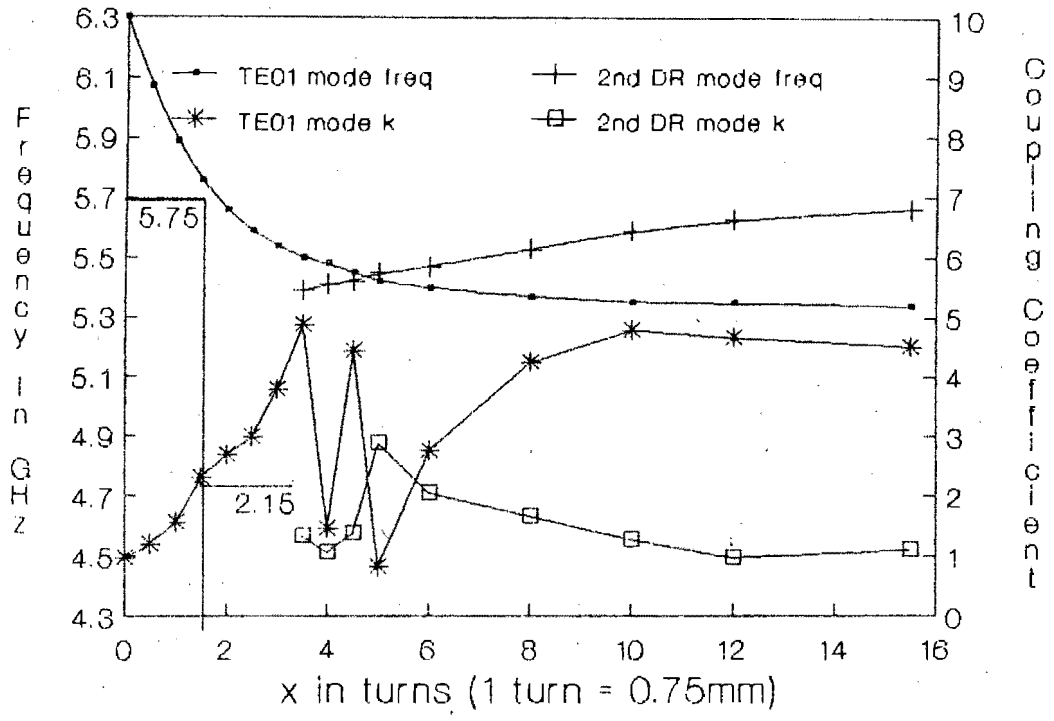

Fig7.7 Graphs of Qu and Ql vs x for 2 DR resonant modes (31mil,d=1.38)

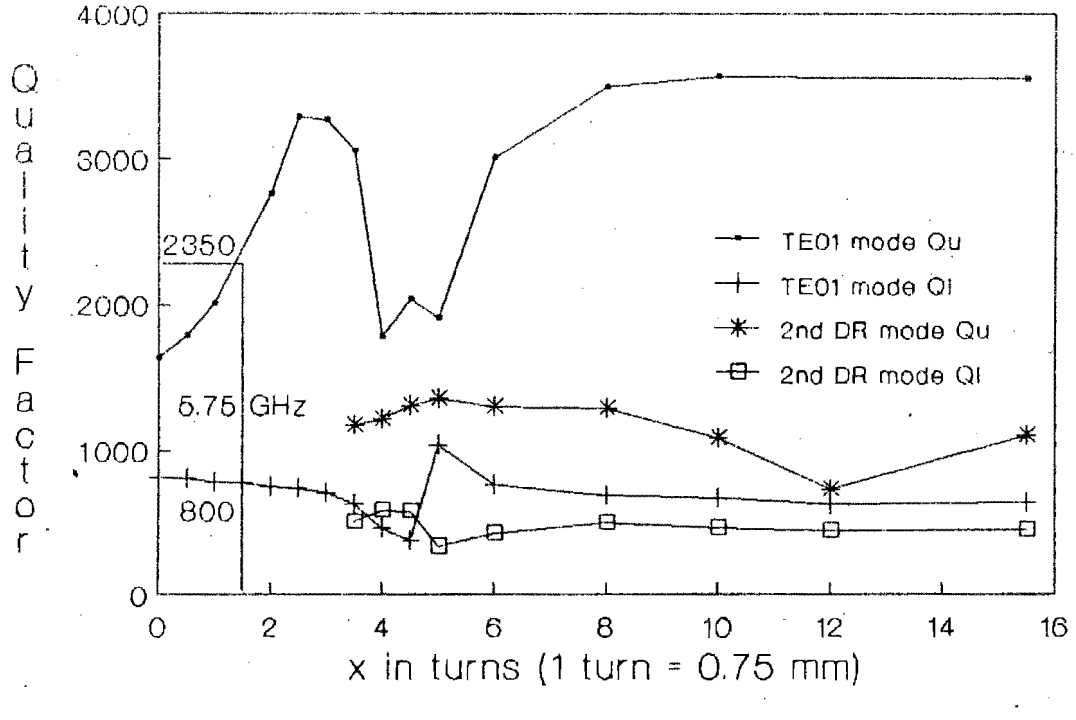

From the graphs the following results apply for the TE_{01}, DR resonant mode at 5.75 GHz:

κ = 2.15, this agrees well with κ = 2.16 from Figure 7.3

Q_U = 2350, this agrees well with Q_U = 2400 from Figure 7.4

Q_L = 800, this agrees well with Q_L = 800 from Figure 7.5

The good agreement indicates no serious measurement errors were made. Further discussion of these results is left to Chapter 10.

7.5 Measured Dependence of f, κ, Q_U and Q_L as a Function of Airgap Distance x for a d = 0.60mm 10mil DR BRF

Chapter 9 describes the construction of a DR stabilised oscillator on 10mil RT DUROID 5880. The stabilising DR was positioned 0.6mm from the edge of the 50 Ω output line. Figure 7.8 and Figure 7.9 show the properties of such a BRF as a function of airgap height x.

Fig7.8 Graphs of k and f vs x (10 mil DR BRF,d=0.6mm)

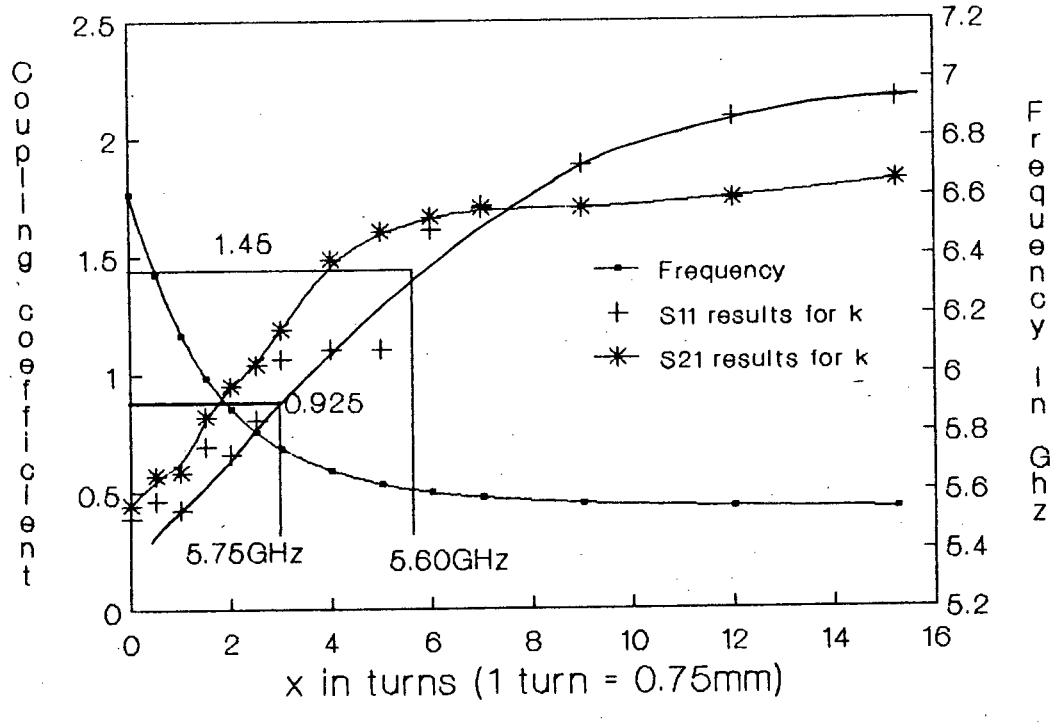

Fig7.9 Graphs of Qu and Ql vs x
(10 mil DR BRF,d=0.6mm)

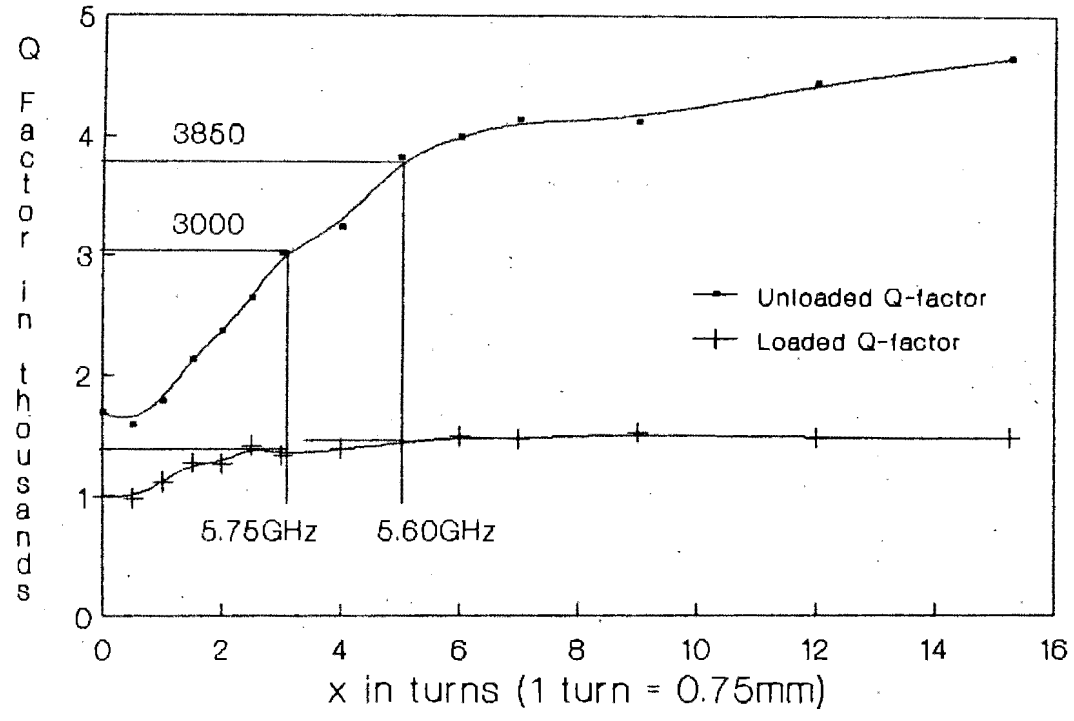

In Figure 7.8 two curves are shown for κ, the one plots results from S_{11} measurements, the other results from S_{21} measurements. As a stabilising element the BRF is used to reflect power, thus the S_{11} curve is the most appropriate in this case. Figure 7.9 shows S_{11} and S_{21} averaged results for Q_U and Q_L.

From the graphs the following results apply at 5.75 GHz:

κ = 0.925, this agrees well with κ = 0.9 from Figure 7.3

Q_U = 3000, this agrees well with Q_U = 2950 from Figure 7.4

Q_L = 1350, this agrees well with Q_L = 1400 from Figure 7.5

At 5.60 GHz the properties of the BRF are as follows:

κ = 1.45

Q_U = 3850

Q_L = 1500

These results are used in Chapter 9.

7.6 Temperature Dependence of Resonant Frequency for d = 1.36mm 31mil DR Bandstop Filter

Figure 7.10 is a graph of frequency deviation vs temperature for a 31mil BRF with d = 1.38mm. The slope of the fitted straight-line is -40.3 KHz/°C or -7ppm/°C

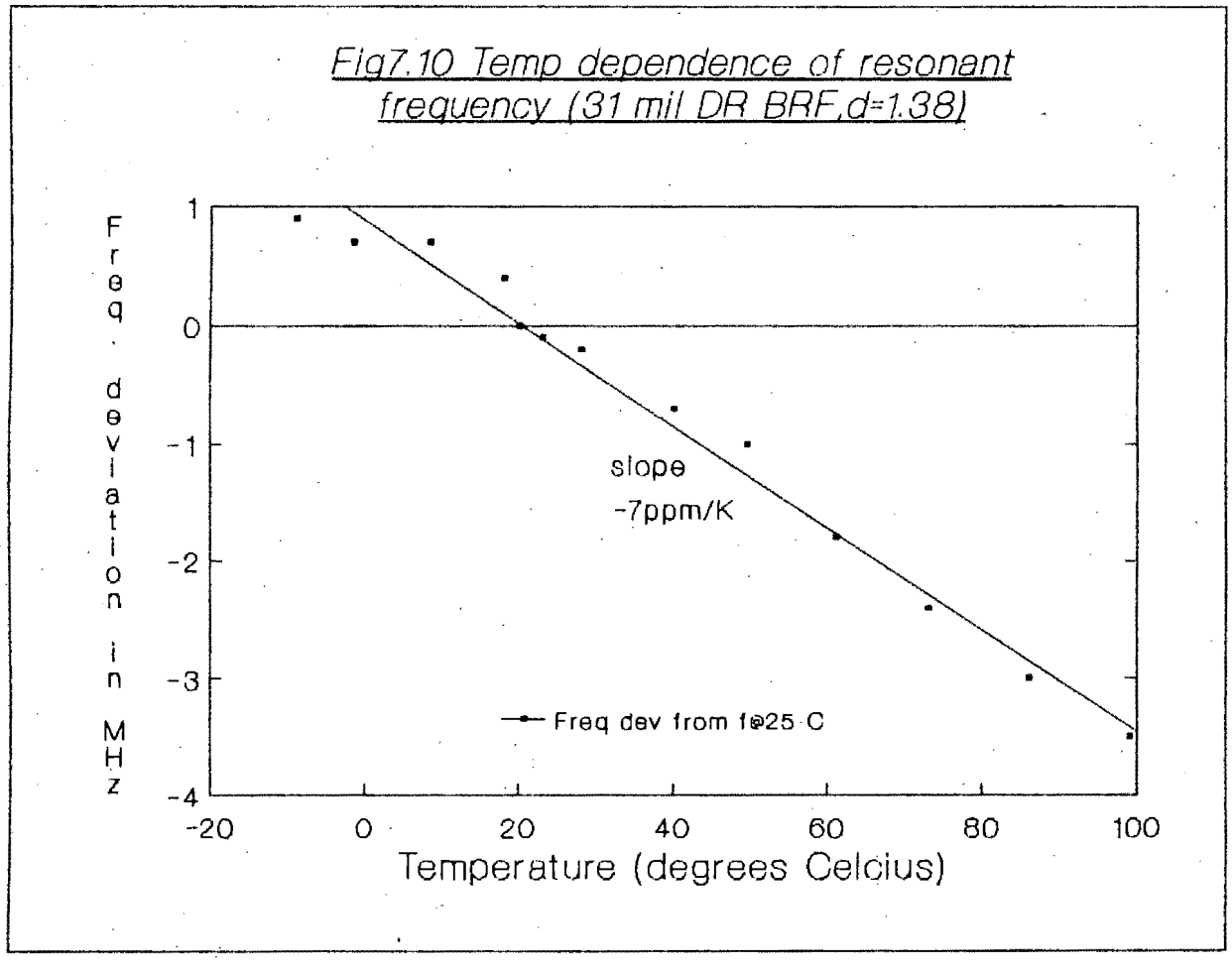

CHAPTER 8

MEASUREMENT AND MODELLING OF DR BANDPASS FILTERS

8.1 Introduction

This chapter describes measurements taken to characterise DR bandpass filters with a designed resonant frequency of 5.75 GHz.

The chapter begins with details of the mechanical construction of the filters. This is followed by an investigation into how the coupling coefficient (κ), loaded quality factor (Q_L) and the unloaded quality factor (Q_U) vary as functions of the distance between the DR and the edge of the microstripline (d).

Using the results obtained from the investigation, κ and Q_U are expressed as fitted polynomial functions of d. This allows an accurate TOUCHSTONE model of a bandpass filter to be produced. Section 8.4 compares results obtained using the model with direct measurements from the network analyser display.

Section 8.5 looks at the dependence of κ, frequency (f), Q_L and Q_U on the airgap distance x for d = 1.5mm. The results obtained give information on the frequency tuning characteristics and the usable tuning range of the filter.

The last section investigates the temperature dependence of f and Q_L for a DR bandpass filter with d = 1.5mm.

8.2 DR Bandpass Filters Constructed with 10mil RT Duroid

A DR suitable for constructing filters at 5.75 GHz was available. For a bandpass filter the DR is coupled between two 50Ω microstriplines as described in Chapter 5. All bandpass filters tested were constructed on 10mil RT DUROID 5880 (50Ω line width = 0.76mm) due to a shortage of other materials.

8.2.1 Construction

Microstripboards were etched for d = -1.0, -0.5, 0.0, 0.5, 1.0, 1.5, 2.0 and 3.0mm on 10mil dielectric RT DUROID 5880. The open circuit lines on the boards were designed to produce a short circuit at the reference plane for a frequency of 5.75 GHz. Figure 8.1 is a schematic diagram showing the layout and dimensions of these boards and their brass cavities.

Fig 8.1 Schematic diagram of constructed bandpass filters

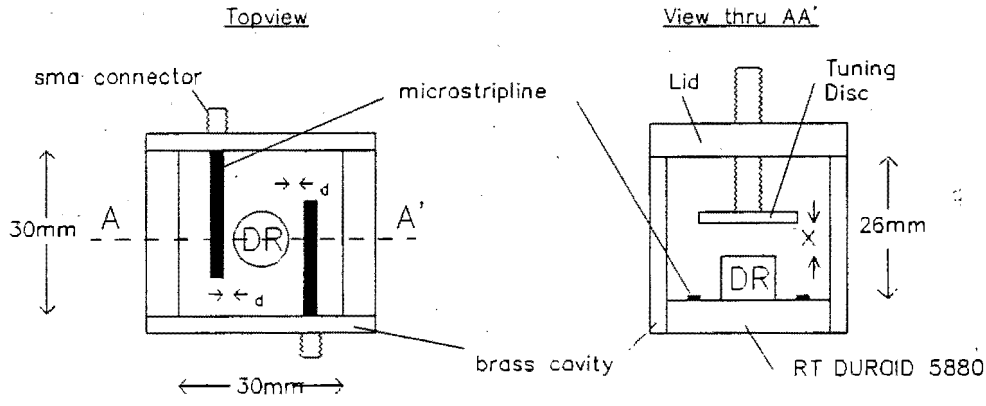

Figure 8.2 shows the microstrip etching mask for the d = 1.5mm DR bandpass filter. Figure 8.3 is a photograph of this filter with the lid removed.

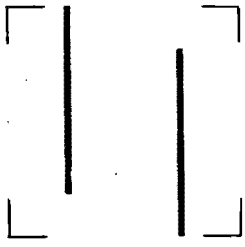

t575g15

Fig 8.2 Microstrip etching mask for d = 1.5mm DR bandpass filter

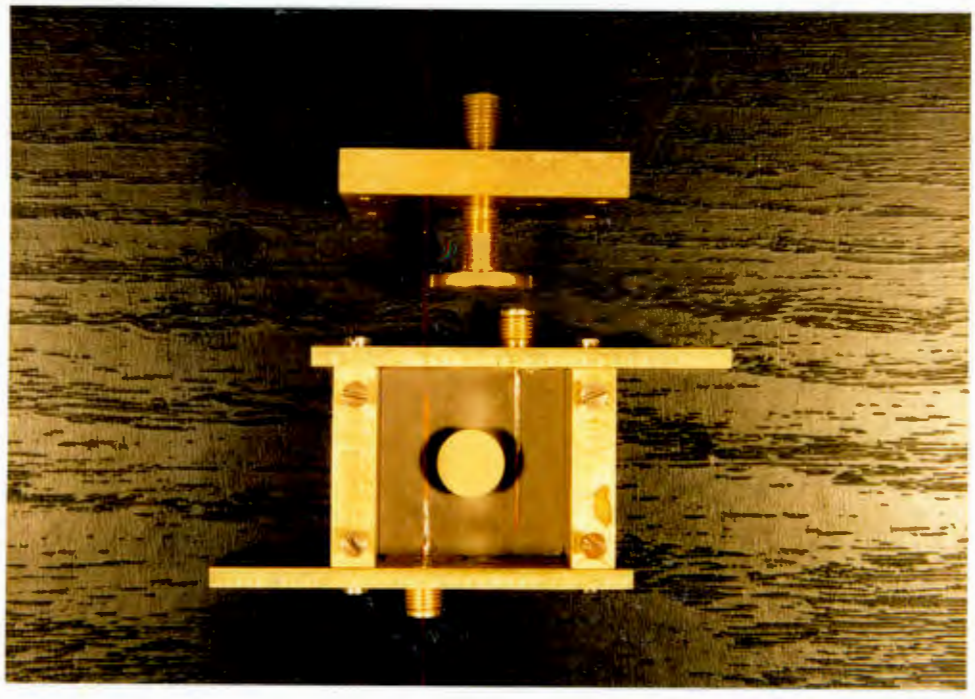

Fig 8.3 Photograph of d = 1.5mm bandpass filter

8.3 Measured Dependence of Coupling Coefficient, Unloaded Quality Factor and Loaded Quality Factor as a Function of d for Resonance at 5.75 GHz

8.3.1 Measurement Procedure

Chapter 5 explains how the network analyser display can be used to determine the coupling coefficient, the unloaded Q factor and the loaded Q factor of an equally coupled DR filter. The equations derived in Section 5.2.2. were used to calculate κ, Q_U and Q_L from the network analyser display of S_{11} and S_{21}.

To try to ensure equal coupling of the DR to the two microstriplines the position of the DR was adjusted until the insertion loss was minimised. All measurements were taken for the filters tuned to 5.75 GHz.

8.3.2 Results

Figure 8.4 and Figure 8.5 show the results obtained from measurements in both the reflection (S_{11}) and transmission (S_{21}) planes. Graphs of κ vs d and insertion loss vs d are shown in Figure 8.4 and graphs of Q_U and Q_L vs d in Figure 8.5.

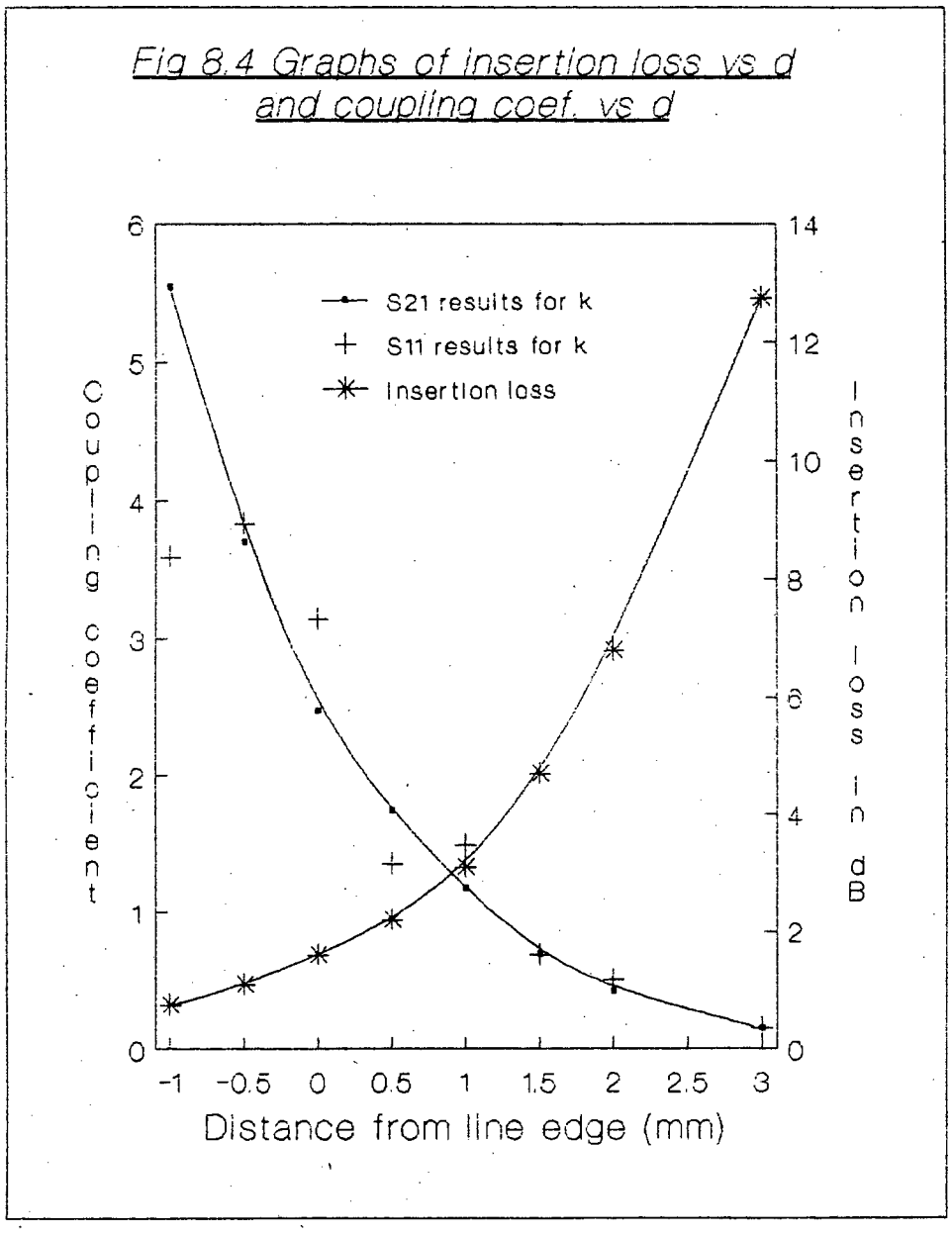

Fig 8.4 Graphs of insertion loss vs d and coupling coef. vs d

Fig 8.5 Graphs of Unloaded and Loaded Q vs d

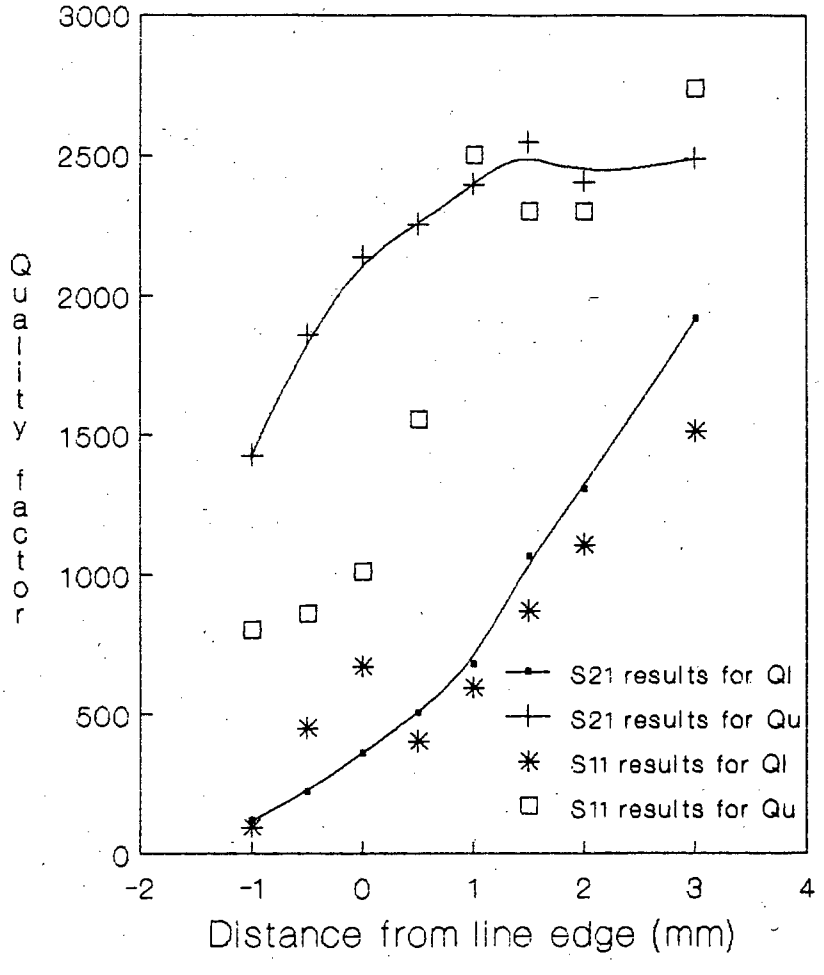

8.3.3 Discussion of Results

The results show that in general the measurements taken in the S_{11} plane are less reliable than those taken in the S_{21} plane. There are two possible reasons for this:

(1) the coupling to the two microstriplines may not, in fact, have been equal. One would expect this to have more effect on a S_{11} measurement than a S_{21} measurement

(2) S_{11} measurements are more sensitive to mismatches due to launcher discontinuities etc than are S_{21} measurements

The S_{21} measurements yielded smooth curves and are the more appropriate measurements to take when characterising a bandpass filter.

8.4 Computer Modelling of 5.75 GHz Bandpass Filters with d as a Fitted Variable

As shown in Section 5.2.2.3 a DR bandpass filter can be modelled as shown in Figure 8.6 below for the case of equal coupling to the two lines.

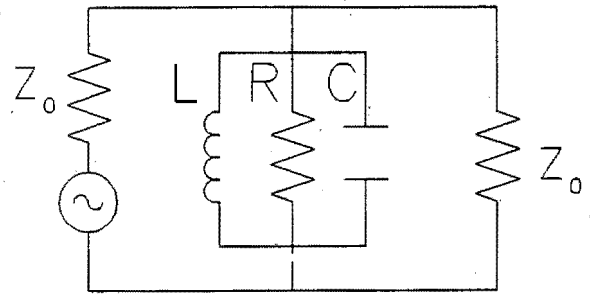

Fig 8.6 Model of bandpass filter for the case of equal coupling

R is a function of κ which is a function of d

$$R(d) = \kappa(d) * Z_0 \qquad (8.1)$$

L and C are functions of Q_U and R which are both functions of d.

$$L(d) = \frac{R(d)}{2\pi * f_0 * Q_U(d)} \qquad (8.2)$$

$$C(d) = \frac{Q_U(d)}{R(d) * 2\pi * f_0} \qquad (8.3)$$

The aim here is to express κ and Q_U as functions of d. R(d), L(d) and C(d) can then be calculated and used to model the DR bandpass filter for any value of d.

8.4.1 Expressing κ, Q_L and Q_U as Polynomial Functions of d

Programme LAGRANGE from TURBOPASCAL TOOLBOX was used to fit polynomials in d to κ, Q_L and Q_U. The polynomials so determined are given below. The order of the fitted polynomial is determined by the number of data points used in the fit.

$$\kappa(d) = 2.541 - 1.849d + 0.6817d^2 - 0.2930d^3 + 0.1594d^4 - 0.0178d^5 \quad (8.4)$$

$$Q_L(d) = -6.4941 + 79.379d + 336.43d^2 + 368.557d^3 \quad (8.5)$$

$$Q_U(d) = 2244 + 665.841d - 309.192d^2 - 169.867d^3 + 85.958d^4 + 56.683d^5 - 36.767d^6 + 5.343d^7 \quad (8.6)$$

The polynomial for $Q_U(d)$ was fitted to data points calculated from $\kappa(d)$ and $Q_L(d)$ according to the formula $Q_U = Q_L(1 + \kappa)$ (8.7)

8.4.2 TOUCHSTONE Computer Model and Results

A TOUCHSTONE program was written to model the bandpass filter as a function of d according to equations (8.1) through (8.7).

The model was checked by comparing calculated values of insertion loss at frequencies close to resonance with values measured on the network analyser. Figure 8.7 shows calculated and measured values of insertion loss for different values of d.

Fig8.7 Measured and calculated insertion loss vs freq. for different values of d

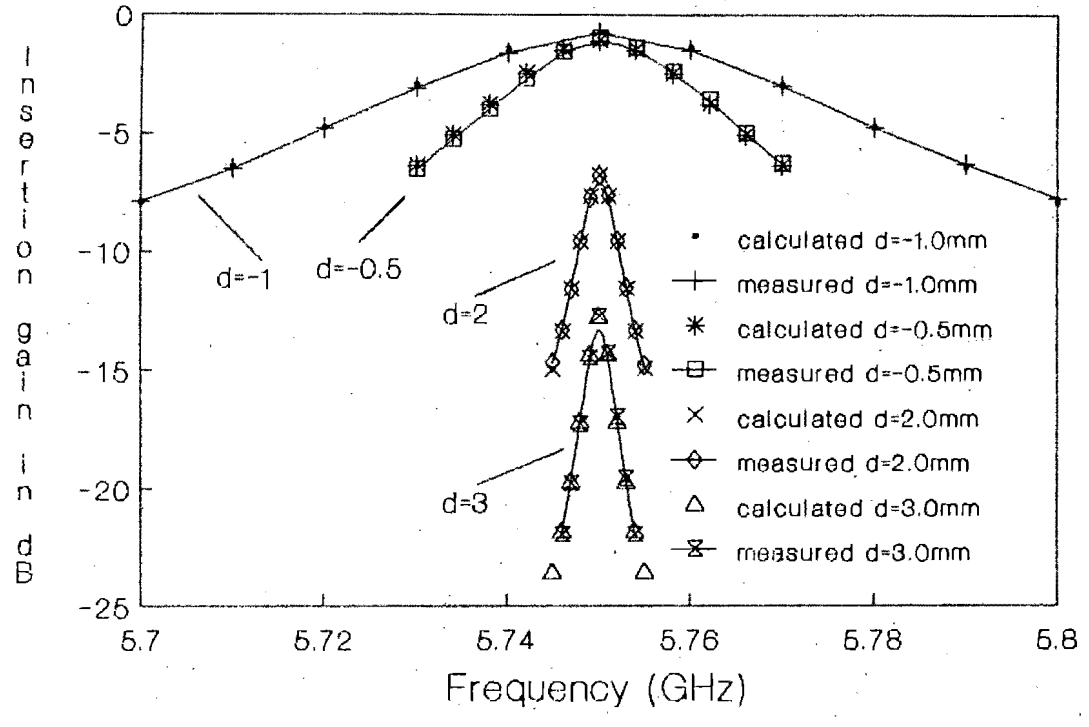

The graphs show that the error between calculated and measured is less than 0.3dB for all values considered. The close agreement indicates that the theory derived in Section 5.2 provides an accurate model of an equally coupled DR bandpass filter.

8.5 Measured Dependence of Frequency, Coupling Coefficient, Unloaded Quality Factor and Loaded Quality Factor as a Function of Airgap Distance x (d = 1.5mm)

The aim of this experiment was to determine the usable frequency range of the bandpass filter. By mechanically altering the airgap distance x the filter can be tuned over a certain bandwidth. Not all of this bandwidth may be usable, however, since K, Q_U and Q_L decrease with decreasing x.

8.5.1 Results and Discussion

The results for f vs x and κ vs x are displayed graphically in Figure 8.8 and those for Q_U and Q_L vs x in Figure 8.9. A frequency scale has also been marked on Figure 8.9. For this experiment distance d was set equal to 1.5mm.

Fig 8.8 Graphs of k and f vs x (d=1.5mm)

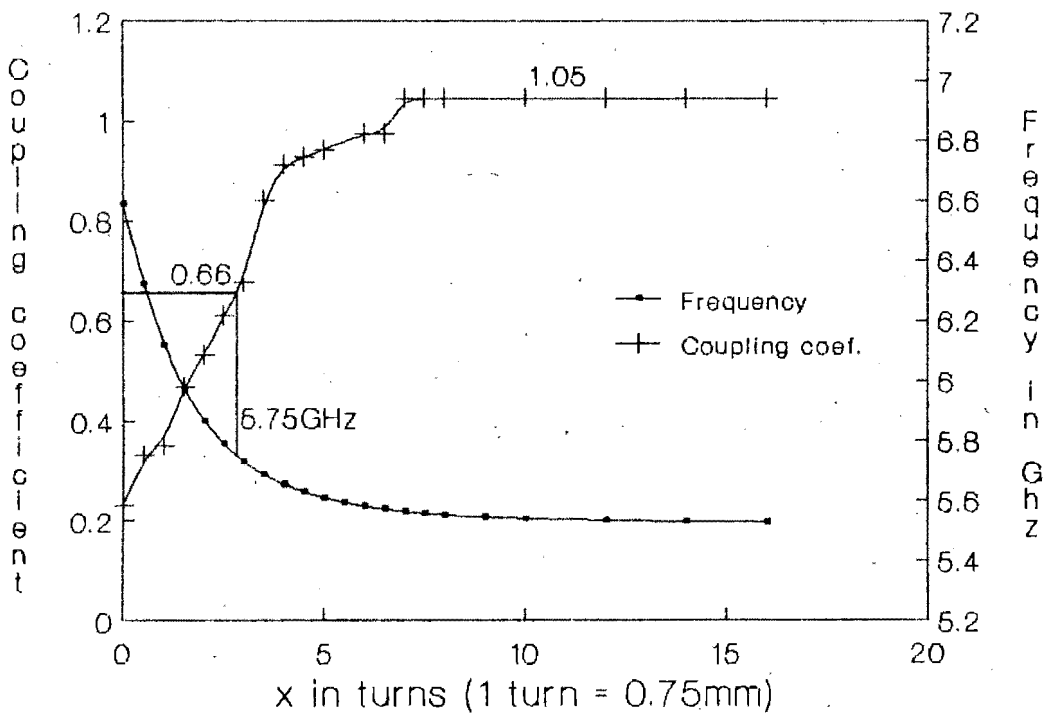

Fig 8.9 Graphs of Unloaded Q and Loaded Q as a fn of x (d=1.5mm)

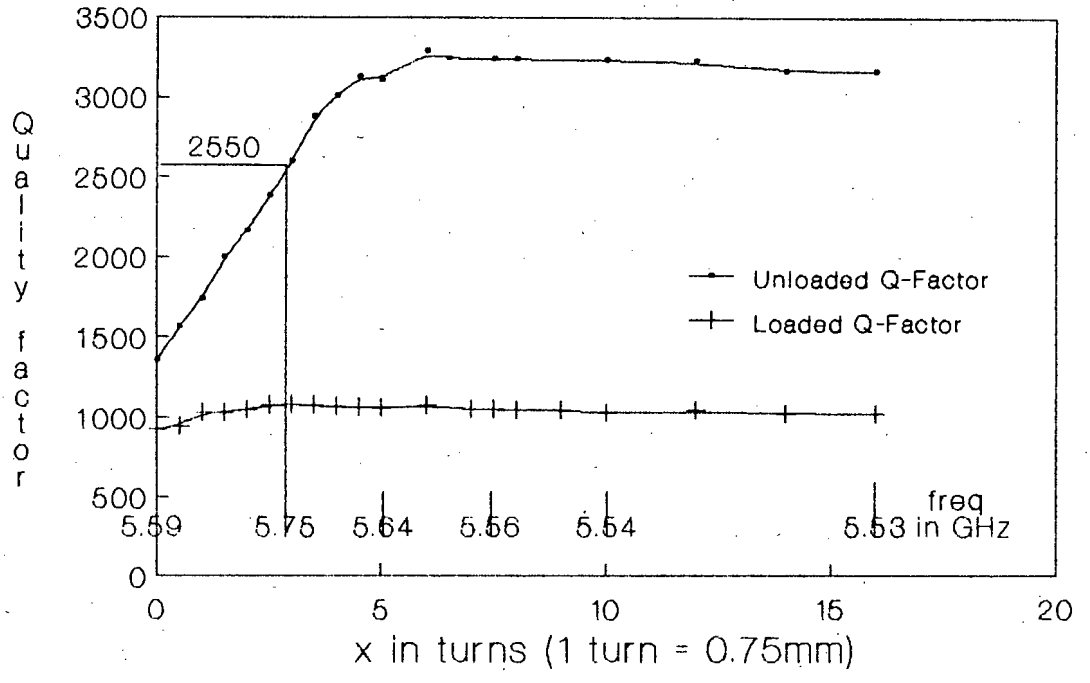

(1) Frequency as a Function of x

The curve of f vs x is seen to have a negative gradient whose magnitude decreases with increasing x i.e. decreasing x has the effect of increasing the frequency with greatest $\frac{\partial f}{\partial x}$ as $x \rightarrow 0$. The resonant frequency of the filter is thus more sensitive to changes in x when x is small.

(2) Coupling Coefficient as a Function of x

The graph of K vs x shows that the coupling is a strong function of x for values of x less than 7 turns. For x between 0mm and 3 turns K is a linearly increasing function of x with a slope of 0.192/mm. An anomaly is apparent in the curve for x between 3 turns and 7 turns. For x greater than 7 turns K is independent of x maintaining a constant value of 1.05.

The value of at 5.75 GHz found from Figure 8.8 is 0.66. This agrees well with the value of 0.69 from Figure 8.4 under the same conditions.

(3) Unloaded Quality Factor as a Function of x

From the graph in Figure 8.9 it can be seen that Q_U is a linearly increasing function of x from x = 0mm to x = 5 turns (gradient 547/mm) and a linearly decreasing one from x = 5turns to x = 16 turns (gradient -160/mm).

For a centre frequency of 5.75 GHz the unloaded Q value from the graph is 2550. This agrees well with the value of 2480 found by substituting d = 1.5mm into equation 8.6.

If the minimum acceptable unloaded Q factor for the bandpass filter is taken as 2000 then, from the graph, the tuning range is found to be 444 MHz. The maximum mechanical tuning range of the filter is 1060 MHz.

(4) Loaded Quality Factor as a Function of x

The graph in Figure 8.9 shows that as x is increased from zero, Q_L increases, reaches a peak at x = 3 turns (f = 5.7305 GHz), and then falls off. The required 5.75 GHz resonant point is very close to the peak value indicating that this resonant frequency is close to optimum for the cavity constructed.

8.6 Temperature Dependence of Resonant Frequency and Loaded Q for d = 1.5mm Bandpass Filter

The d = 1.5mm DR bandpass filter was placed in the environmental chamber with long cables connecting it to the network analyser. An alcohol thermometer was taped to the side of the cavity and the resonant frequency of the filter adjusted to 5.75 GHz at room temperature.

8.6.1 Results and Discussion

Figure 8.10 shows the resonant frequency and loaded Q of the filter as a function of temperature. The loaded Q was measured assuming K remained constant with temperature.

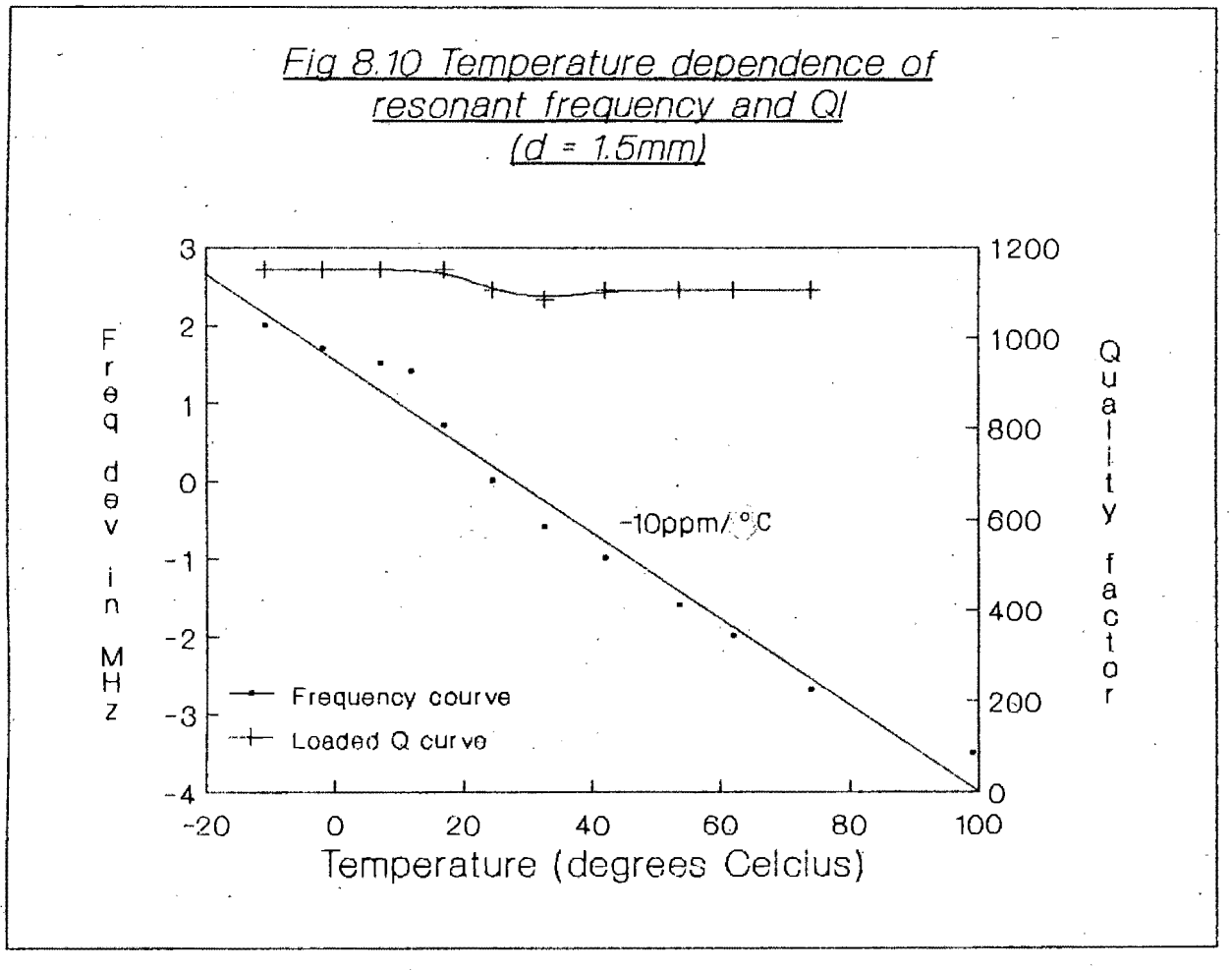

Fig 8.10 Temperature dependence of resonant frequency and Ql (d = 1.5mm)

From Figure 8.10 the resonant frequency appears to have a fairly linear temperature coefficient of about -10ppm/°C whilst Q_L appears almost invariant with temperature.

CHAPTER 9

DIELECTRIC RESONATOR STABILISED MICROSTRIP OSCILLATOR

9.1 Introduction

This chapter describes the design, construction and evaluation of a DR BRF stabilised oscillator.

As discussed in Chapter 5, a stabilised DRO consists of an oscillator with a poor pulling factor which is then stabilised with a DR on the output. The first section, therefore, describes a 3-port microstrip oscillator with poor pulling factor developed at 5.75 GHz.

The second section begins with the theory of DR BRF stabilised oscillators. It then describes how the microstrip oscillator was stabilised with a DR BRF. Practical results obtained are presented together with those predicted by theory.

The last section discusses the results obtained and compares the performance of the stabilised oscillator at 5.60 GHz with that predicted by theory and the performance of the unstabilised oscillator.

9.2 Unstabilised Negative Resistance Microstrip Oscillator at 5.75 GHz

9.2.1 Design of Unstabilised Oscillator

9.2.1.1 Requirements and Chosen Topology

The basic requirements of the unstabilised oscillator are:

(1) that it oscillate at a frequency of 5.75 GHz

(2) that it have a poor pulling figure (low Q_{ex})

(3) that it have a high output power

A microstrip parallel feedback oscillator was designed and constructed but did not meet any of the above criteria. Figure 9.1 shows a schematic diagram of this oscillator.

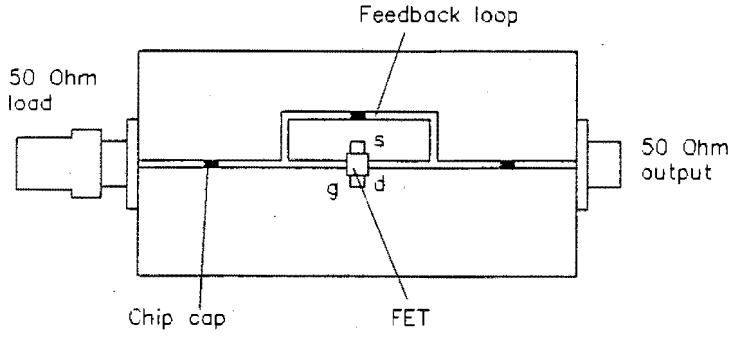

Fig 9.1 Schematic diagram of microstrip parallel feedback oscillator

A microstrip oscillator which did meet the requirements listed above had the topology shown in Figure 9.2.

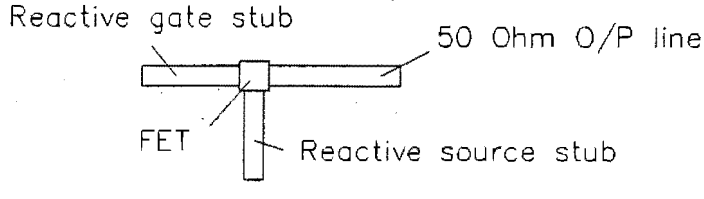

Fig 9.2 Topology of unstabilised microstrip oscillator

This oscillator consists of a MGF1801 transistor in 3-port configuration with reactive loads on the gate and source. The drain is connected to a 50Ω output line which is matched for maximum output power. The design and construction of this oscillator is now described.

9.2.1.2 6 Step Design Procedure for Chosen Oscillator Topology

This section describes the design of two possible 5.75 GHz microstrip oscillators with the topology of Figure 9.2. The basic aim of the design procedure is to determine suitable loads on the source and gate ports for

steady-state oscillation at 5.75 GHz. The procedure is laid out in logical steps. Step 4 results in two possible source reactances and hence two oscillator configurations. Steps 5 and 6 are applied to both configurations to produce two oscillator designs with the same topology but different reactive loads on the source and gate.

Step 1: Interpolation of manufacturer's small signal data to give small signal common source S-parameters at 5.75 GHz.

Appendix H documents the manufacturer's small signal S-parameter data for the MGF1801. To build oscillators at 5.75 GHz TOUCHSTONE was used to interpolate this data. The resulting common source small signal S-parameters at 5.75 GHz are:

$$\underline{S} = \begin{bmatrix} 0.598\ \underline{/177.7^\circ} & 0.55\ \underline{/65.2^\circ} \\ 2.807\ \underline{/27.2^\circ} & 0.510\ \underline{/-99.7^\circ} \end{bmatrix} \qquad (9.1)$$

Step 2: Conversion of 5.75 GHz common source S-parameters to 5.75 GHz 3-port S-parameters.

Since we are dealing with a 3-port topology it is necessary to obtain the 3-port S-parameters from the 2-port common source S-parameters. This can be done using the equations derived in Appendix G. The calculated 3-port small signal S-parameters at 5.75 GHz are:

$$\underline{S} = \begin{bmatrix} 1.346\ \underline{/-131.28^\circ} & 0.834\ \underline{/43.43^\circ} & 1.355\ \underline{/18.86^\circ} \\ 3.208\ \underline{/46.84^\circ} & 1.308\ \underline{/-103.82^\circ} & 1.386\ \underline{/-129.51^\circ} \\ 1.364\ \underline{/-103.00^\circ} & 0.993\ \underline{/44.61^\circ} & 0.870\ \underline{/46.48^\circ} \end{bmatrix} \qquad (9.2)$$

Step 3: Mapping the reactive load circle of the source port into the gate reflection coefficient plane with the drain port terminated in 50Ω.

An important piece of theory which is very useful for oscillator design was published by Wagner in 1979 (Wagner, 1979). In his paper Wagner derives an equation which describes the conformal mapping of the load reflection coefficient plane into the input reflection coefficient plane for a 2-port network. This equation is derived in Appendix I.

Wagner's equation can be used to map the source reactance circle into the gate reflection coefficient plane with the drain terminated in a fixed impedance of 50Ω. Terminating the drain in 50Ω results in a reduced 2-port network to which Wagner's equation can be applied as illustrated in Figure 9.3.

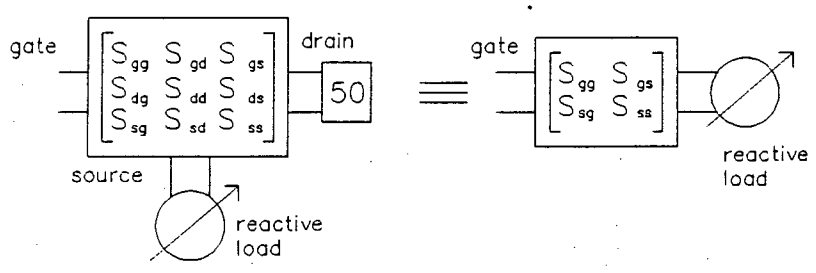

Fig 9.3 The reduced 2-port S-parameter matrix for a 3-port device terminated in 50 Ohms

The reflected waves on the gate, drain and source are given by:

$$b_g = S_{gg}a_g + S_{gd}a_d + S_{gs}a_s \quad (9.3)$$

$$b_d = S_{dg}a_g + S_{dd}a_d + S_{ds}a_s \quad (9.4)$$

$$b_s = S_{sg}a_g + S_{sd}a_d + S_{ss}a_s \quad (9.5)$$

If the drain is terminated with a load with reflection coefficient Γ_d then the incident and reflected waves on the drain are related by

$$a_d = \Gamma_d b_d \quad (9.6)$$

Substituting (9.6) into (9.3), (9.4) and (9.5) gives:

$$b_g = S_{gg}a_g + S_{gd}\Gamma_d b_d + S_{gs}a_s \quad (9.7)$$

$$b_d = S_{dg}a_g + S_{dd}\Gamma_d b_d + S_{ds}a_s \quad (9.8)$$

$$b_s = S_{sg}a_g + S_{sd}\Gamma_d b_d + S_{ss}a_s \quad (9.9)$$

b_d can now be eliminated to give the reduced 2-port networks $\underline{S}_{dl}$

$$\underline{S}_{dl} = \begin{bmatrix} S_{gg} + \dfrac{S_{gd}S_{dg}\Gamma_d}{1 - S_{dd}\Gamma_d} & S_{gs} + \dfrac{S_{gd}S_{ds}\Gamma_d}{1 - S_{dd}\Gamma_d} \\ S_{sg} + \dfrac{S_{sd}S_{dg}\Gamma_d}{1 - S_{dd}\Gamma_d} & S_{ss} + \dfrac{S_{sd}S_{ds}\Gamma_d}{1 - S_{dd}\Gamma_d} \end{bmatrix} \qquad (9.10)$$

If the load on the drain is 50Ω then $\Gamma_d = \dfrac{Z_d - Z_0}{Z_d + Z_0} = 0$ (9.11)

so that the reduced S-parameter matrix becomes

$$\underline{S}_{d50} = \begin{bmatrix} S_{gg} & S_{gs} \\ S_{sg} & S_{ss} \end{bmatrix} = \begin{bmatrix} 1.342 \angle -131.1^\circ & 1.352 \angle 18.9^\circ \\ 1.373 \angle -103.2^\circ & 0.877 \angle 46.5^\circ \end{bmatrix} \qquad (9.12)$$

Since Wagner's mapping is conformal the reactance circle $|\Gamma_s| = 1$ for the source maps into a circle in the gate reflection coefficient plane. From Appendix I and (9.12) the centre of this circle is given by:

$$\frac{S_{11} - \Delta S_{22}^*}{1 - |S_{22}|^2} = \frac{S_{gg} - \Delta_{d50} S_{ss}^*}{1 - |S_{ss}|^2} = 7.99 \angle -130.7^\circ \qquad (9.13)$$

where $\Delta_{d50} = S_{gg}S_{ss} - S_{sg}S_{gs}$ (9.14)

and the radius by $\left| \dfrac{S_{12}S_{21}}{1 - |S_{22}|^2} \right| = \left| \dfrac{S_{sg}S_{gs}}{1 - |S_{22}|^2} \right| = 7.63$ (9.15)

Figure 9.4 shows the $|\Gamma_s| = 1$ circle mapped into the gate input reflection coefficient plane. Source reactance values have also been marked on the circle.

Step 5: Calculation of the common source S_{21} magnitude and gate input reflection coefficient under large signal conditions.

As shown in Chapter 4, the steady state oscillation condition on the gate port is given by $\Gamma_g \Gamma_{gl} = 1$ (9.16) where:

$\Gamma_g = \gamma \angle \Gamma_g$ is the large signal reflection coefficient looking into the gate, and

$\Gamma_{gl} = |\Gamma_{gl}| \angle \Gamma_{gl}$ is the reflection coefficient of the load on the gate.

For a reactive load on the gate $|\Gamma_{gl}| = 1$ (9.17). For small signal conditions $\gamma = 2$ and hence $|\Gamma_{gl}| \gamma > 1$ giving reliable startup. As the oscillations build up the transistor saturates, its 3-port S-parameters change and γ decreases until $\gamma = 1$ at which point the conditions for steady state oscillation are satisfied.

Work by Johnson (Johnson, 1979: 219) has shown that the common source parameter which changes the most under large signal conditions it the magnitude of S_{21} i.e. $|(S_{21})_{cs}|$. Assuming that this is the only parameter which changes, an iterative program was written which converges to a solution of $\gamma = 1$. Figure 9.5 is a flowchart of the program which prints out $|(S_{21})_{cs}|$ and Γ_g after 20 iterations. The fortran code for the program is included in program DESIGN (Appendix K), discussed in Section 9.2.1.3.

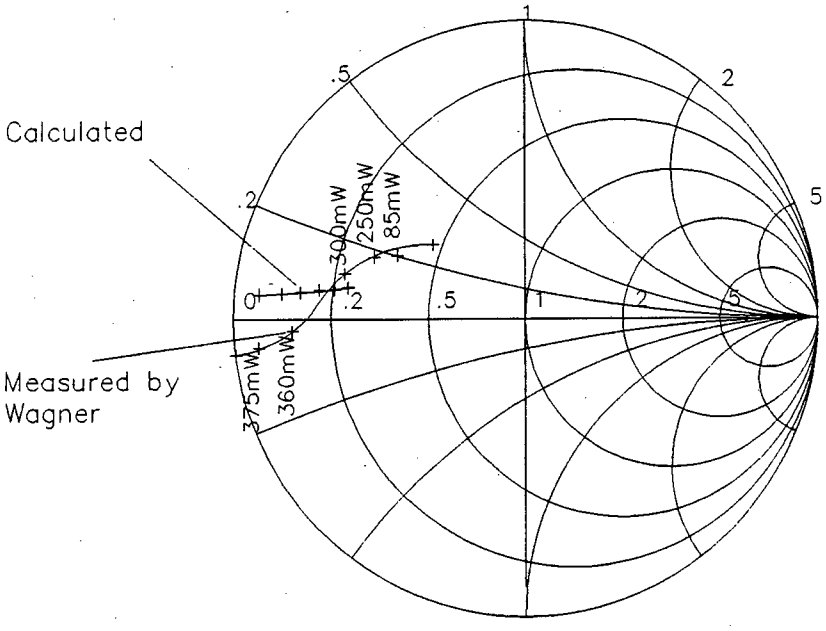

Fig 9.6 Theoretical and Practical deviceline for Wagner's oscillator

The results for the two possible source values are tabulated in Table 9.1 below.

Table 9.1 Design results for the two values of source reactance

Osc	Source React	Equiv. Cap/Ind	$\lvert(S_{21})_{cs}\rvert$	$T_s = \angle T_s$	$\angle T_{gl} = -\angle T_s$	Gate React.	Equiv. Cap/Ind
Osc B	−j39.05	0.7088pF	1.592	$1\angle -163.9°$	163.9°	j7.085	0.1961nH
Osc A	j554.1	15.35nH	1.815	$1\angle -96.8°$	96.8°	j44.4	1.229nH

Step 6: Calculation of reactive load on the gate for oscillation at 5.75 GHz.

Under steady state oscillation conditions:

$$\angle\Gamma_g \; \angle\Gamma_{gl} = 1 \quad \text{giving} \quad \angle\Gamma_{gl} = -\angle\Gamma_g \qquad (9.18)$$

$\angle\Gamma_{gl}$ and the corresponding gate reactance for each of the two source loads are tabulated in Table 9.1.

9.2.1.3 Program DESIGN

To automate the design procedure discussed in the previous section, a fortran program called DESIGN was written. The flow chart of this program appears on the next page in Figure 9.7 and a listing is included as Appendix K.

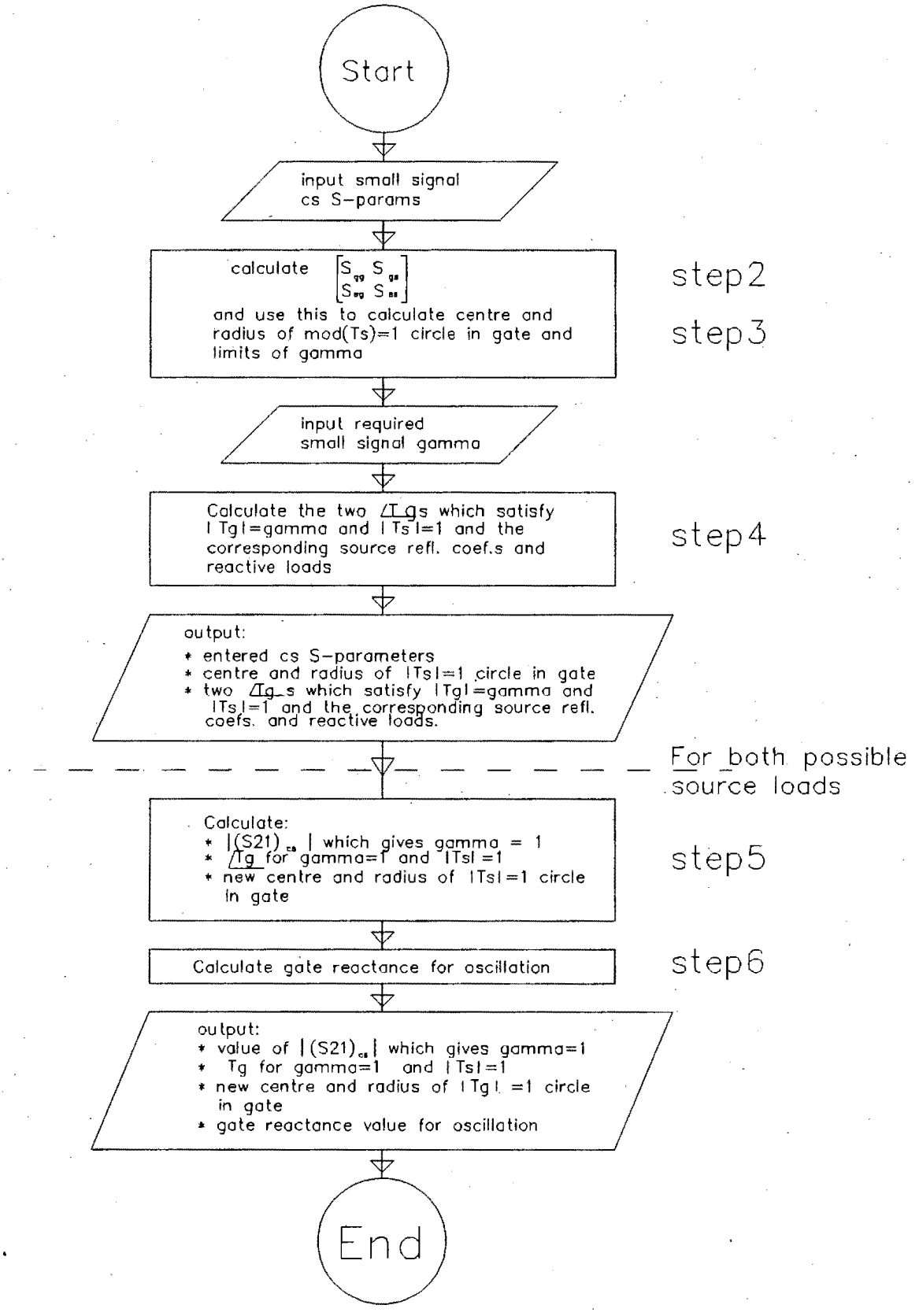

Fig 9.7 Flowchart of program DESIGN

9.2.1.4 Evaluation of the Two Possible Oscillator Configurations

Section 9.2.1.2 described a design procedure which resulted in two possible oscillator configurations. This section evaluates the two configurations, using TOUCHSTONE models, to determine which best meets the requirements for an unstabilised oscillator at 5.75 GHz.

(a) TOUCHSTONE Models of 2 Oscillators

Figure 9.8 shows the two configurations, labelled oscillator A and oscillator B, with ideal lumped elements on the source and gate.

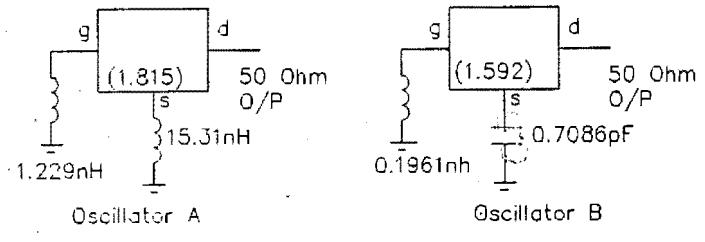

Fig 9.8 Oscillator models with ideal lumped elements

Figure 9.9 shows the same configurations with 30Ω microstrip open circuit stubs used as the reactive elements. The lengths of the stubs were calculated using the MLEF TOUCHSTONE model of an open circuit microstripline. 30Ω stubs (1.56mm wide) were used to avoid a discontinuity between the transistor and the stub on the source port.

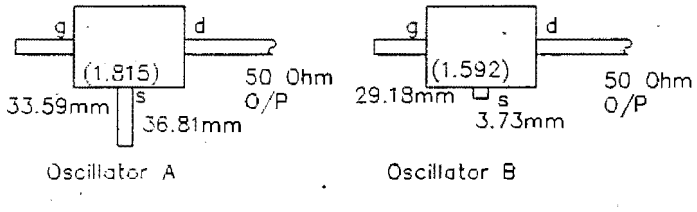

Fig 9.9 Oscillator models with microstrip elements

The two microstrip oscillators of Figure 9.9 were modelled on TOUCHSTONE to determine the frequency response of their output characteristics. To do a frequency sweep S-parameters were required at frequencies above and below 5.75 GHz.

Small signal S-parameters supplied by the manufacturers were used with $|(S_{21})_{CS}|$ reduced by the same factor as for the 5.75 GHz value.

(b) Results Obtained from TOUCHSTONE Models

Figure 9.10 and Figure 9.11 show the output characteristics of oscillator A and oscillator B respectively. Appendix L is a listing of the TOUCHSTONE file used to produce Figure 9.10.

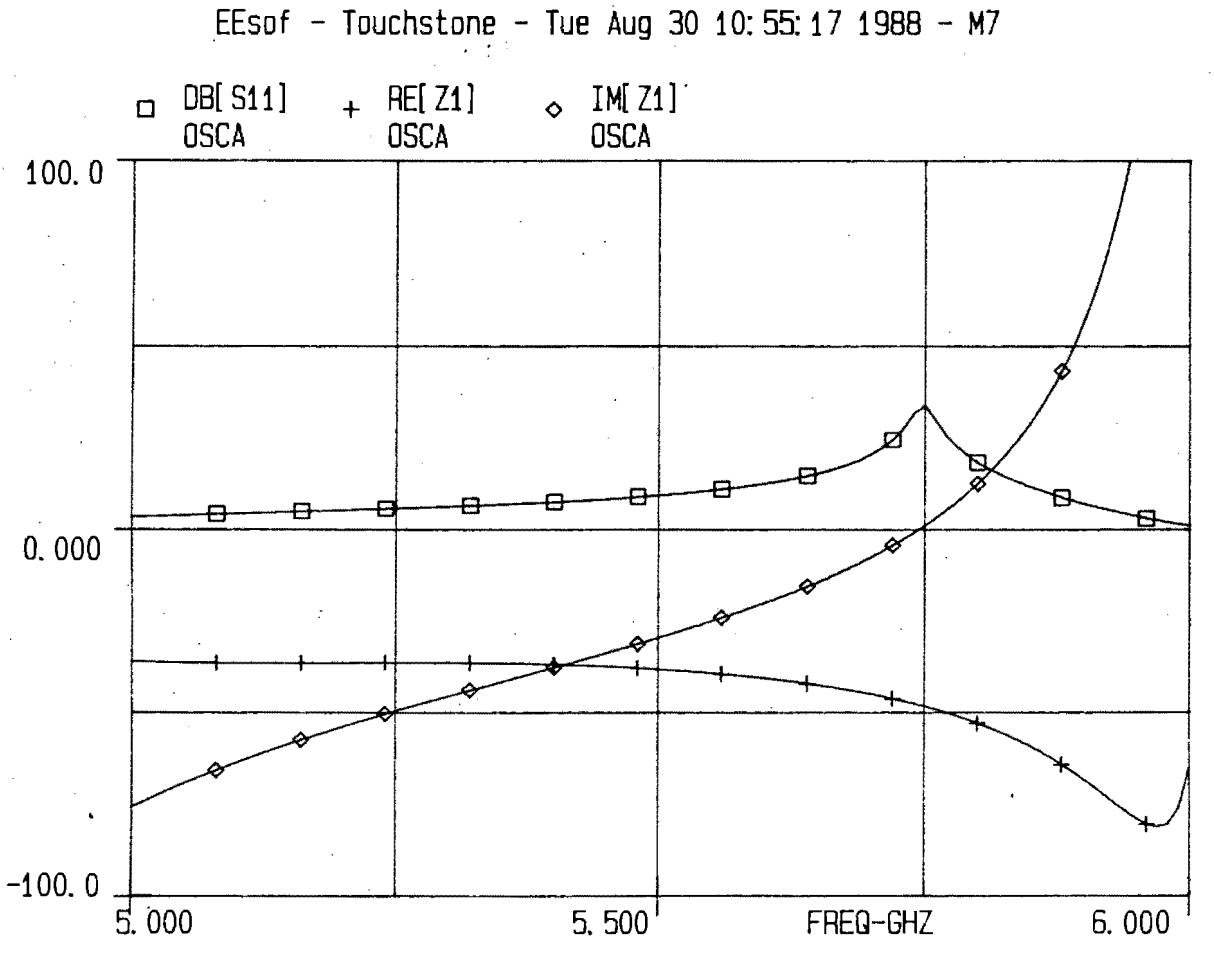

Fig 9.10 Output characteristics of oscillator A from TS model

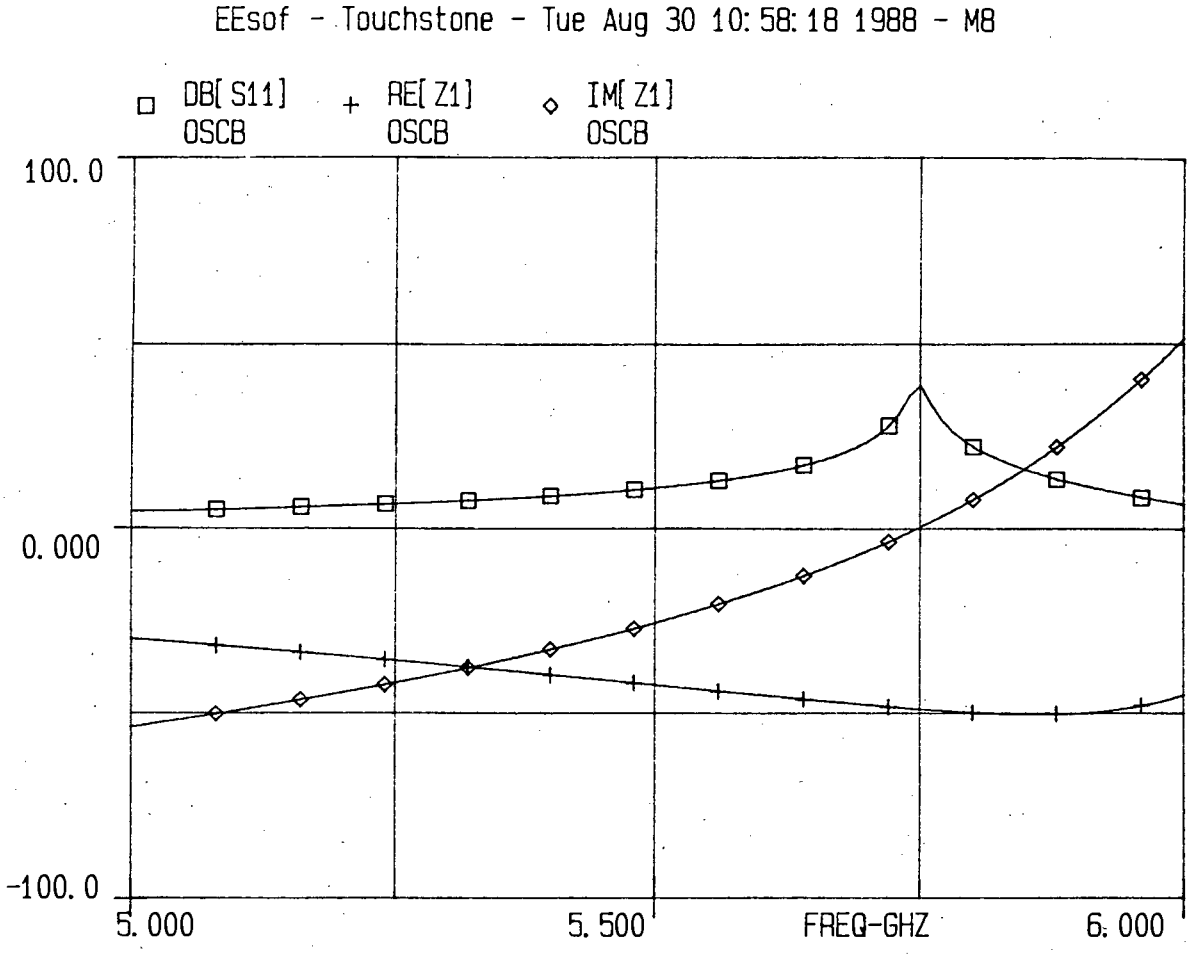

Fig 9.11 Output characteristics of oscillator B from TS model

Table 9.2, below, summarised the important results from the graphs at 5.75 GHz. Also included are frequency pulling results obtained from terminating the oscillators in different real impedances.

Table 9.2 Comparison of Touchstone model results for oscillators A and B at 5.75 GHz

Factor	Oscillator A	Oscillator B
$\lvert S_{osc} \rvert$	33.9 dB	38.9 dB
R_{osc}	−48.4 Ohms	−49.0 Ohms
X_{osc}	0 Ohms	0 Ohms
$\frac{dX_{osc}}{df}$	+ve	+ve
$(\Delta f)_{pull}$ for VSWR of 1.2	69 MHz	−35 MHz
$(\Delta f)_{pull}$ for VSWR of 1.5	157 MHz	−83 MHz

(c) Evaluation of Results

The results obtained from the TOUCHSTONE models can be used to decide which of the 2 configurations best meets the requirements of an unstabilised oscillator:

(1) oscillation frequency: both configurations oscillate at a frequency of 5.75 GHz. This is illustrated by the fact that $|S_{osc}|$ peaks at 5.75 GHz and $X_{osc} = 0$ at 5.75 GHz in both cases

(2) output power: we would expect $|S_{osc}|$ and R_{osc} to be indicative of the output power one could expect. Judging by criteria oscillator B is the better candidate. In terms of R_{osc} it is, however, only marginally better than oscillator A

(3) pulling characteristic: the results show that the pulling characteristic of oscillator A is twice as bad as that of B. A positive sign in Table 9.2 indicates that f_{osc} increases as the real termination impedance is increased, thus the frequency moves in different directions for the two oscillators. This is due to the fact that oscillator A has an inductive stub on the source and oscillator B a capacitive one

To ensure good stabilisation using a DR BRF it is essential for the unstabilised oscillator to have a poor pulling figure. It was thus decided to construct oscillator A rather than oscillator B.

9.2.2 Construction of Chosen Oscillator Configuration

Figure 9.20 (p. 124) is a photograph of the constructed oscillator tuned for maximum power at 5.75 GHz. In this photograph the stabilising DR BRF is shown in position on the output.

Since the transistor operates in a 3-port configuration it was mounted on top of the microstrip and its unused source lead cut off completely. The other leads were clipped as close to the transistor as possible. Figure

9.12 shows the bias arrangements used to dc bias the device. An RF choke consisting of 5 turns of 0.08mm diameter self-tinning wire was found to work well as frequencies around 6 GHz.

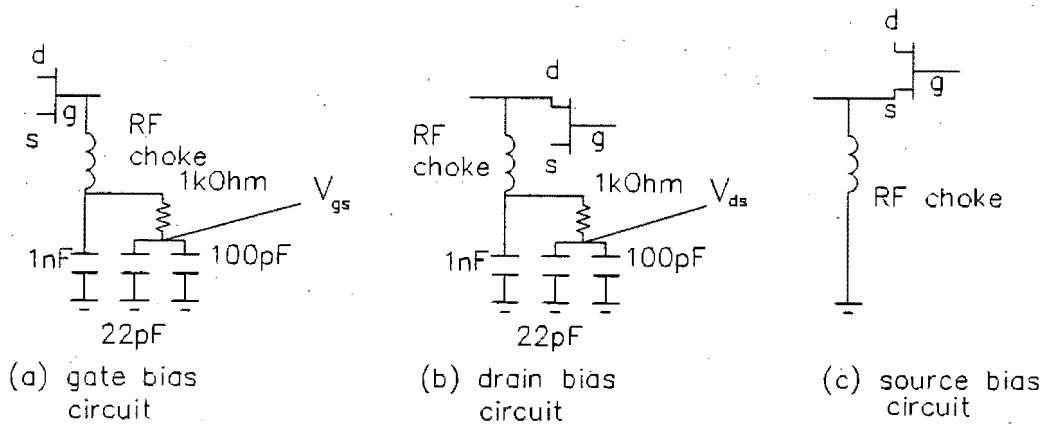

Fig 9.12 Bias circuits used to supply dc bias to the device

To optimise the output power into 50 Ohms at a frequency of 5.75 GHz, tuning discs were placed on the gate and source stubs. Varying the position of the tuning discs affected both the frequency and the output power and a process of trial and error was thus required to determine their optimal positions.

9.2.3 Performance Results for Unstabilised Oscillator

(a) Performance as a Function of V_{ds}.

The unstabilised microstrip oscillator performance is shown in Figure 9.13 as a function of drain bias voltage V_{ds} with gate bias voltage, V_{gs}, fixed at -1.0 volts

Fig 9.13 Unstabilised Microstrip Oscillator Performance

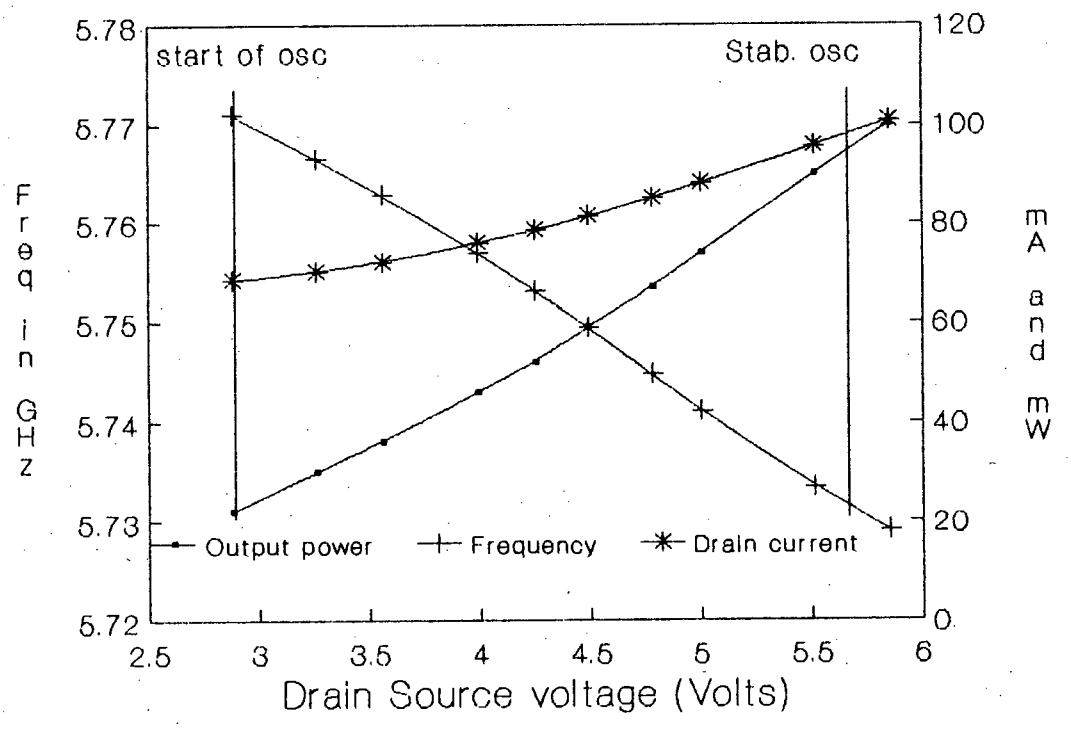

The output power was optimised at 5.75 GHz for V_{ds} = 4.5V, thus f = 5.75 GHz at this V_{ds} value. When tuning a FET oscillator it is easy to exceed the maximum V_{ds} rating with large transient VSWRs. Tuning at a lower V_{ds} reduces the probability of destroying the device.

Figure 9.13 shows that oscillation is only possible for V_{ds} > 2.85V. Increasing V_{ds} results in an increase in output power and a decrease in the oscillation frequency. When stabilised with a DR the oscillator was biased at V_{ds} = 5.65V. This corresponds to an unstabilised output power of 93 mW and a frequency of 5733 MHz.

(b) Noise Performance

No equipment was available to measure the noise performance of the oscillators built. The DROs had a noise performance which was better than that of the local oscillator in the spectrum analyser preventing this from being used for noise measurement.

(c) Pushing Factor

Figure 9.14 is a graph of frequency deviation from 5.75 GHz versus V_{gs}. The results show a very linear relationship with the slope of the fitted straightline giving a pushing figure of 42.7 MHz/volt.

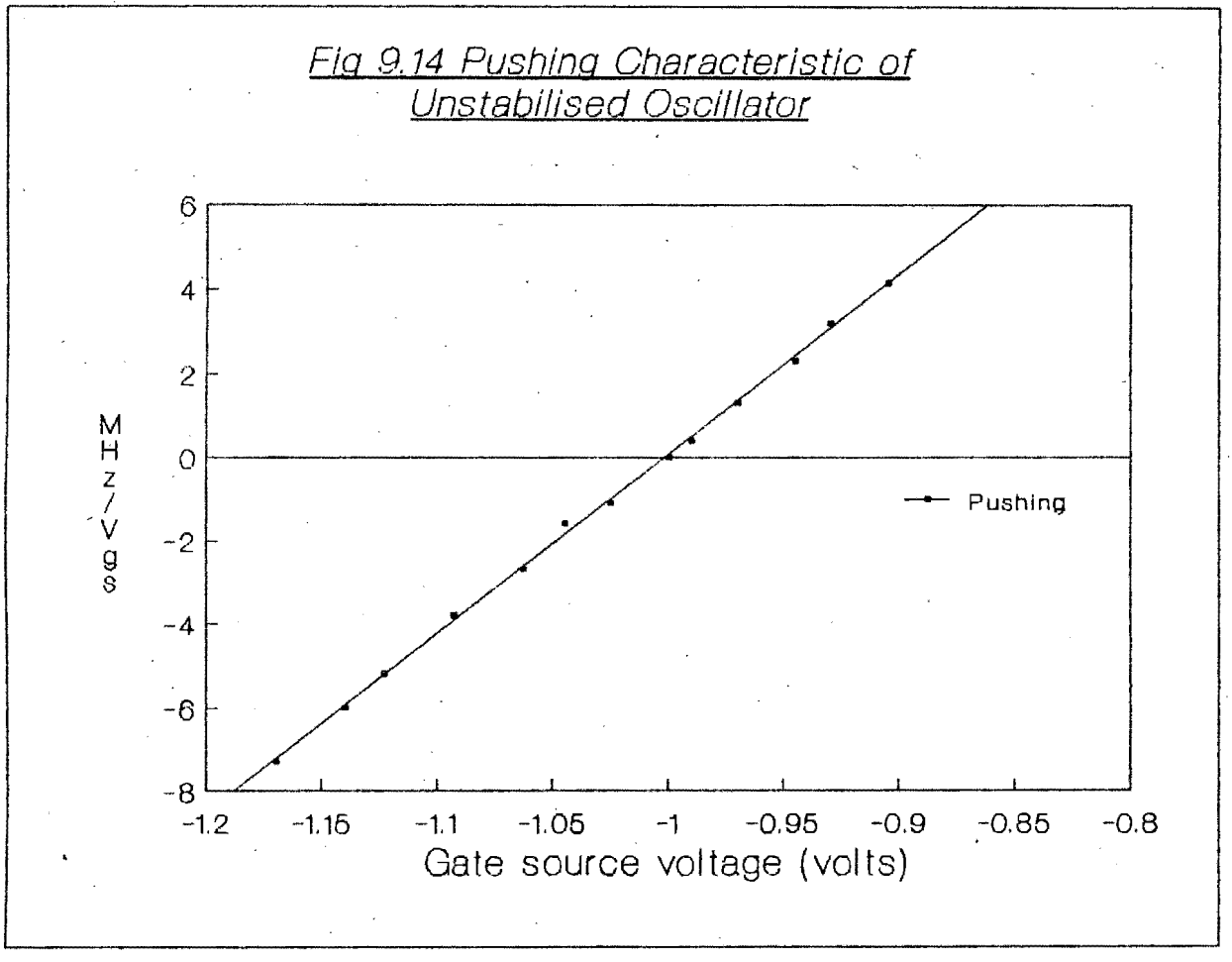

(d) Pulling Factor

Figure 9.15 shows the arrangement used to perform frequency pulling measurements.

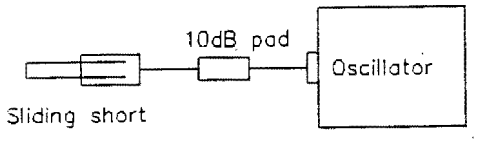

Fig 9.15 Frequency Pulling Measurement

The output spectrum varied cyclically through Δf as the position of the sliding short was varied.

The external Q of the oscillator, Q_{ex}, was determined using a formula due to Adler (Adler, 1946):

$$Q_{ex} = \frac{f_0}{\Delta f}\sqrt{\frac{P_i}{P_o}} \qquad (9.19)$$

where P_0 = output power of the oscillator
P_i = input injection locking power
f_0 = frequency of oscillation

For the arrangement of Figure 9.16 the oscillator is self-locked by the power reflected from the sliding short. Since there is a 10dB pad between the oscillator and the sliding short P is down by a factor of 100 on P_0 i.e.: $\frac{P_i}{P_o} = \frac{1}{100}$

Δf was measured to be 82 MHz giving a Q_{ex} of 7.01.

(e) Temperature Dependence

Figure 9.16 is a graph of the frequency deviation from f_{osc} at 25°C versus temperature. The slope of the fitted straightline is -0.548 MHz/°C i.e. a temperature coefficient of -95.3 ppm/°C.

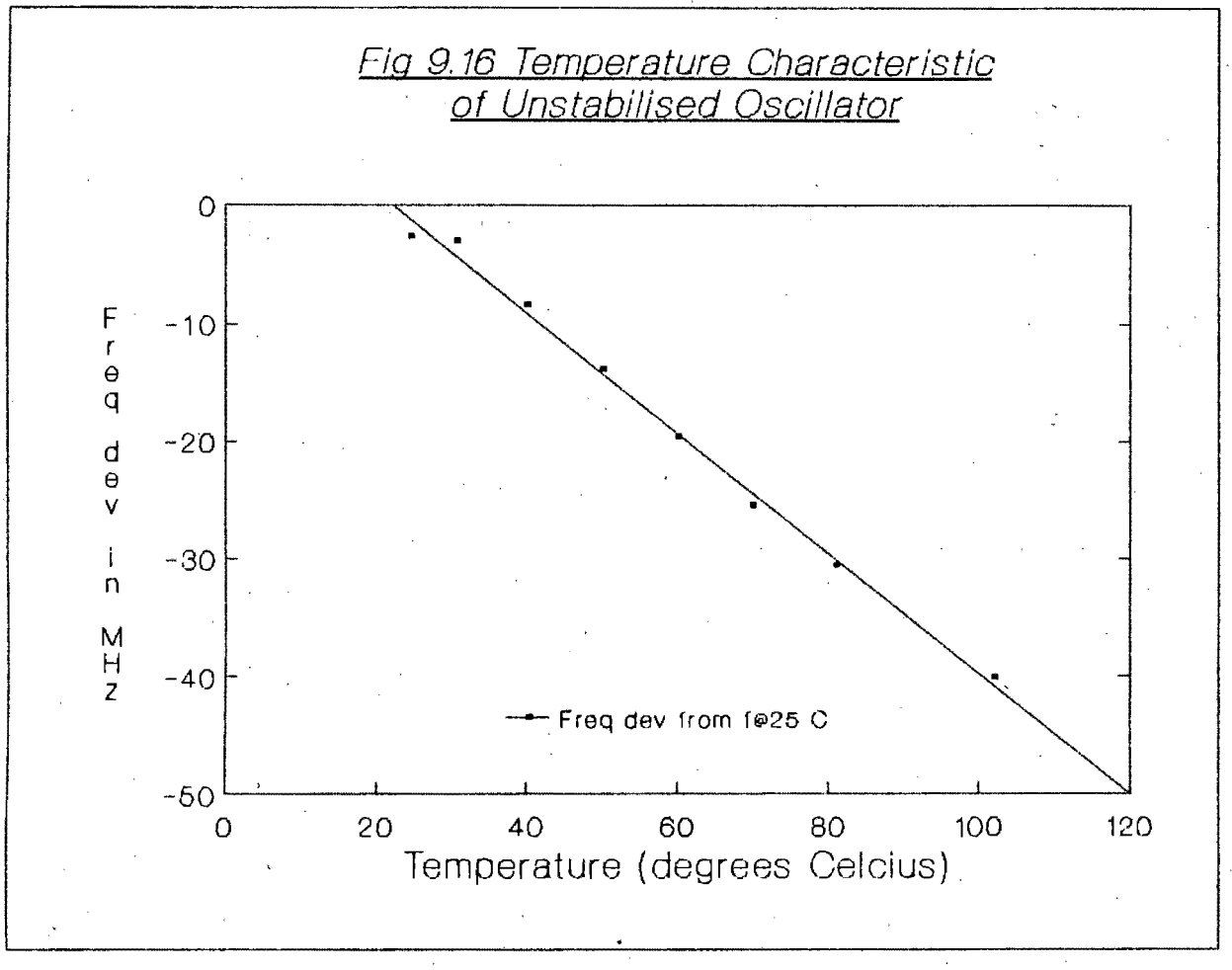

9.3 Stabilised DRO

9.3.1 Theory of DR Bandreject Filter (BRF) Stabilised Oscillators

Stabilisation of a solid state microwave oscillator using a DR BRF was first theoretically investigated by Shirahata (Abe, 1978: 159).

The output reactance X of a microwave oscillator either rises or falls with increasing frequency. Oscillators with $dX/dw > 0$ should be modelled by a series resonant circuit and those with $dX/dw < 0$ by a parallel resonant circuit (see Chapter 4). We consider here the stabilisation of an oscillator with $dX/dw < 0$ i.e. $dB/dw > 0$.

Symbols used

The following symbols are used in this section:

f_0 unstabilised oscillator oscillation frequency
f_r resonant circuit resonant frequency
f stabilised oscillator oscillation frequency
Q_o unloaded Q value of equivalent unstabilised oscillator circuit
Q_{oex} external Q value of unstabiised oscillator
Q_r resonant circuit unloaded Q value
κ coupliing coefficient between resonant circuit and transmission line

$$\delta \equiv \frac{f - f_r}{f_r}$$

$$\delta' \equiv \frac{f - f_0}{f_0}$$

Susceptance of an Unstabilised Oscillator

For an oscillator with dB/dw>0 the input impedance Y_{osc} for the equivalent parallel LRC circuit (see Figure 9.17) is given by:

$$Y_{osc} = \frac{1}{Z_{osc}} = \frac{1 + 2jQ_o\delta'}{R} \qquad (9.20)$$

where $$\delta' = \frac{f - f_0}{f_0} = \left[\frac{f - f_r}{f_r} + \frac{f_r - f_0}{f_r}\right]\left[\frac{f_r}{f_0}\right] \qquad (9.21)$$

The input susceptance B is thus

$$B_{osc} = \frac{2Q_o\delta'}{R} = \frac{2Q_{oex}}{Z_0}\left[\frac{f - f_r}{f_r} + \frac{f_r - f_0}{f_r}\right]\left[\frac{f_r}{f_0}\right] \qquad (9.22)$$

where

$$Q_{oex} \equiv \frac{Q_o Z_0}{R} \qquad (9.23)$$

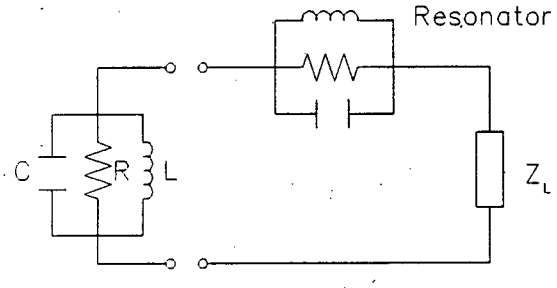

Fig 9.17 Equivalent circuit of stabilised oscillator

Susceptance of DR Stabilising Circuit

At the filter reference plane, the input impedance of the DR BRF terminated in a load $Z_L = ([1 + a] + jb)Z_0$ is given by:

$$Z_{stab} = \frac{2KZ_0}{1 + j2Q_r\delta} + ((1 + a) + jb) \qquad (9.24)$$

$$\text{Thus } Y_{stab} = \frac{1}{Z_0} \cdot \frac{1 + j2Q_r\delta}{(1 + a + 2K - 2bQ_r\delta) + j(b + 2Q_r\delta(1 + a))} \qquad (9.25)$$

the imaginary part of which,

$$B_{stab} = \frac{1}{Z_0} \cdot \frac{K4Q_r\delta - b(1 + 4Q_r^2\delta^2)}{(1 + a + 2K - 2bQ_r\delta)^2 + (b + 2Q_r\delta(1 + a))^2} \qquad (9.26)$$

Stabilisation Condition and Oscillation Frequency

To stabilise an oscillator with $dB/dw > 0$ the stabilising circuit should have the same characteristic to ensure that the condition

$$\frac{\partial B_{total}}{\partial w} > 0 \quad \text{is met.}$$

As shown in Section 5.3, the condition

$$\frac{\partial B_{stab}}{\partial w} > 0$$

can be met by placing the BRF at a point $n\lambda_g/2$ away from the unstabilised oscillator reference plane.

The oscillation frequency is found by equating the total susceptance $B_{osc} + B_{stab}$ to zero

$$\frac{2Q_{oex}}{Z_0}\left[\frac{f - f_r}{f_r} + \frac{f_r - f_0}{f_r}\right]\left[\frac{f_r}{f_0}\right] + \frac{1}{Z_0} \cdot \frac{K4Q_r\delta - b(1 + 4Q_r^2\delta^2)}{(1 + a + 2K - 2bQ_r\delta)^2 + (b + 2Q_r\delta(1 + a))^2} = 0 \qquad (9.27)$$

If the DR BRF is terminated in a non-reflecting load and f_r/f_o is approximated as unity, then:

$$0 = 2Q_{oex}\left[\frac{f - f_r}{f_r} + \frac{f_r - f_0}{f_r}\right] + \frac{4\kappa Q_r \delta}{(1 + 2\kappa)^2 + (2Q_r\delta)^2}$$

$$\frac{f_0 - f_r}{f_r} = \left[\frac{f - f_r}{f_r}\right]\left[1 + \frac{2\kappa}{(1 + 2\kappa)^2}\cdot\frac{Q_r}{Q_{oex}}\cdot\frac{1}{1 + \left[\frac{2Q_r}{1 + 2\kappa}\left[\frac{f - f_r}{f_r}\right]\right]^2}\right] \tag{9.28}$$

$$\text{or } \frac{f_0 - f_r}{f_r} = F\left[\frac{f - f_r}{f_r}\right] \tag{9.29}$$

Derivatives $\left(\frac{\partial f}{\partial f_o}\right)_{f_r}$ and $\left(\frac{\partial f}{\partial f_r}\right)_{f_o}$ are obtained as follows:

applying $\frac{\partial}{\partial f_o}$ to both sides of (9.29) gives

$$\frac{1}{f_r} = F'.\frac{\partial}{\partial f_0}\left[\frac{f - f_r}{f_r}\right] = F'.\frac{1}{f_r}.\frac{\partial f}{\partial f_0} \tag{9.30}$$

hence $$\left.\frac{\partial f}{\partial f_0}\right|_{f_r} = \frac{1}{F'\left[\frac{f - f_r}{f_r}\right]} \tag{9.31}$$

applying $\frac{\partial}{\partial f_r}$ to both sides of (9.29) gives

$$-\frac{f_0}{f_r^2} = F'.\left[\frac{1}{f_r}.\frac{\partial f}{\partial f_r} - \frac{f}{f_r^2}\right] \tag{9.32}$$

rearranging, $$\left.\frac{\partial f}{\partial f_r}\right|_{f_0} = \frac{1}{f_r}.\left[f - \frac{f_0}{F'}\right] \tag{9.33}$$

Hysteresis Phenomenon

From (9.33), $\left(\frac{\partial f}{\partial f_r}\right)_{f_o}$ becomes infinite when $F'\left(\frac{f - f_r}{f_r}\right) = 0$ (9.34)

Solving (9.34) give four values of $(\frac{f - f_r}{f_r})$ and substituting these values into (9.28) gives the four values of oscillator frequency f_o for which $(\partial f/\partial f_r)f_0$ becomes infinite. These can be labelled f_r-f_a, f_r-f_b, f_r+f_b, f_r+f_a as shown in Figure 9.18. Approximate values for f_a and f_b are derived in Appendix M assuming $Q_{ex} << Q_r$. They are:

$$f_a = \frac{K}{(2K+1)} \cdot \frac{1}{Qoex} \cdot f_r \qquad (9.35)$$

and

$$f_b = \sqrt{\frac{2}{Q_{oex}Q_r}} \cdot f_r \qquad (9.36)$$

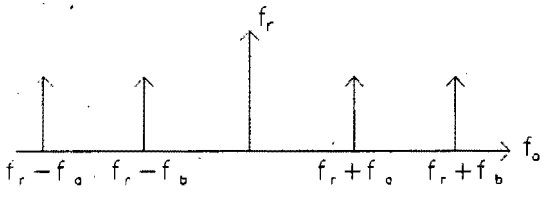

Fig 9.18 Unstabilised oscillator frequencies at which $\left(\frac{\partial f}{\partial f_r}\right)_{f_0}$ becomes infinite

For f_o lying between $f_r-f_b < f_o < f_r+f_b$ only one stable value of f exists which satisfies (9.28). Hence for f_o in this range no hysteresis results.

For f_o lying between $f_r-f_a < f_o < f_r-f_b$ and $f_r+f_b < f_o < f_r+f_a$ three possible values of f exist which satisfy (9.28). Of these only the smallest and largest satisfy the stable oscillating condition $\partial B_r/\partial f > 0$. Since there are two possible stable modes of oscillation, hysteresis occurs within this range.

Thus two stabilisation ranges exist, Δa which includes hysteresis and Δb which does not. From Figure 9.18 and equations (9.35) and (9.36) Δa and Δb can be approximated by:

$$\Delta a = 2f_a \approx \frac{1}{Qoex} \cdot \frac{K}{1 + 2K} \cdot f_r \qquad (9.37)$$

$$\Delta b = 2f_b \approx 2\sqrt{\frac{2K}{Q_{oex}Q_r}}.f_r \qquad (9.38)$$

Stabilised Temperature Coefficient

The stabiised oscillator temperature coefficient is given by:

$$p = \frac{1}{f}\left[\left[\frac{\partial f}{\partial f_r}\right]_{f_0}.\frac{\Delta f_r}{\Delta T} + \left[\frac{\partial f}{\partial f_0}\right]_{f_r}.\frac{\Delta f_0}{\Delta T}\right]$$

For $f = f_r = f_0$, $\frac{\partial f}{\partial f_r} = 1$ and $\frac{f - f_r}{f_r} = 0$

$$p = \frac{1}{f_r}.\frac{\Delta f_r}{\Delta T} + \frac{1}{F'(0)f_0}.\frac{\Delta f_0}{\Delta T}$$

$$= \left|\frac{1}{f_r}.\frac{\Delta f_r}{\Delta T}\right| + \frac{1}{1 + \frac{2K}{(1 + 2K)^2}.\frac{Q_r}{Q_{oex}}}.\left|\frac{1}{f_0}.\frac{\Delta f_0}{\Delta T}\right| \qquad (9.39)$$

Stabilised Pushing Figure

The stabilised oscillator pushing figure q is given by:

$$q = \left.\frac{\partial f}{\partial f_0}\right|_{f_r}.\frac{\Delta f_0}{\Delta V_{gs}}$$

For $f = f_o = f_r$ $\quad q = \frac{1}{F'(0)}.\frac{\Delta f_0}{\Delta V_{gs}} = \frac{1}{1 + \frac{2K}{(1 + 2K)^2}.\frac{Q_r}{Q_{oex}}}.\frac{\Delta f_r}{\Delta V_{gs}}$ (9.40)

Stabilised Pulling Characteristic

The pulling characteristic when $f_0 = f_r$ is obtained as follows:

The reflection coefficient of the load $= |\Gamma|e^{j\phi}$ (9.41)

$$\text{thus} \qquad (a + 1) + jb = \frac{1 + |\Gamma|e^{j\phi}}{1 - |\Gamma|e^{j\phi}}$$

$$\text{or} \qquad a + jb = \frac{2|\Gamma|e^{j\phi}}{1 - |\Gamma|e^{j\phi}} \approx 2|\Gamma|e^{j\phi} \qquad (9.42)$$

splitting (9.42) into real and imaginary parts gives:

$$a \approx 2|\Gamma|\cos\phi \qquad (9.43)$$

and

$$b \approx 2|\Gamma|\sin\phi \qquad (9.44)$$

Approximately solving (9.28) on the assumption that $\Gamma << K$ and $\Gamma << 1$ gives:

$$\frac{f - f_r}{f_r} \approx \frac{b}{4Q_r K} = \frac{\Gamma\sin\phi}{2Q_r K} \qquad (9.45)$$

$$\text{Thus} \quad (\Delta f)_{pull} = f - f_r = \frac{|\Gamma|\sin\phi}{2Q_r K}.f_r \qquad (9.46)$$

9.3.2 Stabilising the Microstrip Oscillator using a DR BRF on the Output

(a) dX/dw Characteristic of Unstabilised Oscillator

The distance of the DR from the output plane of the unstabilised oscillator is determined by the (dX/dw) characteristic of the oscillator.

Figure 9.10 (p.108) includes a plot of output reactance, X, versus frequency for the TS model of the unstabilised oscillator. At 5.75 GHz $dX/df = 1.79 \times 10^{-7}$ Ohms/Hz giving $dX/dw = 2.85 \times 10^{-8}$ radians/sec. Since dX/dw is positive a series RLC circuit is appropriate to model the oscillator at 5.75 GHz. The values of R, L and C are found as follows:

1. from Table 9.2 $R = -48.4\Omega$ (9.47)

2. from (4.46) $L = \frac{1}{2}.\frac{dX}{dw} = 14.25\text{nH}$ (9.48)

3. at resonance $f_{osc} = \frac{1}{2\pi\sqrt{(LC)}}$ giving $C = 0.0538pF$ (9.49)

Figure 9.19 shows the series RLC model and its output characteristics as a function of frequency. Comparison of Figure 9.19 with Figure 9.10 (p. 108) shows that the series RLC circuit provides an accurate model for the oscillator at 5.75 GHz.

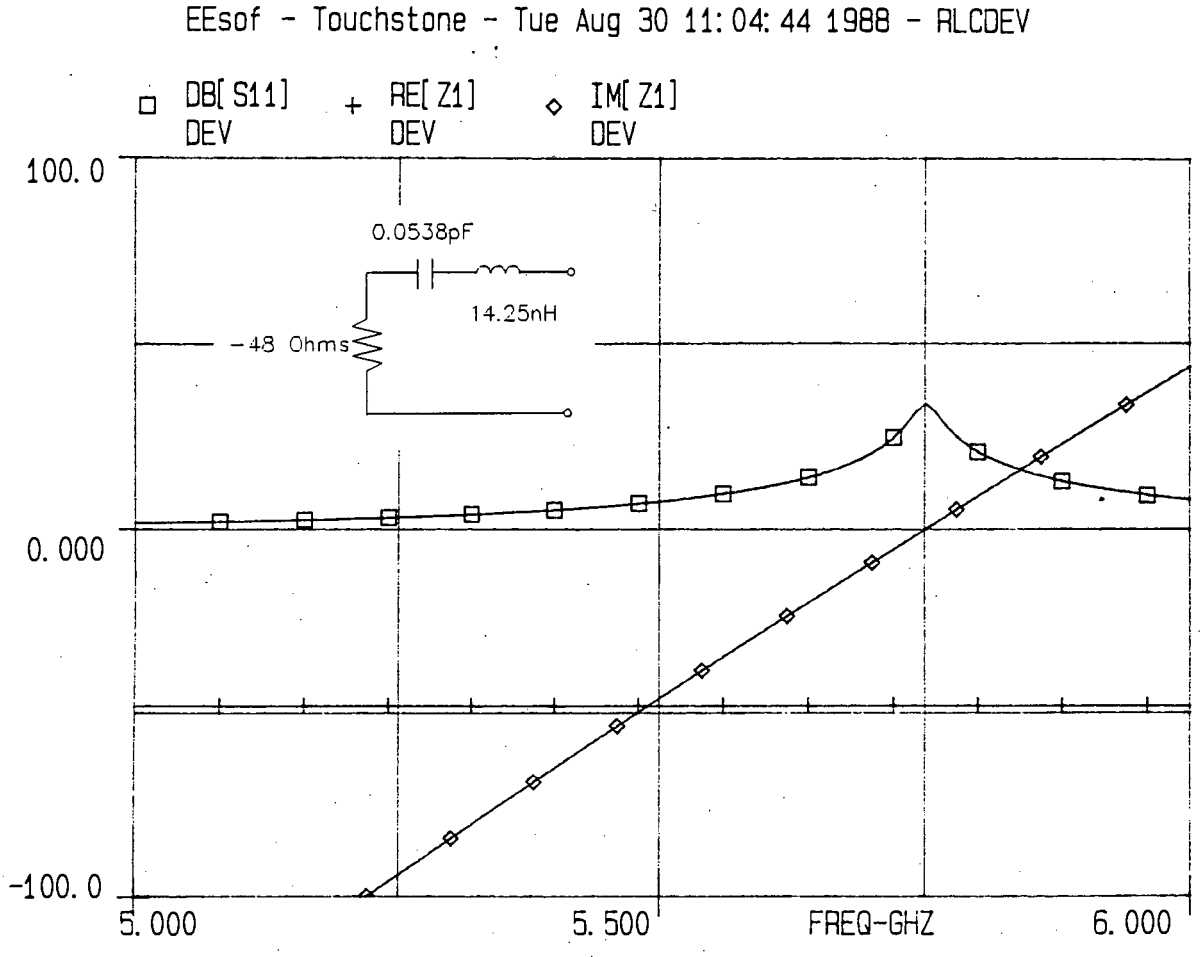

Fig 9.19 RLC model of microstrip oscillator at 5.75 GHz

(b) Positioning the DR on the Output

For an unstabilised oscillator with dX/dw positive the stabilising DR should be placed $\lambda_g/4$ (9.6mm) away from the oscillator output plane. The photograph of Figure 9.20 shows the stabilised microstrip oscillator with the DR in position. The distance of the DR from the line was made equal to 0.6mm to give a coupling coefficient at 5.75 GHz of 0.9.

Fig 9.20 Photograph of BRF stabilised DRO

9.3.3 Practical Results for BRF DR Stabilised Microstrip Oscillator

(a) Mechanical Tuning Characteristics of Stabilised Oscillator

Figure 9.21 shows f, I_{ds} and output power of the stabilised oscillator as a function of x, the height of the tuning disc above the DR.

Fig 9.21 Mechanical Tuning Characteristics of Stabilised Oscillator

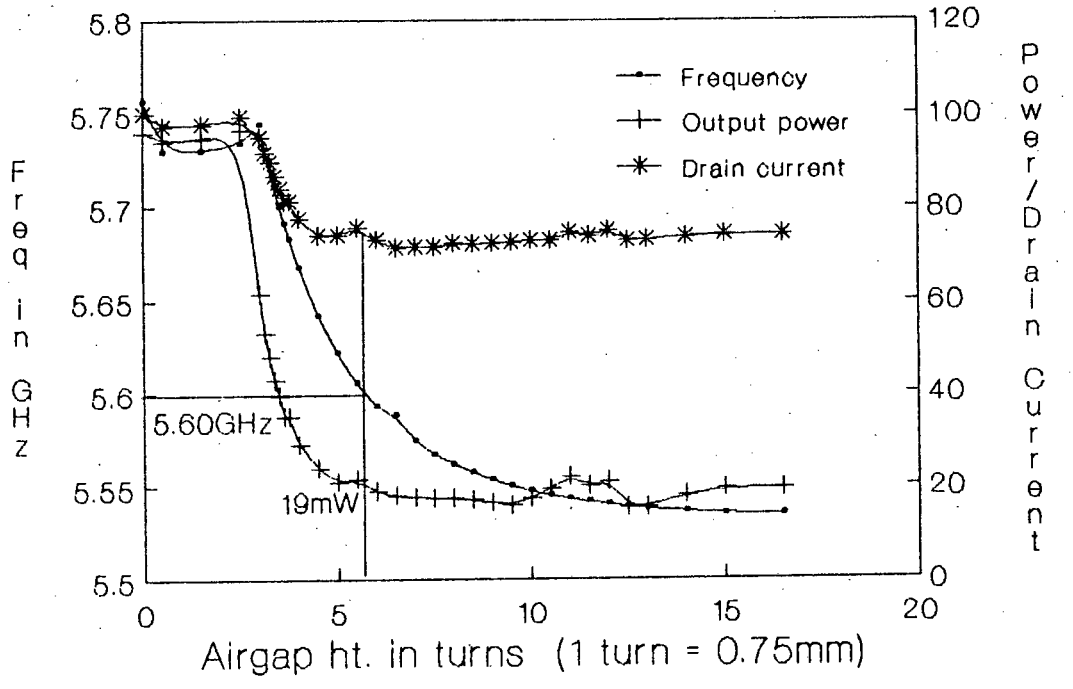

From the graph of f vs x it is seen that the unstabilised oscillator only locks to the DR at a frequency of 5.745 GHz which is the highest stabilised oscillation frequency. The stabilised frequency range extends from 5745 MHz to 5533 MHz, giving a bandwidth of 212 MHz. Comparing the frequency curve of Figure 9.21 with Figure 7.8 it is seen that the stabilised oscillation frequency is determined by the DR and tuning disc. No hysteresis was observed for the stabilised bandwidth.

The oscillator was not stabilised at 5.75 GHz. Stabilised oscillator measurements were therefore taken at a frequency of 5600 MHz which falls in the centre of the stabilised range.

(b) Pushing Factor

Figure 9.22 is a graph of V_{gs} pushing factor as a function of frequency. The pushing factor at 5600 MHz is 0.3 MHz/V.

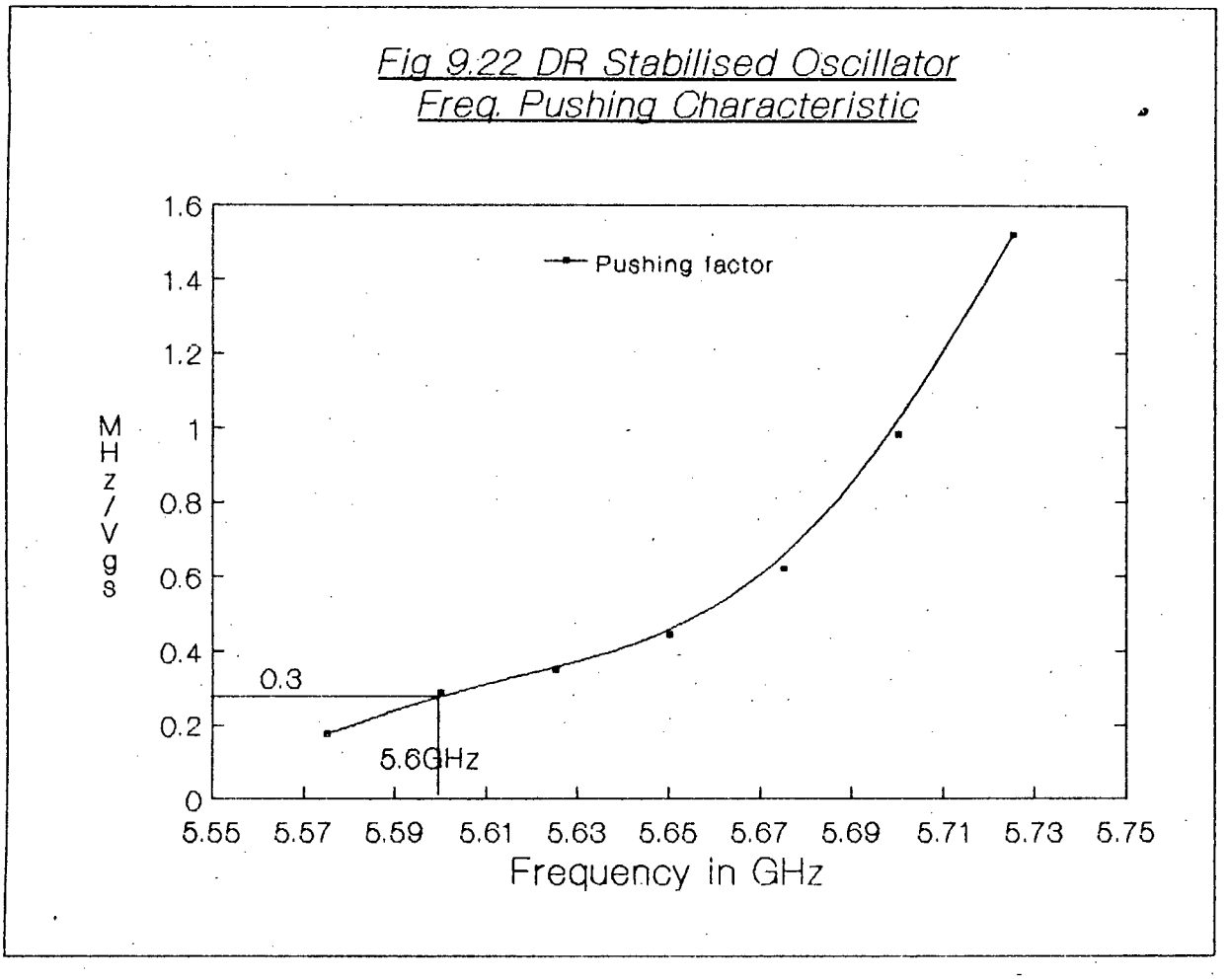

(c) Pulling Factor

Figure 9.23 shows $(\Delta f)_{pull}$ and Q_{ex} for the stabilised oscillator as a function of frequency. At 5600 MHz $(\Delta f)_{pull}$ is 90 KHz and Q_{ex} is 6000.

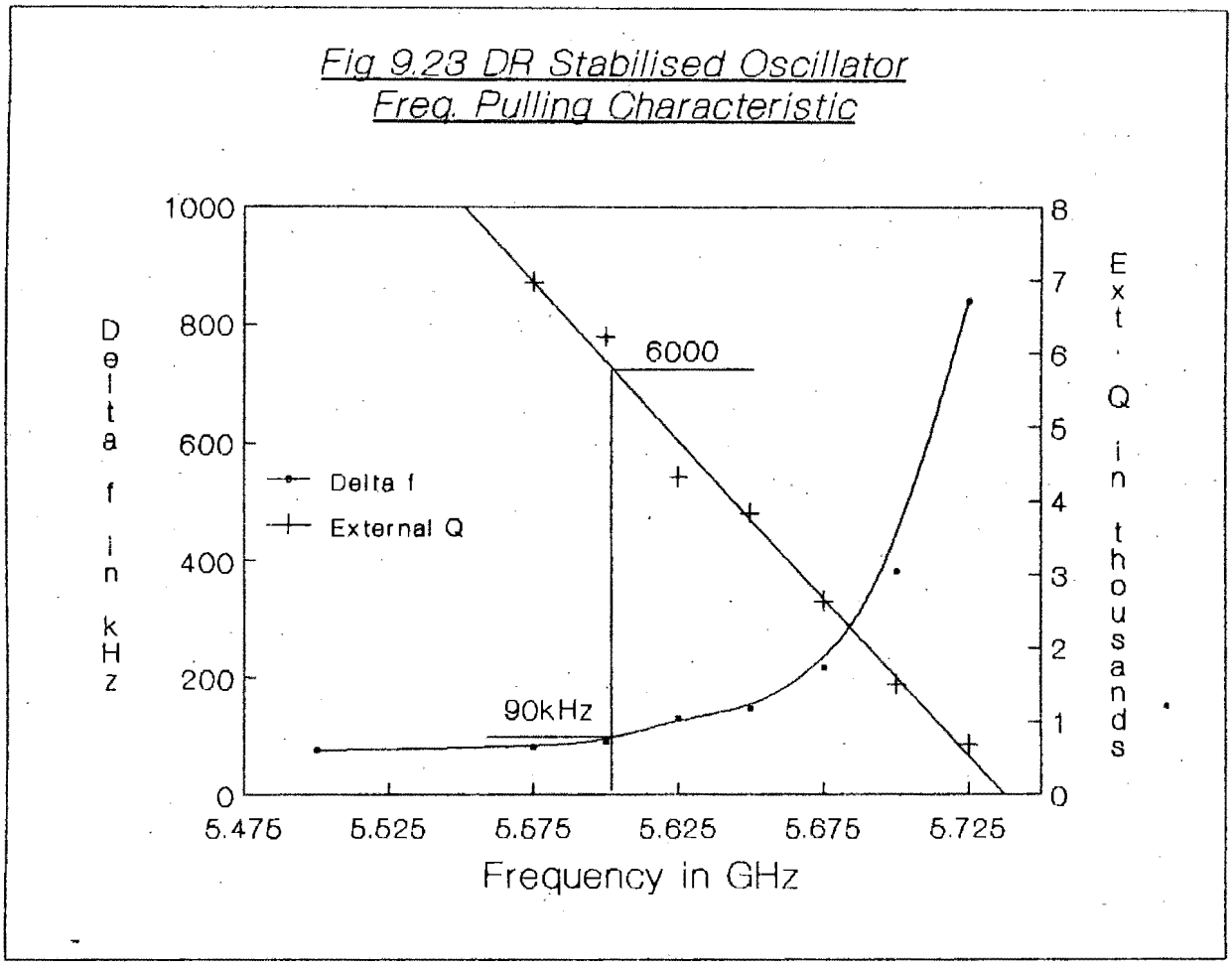

(d) Temperature Dependence

Figure 9.24 shows the frequency deviation with temperature for the stabilised oscillator. The frequency temperature dependence of the unstabilised oscillator has also been included for comparison. The frequency temperature relationship for the stabilised oscillator is not really linear but the fitted straightline shown has a gradient of 0.11 MHz/°C (i.e. -19.6ppm/°C).

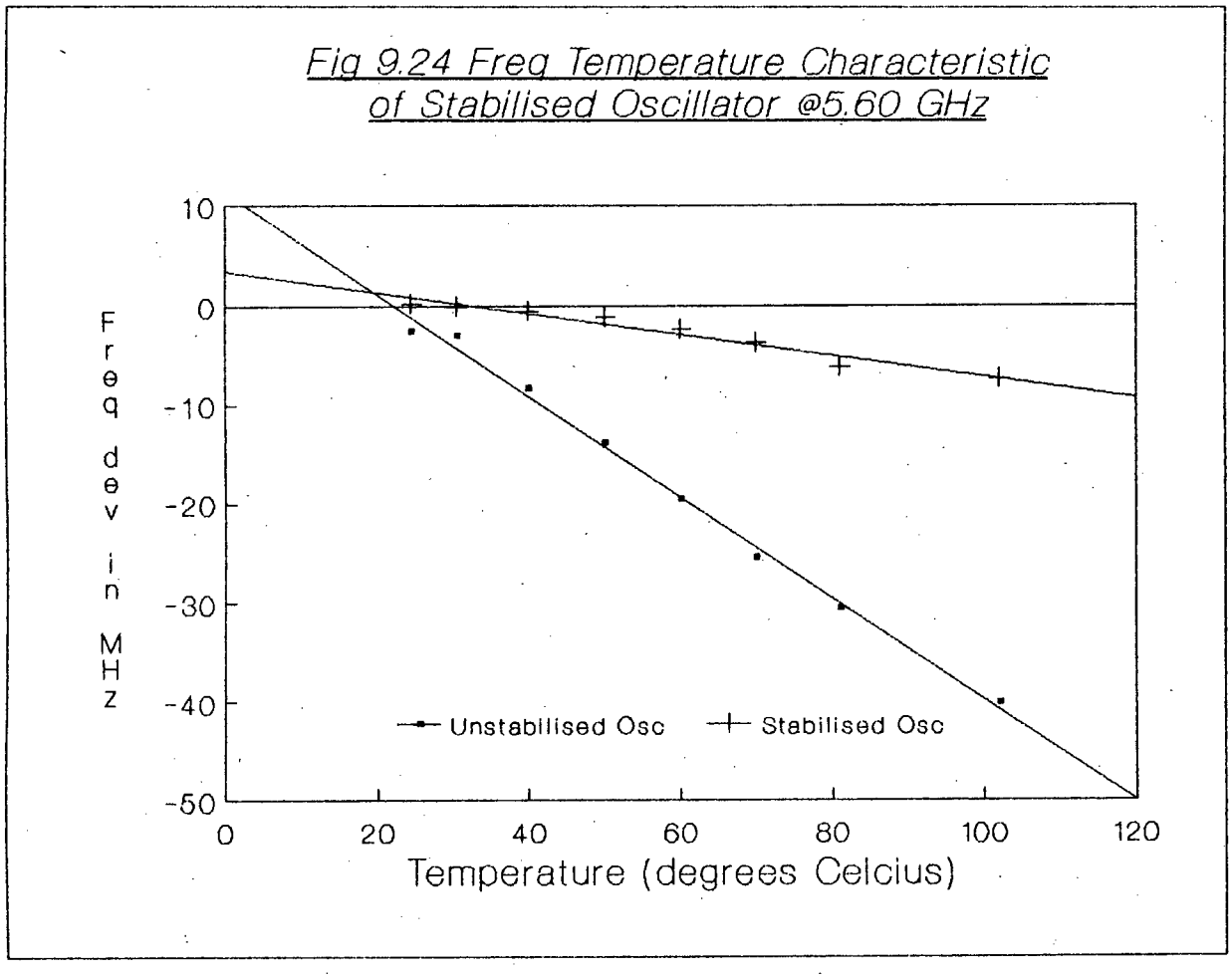

9.3.4 Theoretically Expected Results

The theory of DR BRF stabilised oscillators derived in Section 9.3.1 was for an oscillator with dB/dw positive and the DR placed $n\lambda_g/2$ from the oscillator output. For an oscillator with dX/dw positive and the DR $n\lambda_g/4$ from the output the same results hold. The only difference is that the derivation proceeds in terms of reactances rather than susceptances.

Table 9.3 tabulates the theoretically expected results at 5.75 GHz and 5.60 GHz.

The following results were used in the calculations:

$$Q_{oex} = 7.01 \tag{9.50}$$

$$\left|\frac{\Delta f}{\Delta V_{gs}}\right| = 43\ \text{MHz/V}_{gs} \tag{9.51}$$

$$|\Gamma| = 0.1 \tag{9.52}$$

$$\frac{1}{f_0}.\frac{\Delta f_0}{\Delta T} = -95.3\text{ppm/°C} \tag{9.53}$$

$$\frac{1}{f_r}.\frac{\Delta f_r}{\Delta T} = -10\text{ppm/°C} \tag{9.54}$$

From Figure 7.8 and Figure 7.9 at 5.75 GHz: $\kappa = 0.925$ (9.55); $Q_r = 3000$ (9.56) at 5.60 GHz: $\kappa = 1.45$ (9.57); $Q_r = 3850$ (9.58);

Table 9.3 Theoretical results at 5.75 GHz and 5.60 GHz

Factor	5.75 GHz results	5.60 GHz results
Total stabilised locking range	266 MHz	297 Mhz
locking range with no hysteresis	108 MHz	116 MHz
Stabilised temp. coef.	−11.0 ppm/K	−10.9 ppm/K
Stabilised Pushing Factor	0.44 MHz/V_{gs}	0.41 MHz/V_{gs}
Stabilised $(\Delta f)_{pus}$	104 KHz	50 KHz

9.4 Comparison of Actual Results for Stabilised Oscillator with Theoretically Expected Results and Results for the Unstabilised Oscillator

There are major discrepancies between the theory of Section 9.3.1 and the practical results obtained. According to the theory the centre of the stabilisation range should coincide with the unstabilised oscillator frequency so that stabilised oscillation at 5.75 GHz should be possible. Theory also predicts that no more than about 100 MHz of the stabilisation range should be free of hysteresis yet no hysteresis was observed over the mechanical tuning range of roughly 200 MHz.

Good agreement was, however, obtained between the practical and theoretical results for a stabilised oscillator at 5600 MHz as shown in Table 9.4. Table 9.4 compares the stabilised oscillator at 5.60 GHz with the unstabilised oscillator and the theoretically predicted results.

Table 9.4 Comparison of results for 5.60 GHz stabilised oscillator with unstabilised results and theoretical results

Factor	Unstabilised oscillator at 5.75 GHz	Stabilised oscillator at 5.60 GHz	Theoretical Stabilised results at 5.60 GHz
Stabilised tuning range	——	209 MHz	297 MHz
Pushing Factor	43 MHz/V	0.3 MHz/V	0.41 MHz/V
$(\Delta f)_{pull}$	82 MHz	90 KHz	50 KHz
Temperature coefficient	−95.3 ppm/K	−19.6 ppm/K	−10.9 ppm/K
Output Power	95 mW	19 mW	——
Efficiency	17.3%	4.5%	——

The pushing and pulling factors of the stabilised oscillator have been improved by factors of 100 and 1000 respectively over the unstabilised results. The temperature coefficient of the stabilised oscillator is 5

times better than that of the unstabilised oscillator. These results demonstrate that the frequency stability of the oscillator has been dramatically improved by the DR BRF.

CHAPTER 10

COMMON SOURCE, COMMON DRAIN AND COMMON GATE SERIES FEEDBACK STDROs

10.1 Introduction

This chapter describes the design, construction and comparison of common drain (CD), common source (CS) and common gate (CG) series feedback oscillators.

The first section, Section 10.2, details the step-by-step design of a CS series feedback STDRO at 5.75 GHz. CD and CG oscillators can be designed using the same procedure and their design results are given in Section 10.3. Section 10.4 checks the theoretical design results using the Touchstone (TS) computer program.

Section 10.5 details the practical construction, determination of resonator position and technical problems of the three series feedback configurations. The difference between the practical and predicted resonator positions is then discussed in Section 10.6.

The practical results obtained for the CD, CS and CG oscillators are the subject of Section 10.7 and these results are compared in Section 10.8 to determine which series feedback configuration gave the best results.

The chapter ends with the conclusions which can be drawn from the results obtained.

10.2 Step-by-Step Design of a Common Source Series Feedback STDRO

Chapter 5 outlined the basic concepts involved in designing a series feedback STDRO. This section details the step-by-step design of a common source series feedback STDRO at 5.75 GHz. This SDTRO is designed for maximum frequency stability.

10.2.1 Determining a Value of Source Reactance Which Gives Greater Than Unity Reflection Coefficient on the Gate and on the Drain

The first step in the design is to determine a value of source reactance X_s (see Figure 10.1) which gives $|\Gamma_g| > 1$ and $|\Gamma_d| > 1$ for a 50Ω measuring system.

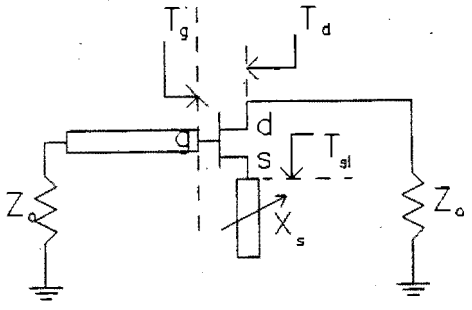

Fig 10.1 Determination of source reactance Xs

For the case of an oscillator constructed in microstrip an open circuit stub can be used to provide a reactive impedance X_s between $-j\infty\Omega$ and $+j\infty\Omega$. Such an impedance presents a reflection coefficient Γ_{sl} to the source with unity magnitude and an angle dependent on the length of the open circuit stub.

Γ_{sl} is given by $$\Gamma_{sl} = \frac{X_s - Z_0}{X_s + Z_0} \qquad (10.1)$$

Γ_{sl} relates the wave incident on the source port, a_s, to the reflected wave b_s.

$$a_s = \Gamma_{sl} b_s \qquad (10.2)$$

Applying this condition to the 3-port matrix of the transistor reduces it to the 2-port matrix $\underline{S}_{sl}$ below (see Section 9.2.1.2).

$$\underline{S}_{sl} = \begin{bmatrix} S_{gg} + \frac{S_{gs}S_{sg}\Gamma_{sl}}{1 - S_{ss}\Gamma_{sl}} & S_{gd} + \frac{S_{gs}S_{sd}\Gamma_{sl}}{1 - S_{ss}\Gamma_{sl}} \\ S_{dg} + \frac{S_{ds}S_{sg}\Gamma_{sl}}{1 - S_{ss}\Gamma_{sl}} & S_{dd} + \frac{S_{ds}S_{sd}\Gamma_{sl}}{1 - S_{ss}\Gamma_{sl}} \end{bmatrix} \qquad (10.3)$$

From (9.2) the 3-port matrix elements for the MGF1801 at 5.75 GHz are:

$$\begin{bmatrix} S_{gg} & S_{gd} & S_{gs} \\ S_{dg} & S_{dd} & S_{ds} \\ S_{sg} & S_{sd} & S_{ss} \end{bmatrix} = \begin{bmatrix} 1.346\angle\underline{-131.28^\circ} & 0.834\angle\underline{43.43^\circ} & 1.355\angle\underline{18.56^\circ} \\ 3.208\angle\underline{46.84^\circ} & 1.308\angle\underline{-103.82^\circ} & 1.386\angle\underline{-129.51^\circ} \\ 1.364\angle\underline{-103.00^\circ} & 0.993\angle\underline{44.61^\circ} & 0.807\angle\underline{46.48^\circ} \end{bmatrix} \quad (10.4)$$

To determine the values of source reactance which give $|\Gamma_g| > 1$ Wagner's equation is used to plot the $|\Gamma_{sl}| = 1$ circle into the gate reflection coefficient plane with the drain terminated in 50Ω. This procedure has been described as Step 2 of Section 9.2.1.2. From (9.13) and (9.15) the centre of the $|\Gamma_{sl}| = 1$ circle in the gate reflection coefficient plane is

$$\Omega_g = 7.99\ \underline{/-130.7^\circ} \quad (10.5)$$

and the radius is $R_g = 7.63$ (10.6)

The same technique can be used to map the $|\Gamma_{sl}| = 1$ circle into the drain reflection coefficient plane with the gate terminated in 50 Ω. In this case the 3-port matrix reduces to:

$$\underline{S}_{g50} = \begin{bmatrix} S_{dd} & S_{ds} \\ S_{sd} & S_{ss} \end{bmatrix} = \begin{bmatrix} 1.308\ \underline{/-103.82^\circ} & 1.386\ \underline{/-129.51^\circ} \\ 0.993\ \underline{/44.61^\circ} & 0.870\ \underline{/46.48^\circ} \end{bmatrix} \quad (10.7)$$

The centre of the $|\Gamma_{sl}| = 1$ circle in the drain reflection coefficient is thus given by:

$$\Omega_d = \frac{S_{dd} - \Delta_{g50} S_{ss}^*}{1 - |S_{ss}|^2} = 6.14\ \underline{/-125.7^\circ} \quad (10.8)$$

where $\Delta_{g50} = S_{dd}S_{ss} - S_{sd}S_{ds}$ (10.9)

and the radius by $\left[\frac{S_{ds}S_{sd}}{1 - |S_{ss}|^2}\right] = 5.68$ (10.10)

Program MAPPING (Appendix N) automates the calculation of the centre and radius of the load reactance circle in the input reflection coefficient

plane for a 2-port network. It also calculates the maximum input reflection value and the corresponding load reactance.

Applying MAPPING to the reduced 2-port matrices (9.12) and (10.7) gives results (10.5) through (10.10) as well as

$$(\Gamma_g)_{max} = 15.61 \angle -130.7^\circ \text{ for } X_s = 116.4\ \Omega \qquad (10.11)$$

$$(\Gamma_d)_{max} = 11.82 \angle -125.7^\circ \text{ for } X_s = 117.6\ \Omega \qquad (10.12)$$

Thus the value of source reactance required to maximise Γ_g differs slightly from that required to maximise Γ_d. A value of source reactance $-j100\Omega$ was chosen for this oscillator which gives:

$$\Gamma_g = 11.99 \angle -169.5^\circ \qquad (10.13)$$

and

$$\Gamma_d = 8.86 \angle -166.5^\circ \qquad (10.14)$$

Figures 10.2(a) and 10.2(b) show the $|\Gamma_{sl}| = 1$ circle plotted into the gate and drain reflection coefficient planes respectively. The diagonal matrix elements in (10.3) can be used to calculate the drain and gate reflection coefficients for different source reactance values. These values of X_s can then be marked on the circles. The chosen source reactance of $-j100\Omega$ is marked with an arrow in both diagrams.

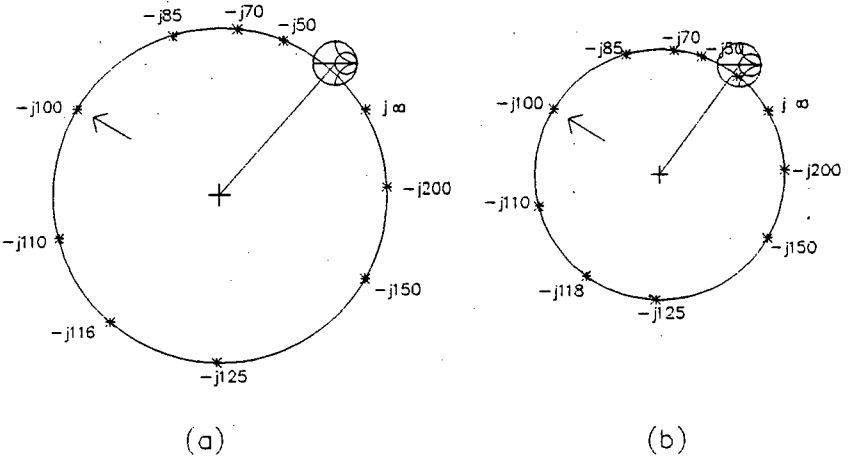

Fig 10.2 Mapping of |Tsll = 1 into (a) Tg and (b) Td reflection coefficient planes for CS oscillator

For $X_s = -j100\Omega$, $\Gamma_{sl} = 1 \angle -53.1°$. Substituting this into matrix (10.3) gives the reduced 2-port matrix $\underline{S}^T$ for the transistor terminated in a source impedance of $-j100\Omega$.

$$\underline{S}^T = \begin{bmatrix} S_{gg}{}^T & S_{gd}{}^T \\ S_{dg}{}^T & S_{dd}{}^T \end{bmatrix} = \begin{bmatrix} 1.989 \angle -169.54° & 8.310 \angle -20.9° \\ 14.391 \angle 39.76° & 8.684 \angle -166.48° \end{bmatrix} \quad (10.15)$$

10.2.2 Determination of Optimum Resonator Position for Maximum Drain Reflection Coefficient

Having set the value of the source impedance at $-j100\Omega$ the resulting 2-port S-parameters are given by (10.15). The second step of the procedure is to determine the value of reflection coefficient Γ_{gl} which maximises the reflection coefficient Γ_d at the drain port (Figure 10.3) from the relation

$$\Gamma_d = S_{dd}{}^T + \frac{S_{gd}{}^T S_{dg}{}^T \Gamma_{gl}}{1 - S_{gg}{}^T \Gamma_{gl}} \quad (10.16)$$

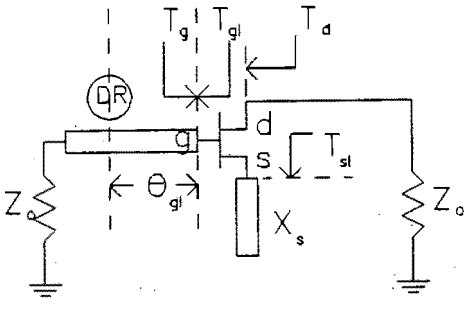

Fig 10.3 Determination of DR position on gate for CS oscillator

Γ_{gl} as shown in Figure 10.3 is the reflection coefficient provided by a DR coupled to a microstripline in bandstop configuration. The magnitude of the reflection coefficient Γ_{gl} is set by the coupling of the DR to the

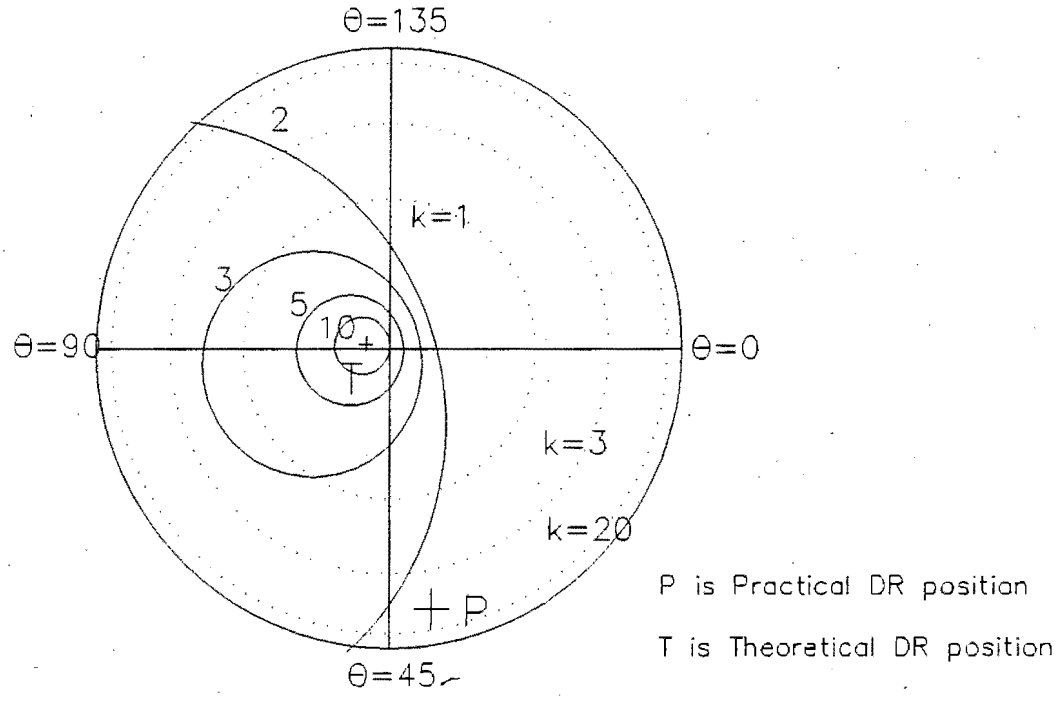

Fig 10.4 $|T_d|$ = constant circles in the gate load refl. coef. plane for CS oscillator

The figure shows that as $|\Gamma_d|$ increases the radius of the $|\Gamma_d|$ circle decreases until eventually it converges to a point in the Γ_g $(\kappa_{gl}, \theta_{gl})$ plane. This is in agreement with what we would expect from (10.17) and (10.18) as shown below:

$$R = \frac{|\Gamma_d S_{gd}{}^T S_{dg}{}^T|}{|\Gamma_d|^2 |S_{gg}{}^T|^2 - |\Delta^T|^2}$$

$$= \frac{|\Gamma_d| |S_{gd}{}^T| |S_{dg}{}^T|}{|\Gamma_d|^2 |S_{gg}{}^T|^2 - |\Delta^T|^2} \qquad (10.21)$$

Thus as $|\Gamma_d| \to \infty$, $R \to 0$ (10.22)

Also, for $|\Gamma_d| \to \infty$, $\Omega \to \frac{S_{gg}{}^{T*}}{|S_{gg}{}^T|^2} = \frac{1}{S_{gg}{}^T}$ (10.23)

For the gate terminated in 50 Ω, $S_{gg}{}^T = \Gamma_g$

microstripline and the phase is set by the distance of the centre of the DR from the gate.

Since $|S_{gg}{}^T|$ and $|S_{dd}{}^T|$ are both greater than one, the expressions derived in Appendix I cannot be used to find the value of $\Gamma_{gl}(\kappa_{gl},\theta_{gl})$ which maximises Γd. The approach used in this case is the constant reflection coefficient approach in which circles of constant reflection coefficient magnitude $|\Gamma_d|$ are plotted in the $\Gamma_{gl}(\kappa_{gl}, \theta_{gl})$ plane.

The radius R and centre Ω of the constant reflection circles are (Papp, 1980: 764):

$$R = \frac{|\Gamma_d S_{gd}{}^T S_{dg}{}^T|}{|\Gamma_d|^2|S_{gg}{}^T|^2 - |\Delta^T|^2} \qquad (10.17)$$

$$\Omega = \frac{S_{gg}{}^{T*}(|\Gamma_d|^2 - |S_{dd}{}^T|^2) + S_{dd}{}^T S_{gd}{}^{T*} S_{dg}{}^{T*}}{|\Gamma_d|^2|S_{gg}{}^T|^2 - |\Delta^T|^2} \qquad (10.18)$$

where $\Delta^T = S_{gg}{}^T S_{dd}{}^T - S_{gd}{}^T S_{dg}{}^T \qquad (10.19)$

Figure 10.4 shows $|\Gamma_d|$ = constant circles plotted in the $\Gamma_{gl}(\kappa_{gl},\theta_{gl})$ plane. Note that once round the $\Gamma_{gl}(\kappa_{gl},\theta_{gl})$ plane is equal to 180° since for a DR θ_{gl} degrees away

$$\theta_{gl} = 0.5(360 - \angle\Gamma_{gl}) \qquad (10.20)$$

Thus as $|\Gamma_d| \rightarrow \infty$

$$\Omega \rightarrow \frac{1}{|\Gamma_g|} \angle -\Gamma_g \qquad (10.24)$$

The optimal resonator position for maximum drain reflection coefficient is thus determined by plotting the point

$$\frac{1}{|\Gamma_g|} \angle -\Gamma_g \quad \text{in the } \Gamma_{gl}(\kappa_{gl}, \theta_{gl}) \text{ plane}$$

For the source terminated in -j100Ω and the drain in 50Ω
$\Gamma_g = 11.99 \angle -169.5°$ giving

$$\Gamma_{gl} = \frac{1}{|\Gamma_g|} \angle -\Gamma_g = 0.084 \angle 169.5° \qquad (10.25)$$

From (5.8) at resonance $$|\Gamma_{gl}| = \frac{\kappa}{\kappa + 1} \qquad (10.26)$$

$$\text{giving} \quad \kappa = \frac{|\Gamma_{gl}|}{1 - |\Gamma_{gl}|} \qquad (10.27)$$

$$= \frac{1}{|\Gamma_g| - 1} \qquad (10.28)$$

For $|\Gamma_g| > 1$ as $|\Gamma_g|$ increases so κ decreases (10.29)

For $|\Gamma_g| = 11.99$, $\kappa = 0.091$ from (10.28)

From (10.20) $\theta_{gl} = 0.5(360 - \angle \Gamma_{gl})$

$$= 95.3° \qquad (10.30)$$

10.2.3 Designing for Best Frequency Performance

From equations (10.25) and (10.28) above, increasing $|\Gamma_g|$ moves the point $|\Gamma d| = \infty$ closer to the centre of the $\Gamma_{gl}(\kappa_{gl}, \theta_{gl})$ chart i.e. closer

to 50Ω . Thus maximising $|\Gamma_g|$ minimises the required DR coupling coefficient and results in a DR resonant circuit with a high loaded Q factor. This brings about better frequency stability characteristics as described in Chapter 6.

Figure 10.5 shows the locus of the $|\Gamma_d|$ = infinity point in the gate reflection coefficient plane as a function of source reactance. As predicted a source reactance of -j118Ω requires the smallest coupling coefficient for oscillation at 5.75 GHz. The chosen value of -j100Ω is very close to optimum.

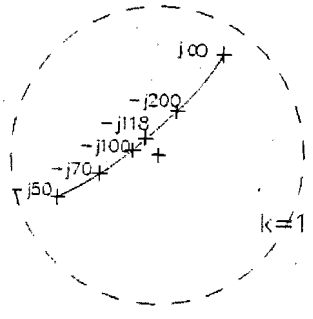

Fig 10.5 Locus of the |Td| = infinity point in the gate refl. coef. plane as a fn of source reactance

10.3 Design Results for Common Drain and Common Gate 5.75 GHz Series Feedback Oscillators

Figure 10.6 overleaf shows (a) common drain (CD) and (b) common gate (CG) topologies used to realise 5.75 GHz series feedback oscillators with the MGF1801 transistor.

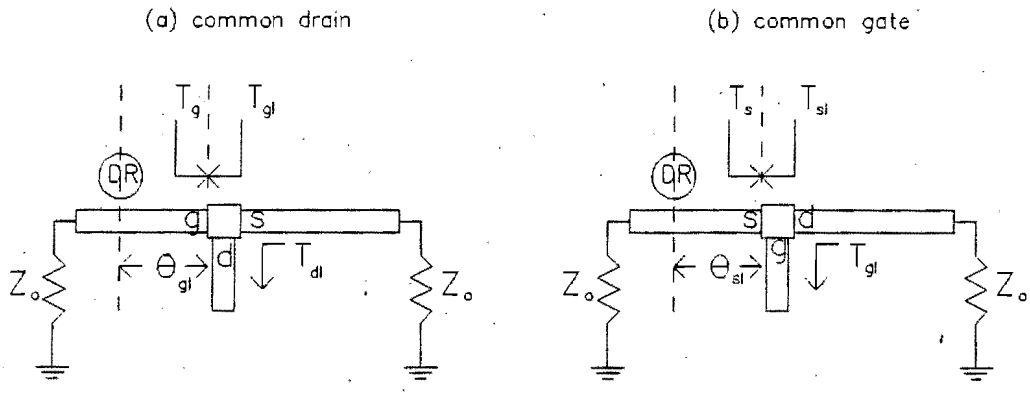

Fig 10.6 Series feedback oscillator topologies

10.3.1 Common Drain Design Results

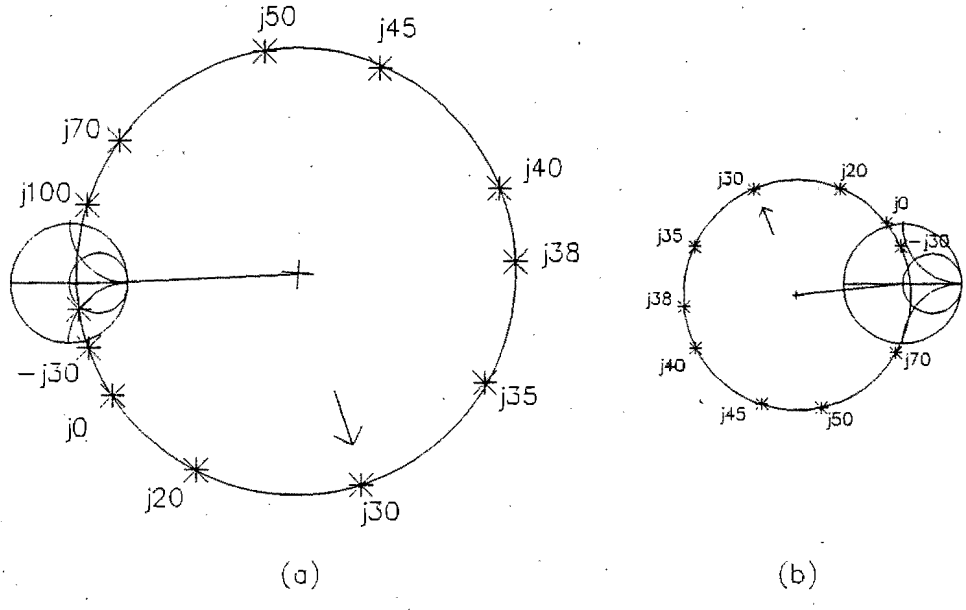

Fig 10.7 Mapping of |Tdl| = 1 into (a) Tg and (b)Ts reflection coefficient planes for CD oscillator

Figure 10.7(a) and Figure 10.7(b) show the $|\Gamma_{dl}|$ circle plotted into the gate and source reflection coefficient planes respectively for the CD oscillator. The following results apply:

centre of $|\Gamma_{dl}|$ circle in the gate refl. coef. plane is $3.88\ \underline{/2.7°}$ (10.31)

radius of $|\Gamma_{dl}|$ circle in the gate refl. coef. plane is 3.76 (10.32)

$(\Gamma_g)_{max}$ is 7.64 for $X_d = 38.1\Omega$ (10.33)

centre of $|\Gamma_{dl}|$ circle in the source refl. coef. plane is $1.80\ \underline{/-140.0°}$ (10.34)

radius of $|\Gamma_{dl}|$ circle in the source refl. coef. plane is 1.93 (10.35)

$(\Gamma_s)_{max}$ is 3.74 for $X_d = 38.0\Omega$ (10.36)

A drain load of $j30\Omega$ was selected (Marked with an arrow in Figure 10.7(a) and Figure 10.7(b) which gives

$\Gamma_g = 6.01\ \underline{/-33.7°}$ (10.37)

$\Gamma_s = 2.99\ \underline{/148.1°}$ (10.38)

Figure 10.8 shows $|\Gamma_s|$ = constant circles plotted in the $\Gamma_{gl}(\kappa_{gl}, \theta_{gl})$ plane. The optimal resonator position is given by:

$$\Gamma_{gl} = \frac{1}{|\Gamma_g|}\ \underline{/-\Gamma_g} = 0.166\ \underline{/33.7°} = \frac{\kappa_{gl}}{\kappa_{gl} + 1}\ \underline{/360 - 2\theta_{gl}} \quad (10.39)$$

from which $\kappa_{gl} = 0.20$ (10.40)

$\theta_{gl} = 163.2°$ (10.41)

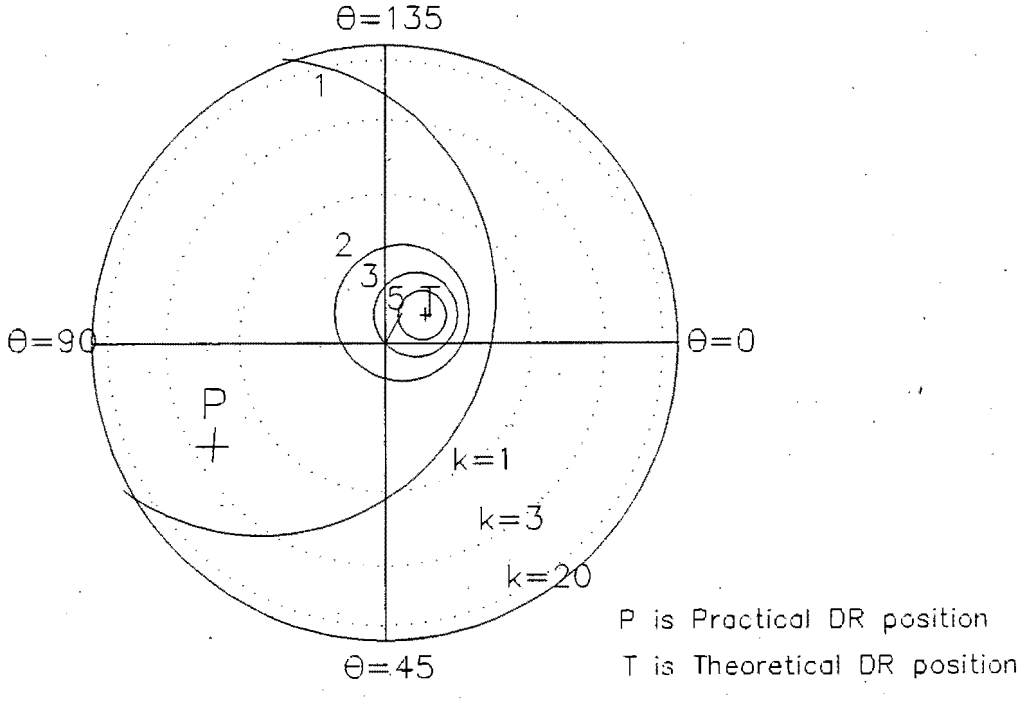

Fig 10.8 $|T_S|$ = constant circles in the gate load refl. coef. plane for CD oscillator

10.3.2 Common Gate Design Results

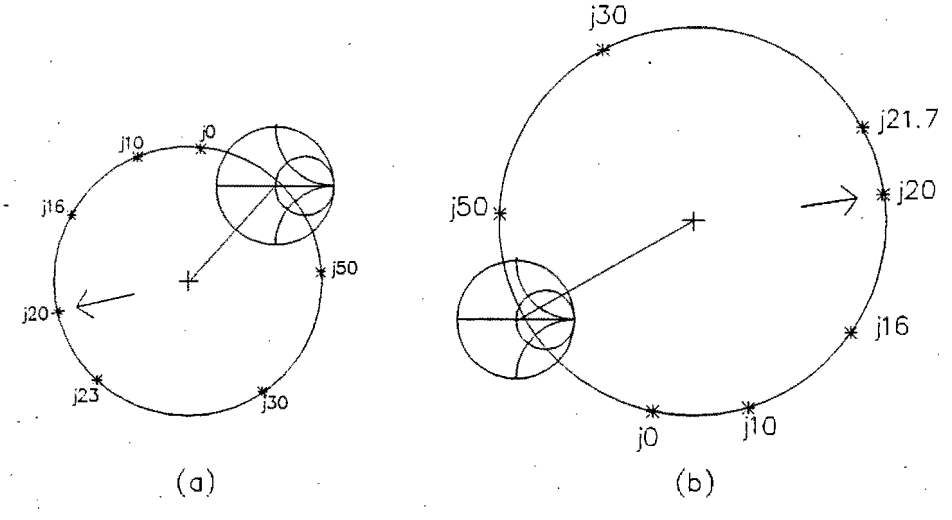

Fig 10.9 Mapping of $|T_G| = 1$ into (a) Ts and (b) Td reflection coefficient planes for CG oscillator

Figure 10.9(a) and Figure 10.9(b) show the $|\Gamma_{gl}| = 1$ circle plotted into the source and drain reflection coefficient planes for the CG oscillator. The following results apply:

centre of $|\Gamma_{gl}|$ circle in the source refl. coef. plane is $2.20 \underline{/-132.6°}$ (10.42)

radius of $|\Gamma_{gl}|$ circle in the source refl. coef. plane is 2.28 (10.43)

$(\Gamma_s)_{max}$ is 4.48 for $X_g = 22.7\Omega$ (10.44)

centre of $|\Gamma_{gl}|$ circle in the drain refl. coef. plane is $3.44 \underline{/29.1°}$ (10.45)

radius of $|\Gamma_{gl}|$ circle in the drain refl. coef. plane is 3.30 (10.46)

$(\Gamma_d)_{max}$ is 6.74 for $X_d = 21.7\Omega$ (10.47)

A drain load of $j20\Omega$ was selected (Marked with an arrow in Figure 10.9(a) and Figure 10.9(b) which gives

$\Gamma_s = 4.28 \underline{/-149.9°}$ (10.48)

$\Gamma_d = 6.63 \underline{/18.7°}$ (10.49)

Figure 10.10 shows $|\Gamma_d|$ = constant circles plotted in the $\Gamma_{sl}(K_{sl}, \theta_{sl})$ plane. The optimal resonator position is given by:

$$\Gamma_{sl} = \frac{1}{|\Gamma_s|} \underline{/-\Gamma_s} = 0.233 \underline{/149.9°} = \frac{K_{sl}}{K_{sl} + 1} \underline{/360 - 2\theta_{sl}} \quad (10.50)$$

from which $K_{sl} = 0.305$ (10.51)

$\theta_{sl} = 105.1°$ (10.52)

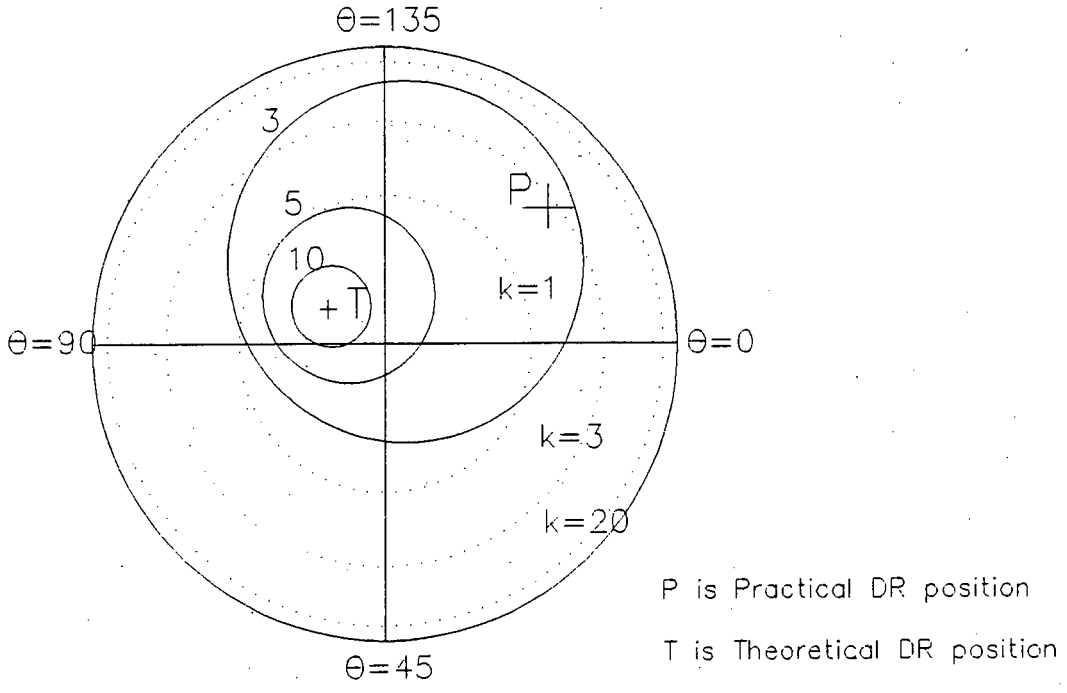

Fig 10.10 | Td | = constant circles in the source load refl. coef. plane for CG oscillator

10.4 Modelling Theoretical CS, CD and CG Oscillators on TOUCHSTONE (TS)

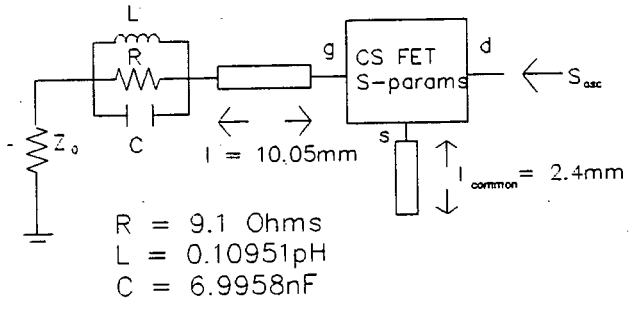

Fig 10.11 TS model of common source oscillator

Figure 10.11 shows the circuit diagram of the TS model of the CS oscillator used to check the best theoretical position for the resonator. Values of R, L and C were calculated using equations (5.15), (5.17) and (5.18) with κ = 0.091 from (10.29) and Q_U = 2300 from Figure 7.4. The value of l was determined from (10.30) and λ_g = 37.99mm.

Table 10.1 tabulates l_{common} (length of reactive stub), κ, R, L. C and l for all three oscillators. Also tabulated are R_{opt} and l_{opt} which are optimised values of R and l which give the best output reflection coefficient magnitude at 5.75 GHz.

Table 10.1 Theoretical resonator position results from TS models of oscillators

Osc	l_{common}	Kappa	L (pH)	C (nF)	R	R_{opt}	θ (deg.)	l (mm)	l_{opt} (mm)
CS	2.40	0.0910	0.10951	6.9958	9.10	9.03	95.25	10.05	10.25
CD	12.36	0.200	0.24069	3.1831	20.0	19.71	163.2	17.22	17.14
CG	11.39	0.3047	0.366679	2.08939	30.47	30.03	105.1	11.09	11.05

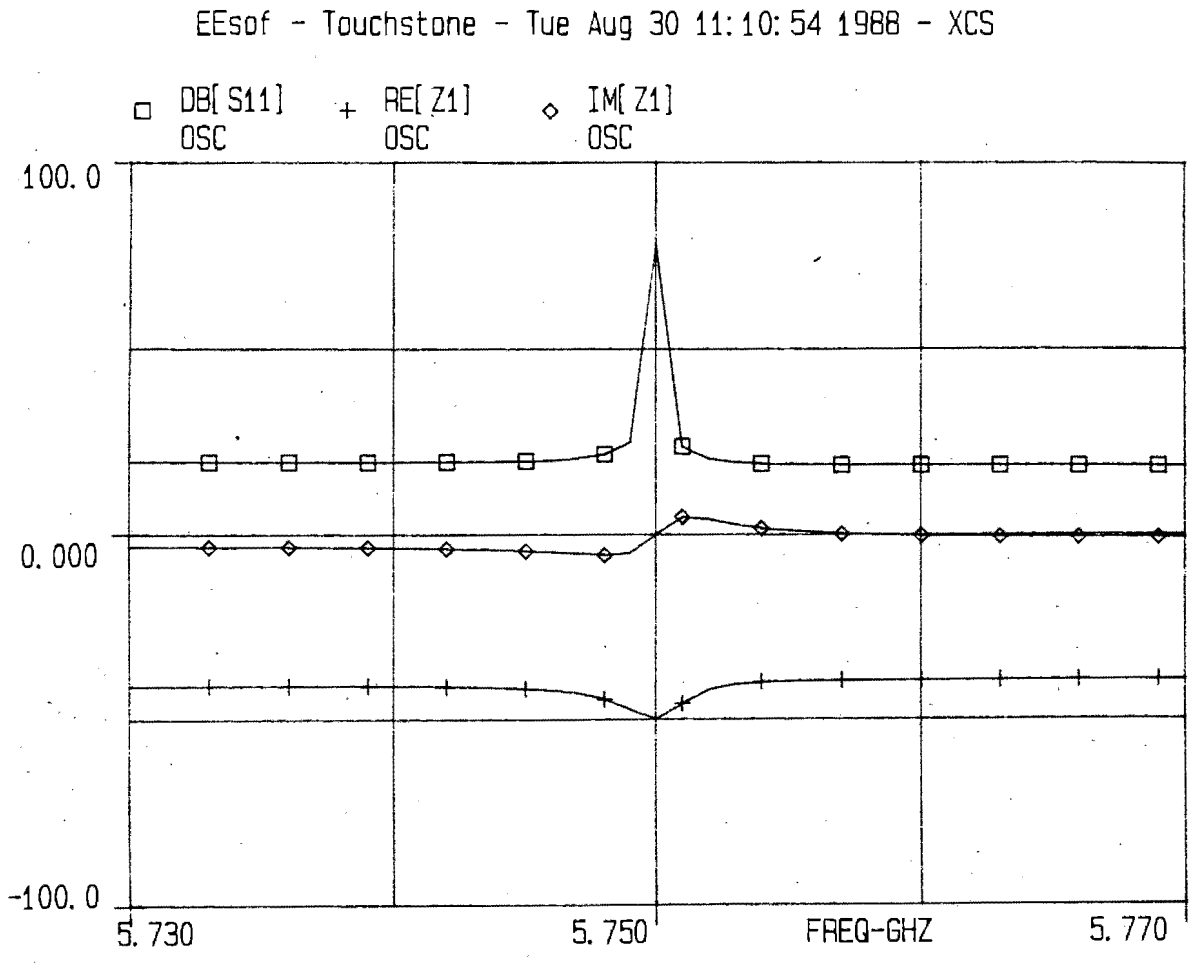

Fig 10.12 Touchstone generated output for optomised CS oscillator

Figure 10.12 shows the TS generated output for the CS oscillator with R_{opt} and l_{opt} values. The optimised values of R and C agree very closely with the calculated values of R and C for all three oscillators. These results validate the design calculations of Section 10.2 and 10.2

10.5 Construction of Oscillators, Practical Determination of Resonator Position and Practical Details

10.5.1 Construction

Figures 10.13(a), 10.14(a)and 10.15(a) are photographs of the constructed CS, CD and CG oscillators respectively. Figures 10.13(b), 10.14(b) and 10.15(b) are corresponding schematic diagrams. The bias circuit of Figure 9.13(a) was used to bias the gate and that of Figure 9.13(b) for the source and drain.

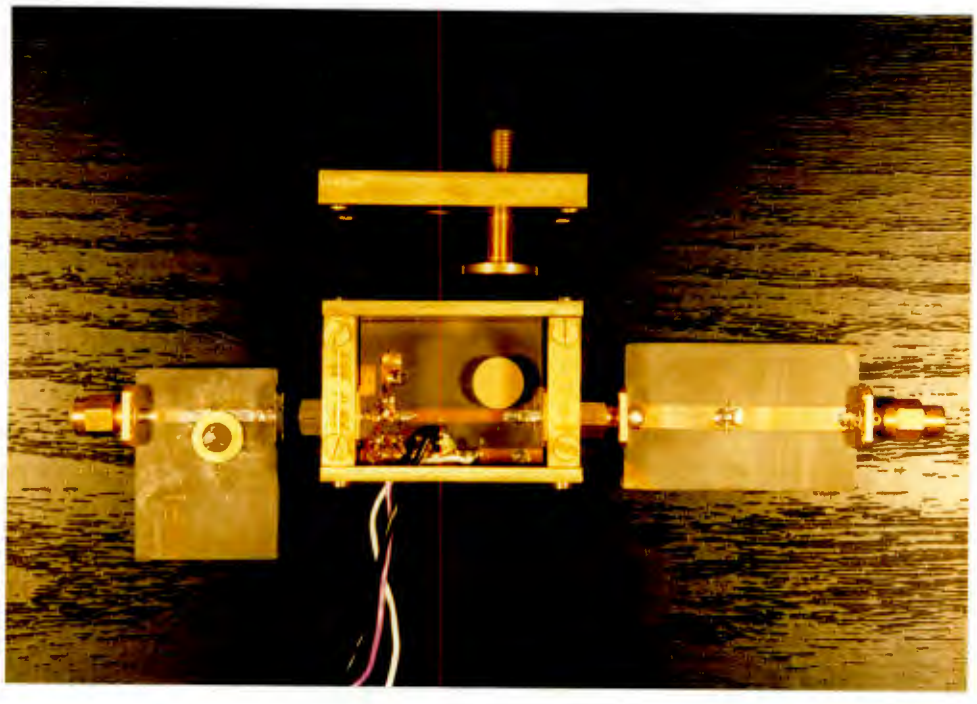

(a) Photograph

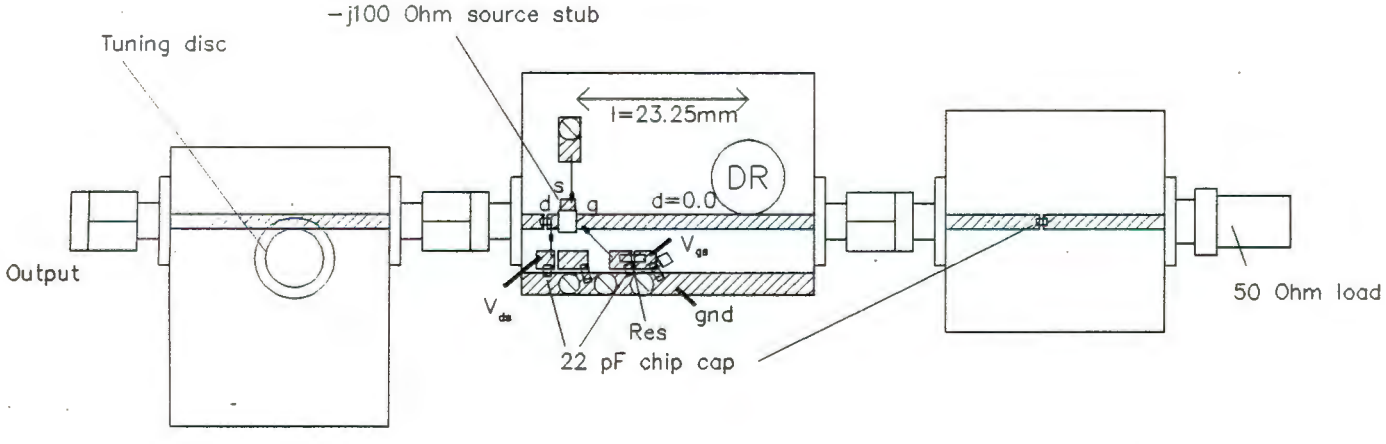

(b) Schematic diagram (dc bias ccts shown)

Fig 10.13 Constructed Common Source oscillator

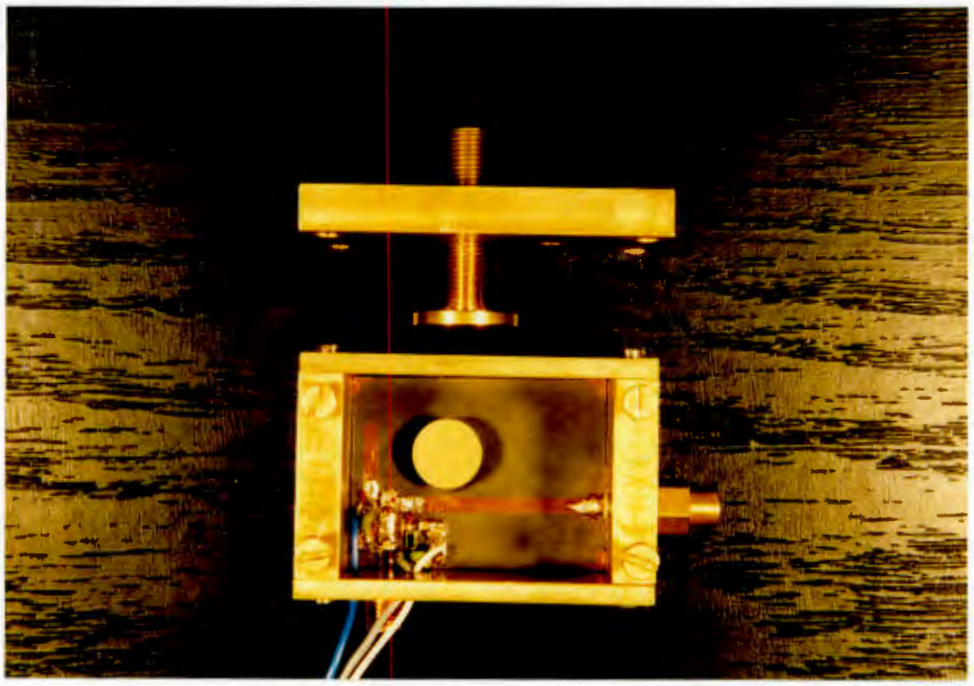

(a) Photograph

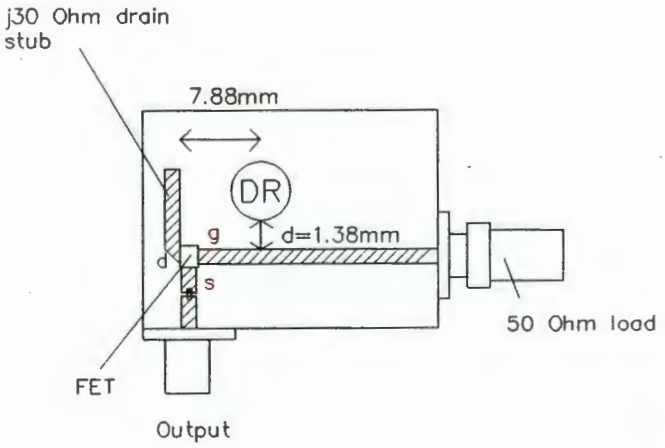

(b) Schematic diagram (dc bias ccts NOT shown)

Fig 10.14 Constructed Common Drain oscillator

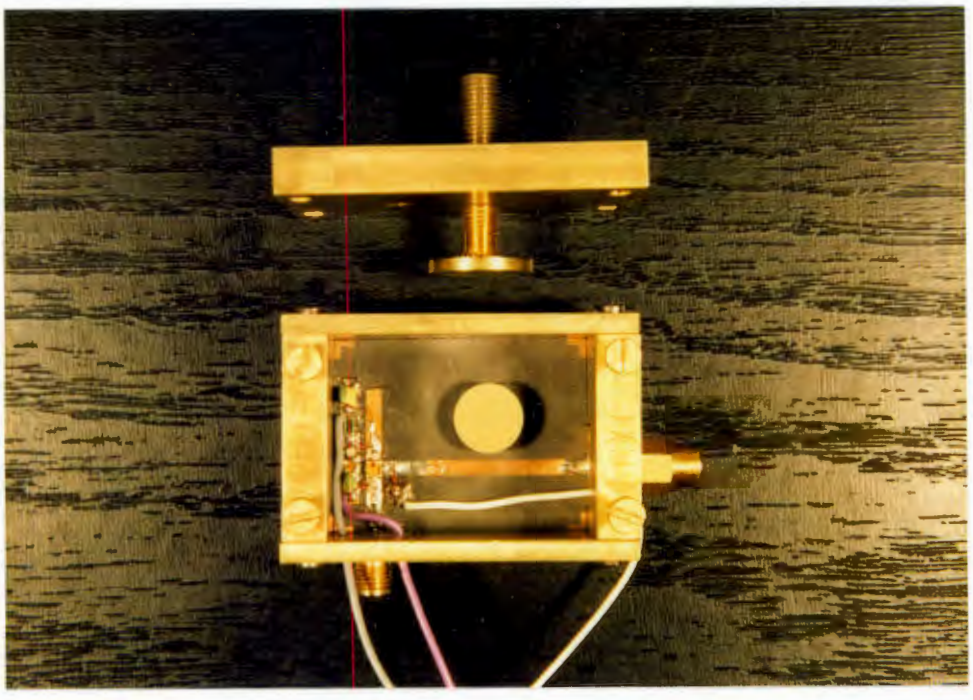

(a) Photograph

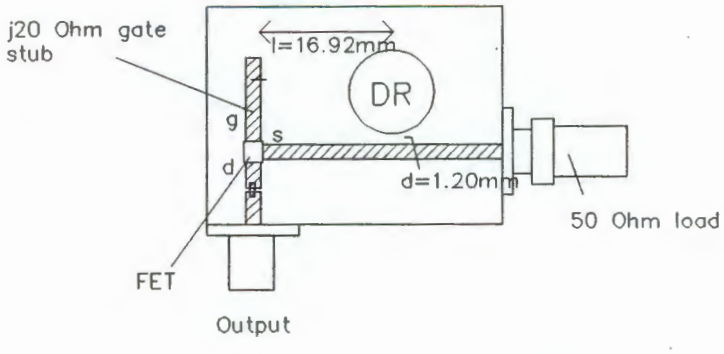

(b) Schematic diagram (dc bias NOT shown)

Fig 10.15 Constructed Common Gate oscillator

10.5.2 Practical Determination of Resonator Position

The best practical positions found for the resonators are shown marked on the schematic diagrams. The corresponding positions in the $\Gamma(_{gl})_{cs}$, $\Gamma(_{gl})_{cd}$ and $\Gamma(_{l})_{cg}$ planes have been marked on Figures 10.4, 10.8 and 10.10 respectively. The best practical position for the resonator was found by a process of trial and error. The distance of the DR from the FET was fairly critical with oscillation only occurring for 0.5mm from the best position. The distance d of the resonator from the microstripline was adjusted to give the minimum coupling for which reliable startup occurred across the bandwidth of the oscillator.

Table 10.2 tabulates the values of d, κ, $|\Gamma_{gl}|$, l and $\angle\Gamma_{gl}$ corresponding to the practical resonator positions. κ is found from d using the graph in Figure 7.3, $|\Gamma_{gl}|$ from κ using equation (10.26) and $\angle\Gamma_{gl}$ from l using equation (10.20).

Table 10.2 Practical resonator position results

Osc	d (mm)	k	$\lvert\Gamma_{gl}\rvert$	l (mm)	$\angle\Gamma_{gl}$ (deg.)
CS	0.0	7.2	0.8780	23.25	−80.6
CD	1.38	2.15	0.6826	7.88	−149.7
CG	1.20	2.6	0.7220	16.92	39.3

10.5.3 Practical Details

(i) Bias circuit problems

To achieve maximum bandwidth from the oscillators it was found that the bias circuits had to be very well decoupled from the microwave circuit. To achieve this the positions of the RF dc bias chokes on the microstriplines were adjusted and new chokes wound if necessary. The best test to determine whether satisfactory biasing had been achieved was to start the oscillator up with the DR in position and then remove the DR. No oscillation at any frequency indicated the bias circuits were in fact decoupled. With the first CS oscillator built the 1nF capacitor shown in

Figure 9.12 was not included. This resulted in bias circuit oscillations at around 10 MHz. No RF power was detected out of the oscillator since the 22pF capacitor and 50Ω load on the output formed a high pass filter with a 3dB cut off frequency of roughly 1 GHz. That the FET was oscillating was evident from the fact that the drain current was unresponsive to variations in V_{gs}. Oscillation was detected by placing a probe connected to the spectrum analyser near the FET.

(2) Proximity of DR to dc Blocking Chip Capacitor

An interesting effect was observed with the first CS oscillator built. The initial placement of the gate dc isolating chip capacitor was close to the optimal position of the DR. As a result the dominant coupling between the microstripline and the DR was no longer the TE_{01} mode but the second DR mode noted in Chapter 7. This was evident from the fact that decreasing the airgap distance x had the effect of decreasing the oscillation frequency rather than increasing it. The problem was solved by moving the dc blocking capacitor well away from the DR.

(3) Tuning Output for Maximum Power

As pointed out in Chapter 5 the last stage in the design of a series feedback STDRO is to tune the output for maximum power. In the case of the CS oscillator, tuning the output by means of a tuning disc, as shown in Figure 10.13, significantly increased the output power and enhanced the bandwidth. Using a metal tuning disc on the output of the CD and CG oscillators resulted in only a slight increase in power at 5.75 GHz and this at the expense of other oscillator parameters such as mechanical tuning range. For this reason no output tuning was performed on these two oscillators.

10.6 Comparison of Theoretical and Practical Resonator Positions

Figures 10.4, 10.8 and 10.10 show the theoretical and practical DR positions in the DR reflection coefficient plane for the three types of oscillator. All the practical points lie within regions where oscillation is possible for the output terminated in a passive load i.e. within the $|\Gamma_{output}| = 1$ circle.

However, a comparison of the actual results for K and l in Table 10.2 with the predicted values of Table 10.1 shows that agreement is not that good.

The practical coupling coefficient values are roughly three times larger than the theoretical ones for the CD and CG oscillators. This deviation is not that unreasonable considering that the coupling was adjusted to allow startup across the entire oscillator bandwidth and the FETs are operating under large signal conditions with a resultant drop in gain. The CS oscillator, whilst theoretically requiring the smallest coupling coefficient, in practice required the largest. This was due partly to the fact that the DR was adjusted to produce maximum output power under high power conditions.

The difference in the theoretical and practical values of l is harder to explain. For reliable startup at 5.75 GHz one would expect that $l_{theoret}$ would be the best distance of the DR from the FET since this distance should give the best probability of oscillation under small signal conditions. Placing the DRs at distance $l_{theoret}$ did not, however, result in oscillation. This was probably due to a combination of the following factors:

(1) the actual small signal S-parameters of the FET were different to those quoted by the manufacturer

(2) the bias circuits were not entirely decoupled and contributed to the terminating impedances seen by the FET although every effort was made to ensure this did not happen

(3) the transistor leads did not make contact with the microstriplines right at the transistor - the FET leads were cut short to 1mm to try to eradicate this problem

10.7 Practical Results Obtained for CD, CS and CG Oscillators

This section presents the results obtained from the CD, CS and CG series feedback oscillators. The next section compares the three types of oscillator on the results obtained.

The results of the CD oscillator are presented and discussed first since this oscillator had the best frequency stability characteristics.

10.7.1 Practical Results for CD Series Feedback Oscillator

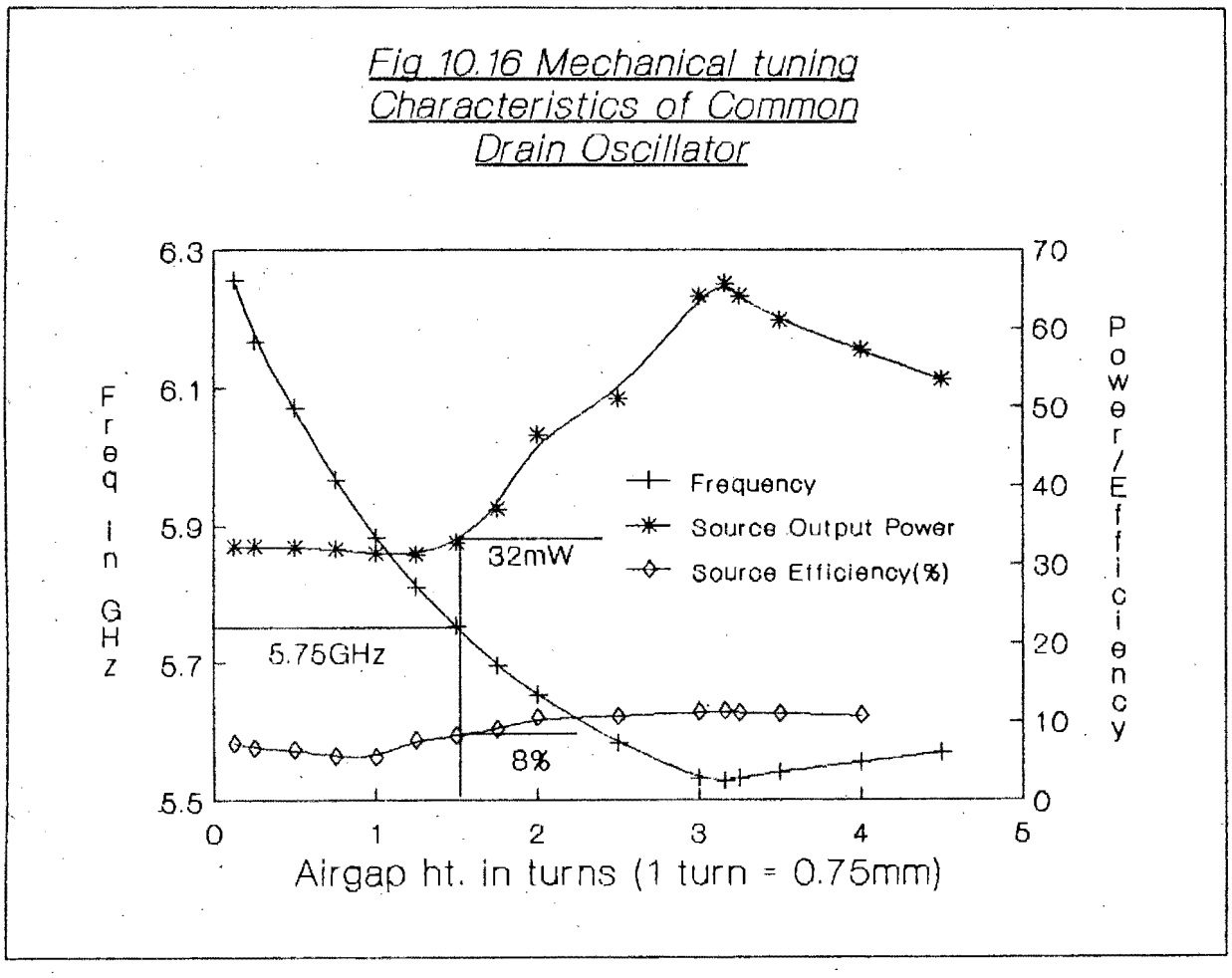

Figure 10.16 shows frequency, power out of the source port, power out of the gate port and output efficiency as a function of tuning disc height x above the DR.

From Figure 7.6 is is seen that TE_{01} mode coupling increases with x from 0 to 3.5 turns. Since the DR coupled to the gate microstripline constitutes a bandstop filter, as the coupling increases so a higher percentage of the power incident on the DR is reflected back. We would, therefore, expect

an increase in source output power as x is increased. Figure 10.16 shows this is true for x between 1 and 3.2 turns. For x below 1 turn the source output power is roughly constant with x. This can be attributed to the fact that other factors determine output power, such as the matching conditions on the gate due to the DR bandstop filter and the frequency of oscillation which affects matching conditions on the other ports. These factors are both functions of x. At 3.2 turns the slope of the f vs x curve changes from negative to positive indicating that the mode of oscillation has changed from the TE_{01} mode to the DR mode investigated in Chapter 7. Figure 7.6 indicates that this change over occurs for $x \sim 4.15$ turns for a passive DR BRF. However, as discussed in Section 10.5.3, the dominant DR mode is very dependent on conditions in the cavity such as the proximity of the DR to other microwave components.

Figure 10.16 also shows the output power efficiency as a function of x. This curve has a shape which is similar to that of the output power which is what we would expect from the theory presented in Chapter 6.

Fig 10.17 CD Pushing and Pulling Characteristics vs Airgap ht.

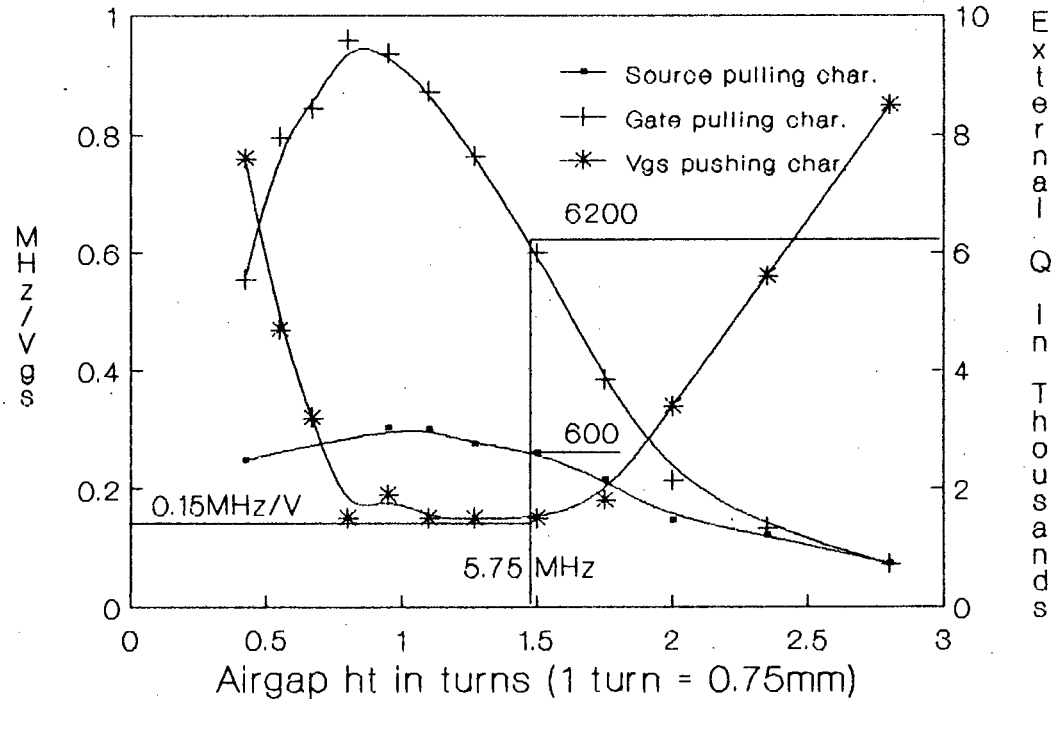

Figure 10.17 shows the V_{gs} pushing characteristic as a function of x for x between 0 and 3 turns. Figure 7.7 shows that Q_L is approximately constant for the TE_{01} mode for x = 0 to 2.5 turns. If Q_L was the only factor affecting frequency stability then we would expect the frequency stability to decrease slightly from 0 to 2.5 turns. Instead, best frequency stability, as measured by the pushing characteristic, occurs at 1.5 turns. This indicates that the pushing characteristic observed is dependent on non-linear characteristics of the FET and not just on the DR BRF.

Figure 10.17 also shows the pulling characteristics of the CD oscillator on the gate port and on the source (output) port as a function of x. The results are expressed in terms of Q_{ex} where Q_{ex} is defined by (9.19). It is seen that the best frequency stability on the source port occurs at $x \sim 1$ turn corresponding to a frequency of 5.880 GHz. The external Q measured on the gate port is about three times that for the source port. This is because the DR acts as a buffer between the perturbing load and the oscillating system.

Fig 10.18 Frequency vs Temperature Characteristics of CD oscillator

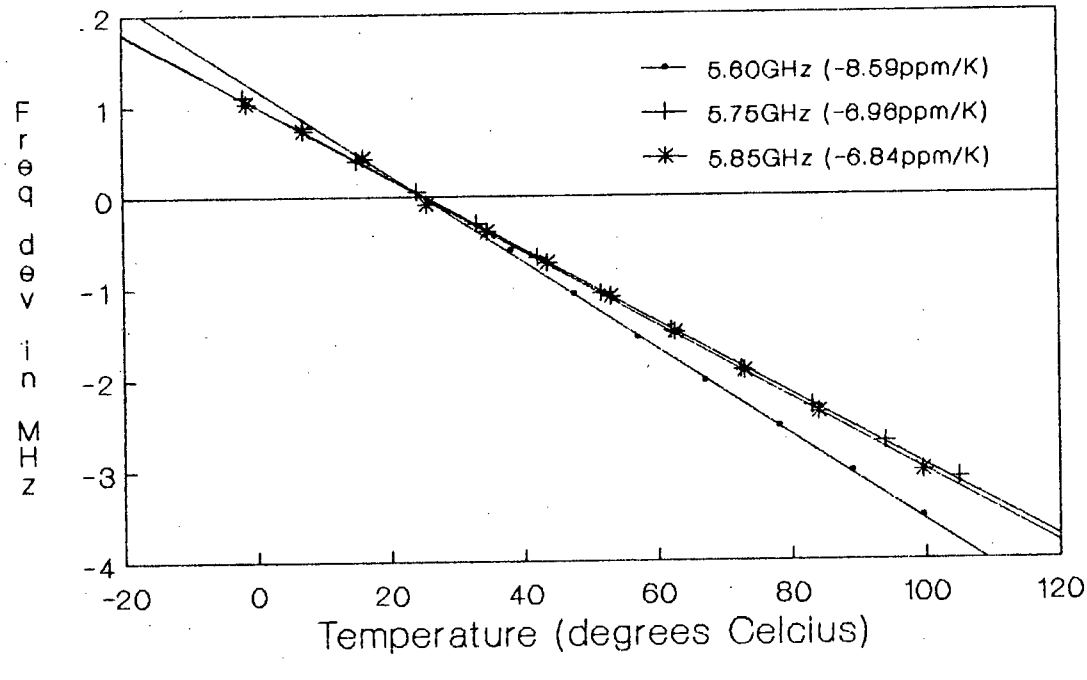

Figure 10.18 shows the variation in oscillation frequency as a function of temperature for oscillation frequencies of 5.85 GHz, 5.75 GHz and 5.60 GHz. The measured slopes of the straightline graphs are -0.04 MHz/°C (-6.84 ppm/°C), -0.04 MHz/°C (-6.96 ppm/°C) and -0.0481 MHz/°C (-8.59 ppm/°C) respectively.

Figure 7.10 shows the measured variation of the filter's notch frequency for a frequency of 5.75 GHz. The slope of the straightline graph corresponds to a temperature coefficient of -7 ppm/°C.

The fact that, at 5.75 GHz, the measured temperature coefficient for the BRF is almost exactly the same as the temperature coefficient of the oscillator indicates that the phase shift with temperature of the FET is small. $(\partial\phi_G/\partial T)$ for the FET can be calculated using equation (6.9) and from this equation it follows that if $(df_r/f_r dT)$ is equal to (df/fdT) then $(\partial\phi_G/\partial T) = 0$. That is, for $(\partial\phi_G/\partial T) = 0$, the temperature coefficient of the oscillator is determined solely by the temperature coefficient of the BRF.

10.7.2 Practical Results for CS Series Feedback Oscillator

Fig 10.19 Mechanical tuning Characteristics of Common Source Oscillator

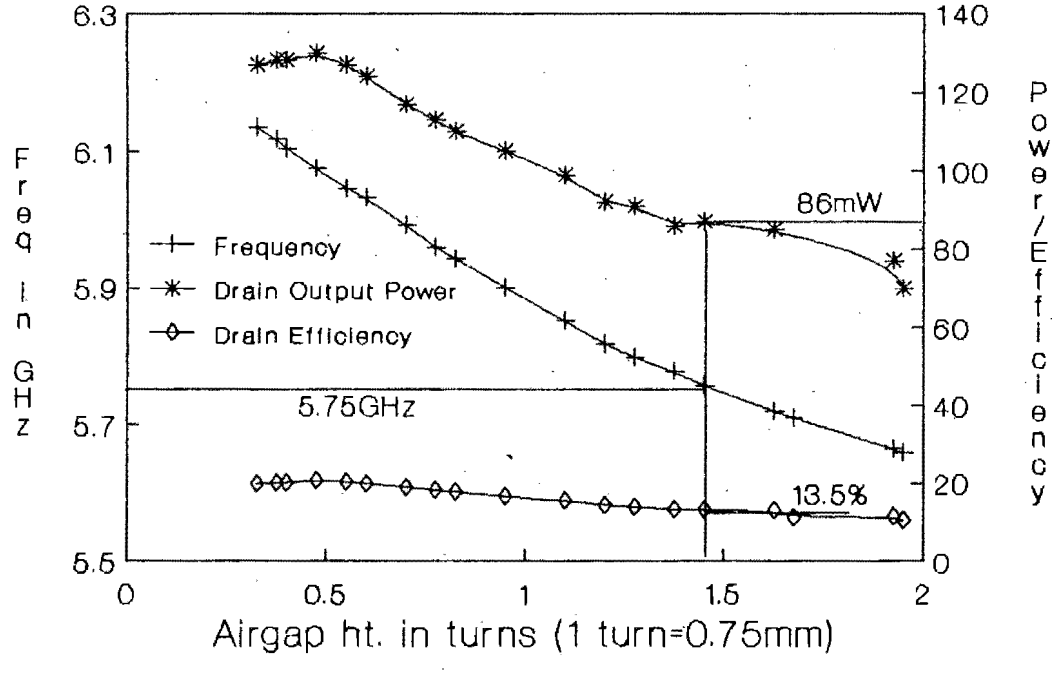

Figure 10.19 shows frequency, power out of the drain port, power out of the gate port and output efficiency as a function of airgap height x.

From Figure 10.19 it is seen that drain output power drops and the power out of the gate port increases with increasing x (decreasing f). This indicates that the coupling of the DR BRF decreases with increasing x. The output efficiency curve follows the output power curve closely as theory predicts.

Fig 10.20 CS Pushing and Pulling Characteristics vs Airgap ht.

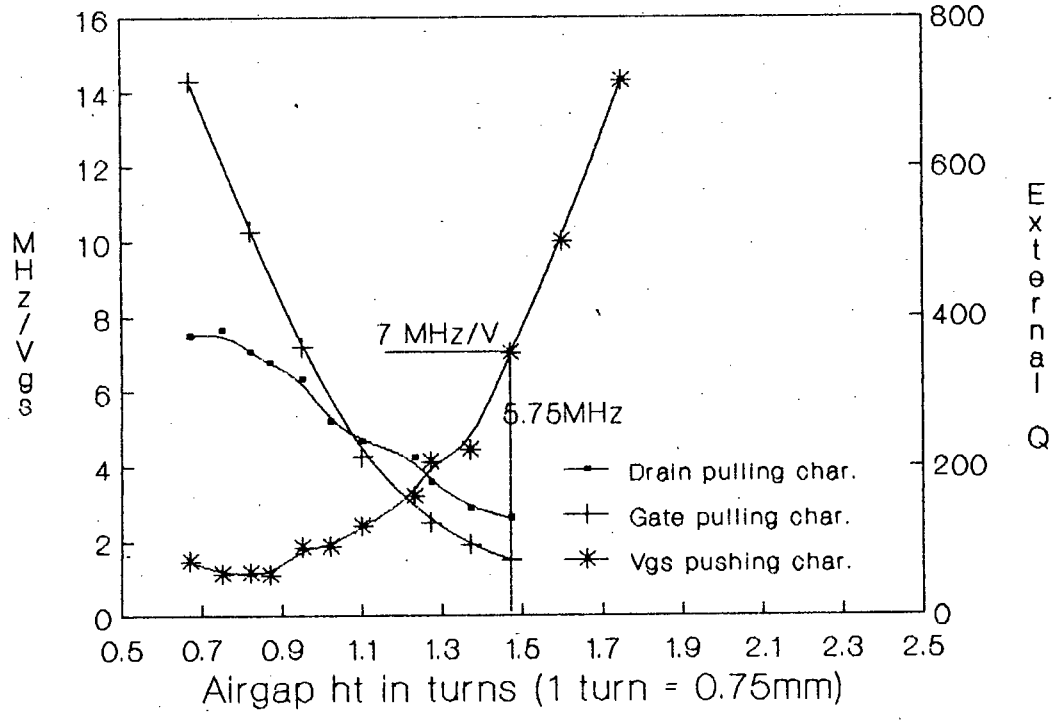

Figure 10.20 shows the V_{gs} pushing characteristic and the drain (output) and gate pulling characteristics (in terms of Q_{ex}) as a function of x. The best output frequency stability occurs at 5.950 GHz (0.75 turns) as indicated by both the pushing and the drain output pulling curves.

Fig 10.21 Frequency vs Temperature Characteristics of CS oscillator

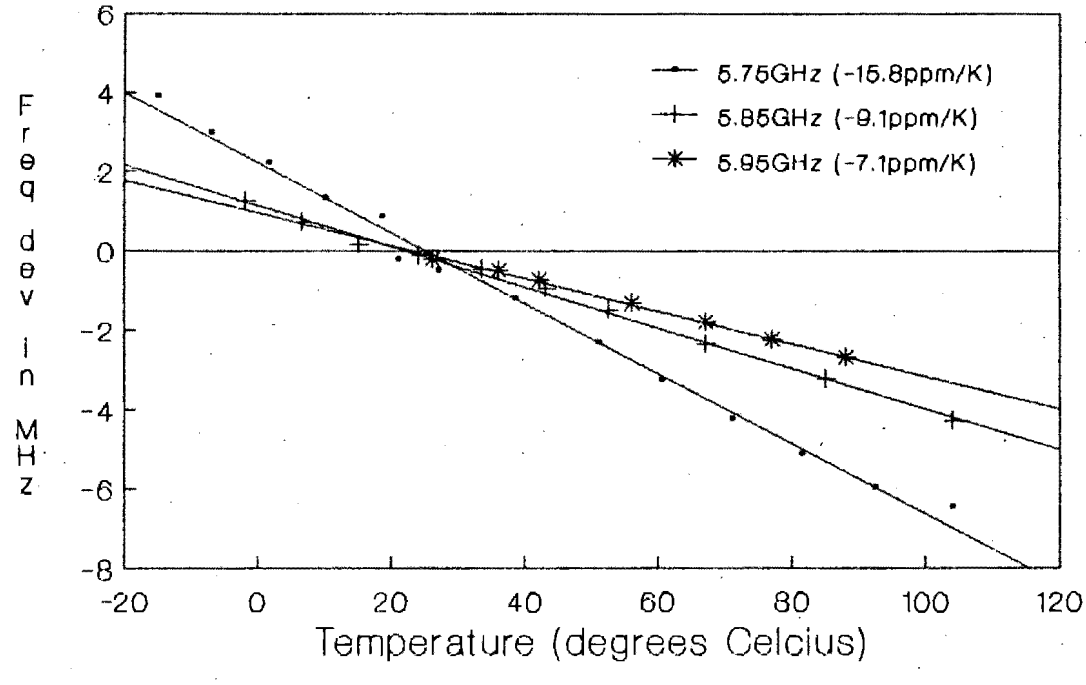

Figure 10.21 shows the frequency vs temperature characteristics of the CS oscillator for oscillation frequencies of 5.95 GHz, 5.85 GHz and 5.75 GHz. The measured slopes of the straightline graphs are -7.1 ppm/°C, -9.1 ppm/°C and -15.8 ppm/°C respectively, i.e. the temperature stability gets worse as x is increased. This agrees with the frequency stability trends indicated by the pushing and pulling results.

10.7.3 Practical Results for CG Series Feedback Oscillator

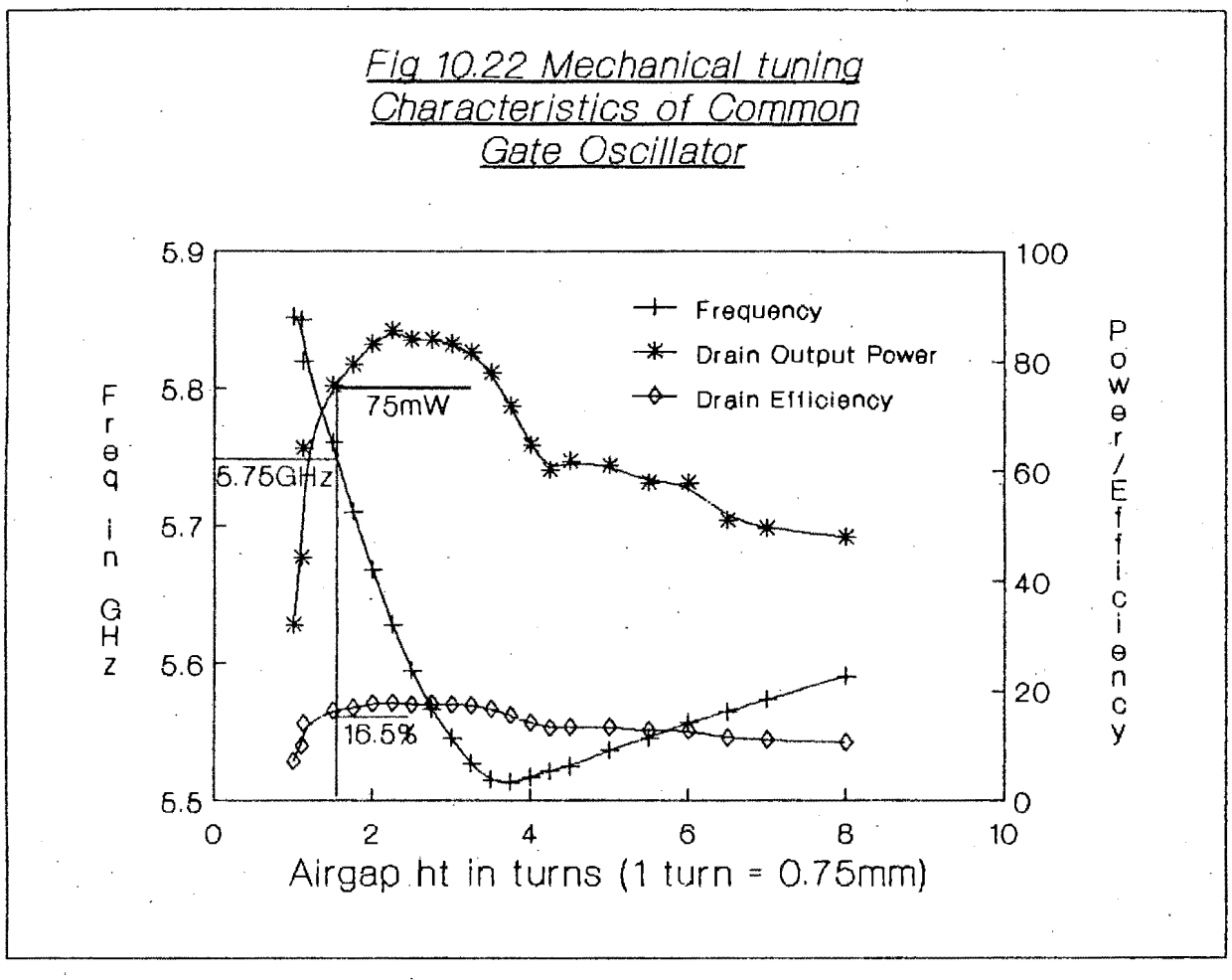

Fig 10.22 Mechanical tuning Characteristics of Common Gate Oscillator

Figure 10.22 shows frequency, power out of the drain port, power out of the source port and output efficiency as a function of airgap height x. The figure shows that the drain output power increases, reaches a maximum and then decreases as x is increased. Maximum output power occurs at about 5.6 GHz (2.5 turns). The turning point in the frequency versus x curve indicates that, as for the CD oscillator, the mode of oscillation switches from the TE_{01} mode to a second DR mode at around 5.15 GHz. As for the other two oscillators the output efficiency curve follows the output power curve closely.

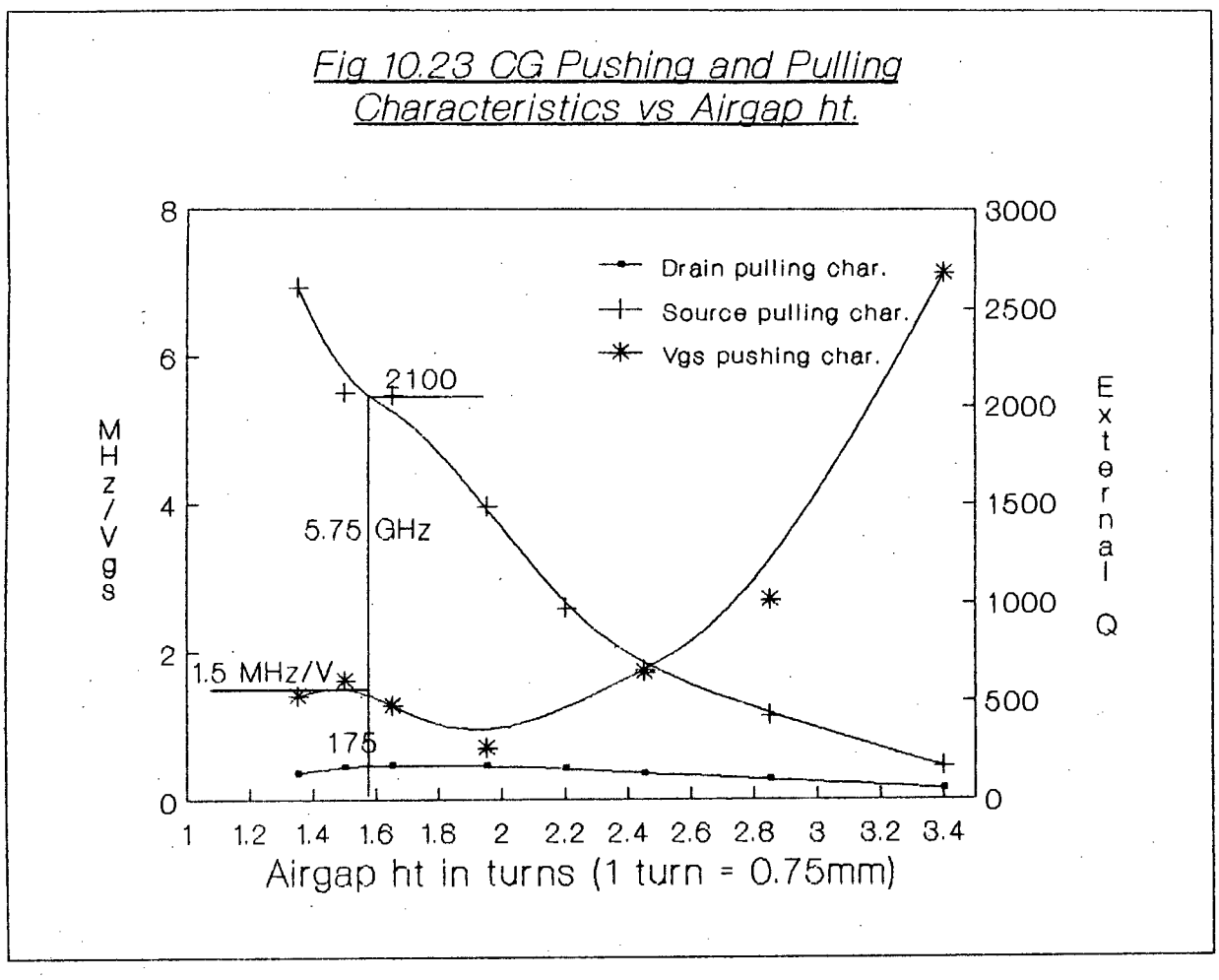

Figure 10.23 shows the V_{gs} pushing characteristic and the drain (output) and source pulling characteristics (in terms of Q_{ex}) as a function of x. The best output frequency stability occurs at around 5.7 GHz (1.85 turns).

Fig 10.24 Frequency vs Temperature Characteristics of CG oscillator

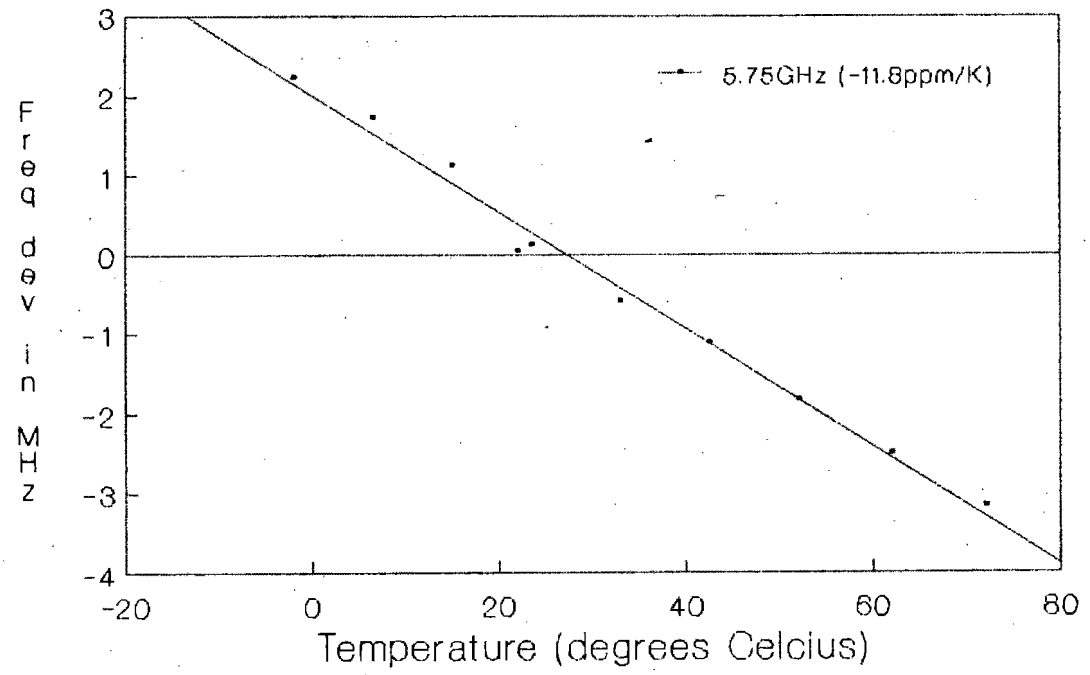

Figure 10.24 shows the frequency versus temperature characteristic at 5.75 GHz. The measured slope of the straightline graph is -11.8 ppm/°C.

10.8 Comparison of Practical Results Obtained for the CD, CS and CG Oscillators

Table 10.3 compares the results obtained for the three series feedback configurations.

The results show that the CD oscillator performed best for all criteria evaluated with the exception of output power and efficiency. The superior frequency stability of the CD oscillator is to be expected since the Q_L of the DR BRF (760 from Figure 7.5) is highest for this oscillator. The DR BRF of the CG oscillator has the next highest Q_L (670) and the oscillator has the second best frequency performance. Although the Q_Ls of the CD & CG oscillators are within 15%, the frequency performance of the CD oscillator

Table 10.3 Comparison of practical results obtained for CD , CS and CG oscillators

Factor	Common Drain	Common Source	Common Gate
Highest oscillation frequency	6256 MHz	6136 MHz	5851 MHz
Lowest oscillation frequency	5528 MHz	5665 MHz	5512 MHz
Tuning range (MHz)	728 MHz	471 MHz	339 MHz
(%BW)	12.7%	8.2%	6.0%
Highest output power over osc range	65mW @5528 MHz	130mW @6070 MHz	85 mW @5600 MHz
Output power @5.75 GHz	32mW	86mW	75 mW
Highest output pwr eff. over osc. range	11% @5528 MHz	20.5% @6070 MHz	18% @5600 MHz
Output power eff. @5.75GHz	8%	13.5%	16.5%
Best pushing factor over osc range	0.145 MHZ/V @5400 MHz	1.1MHz/V @5950 MHz	0.75 MHz/V @5680 MHz
Pushing factor @5.75 GHz	0.15 MHz/V	7 MHz/v	1.5 MHz/V
Highest Q over osc. range [output]	3000 @5900 MHz	380 @5975 MHz	180 @5720 MHz
Q @5.75 GHz [output port]	2600	130	175
Highest Q over osc. range [DR port]	9600 @5950 MHz	720 @6000 MHz	2600 @5851
Q @5.75 GHz [DR port]	6300	75	2100
Best Temp. coef. over osc. range	−6.8ppm/K @5.85 GHz	−7.1ppm/K @5.95 GHz	−11.8ppm/K
Temp. coef. @5.75 GHz	−7.0ppm/K	−15.8ppm/K	−11.8ppm/K

is at least three times as good as that of the CG oscillator in terms of the pushing and pulling characteristics. This indicates that for the particular FET used the CD configuration results in a DRO with the best frequency stability characteristics.

The CG oscillator configuration is traditionally the configuration used for maximum bandwidth. Figure 10.23 shows that the CG oscillator achieved maximum bandwidth for operation in the 2nd DR mode. In the TE_{01} mode, however, the highest CG oscillator frequency was 5851 MHz which falls far short of the highest frequency of either the CS (6136 MHz) or CD (6256 MHz) oscillators.

The CS oscillator recorded the highest output power results. This can be seen as the result of the tight DR BRF coupling giving maximum reflected power and the fact that this configuration is that normally used for the FET as a power amplifier. The high efficiency of the CS oscillator at 6.07 GHz (20.5%) results from the high output power of 130mW at this frequency. The best efficiency at 5.75 GHz was recorded for the CG oscillator (16.5%) although output power at this frequency was less than that of the CS oscillator.

10.9 Conclusions

From the results presented in Sections 10.6, 10.7 and 10.8 the following conclusions can be drawn:

(1) the small signal S-parameters supplied by the manufacturer can be used to calculate the required reactance of the common stub - they are not particularly useful concerning the placement of the DR

(2) the placement of the DR is best performed practically

(3) the oscillator configuration which will give the best frequency stability results cannot be predicted accurately using the manufacturer's small signal data - this can only be determined from actual construction of the oscillators

(4) frequency stability can be traded off against output power and efficiency

CHAPTER 11

COMPARISON OF SERIES FEEDBACK STDROS WITH DR STABILISED OSCILLATOR

11.1 Comparison of Series Feedback STDRO and DR Stabilised Oscillator Results

Table 11.1 Evaluation of two types of DRO in terms of size, design effort and oscillation at design frequency

Factor	Series feedback Oscillator	DR stabilised Oscillator
Design Effort	Very low	reasonable
Size	compact	large for 3-port microstripline oscillator
Osc at design Frequency	Design freq. near centre of osc range	Stabilised osc did not occur at 5.75 GHz

Table 11.1 compares the two types of DRO constructed in terms of design effort, size and oscillation at the design frequency. The table shows that the series feedback STDROs provide the better design option on all three criteria.

Table 11.2 compares the DROs in terms of the practical results obtained. The table shows that the CD series feedback Stdros outperformed the stabilised microstrip DRO on all accounts.

11.2 Conclusions

From the previous section it can be concluded that, for practical DRO design, series feedback oscillators are the obvious choice. Compared to DR stabilised oscillators they are easy to design, compact and will oscillate

at the design frequency. They also exhibit the best practical oscillation characteristics.

Table 11.2 Comparison of series feedback STDRO and DR stabilised oscillator results

Factor	CD series feedback oscillator	Best series feedback result if not CD	DR Stabilised m/s oscillator
Highest oscillation frequency	6256 MHz		5743 MHz
Lowest oscillation frequency	5528 MHz	5512 MHz (CG)	5534 MHz
Tuning range	728 MHz		209 MHz
Highest output power over tuning range	65 mW @5528 MHz	130 mW @6070MHz (CS)	60 mW @5743 MHz
Output power @5.75 GHz/@5.60 GHz	32 mW	86 mW (CS)	19 mW @5600 MHz
Best Pushing factor over osc range	0.145 MHz/V @5899		0.25 MHz/V @ 5575
Pushing factor @5.75 GHz	0.15 MHz/V		0.3 MHz/V @5600 MHz
Highest external Q over osc range	3000 @5900 MHz		840 @5725 MHz
External Q @5.75 GHz/@5.60 GHz	2600		90 @ 5600 Mhz
Best temp. coef. over osc range	-6.8ppm/K @5850 MHz		
Temp. coef. @5.75 GHz/@5.60 GHz	-7.0ppm/K @5.75 GHz -8.6ppm/K @5.60GHz		-19.6ppm/K @5600 MHz
Highest Output power efficiency over oscillation range	11% @5528 MHz	20.5% @6070 MHz (CS)	
Output power efficiency @5.75 GHz /5.60 GHz	8%	16.5% @5.75 GHz (CG)	4.5% @5.60 GHz

CHAPTER 12

SUMMARY OF MAIN THESIS RESULTS AND CONCLUSIONS

This chapter briefly summarises the main results obtained and conclusions reached in this thesis. They are presented under the following headings :

(1) The GaAs MESFET DRO as a narrowband source (Chapter 3)

(2) Optimal design of microwave oscillators and DROs (Chapter 6)

(3) Practical DR bandreject filters (Chapter 7)

(4) Practical DR bandpass filters (Chapter 8)

(5) DR stabilised 3-port microstrip oscillator (Chapter 9)

(6) Practical series feedback STDROs (Chapter 10)

(7) Comparison of series feedback STDROs with DR stabilised oscillator (Chapter 11)

12.1 The GaAs MESFET DRO as a Narrowband Source

(1) DROs totally outperform Gunn cavity stabilised oscillators. They outperform crystal locked oscillators on all criteria except frequency temperature stability and long term stability

(2) GaAs FET, DR and MIC technologies are ideally suited to the construction of a narrowband source which is highly stable, reliable, compact, low cost and efficient

(3) The long-term stability of GaAs FET devices needs to be investigated further

(4) GaAs MESFET MIC DROs have recorded the best DRO results for efficiency, output power, output power temperature stability and external Q factor

12.2 Optimal Design of Microwave Oscillators and DROs

(1) Once a particular oscillator topology has been chosen, the three basic parameters available for performance optimisation are - selection of the active device, the matching of the device and the coupling of the resonant system into the circuit

(2) In general, optimisation for a particular characteristic proceeds at the expense of other characteristics

12.3 Practical DR Bandreject filters

(1) Since BRFs are used to reflect power, S_{11} results should be used where these differ significantly from S_{21} results

(2) The frequency stability of a BRF (as indicated by Q_L) decreases with increasing coupling

(3) 31mil dielectric DR BRFs have a useful coupling range roughly nine times that of 10mil dielectric filters (0.2 to 13 compared with 0.1 to 1.5) at 5.75 GHz

(4) Within their narrow range of coupling values 10mil dielectric BRFs have higher values of Q_U and Q_L ie they exhibit better frequency stability over the corresponding 31mil dielectric filters

(5) The existence of two DR resonant modes means that, when the BRF is used in an oscillator, resonance can occur in a mode other than the desired TE_{01} mode

12.4 Practical DR Bandpass Filters

(1) Since BPFs are used to transmit power, S_{21} results should be used for characterisation

(2) Practical results for equally coupled DR BRFs agree closely with values from calculated equivalent circuit models. This indicates that

the theory derived provides a good method for producing accurate models of equally coupled BPFs

12.5 DR Stabilised 3-port Microstrip Oscillator

(1) A three-port microstrip oscillator topology is suitable for building an unstabilised microstrip oscillator at a specific frequency with high output power and a poor pulling factor

(2) Such an oscillator can be designed on a frequency domain computer package such as TOUCHSTONE, using the manufacturer's small signal S-parameters, if $|S_{21}|$ is reduced to allow for saturation of the transistor under large signal steady state conditions

(3) The reduction of $|S_{21}|$ can be determined using a convergent numerical method

(4) Under small signal start up conditions there are two possible source load reactances which give a particular gate reflection coefficient - this results in two possible oscillator configurations

(5) TOUCHSTONE models of the two configurations can be evaluated to determine which model to build

(6) Stabilising a microstrip oscillator using a DR on the output dramatically improves the frequency stability over the frequency range for which stabilisation occurs

(7) For the stabilised oscillator constructed, stabilisation performance did not agree well with theory and stabilised oscillation did not occur at the design frequency of 5.75 GHz

12.6 Practical Series Feedback STDROs

(1) Of the three series feedback STDROs constructed, the common drain oscillator exhibited the best tuning range, frequency stability and pushing and pulling characteristics. The common source oscillator

produced the maximum output power at 5.75 GHz and the common gate oscillator the best efficiency at this frequency

(2) Small signal S-parameters supplied by the device manufacturer can be used for calculating the required reactance of the common stub - they are not particularly useful for positioning the DR

(3) DR placement is best performed practically

(4) The oscillator configuration which results in best frequency stability cannot be accurately predicted from the manufacturer's small signal S-parameters - actual construction of the oscillator is required

(5) Frequency stability can be traded off against output power and efficiency

12.7 Comparison of Series Feedback STDROs with DR Stabilised Oscillator.

(1) Compared to the DR stabilised oscillator, the series feedback STDROs were easy to design, compact and oscillated at their design frequency

(2) The series feedback STDROs constructed outperformed the DR stabilised oscillator on all narrowband criteria evaluated

(3) From the above, series feedback STDROs provide a far better design alternative to DR stabilised microstrip oscillators

CHAPTER 13

RECOMMENDATIONS FOR FUTURE RESEARCH

This chapter briefly presents recommendations for future research arising from the practical work undertaken and the literature reviewed. The recommendations are made under the following headings :

(1) DR bandreject filters
(2) DR bandpass filters
(3) Series feedback STDRO's
(4) Other oscillator configurations

13.1 DR Bandreject Filters

(1) One result which is worth further investigation is the existence of the 2nd DR resonant mode and how it can be eliminated. The results of Chapter 10 show that this mode had the effect of limiting the effective tuning range of the series feedback STDROs built. Initial investigations, with conductive card sections placed in the filter cavity, indicate that the 2nd DR mode can be attenuated with little effect on the desired TE_{01} resonance

(2) It would be interesting to examine coupling range and Quality factor as a function of frequency for 10mil and 31mil DR BRFs to see if a specific dielectric thickness is favoured for a specific frequency range

13.2 DR Bandpass Filters

(1) The BRFs constructed were all on 10mil RT DUROID. The effect of dielectric thickness on coupling and Quality factors would be worth investigating

(2) The configuration which results in a phase inversion (see Chapter 5) is worth investigating practically

13.3 Series Feedback STDROs

All design work carried out on the series feedback STDROs constructed was done using the manufacturer's small signal S-parameters. For more accurate design large signal conditions should be taken into account. There are two possible approaches to this. The first is to measure the large signal three-port S-parameters of the device over a range of frequencies and power levels. This is not usually a practical solution since most network analysers are only capable of two-port measurements at low signal levels. The second method is to do three-port load-pull measurements to determine optimum oscillation conditions. This method is time consuming and only really appropriate to the particular device under test. It is doubtful that it would produce better results over the method described in Chapter 10 which amounts to two-port load-pull optimisation with the common reactive stub fixed.

13.4 Other Oscillator Configurations

Two types of DROs whose practical construction have not been discussed in this thesis are DR feedback STDROs and reflection DROs. Both are worthy of practical investigation although reflection DROs have the DR on the output port resulting in reduced output power.

There are two possible approaches to designing parallel feedback oscillators. The first is to design the feedback loop carefully with the FET used as an amplifier (see Chapter 5). This method has the advantage that the FET can be used in the grounded common source mode which allows optimum heatsinking and is the only configuration possible for many packaged FETs. The method has the disadvantage that the transmission coefficient phase angle for the FET is not usually known under large signal conditions. This makes the length of the loop indeterminate although tuning of the coupling lines to the DR is possible. The best MIC layout for this configuration is probably that due to Podcameni (Podcameni, 1985: 1331). The second approach is to use the FET as a three-port device. Microstriplines from two of the ports are arranged at right angles and coupled through a DR to provide the necessary parallel feedback. The third port is the output port. Altering the position of the DR relative to the two coupling lines allows both phase and amplitude of

the feedback circuit to be adjusted practically for best oscillator performance. Ishihara et al. have investigated practically this approach to parallel feedback STDROs (Ishihara, 1980). As yet the literature has not reported on the equivalent circuit of a BRF with microstriplines at right angles. This may well be an avenue for future work.

BIBLIOGRAPHY

Abe, H. et al. "A highly stabilised low-noise Gaas FET integrated oscillator with a dielectric resonator in the C-Band". IEEE Trans. Microwave Tech. Vol. MTT-26. No. 3. March 1978. pp.156-162.

Abe, H,. "Dielectric resonator stabilization. Microwave Journal. October 1978. pp. 65-66.

Agarawal, K.K. "Applications of GaAs heterojunction bipolar transistors in microwave dielectric resonator oscillators". Microwave Journal. November 1986. pp.177-182.

Basawapatna, G.R. and Stancliff, R.B. "A unified approach to the design of wide-band microwave solid state oscillators". IEEE Trans. Microwave Theory Tech. Vol. MTT-27. May 1979. pp.379-385.

Camiade, N. et al. "Low noise design of dielectric resonator FET oscillators". Proc. 13th European Microwave Conf. September 1983. pp.297-301.

Dow, G.S.et al. "Highly stable 35GHz GaAs FET oscillator". IEEE MTT-S Digest. 1986. pp.589-591.

Evans, D.H. "High efficiency Ka- and Ku-band MESFET oscillators". Electron. Lett. Vol. 21. No. 6. March 14, 1985. pp.254-255.

Galwas, B.A. "Scattering matrix description of microwave resonators". IEEE Trans. Microwave Theory Tech. Vol. MTT-31, August 1983. pp.669-670.

Guillon, P. et al. "Microstrip bandstop filter using a dielectric resonator". IEEE Proc. Vol 128. Pt.H. No. 3. June 1981. pp.151-154.

Hagihara, E. et al. "A 26-GHz miniaturised MIC transmitter/receiver". IEEE Trans. Microwave Theory Tech. Vol. MTT-30. March 1982. pp.235-242.

Hamilton, S. "Microwave oscillator circuits". Microwave Journal. April 1978. pp.63-84.

Imai, N. and Yahamoto K. "Design consideration for frequency-stabilised MIC IMPATT oscillators in the 26-GHz band". IEEE Trans. Microwave Theory Tech. Vol. MTT-33. March 1985. pp.242-248.

Johnson, J.M. "Large signal GaAs MESFET oscillator design". IEEE Trans. Microwave Theory Tech. Vol MTT-27. March 1979. pp.217-227.

Kajfez, D. and Guillon P. Dielectric Resonators. Artech House. 1986.

Khanna, A.P.S. et al. "New very high Q microwave transistor oscillators using dielectric resonators". Proc. European Microwave Conf. September 1981. pp.457-463.

Khanna, A.P.S. and Garault, Y. "Determination of loaded, unloaded and external quality factors of a dielectric resonator coupled to a microstripline". IEEE Trans. Microwave Tech. Vol. MTT-31. No. 3. March 1983. pp.261-264.

Kurokawa, K. "Some basic characteristics of broadband negative resistance oscillator circuits". Bell Syst. Tech. J. Vol.48. July-August 1969. pp.1937-1955.

Kurokawa, K. "Injection locking of microwave solid-state oscillators". Proc. IEEE. Vol. 61. No. 10. October 1973. pp.1386-1410.

Lan, G. et al. "Highly stabilised, ultra-low noise FET oscillator with dielectric resonator". IEEE MTT-S Digest. 1986. pp.82-86.

Loboda, M.J. et al. "Frequency stability of L-band, two-port dielectric resonator oscillators". IEEE MTT-S Digest. 1987. pp.859-862.

Makino, T. and Hashima, A. "A highly stabilized MIC Gunn oscillator using a dielectic resonator". IEEE Trans. Microwave Theory Tech. Vol. MTT-27. No. 7. July 1979. pp.633-638.

Mizumura, M. et al. "20 GHz GaAs FET oscillator using a dielectric resonator". Proc. 12th European Microwave Conf. September 1982. pp.175-180.

Muat, R. "Designing oscillators for spectral purity". Microwaves and RF. July 1984. pp.133-142.

Niehenke, E.C. "GaAs : Key to defence electrons". Microwave Journal. September 1985. pp.24-44.

Papp, J.C. "An 8-18 GHz YIG-tuned FET oscillator". IEEE Trans. Microwave Theory Tech. Vol. MTT-28. No. 7. July 1980. pp.762-767.

Plourde, J.K. and Pen, C.L. "Application of dielectric resonators in microwave components". IEEE Trans. Microwave Theory Tech. Vol. MTT-29, August 1981. pp.754-770.

Pucel, R.A. et al. "Experiments on integrated gallium-arsenide FET oscillators at X-band". Electron. Lett. Vol. 11. No. 10. May 15, 1975. pp.219-220.

Purnell, M. "The dielectric resonator oscillator - a new class of microwave signal source". Microwave Journal. November 1981. pp.103-108.

Scherer, D. "Today's lesson - learn about low-noise design". Microwaves. April 1979. pp.116-122.

Tsironis, C. and Lesartre, P. "Temperature stabilisation of GaAs FET oscillators using dielectric resonators". Proc. 12th European Microwave Conf. 1982. pp.181-185.

Tsironis, C. and Hennings, D. "Highly stable FET DROs using new linear dielectric resonator material". Electron. Lett. Vol. 19, September 1983. pp.741-743.

Tsironis, C. "Highly stable dielectric resonator FET oscillators". IEEE Trans. Microwave Theory Tech. Vol. MTT-33. No. 4. April 1985. pp.310-314.

Varian, K.R. "Dielectric resonator oscillators at 4, 6 and 11 GHz". IEEE MTT-S Digest. 1986. pp.87-90.

Varian, K.R. "Long term stability of DROs compared to crystal oscillators" IEEE MTT-S Digest. 1987. pp.583-586.

Vendelin, G.D. Design of Amplifiers and Oscillators by the S-parameter Method. John Wiley and Sons. 1982.

Wagner, W. "Oscillator design by device line measurement". Microwave J. Vol 22. February 1979. pp.43-48.

APPENDIX A

Results from Literature Review of Different Types of DROs

Table A.1 Table of Results from Literature Survey of DROs

Date	Author	Reference	Configuration	Feedback	Osc freq	Oscillator Frequency Stability Characteristics				Effic-iency	Oscillator Output Characteristics				Tuning Range
						noise @10kHz	noise @100kHz	temp	Long-term		Power	temp	Push	Pull Q(ext)	
						In 1 Hz referred to 4GHz									
DIELECTRICALLY STABILISED OSCILLATORS															
Feb 1977	Abe et al	Abe, 1977	common source	Parallel	6 GHz	-89 dBc/Hz	-113 dBc/Hz	2.3 ppm/K		17%	20.0 dBm	0.008 dB/K	3 MHz/V	2000	100 MHz
Aug 1977	Abe	Abe, 1978	common source		11 GHz			1.0 ppm/K		6%	17.8 dBm		2MHz/V		
Apr 1978	Sone	Abe, 1978	common drain		7 GHz	-95 dBc/Hz		1.8 ppm/K		14%	20.0 dBm		0.8 MHz/V		
SERIES FEEDBACK FET STDROs															
Sept 1982	Mizumura	Mizumura, 1982	common drain	DR on Gate	10.5 GHz			0.6 ppm/K		18%	27.0 dBm	0.018 dB/K			
Sept 1982	Tsironis	Tsironis, 1982	common source	DR on Gate	11.5 GHz		-114 dBc/Hz	0.2 ppm/K		9%			0.3 MHz/V	450	
Apr 1985	Tsironis	Tsironis, 1985	common source	DR on Gate	11.0 GHz			0.12ppm/K							200 MHz
Sept 1985	Jacques	Jacques, 1985	common source	DR on Source	24.4 GHz					28%	12.0 dBm				50 MHz
1986	Dow	Dow, 1986	common drain	DR on Gate	35.0 GHz	-97 dBc/Hz		1 ppm/K			1.0 dBm			3000	800-1200
1986	Chen	Chen, 1986	common source	DR on Gate	23.0 GHz		-118 dBc/Hz	0.72 ppm/K			13-16 dBm				
PARALLEL FEEDBACK FET STDROs															
Sept 1978	Lesatre	Lesatre, 1978	common source	Drain-gate	11.0 GHz			1 ppm/K		18%	13.4 dBm		<1 MHz/V	1200	50 MHz
May 1979	Saito	Plourde, 1981		Drain-gate	6.0 GHz	-98 dBc/Hz		0.4 ppm/K		15.5%	13.8 dBm				
Aug 1980	Isihara	Isihara, 1980	source output	Drain-gate	11.85 GHz	-99 dBc/Hz	-135 dBc/Hz	0.32 ppm/K		20%	18.5 dBm	0.02 dB/K	<0.5 MHz/V	>1000	1000-1500
	Isihara		BRF added on	Source Output	11.6 GHz	-104 dBc/Hz		0.2 ppm/K				>0.022 dB/K		4000	1000-1500
Sept 1983	Camiade	Camiade, 1983	common source	Drain-gate	11.0 GHz	-114 dBc/Hz	-143 dBc/Hz	0.5 ppm/K		8%	13.0 dBm			2000	
1984	Kuanna	Niehenke, 1985	drain output	Gate-source	9.0 GHz	-97 dBc/Hz									
1985	Fiedziuszko	Niehenke, 1985	common source	Drain-gate	9.2 GHz	-105 dBc/Hz									
1986	Chen	Chen, 1986	common source	Drain-gate	23.0 GHz		-123 dBc/Hz	0.36 ppm/K			8-13 dBm				50-200 MHz
	Chen	Chen, 1986	common source	Drain-gate	18.0 GHz		-128 dBc/Hz	0.46 ppm/K							50 MHz
Oct 1986	Varian	Varian, 1986	common source	Drain-gate	4.0 GHz	-116 dBc/Hz		0.1 ppm/K			19.2 dBm			~450	40 MHz
	Varian	Varian, 1986	common source	Drain-gate	6.0 GHz	-117 dBc/Hz		0.1 ppm/K			22.5 dBm			~450	100 MHz
	Varian	Varian, 1986	common source	Drain-gate	11.0 GHz	-109 dBc/Hz		0.1 ppm/K			18.9 dBm			~450	100 MHz
REFLECTION FET STDROs															
Sept 1981	Khanna	Khanna, 1981	common source	DR on Gate O/P	6.4 GHz						7.0 dBm		<0.2 MHz/V		
1986	Chen	Chen, 1986	common source	DR on Gate,Drain	9.0 GHz						5.0 dBm		0.25 MHz/V	56500	
	Chen	Chen, 1986	common source	DR on Drain	23.0 GHz		120 dBc/Hz	2.9 ppm/K			12-15 dBm				
Nov 1986	Agarwal	Agarwal, 1986	common source	Drain-gate	4.0 GHz	-95 dBc/Hz		1.36 ppm/K			16.0 dBm				
LAN's FET SEPERATE AMPLIFIER MCC PARALLEL FEEDBACK DRO															
1986	Lan	Lan, 1986	2-Stage amp	Parallel fbk	4.0 GHz	-130 dBc/Hz	-146 dBc/Hz	0.02 ppm/K		6%	11.5 dBm	0.012 dB/K	0.02 MHz/V		1.5 MHz elect
MONOLITHIC OSCILLATOR CHIP															
1987	Moghe	Moghe, 1987	common source	Series fbk	5.0 GHz	-90 dBc/Hz	-117 dBc/Hz	2 ppm/K			12.0 dBm	0.011 dB/K			
					13.0 GHz	-80 dBc/Hz	-110 dBc/Hz	5 ppm/K			10.0 dBm	0.007 dB/K			
GaAs HETEROJUNCTION BIPOLAR TRANSISTOR (HBT) DRO															
Nov 1987	Agarwal	Agarwal, 1986	common emit	Parallel fbk	4.0 GHz	-95 dBc/Hz		2.8 ppm/K			10.2 dBm				400 MHz
PARALLEL FEEDBACK SILICON BIPOLAR DROs															
June 1977	Plourde	Plourde, 1981	common emit	Base-collect	4.0 GHz				5 ppm/yr	12.9%	14.9dBm			4000	80 MHz
Dec 1985	Podcameni	Podcameni, 1985	common emit	B-C (-5dB fbk)	4.0 GHz	-100 dBc/Hz				27.0%	12.0 dBm				300 MHz
			common emit	B-C (-2dB fbk)	4.0 GHz	-95 dBc/Hz				20.0%	13.0 dBm				
Nov 1986	Agarwal	Agarwal, 1986	common emit	Base-collect	4.0 GHz	-100 dBc/Hz		5.3 ppm/K			14.9 dBm				
1987	Loboda	Loboda, 1987	amplifier		1.5 GHz				6 ppm/mth						
1987	Loboda	Loboda, 1987	amplifier		2.0 GHz										
GUNN DIODE DROs															
July 1979	Makino	Makino, 1979	reaction		11.0 GHz			0.2 ppm/k			8.4 dBm		0.06 MHz/V		400 MHz
Mar 1982	Hagihara	Hagihara, 1982	reaction		26.0 GHz			<1.4 ppm/K			16.0 dBm	0.036 dB/K			
IMPATT DIODE DROs															
Mar 1982	Hagihara	Hagihara, 1982	reaction		26.0 GHz			1.4 ppm/K			26.0 dBm	0.036 dB/K			
Mar 1985	Imai	Imai, 1982	reflection		26.0 GHz			1ppm/K			23.0 dBm	0.08 dB/K			

APPENDIX B

Equivalent Impedance and Reflection Coefficient Conditions for Oscillation (Vendelin, 1982: 134)

From (4.2a) and (4.2b),

$$R + \overline{R} = 0 \tag{B.1}$$

$$X + \overline{X} = 0 \tag{B.2}$$

By definition,

$$\overline{\Gamma} = \frac{\overline{R} + j\overline{X} - Z_0}{\overline{R} + j\overline{X} + Z_0} \tag{B.3}$$

$$\Gamma = \frac{R + jX - Z_0}{R + jX + Z_0} \tag{B.4}$$

From (B.1) and (B.2),

$$R = -\overline{R} \quad , \qquad X = -\overline{X}$$

Substituting into (B.4) gives

$$\Gamma = \frac{-\overline{R} - j\overline{X} - Z_0}{-\overline{R} - j\overline{X} + Z_0} = \frac{\overline{R} + j\overline{X} + Z_0}{\overline{R} + j\overline{X} - Z_0} = \frac{1}{\overline{\Gamma}} \tag{B.5}$$

Thus (B.1) and (B.2) imply $\Gamma\,\overline{\Gamma} = 1$ which is (4.3a)

APPENDIX C

Derivation of Normalised Input Impedance for DR Bandstop Filter

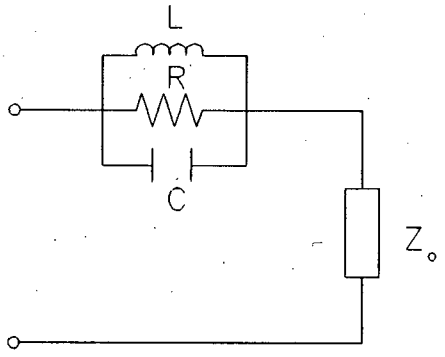

Fig C.1 Equivalent circuit of a DR Bandstop filter

The circuit to be analysed is shown above in Figure C.1

First look at the admittance of the LRC circuit,

$$Y_{LRC} = -\frac{j}{wC} + \frac{1}{R} + jwC \qquad (C.1)$$

Thus

$$Z_{LRC} = \frac{1}{1/R + j(wC - 1/(wL))} \qquad (C.2)$$

Total impedance of circuit in Fig C.1 is given by,

$$Z_{TOTAL} = Z_{LRC} + Z_0 = \frac{1}{1/R + j(wC - 1/(wL))} + Z_0 \qquad (C.3)$$

Thus the normalised input impedance is given by

$$z_{in} = \frac{Z_{TOTAL}}{Z_0} = \frac{1/Z_0}{1/R + j(wC - 1/(wL))} + 1 \qquad (C.4)$$

giving

$$z_{in} = \frac{2K}{1 + j2Q_U\delta} + 1 \qquad (C.5)$$

where $K \equiv \frac{R}{2z_0}$ and $(wRC - R/(wL)) = 2Q_U\delta$, $\delta = \frac{f - f_0}{f_0}$

APPENDIX D

Determination of Unloaded and Loaded Quality Factors for a DR BRF

The initial aim is to determine the loci of the points, on the impedance (S_{11}) and transmittance (S_{21}) planes, for the frequency deviations corresponding to Q_U and Q_L.

Substituting (5.10) into (5.2) we can write

$$z_{in} = 1 + \frac{2K}{1 + j2Q_U\delta} = 1 + \frac{2K}{1 + j2Q_L(1 + K)\delta} \qquad (D.1)$$

The normalised frequency deviations corresponding to Q_U and Q_L are given by

$$\delta_U = \pm \frac{1}{2Q_U} \qquad (D.2) \qquad \text{and} \qquad \delta_L = \pm \frac{1}{2Q_L} \qquad (D.3)$$

Thus the impedance locus of Q_U is given by substitution from (D.2) into (D.1) to give

$$(z_{in})_U = 1 + \frac{2K}{1 + j2(\pm 1/2\delta_U)\delta_U} = 1 + \frac{2K}{1 \pm j}$$

$$= (1 + K) \pm jK \qquad (D.4)$$

Substituting $K = \frac{S_{110}}{1 - S_{110}}$ from (5.1) we can determine $(z_{in})_U$ in terms of S_{110}

$$(z_{in})_U = 1 + \frac{S_{110}}{1 - S_{110}} \pm j.\frac{S_{110}}{1 - S_{110}} = \frac{1 \pm jS_{110}}{1 - S_{110}} \qquad (D.5)$$

The corresponding reflection coefficient $(S_{11})_U$ is found using the relation

$$(S_{11})_U = \frac{(z_{in})_U - 1}{(z_{in})_U + 1} = \frac{S_{110}\,(1 \pm j(1 - S_{110}))}{S_{110}^2 - 2S_{110} + 2}$$

$$(S_{11})_U = \frac{S_{110}}{\sqrt{(S_{110}^2 - 2S_{110} + 2)}} . e^{\pm j\tan^{-1}(1 - S_{110})} \qquad (D.6)$$

The relation for the Q_U locus in the transmittance plane can be obtained using the relation $S_{11} + S_{21} = 1$

$$(S_{21})_U = 1 - (S_{11})_U = 1 - \frac{S_{110}(1 \pm j(1 - S_{110}))}{S_{110}^2 - 2S_{110} + 2}$$

$$= \frac{S_{210}\,(1 + S_{210}) \pm j\, S_{210}(1 - S_{210})}{S_{210}^2 + 1}$$

$$= S_{210} \cdot \frac{\sqrt{2}}{\sqrt{(1 + S_{210}^2)}} . e^{\pm j\tan^{-1}\left(\frac{1 - S_{210}}{1 + S_{210}}\right)} \qquad (D.7)$$

The relations for the loci of the loaded Quality factor in the S_{11} and S_{21} coefficient planes are obtained in an exactly analogous manner. The results are summarised in table D.1.

Table D.1 Summary of results for Qu and Ql loci for DR bandstop filter

	Reflection Coefficient S_{110}		Transmission Coefficient S_{210}	
	$\lvert S_{110} \rvert$	$\arg(S_{110})$	$\lvert S_{210} \rvert$	$\arg(S_{210})$
Q_U	$\frac{S_{110}}{\sqrt{S_{110}^2 - 2S_{110} + 2}}$	$\pm\tan^{-1}(1 - S_{110})$	$S_{210}\sqrt{\frac{2}{1 + S_{210}^2}}$	$\pm\tan^{-1}\left[\frac{1 - S_{210}}{1 + S_{210}}\right]$
Q_L	$\frac{S_{110}}{\sqrt{2}}$	$\pm\frac{\pi}{4}$	$\sqrt{\frac{1 + S_{210}^2}{2}}$	$\pm\tan^{-1}\left[\frac{1 - S_{210}}{1 + S_{210}}\right]$

Determination of Q_U and Q_L from the Transmission Magnitude Display

Referring to Figure 5.3(a) if we can calculate h and m for the transmission coefficient, we can determine Q_U and Q_L from the display.

S_{210} is a voltage coefficient, thus the insertion loss is given by :

$$L_{210}(dB) = -20\log_{10}S_{210} \qquad (D.8)$$

$$\text{thus } S_{210} = 10^{-(\frac{L_{210})}{20})} \qquad (D.9)$$

(1) To determine the value of m

$$\frac{|(S_{21})_U|}{S_{210}} = \frac{S_{210}\sqrt{2}/\sqrt{(1+S_{210}^2)}}{S_{210}} = \frac{\sqrt{2}}{\sqrt{(1 + S_{210}^2)}} \qquad (D.10)$$

$$m = 20\log_{10}\left[\frac{|(S_{21})_U|}{S_{210}}\right] = 10\log_{10}2 - 10\log_{10}(1 + S_{210}^2)$$

$$= 3 - 10\log_{10}(1 + 10^{-0.1L_{210}}) \qquad (D.11)$$

(2) To determine the value of h

$$\frac{1}{|(S_{21})_L|} = \frac{1}{\sqrt{(1+S_{210}^2)/\sqrt{2}}} = \frac{\sqrt{2}}{\sqrt{(1+S_{210}^2)}} \qquad (D.12)$$

$$h = 20\log_{10}\left[\frac{1}{|(S_{21})_L|}\right] = 3 - 10\log_{10}(1 + 10^{-0.1L_{210}}) \qquad (D.13)$$

$$\text{Define } x \equiv h = m = 3 - \log_{10}(1 + 10^{-0.1L_{210}}) \qquad (D.14)$$

Thus by measuring L_{210} we can calculate x and apply this value to the display to determine Q_U and Q_L.

Determination of Q_U and Q_L from the reflection magnitude display

Referring to Figure 5.3(b) if p and n are known then Q_U and Q_L can be determined from the display.

S_{110} is a voltage coefficient, thus the magnitude of L_{110} in dB is given by :

$$L_{110} = 20\log_{10}S_{110} \qquad (D.15)$$

$$S_{110} = 10^{(\frac{L_{110}}{20})} \qquad (D.16)$$

(1) To determine the value of p

$$\frac{S_{110}}{|(S_{11})_U|} = \sqrt{(S_{110}^2 - 2S_{110} + 2)} \qquad (D.17)$$

$$\text{thus} \quad p = 20\log_{10}\left[\frac{S_{110}}{|(S_{11})_U|}\right] = 10\log_{10}(S_{110}^2 - 2S_{110} + 2)$$

$$= 10\log_{10}(10^{0.1L_{110}} - 2.10^{0.05L_{110}} + 2) \qquad (D.18)$$

(2) To determine the value of n

$$\frac{S_{110}}{|(S_{11})_L|} = \sqrt{2} \qquad (D.19)$$

$$\text{thus} \quad n = 20\log_{10}\left[\frac{S_{110}}{|(S_{11})_L|}\right] = 20\log_{10}\sqrt{2}$$

$$= 3\text{dB} \qquad (D.20)$$

Thus by measuring L_{110} we can calculate p and n and use these values to determine Q_U and Q_L from the display.

APPENDIX E

Derivation of S-parameter Matrix for Equally Coupled DR BPF

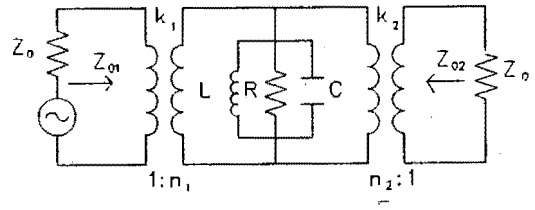

Fig E.1 Equivalent circuit of DR coupled to two microstriplines

Figure E.1 above shows the circuit to be analysed

Calculation of S11

Consider the input admittance looking into the first transformer as shown in Figure E.2 below

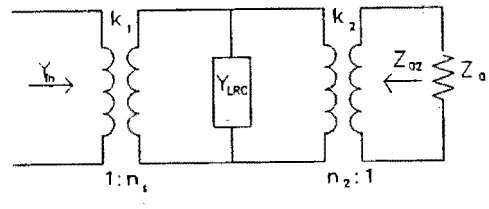

Fig E.2 Input admittance of circuit

The circuit can be simplified to that shown in Figure E.3 below

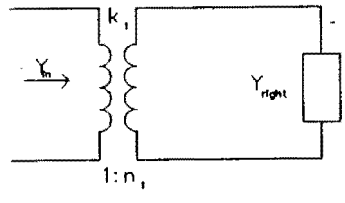

Fig E.3 Input admittance of simplified circuit

where $$Y_{right} = Y_{LRC} + \frac{1}{n_2^2 Z_0} \qquad (E.1)$$

$$Y_{LRC} = \frac{1 + j\Delta}{R} \qquad (E.2)$$

$$\Delta = 2Q_U\delta \qquad (E.3)$$

Thus $$Y_{in} = n_1^2 \left[\frac{1 + j\Delta}{R} + \frac{1}{n_2^2 Z_0}\right] \qquad (E.4)$$

and $$Z_{in} = \frac{1}{Y_{in}} = \frac{1}{n_1^2\left[\frac{1 + j\Delta}{R} + \frac{1}{n_2^2 Z_0}\right]} \qquad (E.5)$$

$$S_{11} = \frac{(\frac{Z_{in}}{Z_0}) - 1}{(\frac{Z_{in}}{Z_0}) + 1} = \frac{1 - \frac{n_1^2 Z_0(1 + j\Delta)}{R} - \frac{n_1^2}{n_2^2}}{1 + \frac{n_1^2 Z_0(1 + j\Delta)}{R} + \frac{n_1^2}{n_2^2}}$$

$$S_{11} = \frac{\frac{R}{n_1^2 Z_0} - \frac{R}{n_2^2 Z_0} - (1 + j\Delta)}{\frac{R}{n_1^2 Z_0} + \frac{R}{n_2^2 Z_0} + (1 + j\Delta)} \qquad (E.6)$$

Defining $$\kappa_1 \equiv \frac{R}{n_1^2 Z_0} \qquad (E.6), \quad \kappa_2 \equiv \frac{R}{n_2^2 Z_0} \qquad (E.7)$$

$$S_{11} = \frac{\kappa_1 - \kappa_2 - 1 - j\Delta}{1 + \kappa_1 + \kappa_2 + j\Delta} \qquad (E.8)$$

Calculation of S_{21}

The easiest method of calculating S_{21} is to express it in terms of voltages and currents as shown in Figure E.4

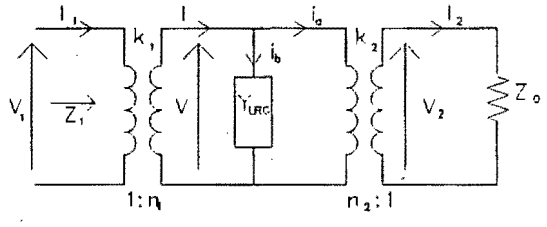

Fig E.4 Calculation of S21 from voltage and current considerations

We need to express V_2, I_1, and I_2 in terms of V_1

$$V = n_1 V_1 \qquad (E.9)$$

$$V_2 = \left(\frac{1}{n_2}\right)V = \left(\frac{n_1}{n_2}\right)V_1 \qquad (E.10)$$

$$I_1 = \frac{V_1}{Z_1} \qquad (E.11)$$

$$I = \frac{I_1}{n_1} = \left[\frac{1}{n_1 Z_1}\right]V_1 \qquad (E.12)$$

$$i_b = VY_{LRC} = n_1\left[\frac{1+j\Delta}{R}\right]V_1 \qquad (E.13)$$

$$i_a = I - i_b = \left[\frac{1}{n_1 Z_1} - \frac{n_1(1 + j\Delta)}{R}\right]V_1 \qquad (E.14)$$

$$I_2 = -i_a n_2 = -n_2 \cdot \left[\frac{1}{n_1 Z_1} - \frac{n_1(1 + j\Delta)}{R}\right].V_1 \qquad (E.15)$$

Now, $$S_{21} \equiv \frac{b_2}{a_1} \tag{E.16}$$

where

$$a_1 \equiv \frac{V_1 + Z_0 I_1}{2\sqrt{Z_0}} \tag{E.17}$$

$$b_2 \equiv \frac{V_2 - Z_0 I_2}{2\sqrt{Z_0}} \tag{E.18}$$

Thus $$S_{21} = \frac{V_2 - Z_0 I_2}{V_1 + Z_0 I_1} \tag{E.19}$$

$$= \frac{V_1 \left[\frac{n_1}{n_2} + Z_0 n_2 \left[\frac{1}{n_1 Z_1} - \frac{n_1(1 + j\Delta)}{R}\right]\right]}{V_1(1 + Z_0/Z_1)} \tag{E.20}$$

From (E.5) $$Z_1 = \frac{1}{n_1^2 \left[\frac{1 + j\Delta}{R} + \frac{1}{n_2^2 Z_0}\right]} \tag{E.21}$$

Substituting (E.21) into (E.20) we end up with

$$S_{21} = \frac{\frac{2R}{n_1 n_2 Z_0}}{\frac{R}{n_1^2 Z_0} + \frac{R}{n_2^2 Z_0} + (1 + j\Delta)} \tag{E.22}$$

By definition, $K_1 \equiv \frac{R}{n_1^2 Z_0}$ (E.23), $K_2 \equiv \frac{R}{n_2^2 Z_0}$ (E.24)

Thus $$S_{21} = \frac{2\sqrt{(K_1 K_2)}}{1 + K_1 + K_2 + j\Delta} \tag{E.25}$$

APPENDIX F

Determination of Unloaded and Loaded Quality Factors for an Equally Coupled DR BPF

At resonance, for equal coupling, we have from (5.19)

$$S_{110} = S_{220} = \frac{-1}{1 + 2K} \tag{F.1}$$

Also $$S_{210} = 1 + S_{110} \tag{F.2}$$

giving $$K = -\frac{(1 + S_{110})}{2S_{110}} = \frac{S_{210}}{2(1 - S_{210})} \tag{F.3}$$

The unloaded and loaded quality factors are related by the coupling coefficient

$$Q_U = Q_L(1 + 2K) \tag{F.4}$$

Loci of Unloaded and Loaded Quality Factors

We require the loci of Q_U and Q_L as a function of S_{110} and of S_{210} in the impedance (S_{11}) and transmittance (S_{21}) planes respectively

From (5.19) $$S_{11} = \frac{-1 - j2Q_U\delta}{1 + 2K + j2Q_U\delta} \tag{F.5}$$

This gives a normalised input impedance

$$z_{in} = \frac{1 + S_{11}}{1 - S_{11}} = \frac{K}{1 + K + j2Q_U\delta} \tag{F.6}$$

The normalised frequency deviations corresponding to Q_U and Q_L are given by

$$\delta_U = \pm \frac{1}{2Q_U} \quad (F.7) \qquad \text{and} \qquad \delta_L = \pm \frac{1}{2Q_L} \quad (F.8)$$

Loci of Q_U in the Impedance (S_{11}) and Transmittance (S_{21}) Planes

Substituting (F.7) into (F.5) gives

$$(S_{11})_U = -\frac{(1 \pm j)}{(2K + 1) \pm j} = \frac{-1}{\sqrt{(2K^2 + 2K + 1)}} . e^{\pm j \tan^{-1}(\frac{K}{K + 1})} \quad (F.9)$$

then substituting for K from (F.3) gives the locus of Q_U in the impedance plane in terms of S_{110}

$$(S_{11})_U = \frac{\sqrt{(2)} . S_{110}}{\sqrt{(1 + S_{110}^2)}} . e^{\pm j \tan^{-1}(\frac{1 + S_{110}}{1 - S_{110}})} \quad (F.10)$$

The relation $S_{21} = 1 + S_{11}$ can be used to find the locus of Q_U in the transmittance plane

$$(S_{21})_U = 1 + (S_{11})_U = 1 - \frac{(1 \pm j)}{(2K + 1) \pm j}$$

$$= \frac{K((2K + 1) - j)}{2K^2 + 2K + 1} = \frac{K\sqrt{2}}{\sqrt{(2K^2 + 2K + 1)}} . e^{\pm j \tan^{-1}(\frac{-1}{2K + 1})} \quad (F.11)$$

Substituting for K in terms of S_{210} using (F.3) gives

$$(S_{21})_U = \frac{S_{210}}{\sqrt{(S_{210}^2 - 2S_{210} + 2)}} . e^{\pm j \tan^{-1}(S_{210} - 1)} \quad (F.12)$$

Loci of Q_L in the Impedance (S_{11}) and Transmittance (S_{21}) Planes

The normalised input impedance expressed in terms of Q_L is

$$z_{in} = \frac{K}{1 + K + j2(1 + 2K)Q_L} \qquad (F.13)$$

For $\delta_L = \pm \frac{1}{2Q_L}$, $(z_{in})_L = \frac{K}{1 + K + j(1 + 2K)}$ (F.14)

This gives $(S_{11})_L = \frac{(z_{in})_L - 1}{(z_{in})_L + 1} = \frac{-(1 + K \pm jK)}{1 + 2K}$

$$= \frac{\sqrt{(2K^2 + 2K + 1)}}{1 + 2K} . e^{\pm j\tan^{-1}(\frac{K}{1 + K})} \qquad (F.15)$$

Substituting for K in terms of S_{110} from (F.3) gives

$$(S_{11})_L = \frac{(S_{110} - 1) - j(S_{110} + 1)}{2}$$

$$(S_{11})_L = \frac{\sqrt{(S_{110}^2 + 1)}}{\sqrt{2}} . e^{\pm j\tan^{-1}(\frac{S_{110} + 1}{1 - S_{110}})} \qquad (F.16)$$

For the transmittance plane

$$(S_{21})_L = 1 + (S_{11})_L = \frac{K(1 \pm j)}{1 + 2K}$$

$$= \frac{\sqrt{2K}}{1 + 2K} . e^{\pm j45} \qquad (F.17)$$

Substituting for K in terms of S_{210} we get

$$(S_{21})_L = \frac{S_{210}}{\sqrt{2}} . e^{\pm j45} \qquad (F.18)$$

Summary of Results

The results obtained are summarised in table F.1

Table F.1 Summary of results for Qu and Ql loci for DR bandpass filter

	Reflection Coefficient S_{110}		Transmission Coefficient S_{210}	
	$\lvert S_{110} \rvert$	$\arg(S_{110})$	$\lvert S_{210} \rvert$	$\arg(S_{210})$
Q_u	$S_{110}\sqrt{\frac{2}{1+S_{110}^2}}$	$\pm \tan^{-1}\left[\frac{1+S_{110}}{1-S_{110}}\right]$	$\frac{S_{210}}{\sqrt{S_{210}^2 - 2S_{210} + 2}}$	$\pm \tan^{-1}(S_{210} - 1)$
Q_L	$\sqrt{\frac{1+S_{110}^2}{2}}$	$\pm \tan^{-1}\left[\frac{1+S_{110}}{1-S_{110}}\right]$	$\frac{S_{210}}{\sqrt{2}}$	$\pm \frac{\pi}{4}$

Determination of Qu and QL from the Transmission Magnitude Display

Referring to Figure 5.9(a), if a and b are known then, Q_U and Q_L can be determined from the display.

S_{210} is a voltage coefficient, thus the insertion loss is given by :

$$L_{210}(dB) = -20\log_{10} S_{210} \qquad (F.19)$$

$$\text{thus } S_{210} = 10^{-(\frac{L_{210})}{20})} \qquad (F.20)$$

(1) To determine the value of a

From (F.12), $$a = -20\log_{10}\left[\frac{|(S_{21})_U|}{S_{210}}\right]$$

$$= -20\log_{10}\left[\frac{1}{\sqrt{(S_{210}^2 - 2S_{210} + 2)}}\right]\text{dB} \quad \text{(F.21)}$$

(2) To determine the value of b

From (F.18), $$b = -20\log_{10}\left[\frac{|(S_{21})_L|}{S_{210}}\right]$$

$$= -20\log_{10}(1/\sqrt{2}) = 3\text{dB} \quad \text{(F.22)}$$

Determination of Q_U and Q_L from the Reflection Magnitude Display

Referring to Figure 5.9(b), if c and d are known then, Q_U and Q_L can be determined from the display.

(1) To determine the value of c

From (F.10), $$c = -20\log_{10}\left[\frac{|(S_{11})_U|}{S_{110}}\right]$$

$$= -20\log_{10}\left[\frac{\sqrt{2}}{\sqrt{(1 + S_{110}^2)}}\right]\text{ dB} \quad \text{(F.23)}$$

(2) To determine the value of d

From (F.16), $$d = 20\log_{10}\left[\frac{|(S_{11})_L|}{\sqrt{2}}\right]$$

$$= 20\log_{10}\left[\frac{\sqrt{(S_{110}^2 + 1)}}{\sqrt{2}}\right]\text{ dB} = c \quad \text{(F.24)}$$

APPENDIX G

Conversion of Two-port S-parameters into Three-port S-parameters

The indefinite three-port S-parameter Matrix satisfies the following conditions (Kajfez, 1986: 482)

$$\sum_{j=1}^{3} S_{ij} = 1, \text{ for } i = 1, 2, 3 \quad (3 \text{ equations}) \qquad (G.1)$$

$$\sum_{i=1}^{3} S_{ij} = 1, \text{ for } j = 1, 2, 3 \quad (3 \text{ equations}) \qquad (G.2)$$

From (5.43) we obtain 3 simultaneous equations in 6 unknowns

$$b_1 = S_{11}a_1 + S_{12}a_2 + S_{13}a_3 \qquad (G.3)$$

$$b_2 = S_{21}a1 + S_{22}a_2 + S_{23}a_3 \qquad (G.4)$$

$$b_3 = S_{31}a_1 + S_{32}a_2 + S_{33}a_3 \qquad (G.5)$$

For the common source configuration we apply the following constraint

$$\Gamma_3 = \frac{a_3}{b_3} = -1 \quad \text{ie port 3 shorted to ground} \qquad (G.6)$$

Using (G.6) in (G.3), (G.4) and (G.5) we get

$$b_1 = S_{11}a1 + S_{12}a_2 - b_3S_{13} \qquad (G.7)$$

$$b_2 = S_{21}a1 + S_{22}a_2 - b_3S_{23} \qquad (G.8)$$

$$b_3 = S_{31}a1 + S_{32}a_2 - b_3S_{33} \qquad (G.9)$$

This gives

$$b_3 = \frac{S_{31}}{1 + S_{33}} a_1 + \frac{S_{32}}{1 + S_{33}} a_2 \qquad (G.10)$$

and eliminating b_3 from (G.7) and (G.8) gives

$$b_1 = \left[S_{11} - \frac{S_{13}S_{31}}{1 + S_{33}}\right]a_1 + \left[S_{12} - \frac{S_{13}S_{32}}{1 + S_{33}}\right]a_2 \qquad (G.11)$$

$$\text{and} \quad b_2 = \left[S_{21} - \frac{S_{23}S_{31}}{1 + S_{33}}\right]a_1 + \left[S_{22} - \frac{S_{23}S_{32}}{1 + S_{33}}\right]a_2 \qquad (G.12)$$

This can be written in matrix form as

$$\begin{bmatrix} b_1 \\ b_2 \end{bmatrix} = \begin{bmatrix} S_{11} - \frac{S_{13}S_{31}}{1 + S_{33}} & S_{12} - \frac{S_{13}S_{32}}{1 + S_{33}} \\ S_{21} - \frac{S_{23}S_{31}}{1 + S_{33}} & S_{22} - \frac{S_{23}S_{32}}{1 + S_{33}} \end{bmatrix} \begin{bmatrix} a_1 \\ a_2 \end{bmatrix} \qquad (G.13)$$

If we denote the 2-port common source S-parameters by

$$\begin{bmatrix} S_{11}^T & S_{12}^T \\ S_{21}^T & S_{22}^T \end{bmatrix} \quad \text{then}$$

$$S_{11}^T = S_{11} - \frac{S_{13}S_{31}}{1 + S_{33}} \qquad (G.14) \qquad S_{12}^T = S_{12} - \frac{S_{13}S_{32}}{1 + S_{33}} \qquad (G.15)$$

$$S_{21}^T = S_{21} - \frac{S_{23}S_{31}}{1 + S_{33}} \qquad (G.16) \qquad S_{22}^T = S_{22} - \frac{S_{23}S_{32}}{1 + S_{33}} \qquad (G.17)$$

Also from (G.1) and (G.2) we have

$$S_{11} + S_{12} + S_{13} = 1 \qquad (G.18) \qquad S_{11} + S_{21} + S_{31} = 1 \qquad (G.21)$$

$$S_{21} + S_{22} + S_{23} = 1 \qquad (G.19) \qquad S_{12} + S_{22} + S_{32} = 1 \qquad (G.22)$$

$$S_{31} + S_{32} + S_{33} = 1 \qquad (G.20) \qquad S_{13} + S_{23} + S_{33} = 1 \qquad (G.23)$$

We thus have ten equations which is sufficient to solve for the nine 3-port S-parameters.

Consider

$$\Sigma S^T = S_{11}{}^T + S_{12}{}^T + S_{21}{}^T + S_{22}{}^T \qquad (G.24)$$

$$\Sigma S^T = S_{11} + S_{12} + S_{21} + S_{22}$$

$$- \frac{S_{13}}{1 + S_{33}} (S_{31} + S_{32}) - \frac{S_{23}}{1 + S_{33}} (S_{31} + S_{32})$$

$$= (1 - S_{13}) + (1 - S_{23}) - \frac{(S_{13} + S_{23})(1 - S_{33})}{1 + S_{33}}$$

$$= 2 + (S_{33} - 1) - \frac{(1-S_{33})^2}{1 + S_{33}}$$

$$(1 + S_{33}) \Sigma S^T = (1 + S_{33})^2 - (1 - S_{33})^2$$

$$S_{33} = \frac{\Sigma S^T}{\Sigma S^T - 4} \qquad (G.25)$$

Now consider

$$1 - S_{12}{}^T - S_{22}{}^T = 1 - S_{12} + \frac{S_{13}S_{32}}{1 + S_{33}} - S_{22} + \frac{S_{23}S_{32}}{1 + S_{33}}$$

$$= (1 - S_{12} - S_{22}) + S_{32} \frac{(S_{13} + S_{23})}{1 + S_{33}}$$

$$= \frac{2S_{32}}{1 + S_{33}}$$

giving $$S_{32} = \frac{1 + S_{33}}{2} (1 - S_{12}{}^T - S_{22}{}^T) \qquad (G.26)$$

Similarly $$S_{23} = \frac{1 + S_{33}}{2} (1 - S_{21}{}^T - S_{22}{}^T) \qquad (G.27)$$

From (G.17) $$S_{22} = S_{22}^{T} + \frac{S_{23}S_{32}}{1 + S_{33}} \quad (G.28)$$

From (G.21) $$S_{11} = 1 - S_{21} - S_{31} \quad (G.29)$$

From (G.23) $$S_{13} = 1 - S_{23} - S_{33} \quad (G.30)$$

From (G.20) $$S_{31} = 1 - S_{32} - S_{33} \quad (G.31)$$

From (G.22) $$S_{12} = 1 - S_{22} - S_{32} \quad (G.32)$$

From (G.19) $$S_{21} = 1 - S_{22} - S_{23} \quad (G.33)$$

Thus all the 3-port S-parameters have been expressed solely in terms of S_{11}^{T}, S_{12}^{T}, S_{21}^{T} and S_{22}^{T} ie they can be evaluated from the common source 2-port S-parameters.

APPENDIX H

Manufacturer's Small Signal S-parameter Data for MGF1801

MITSUBISHI SEMICONDUCTOR (GaAs FET)

MGF1801 (2SK279)

FOR MICROWAVE MEDIUM-POWER AMPLIFIERS
N-CHANNEL SCHOTTKY BARRIER GATE TYPE

S_{11}, S_{22} vs. f

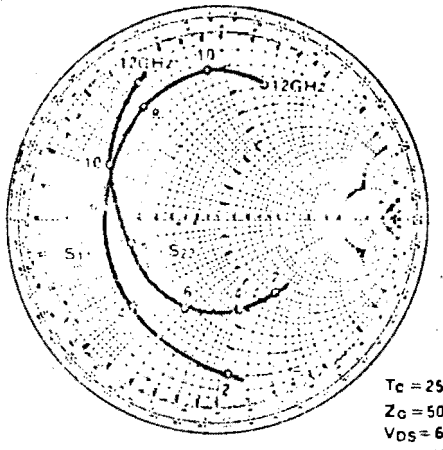

T_C = 25°C
Z_O = 50 Ω
V_{DS} = 6V
I_D = 100mA

S_{12}, S_{21} vs. f

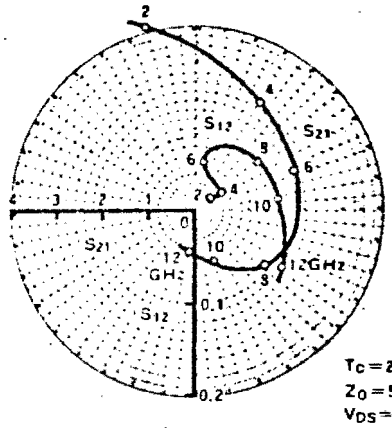

T_C = 25°C
Z_O = 50 Ω
V_{DS} = 6V
I_D = 100mA

S PARAMETERS (T_C = 25°C, V_{DS} = 6V, I_D = 100mA)

f (GHz)	S Parameters (TYP.)							
	S_{11}		S_{12}		S_{21}		S_{22}	
	Magn.	Angle (deg.)	Magn.	Angle (deg.)	Magn.	Angle (deg.)	Magn.	Angle (deg.)
2	0.815	− 87.9	0.042	42.3	4.760	106.7	0.492	− 51.6
4	0.671	−143.5	0.049	23.6	3.311	58.7	0.480	− 82.3
6	0.587	172.2	0.056	71.1	2.735	22.7	0.514	−102.2
8	0.663	116.9	0.079	28.4	2.133	−25.1	0.495	−161.8
10	0.736	88.1	0.090	8.5	1.420	−62.6	0.652	165.9
12	0.695	72.6	0.099	−25.1	1.077	−98.3	0.780	129.2

QUALITY GRADE: INDUSTRIAL GRADE (I.G)

APPENDIX I

Mapping the Load Reflection Plane of a Two-port Network into the Input Reflection Plane (Wagner, 1979)

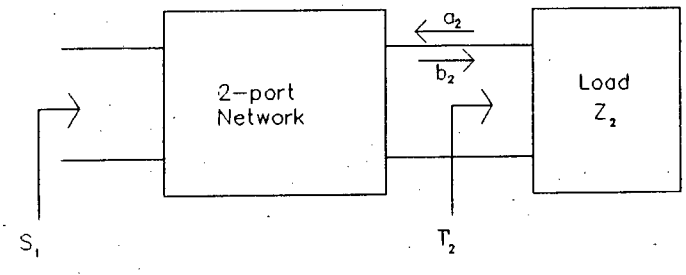

Fig I.1 Two port network terminated in a load

Consider a two-port network terminated in an impedance Z_2 with associated reflection coefficient Γ_2 as shown in Figure I.1. This appendix derives an equation which maps the Γ_2 plane into the S_1 plane. Using this equation the value of Γ_2, Γ_{20}, which maximises S_1 is also determined.

Terminating the two-port network in Z_2 applies the constraint $a_2 = \Gamma_2 b_2$ which reduces the network to a one-port characterised by a single parameter - the reflection coefficient S_1.

$$b_1 = S_{11}a_1 + S_{12}\Gamma_2 b_2 \qquad (I.1)$$

$$b_2 = S_{21}a_1 + S_{22}\Gamma_2 b_2 \qquad (I.2)$$

From (I.2) $\quad b_2(1 - \Gamma_2 S_{22}) = S_{21}a_1 \qquad (I.3)$

Substituting (I.3) into (I.1),

$$b_1 = S_{11}a_1 + \frac{S_{12}\Gamma_2 S_{21}a_1}{1 - \Gamma_2 S_{22}} \qquad (I.4)$$

$$S_1 = \frac{b_1}{a_1} = \frac{S_{11} - \Delta\Gamma_2}{1 - S_{22}\Gamma_2} \qquad (I.5)$$

where $\Delta = S_{11}S_{22} - S_{12}S_{21}$

Equation (I.5) is a conformal mapping of the Γ_2 plane into the S_1 plane ie circles in the Γ_2 plane map into circles in the S_1 plane.

S_1 can be written as the sum of two vectors - one of which is independent of Γ_2 and defines the centre of the mapping.

$$S_1 = \frac{S_{11} - \Delta\Gamma_2}{1 - S_{22}\Gamma_2} = \frac{(S_{11} - \Delta\Gamma_2)(1 - |S_{22}|^2)}{(1 - S_{22}\Gamma_2)(1 - |S_{22}|^2)}$$

$$= \frac{S_{11} - \Delta\Gamma_2 - S_{11}S_{22}S_{22}^* + \Delta\Gamma_2 S_{22}S_{22}^*}{(1 - S_{22}\Gamma_2)(1 - |S_{22}|^2)}$$

$$= \frac{(S_{11} - \Delta S_{22}^*)(1 - S_{22}\Gamma_2)}{(1 - S_{22}\Gamma_2)(1 - |S_{22}|^2)}$$

$$+ \frac{S_{11}S_{22}\Gamma_2 - S_{11}S_{22}S_{22}^* + \Delta(S_{22}^* - \Gamma_2)}{(1 - S_{22}\Gamma_2)(1 - |S_{22}|^2)}$$

$$= \frac{S_{11} - \Delta S_{22}^*}{1 - |S_{22}|^2} + \frac{S_{12}S_{21}}{1 - |S_{22}|^2}\left[\frac{\Gamma_2 - S_{22}^*}{1 - S_{22}\Gamma_2}\right] \qquad (I.6)$$

The factor $\left[\frac{\Gamma_2 - S_{22}^*}{1 - S_{22}\Gamma_2}\right]$ can be written as $\left[\frac{1 - S_{22}^*}{1 - S_{22}}\right]\Gamma_2'$

where Γ_2' is the reflection coefficient of the terminating

impedance Z_2 when normalised to complex impedance Z_{22}

ie $$\Gamma_2' = \frac{Z_2 - Z_{22}^*}{Z_2 + Z_{22}} \qquad (I.7)$$

where $$Z_{22} = \frac{1 + S_{22}}{1 - S_{22}} \qquad (I.8)$$

This is shown below

$$\frac{\Gamma_2 - S_{22}^*}{1 - S_{22}\Gamma_2} = \frac{(Z_2 - Z_0) - S_{22}^*(Z_2 + Z_0)}{(Z_2 + Z_0) - S_{22}(Z_2 - Z_0)}$$

$$= \frac{Z_2(1 - S_{22}^*) - Z_0(1 + S_{22}^*)}{Z_2(1 - S_{22}) + Z_0(1 + S_{22})}$$

$$= \frac{Z_2 - Z_0\left[\frac{1 + S_{22}^*}{1 - S_{22}^*}\right]}{Z_2 + Z_0\left[\frac{1 + S_{22}}{1 - S_{22}}\right]} \cdot \left[\frac{1 - S_{22}^*}{1 - S_{22}}\right]$$

$$= \left[\frac{Z_2 - Z_{22}^*}{Z_2 + Z_{22}}\right]\left[\frac{1 - S_{22}^*}{1 - S_{22}}\right]$$

$$= \left[\frac{1 - S_{22}^*}{1 - S_{22}}\right]\Gamma_2' \qquad (I.9)$$

Γ_2' is phase modified by the factor $\left[\frac{1 - S_{22}^*}{1 - S_{22}}\right]$

which has unity magnitude and phase angle equal to $2 * \arg(1 - S_{22}^*)$

From (I.6) and (I.9) the mapping may be expressed as

$$S_1 = S_{10} + k_1\Gamma_2' \tag{I.10}$$

where $$S_{10} = \frac{S_{11} - \Delta S_{22}^*}{1 - |S_{22}|^2} \tag{I.11}$$

$$k_1 = \frac{S_{12}S_{21}}{1 - |S_{22}|^2}\left[\frac{1 - S_{22}^*}{1 - S_{22}}\right] \tag{I.12}$$

$$\Gamma_2' = \frac{Z_2 - Z_{22}^*}{Z_2 + Z_{22}} \tag{I.13}$$

The form of the mapping given by equation (I.10) can be used to graphically map the Γ_2 plane into the S_1 plane by normalising the Γ_2 plane to Z_{22}, scaling it's magnitude by $|k_1|$, centering this locus at S_{10} in the S_1 plane and rotating it by $\arg(k_1)$.

Equation (I.10) can also be used to optimise the one-port reduction, in the sense of maximising the coefficient S_1. S_1 is easily seen to be a maximum when $|\Gamma_2'|$ is a maximum (ie $|\Gamma_2'| = 1$) and $k_1\Gamma_2'$ is in the direction of S_{10}.

$$S_{1max} = S_{10} + |k_1|u_{10} \tag{I.14}$$

where u_{10} is a unit vector in the direction of S_{10}

The value of Γ_2, Γ_{20}, which maximises S_1 is given by

$$\Gamma_{20} = \frac{1 + (u_{12}/u_{10})S_{22}^*}{(u_{12}/u_{10}) + S_{22}} \tag{I.15}$$

where u_{12} is a unit vector in the direction of $S_{12}S_{21}$

This is shown below :

$$|k_1|u_{10} = \frac{S_{12}S_{21}}{1 - |S_{22}|^2}\left[\frac{\Gamma_{20} - S_{22}^*}{1 - S_{22}\Gamma_{20}}\right] \quad \text{from (I.6) and (I.14)}$$

$$= \frac{|S_{12}S_{21}|}{1 - |S_{22}|^2} u_{12}\left[\frac{\Gamma_{20} - S_{22}^*}{1 - S_{22}\Gamma_{20}}\right] \qquad (I.16)$$

From (I.12) $$|k_1| = \frac{|S_{12}S_{21}|}{1 - |S_{22}|^2} \qquad (I.17)$$

so $$\frac{|S_{12}S_{21}|}{1 - |S_{22}|^2}u_{10} = \frac{|S_{12}S_{21}|}{1 - |S_{22}|^2} u_{12}\left[\frac{\Gamma_{20} - S_{22}^*}{1 - S_{22}\Gamma_{20}}\right] \qquad (I.18)$$

$$\frac{u_{12}}{u_{10}} = \frac{1 - S_{22}\Gamma_{20}}{\Gamma_{20} - S_{22}^*} \qquad (I.19)$$

giving $$\Gamma_{20} = \frac{1 + (u_{12}/u_{10})S_{22}^*}{(u_{12}/u_{10}) + S_{22}} \qquad (I.20)$$

The optimum terminating impedance z_{20} corresponding to Γ_{20} is given by

$$z_{20} = \frac{1 + \Gamma_{20}}{1 - \Gamma_{20}} \qquad (I.21)$$

and the optimum input impedance by

$$z_{10} = \frac{1 + S_{1max}}{1 - S_{1max}} \qquad (I.22)$$

APPENDIX J

Calculating the Two Load Reactances which give a Specific Value of Gamma in the Input Plane

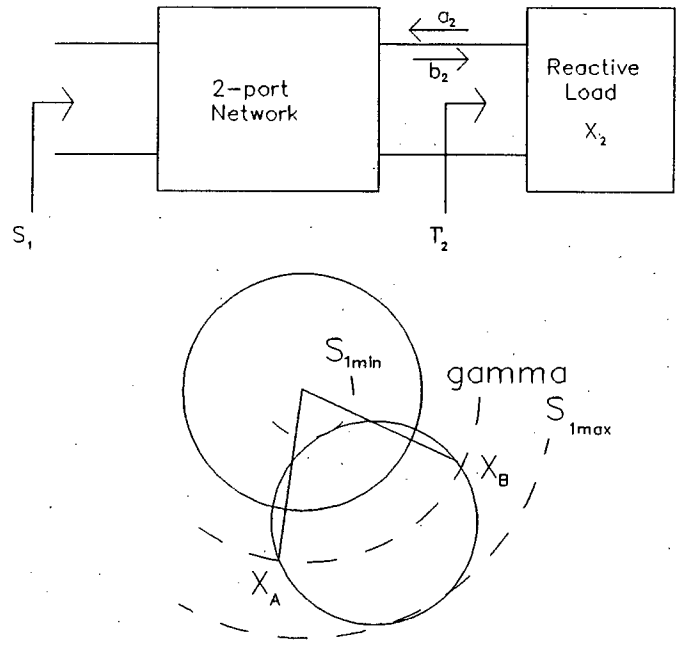

Fig J.1 Reactive termination of a two-port

The situation to be investigated is shown above in Figure J.1. For $S_{1max} < \gamma < S_{1min}$ there are two load reactance values, X_a and X_b which give $|S_1| = \gamma$ on the input. These have reflection coefficients Γ_{2a} and Γ_{2b} respectively.

(a) Expressing Γ_2 in terms of the 2-port S-parameters and the input reflection coefficient

From Appendix I

$$S_1 = \gamma \angle \underline{S_1} = S_{11} + \frac{S_{12}S_{21}S_{22}^*}{1 - |S_{22}|^2} + \frac{S_{12}S_{21}}{1 - |S_{22}|^2} \cdot \left[\frac{\Gamma_2 - S_{22}^*}{1 - S_{22}\Gamma_2}\right] \quad (J.1)$$

$$\frac{S_1 - S_{11} - \dfrac{S_{12}S_{21}S_{22}^*}{1 - |S_{22}|^2}}{\dfrac{1 - |S_{22}|^2}{S_{12}S_{21}}} \equiv A = \frac{\Gamma_2 - S_{22}^*}{1 - S_{22}\Gamma_2} \qquad (J.2)$$

rearranging,

$$\Gamma_2 = \frac{A + S_{22}^*}{1 + S_{22}A} = \frac{\gamma\,\underline{/S_1} + x}{[\gamma\underline{/S_1}]S_{22} + y} \qquad (J.3)$$

where $x = -S_{11}$ (J.4)

$$y = \frac{S_{12}S_{21}}{1 - |S_{22}|^2} - S_{11}S_{22} - \frac{S_{12}S_{21}\,|S_{22}|^2}{1 - |S_{22}|^2} \qquad (J.5)$$

(b) Solving for $\underline{/S_1}$ values corresonding to $|S_1| = \gamma$ and $|\Gamma_2| = 1$

Limiting Z_2 to reactive loads puts the constraint $|\Gamma_2| = 1$ on Γ_2 values ie

$$\Gamma_2.\Gamma_2^* = 1 \qquad (J.6)$$

Thus $$\left| \frac{\gamma\,\underline{/S_1} + x}{y + S_{22}\gamma\underline{/S_1}} \right| \left| \frac{\gamma\,\underline{/-S_1} + x^*}{y^* + S_{22}^*\gamma\underline{/-S_1}} \right| = 1 \qquad (J.7)$$

Cross-multiplying and multiplying through by $\underline{/S1}$ produces a quadratic in $\underline{/S1}$

$$A(\underline{/S1})^2 + B(\underline{/S1}) + C = 0 \qquad (J.8)$$

where $A = x^*\gamma - y^*\gamma S_{22}$ (J.9)

$B = \gamma^2 + |x| - |y|^2 - |S_{22}|^2\gamma^2$ (J.10)

$C = x\gamma - yS_{22}^*\gamma$ (J.11)

The roots of this equation are calculated using

$$(\underline{/S1})_{a,b} = \frac{-B \pm \sqrt{(B^2 - 4AC)}}{2A} \qquad (J.12)$$

(c) Determining Γ_2 and load reactance values

Substituting the values of ($\underline{/S1}$) obtained from (J.12) back into (J.3) gives two values of Γ_2. These Γ_2 values correspond to the reactive loads X_a and X_b which give $|S_1| = \gamma$ on the input port.

APPENDIX K

Program DESIGN

```
c
*************************************************************************
c    Name of program: DESIGN
c    Author         : D A Crouch
c    Date           : 23 February 1988/last update 12 July 1988
c
c    This program incorporates the design steps for a microstrip resonated
c    oscillator as described in chapter 9.
c
c    inputs : the small signal common source s-parameters of the device
c           : a keyboard entry for gamma - the small signal reflection coef.
c             on the gate.
c
c    outputs : the centre and radius of the mod(Ts)=1 circle in the gate
c              the infinite load direction
c
c              for the two possible source reactances which give gamma -
c
c              the reflection coef. on the gate
c              the value of source load refl. coef.
c              the corresponding source reactance value.
c
c              the reduced common source S21 value which gives gamma =1
c              the refl. coef. on the gate with new S21
c              the centre of the mod(Ts)=1 circle in the gate with new S21
c              the radius of the mod(Ts)=1 circle in the gate with new S21
c              the new infinite load direction
c              the gate reactance value for oscillation
c
c
*************************************************************************
      program design
      implicit complex*16 (p,r)
      complex*16 S11T,S12T,S21T,S22T,S11,S12,S13,S21,S22
      complex*16 S23,S31,S32,S33,ST
      complex*16 S11T3,S21TA
      complex*16 S22T3,S12T3,S21T3,T3
      complex*16 DEL,K1,S10,U10,U12,S1MAX,S1MIN,a,b,c
      complex*16 angle1,angle2,adash,bdash,cdash,T2A,T2B,Ttwo
      complex*16 ZA,ZB,S1,S21ANG,ZG
      real*8 x,y,thet,theta,arg
      real*8 MS1MIN,MS1MAX,GREAL,GAMMA,S21TOP,S21BOT,S21CALC

      write(1,201)
201   format(1h ,'    Entered common source S-parameters',//)
      read(2,*) x,y
      S11T=dcmplx(x,y)
      write(1,'(a\)') ' S11                                    '
      write(1,'(2f10.4)') dreal(S11T),dimag(S11T)
      read(2,*) x,y
      S12T=dcmplx(x,y)
      write(1,'(a\)') ' S12                                    '
      write(1,'(2f10.4)') dreal(S12T),dimag(S12T)
```

```
      read(2,*) x,y
      S21T = dcmplx(x,y)
      write(1,'(a\)') ' S21                          '
      write(1,'(2f10.4)') dreal(S21T),dimag(S21T)
      read(2,*) x,y
      S22T = dcmplx(x,y)
      write(1,'(a\)') ' S22                          '
      write(1,'(2f10.4)') dreal(S22T),dimag(S22T)
      write(1,50)
50    format(//)

      S11T=ptor(S11T)
      S12T=ptor(S12T)
      S21T=ptor(S21T)
      S22T=ptor(S22T)

      ST=S11T+S12T+S21T+S22T
      S33=ST/((4.0,0.0)-ST)
      S32=((1.0,0.0)+S33)*((1.0,0.0)-S12T-S22T)/(2.0,0.0)
      S23=((1.0,0.0)+S33)*((1.0,0.0)-S21T-S22T)/(2.0,0.0)
      S22=S22T+S23*S32/((1.0,0.0)+S33)
      S13=(1.0,0.0)-S23-S33
      S31=(1.0,0.0)-S33-S32
      S12=(1.0,0.0)-S22-S32
      S21=(1.0,0.0)-S22-S23
      S11=(1.0,0.0)-S21-S31

         S11T3=S11
         S12T3=S13
         S21T3=S31
         S22T3=S33

      DEL=S11T3*S22T3-S12T3*S21T3
      S10=(S11T3-DEL*DCONJG(S22T3))
      S10=S10/((1.0,0.0)-(DCONJG(S22T3))*S22T3)
      K1=(S12T3*S21T3)/((1.0,0.0)-(DCONJG(S22T3))*S22T3)
      K1=K1*((1.0,0.0)-DCONJG(S22T3))/((1.0,0.0)-S22T3)

      WRITE(1,500) dreal(recp(S10)),dimag(recp(S10)),
     +  dreal(recp(K1)),dimag(recp(k1))
500   format(1h ,'Centre of common reactive load circle '/
     + ' mapped into input          ',f10.4,'  ',f10.4,/
     + ' radius is                  ',f10.4,/
     + ' infinite load direction is ',f10.4//)

      U10=S10/CDABS(S10)
      U12=(S12T3*S21T3)/CDABS(S21T3*S12T3)
      S1MIN=S10-CDABS(K1)*U10
      S1MAX=S10+CDABS(K1)*U10
      S1MIN=recp(S1MIN)
      S1MAX=recp(S1MAX)
      MS1MIN=dreal(S1MIN)
      MS1MAX=dreal(S1MAX)

      write(*,10) MS1min,MS1max
10    format(1h , 'Enter required magnitude of S1'/
     + '  This value can lie between',f10.3,' and ',f10.3,//)
```

```
      read(*,*) GAMMA
      write(1,501)MS1min,MS1max,Gamma
501   format(1h ,'Minimum Gamma is  'f8.2/
     +           ' Maximum Gamma is  'f8.2/
     +           ' Selected Gamma is 'f8.2//)

        GREAL=GAMMA

        If (GREAL.lt.MS1min) then
           write(*,*) 'Value entered too low'
        Elseif (GREAL.gt.MS1max) then
           write(*,*) 'Value entered too big'
        else
           c=S12T3*S21T3/((1.0,0.0)-S22T3*DCONJG(S22T3))
           a=-S11T3
           b=c-S11T3*S22T3-S22T3*DCONJG(S22T3)*c
           adash=dconjg(a)-dconjg(b)*S22T3
           bdash=GAMMA*GAMMA*((1.0,0.0)-S22T3*dconjg(S22T3))+
     +             a*dconjg(a)-b*dconjg(b)
           cdash=a*GAMMA*GAMMA-b*dconjg(S22T3)*GAMMA*GAMMA
           angle1=(-bdash+CDSQRT(bdash*bdash-(4.0,0.0)*adash*cdash))/
     +          (2.0*adash)
           angle2=(-bdash-CDSQRT(bdash*bdash-(4.0,0.0)*adash*cdash))/
     +           (2*adash)
           T2A=(angle1+a)/(b+angle1*S22T3)
           T2B=(angle2+a)/(b+angle2*S22T3)
           ZA=50.0*(T2A+(1.0,0.0))/((1.0,0.0)-T2A)
           ZB=50.0*(T2B+(1.0,0.0))/((1.0,0.0)-T2B)

           write(1,110) gamma
           write(1,112) dreal(recp(angle1)),dimag(recp(angle1)),
     +     dreal(recp(T2A)),dimag(recp(T2A)),
     +     dimag(ZA)

           write(1,111) gamma
           write(1,112) dreal(recp(angle2)),dimag(recp(angle2)),
     +     dreal(recp(T2B)),dimag(recp(T2B)),
     +     dimag(ZB)

110        format(1h ,'Ist reactive source load giving Gamma = 'f8.2/)
111        format(1h ,//' 2nd reactive source load giving Gamma = 'f8.2/)

112        format(1h ,'Reflection coef. on gate is    'f8.3' angle 'f8.2/
     +                ' Source load refl. coef. is     'f8.3' angle '
     +           f8.2/' Source reactance is            'f8.3' Ohms'
     +                f8.2//)
        endif

        write(1,50)

        Do 400 j=1,2

        if (j.eq.1) then
            S1=angle1
            Ttwo=T2A
            write(1,'(a\)') ' First reactive source load '
```

```
      else
          S1=angle2
          Ttwo=T2B
          write(1,'(a\)') ' Second reactive source load '
      endif

          write(1,50)

      S21ANG=S21T/CDABS(S21T)
      S21TOP=CDABS(S21T)

      DO 300 I=1,20
    IF (I.EQ.1) THEN
         S21TOP=CDABS(S21T)
         S21BOT=0.0
       ELSE
        IF (CDABS(S1).GT.1.0) THEN
          S21TOP=S21CALC
          S21BOT=S21BOT
        ELSE
          S21TOP=S21TOP
          S21BOT=S21CALC
        ENDIF
       ENDIF
        S21CALC=(S21TOP+S21BOT)/2.0
        S21TA=S21CALC*S21ANG

       ST=S11T+S12T+S21TA+S22T
       S33=ST/((4.0,0.0)-ST)
       S32=((1.0,0.0)+S33)*((1.0,0.0)-S12T-S22T)/(2.0,0.0)
       S23=((1.0,0.0)+S33)*((1.0,0.0)-S21TA-S22T)/(2.0,0.0)
       S22=S22T+S23*S32/((1.0,0.0)+S33)
       S13=(1.0,0.0)-S23-S33
       S31=(1.0,0.0)-S33-S32
       S12=(1.0,0.0)-S22-S32
       S21=(1.0,0.0)-S22-S23
       S11=(1.0,0.0)-S21-S31

       S1=S11+(S31*S13*Ttwo)/((1.0,0.0)-S33*Ttwo)

        S11T3=S11
        S12T3=S13
        S21T3=S31
        S22T3=S33

     DEL=S11T3*S22T3-S12T3*S21T3
     S10=(S11T3-DEL*DCONJG(S22T3))
     S10=S10/((1.0,0.0)-(DCONJG(S22T3))*S22T3)
     K1=(S12T3*S21T3)/((1.0,0.0)-(DCONJG(S22T3))*S22T3)
     K1=K1*((1.0,0.0)-DCONJG(S22T3))/((1.0,0.0)-S22T3)

300        continue

          ZG=50.0*(1.0+S1)/(1.0-S1)

          write(1,113) dreal(recp(S21TA)),dimag(recp(S21TA)),
     +                 dreal(recp(S1)),dimag(recp(S1)),
```

```
     +                dreal(recp(S10)),dimag(recp(S10)),
     +                dreal(recp(K1)),dimag(recp(K1)),
     +                dreal(recp(ZG)),-dimag(recp(ZG))

113       format(1h ,'Reduced common source S21 is   'f8.3' angle 'f8.2/
     +   ' Gate refl. coef. is            'f8.3' angle 'f8.2/
     +   ' Centre of mod(Ts)=1 in gate is 'f8.3' angle 'f8.2/
     +   ' Radius of mod(Ts)=1 in gate is 'f8.3/
     +   ' Infinite source load direction 'f8.3/
     +   ' Gate reactance for oscillation 'f8.3' angle 'f8.2//)
400    continue

       stop
       end
c
*******************************************************************************

       complex*16 function ptor(rect)
       complex*16 rect

       real*8 rad,theta

       theta = dimag(rect)*(3.14159265/180.0)
       rad = dreal(rect)

       ptor = dcmplx(rad*cos(theta),rad*sin(theta))
       return
       end

c
*******************************************************************************

       complex*16 function recp(polar)
       complex*16 polar
       real*8 x,y,r,thet

       x=dreal(polar)
       y=dimag(polar)
       r=sqrt(x*x+y*y)

       if (x.eq.0.0) then
         thet=0.0
       else
         thet=atan(y/x)
       endif

       thet=thet*(180.0/3.1415926)

       if (x.lt.0.0) then
         if (y.gt.0.0) then
           thet=thet+180
         else
           thet=-180.0+thet
         endif
       endif

       recp = dcmplx(r,thet)
```

```
      return
      end
```

****

APPENDIX L

Listing of TOUCHSTONE Model for Oscillator A

```
! Program to model oscillator A
! 30 ohm stubs on gate and source,50 ohms on output
! Written by D A Crouch
! Date 16.6.88

DIM
        FREQ    GHZ
        RES     OH
        IND     NH
        CAP     PF
        LNG     MM
        ANG     DEG
CKT
        msub er=2.2 H=0.2540 T=0.01778 RHO=0.84 RGH=0.0
        S2PA 1 2 3 M7sp.s2p
        MLEF 3 W=1.56 L=36.81
        MLEF 1 W=1.56 L=33.59
        def1p 2  OSCA
TERM
        Z0=50.
OUT
        OSCA DB[S11] GR1
        OSCA RE[Z1] GR1
        OSCA IM[Z1] GR1

FREQ

        SWEEP  5 6 0.01
GRID
        RANGE 5 6 0.25
        GR1 -100 100 50
```

APPENDIX M

Determining the Limits of the Stabilisation Ranges

The edges of the stabilisation ranges occur when $(\partial f/\partial f_r)_{f0}$ becomes infinite. ie when

$$F'\left(\frac{f - f_r}{f_r}\right) = 0$$

From (9.28) $F\left(\frac{f - f_r}{f_r}\right)$ can be written as

$$F(x) = x.\left(1 + \frac{A}{1 + Bx^2}\right) \qquad (M.1)$$

where

$$x = \left(\frac{f - f_r}{f_r}\right) \qquad (M.2)$$

$$A = \frac{2K}{(1 + 2K)^2}.\frac{Q_r}{Q_{oex}} \qquad (M.3)$$

$$B = \frac{4Q_r^2}{(1 + 2K)^2} \qquad (M.4)$$

Then

$$F'(x) = \frac{(1 + Bx^2)^2 + A(1 + Bx^2) - 2ABx^2}{(1 + Bx^2)^2} \qquad (M.5)$$

For $F'(x) = 0$, $(B^2)x^4 + (2B - AB)x^2 + (A + 1) = 0$

ie $$(x^2)_{a,b} = \frac{(AB - 2B) \pm \sqrt{((2B - AB)^2 - 4(B^2)(A + 1))}}{2B}$$

$$= \frac{(A - 2) \pm A\sqrt{(1 - 8/A)}}{2B}$$

$$= \frac{(A - 2) \pm A(1 - 4/A + \ldots.)}{2B} \quad \text{Since } A >> 1 \qquad (M.6)$$

This gives $(x^2)_b = \frac{A - 3}{B} \approx \frac{A}{B}$ (M.7)

and $(x^2)_a = \frac{1}{B}$ (M.8)

ie $x_b = \pm\sqrt{(A/B)}$ (M.9)

and $x_a = \pm\sqrt{(1/B)}$ (M.10)

f_a and f_b can be found by substituting in equation (M.1) as follows

for $f_0 = f_b + f_r$, $\frac{(f_b + f_r) - f_r}{f_r} = F(x_b^+)$

$= F(\sqrt{A}/B)$ (M.11)

$$f_b = \sqrt{(A/B)}.(1 + \frac{A}{1 + A}).f_r$$

$\approx 2\sqrt{(A/B)}.f_r$ for $A >> 1$ (M.12)

Substituting for A, B $f_b = \frac{\sqrt{(2K)}}{\sqrt{(Q_{oex}Q_r)}}$ (M.13)

for $f_0 = f_a + f_r$, $\frac{(f_a + f_r) - f_r}{f_r} = F(x_a^+)$

$= F(1/\sqrt{B})$ (M.14)

$f_a = \frac{1}{\sqrt{B}}.(1 + A/2).f_r \approx \frac{A}{2\sqrt{B}}$ for $A >> 1$ (M.15)

Substituting for A, B

$$f_a = \frac{K}{(2K + 1)} \cdot \frac{1}{Q_{oex}} \cdot f_r \qquad (M.16)$$

ADDENDIX N

Program MAPPING

```
c*************************************************************************
c     Program MAPPING
c     Written by D A CROUCH
c     Date 23rd October 1987/last update 28th June 1988
c     Ref Oscillator Design by Device Line Measurement - Walter Wagner
c
c     Description:
c
c     This program maps the load reactance circle of a 2-port network into
c     the input reflection coefficient plane.
c
c     Inputs:  The S-parameters of the 2-port network
c
c     Outputs: K  - the stability factor of the 2-port
c              S10- the centre of the load reactance circle in the input refl
c                   coef plane
c              K1 - the radius of the load reactance circle in the input refl
c                   coef plane
c              U10- unit vector in the direction of S1MAX
c              U12- unit vector in the direction of S12*S21
c              S1MAX - maximum value of refl coef in input for a reactive loa
c                   on output.This occurs for a reactive load Z20 on output
c              T20- refl coef of load on output which gives S1MAX
c              Z20- reactive load on output which gives S1MAX
c              Z10- optimum small signal input impedance for 2-port terminate
c                   in Z20
c
c *************************************************************************
      program mapping
      implicit complex*16 (p,r)
      character*64 datfil,datname
      complex*16 S11,S12,S21,S22,DEL,S10,K1,T20,S1MAX,Z10,z20
      complex*16 U10,U12,CHECK,K
      real*8 x,y,thet

      write(*,'(a\)') '  enter S11 (rho , theta) '
      read(*,*) x,y
      S11=dcmplx(x,y)
      write(*,'(2f10.4)') dreal(S11),dimag(S11)

      write(*,'(a\)') '  enter s12 (rho , theta) '
      read(*,*) x,y
      S12=dcmplx(x,y)
      write(*,'(2f10.4)') dreal(S12),dimag(S12)

      write(*,'(a\)') '  enter s21 (rho , theta) '
      read(*,*) x,y
      S21 = dcmplx(x,y)
      write(*,'(2f10.4)') dreal(S21),dimag(S21)

      write(*,'(a\)') '  enter s22 (rho , theta) '
      read(*,*) x,y
```

```
S22 = dcmplx(x,y)
write(*,'(2f10.4)') dreal(S22),dimag(S22)

write(1,'(a\)') '      S11      '
write(1,'(2f10.4)') dreal(S11),dimag(S11)
write(1,'(a\)') '      S12      '
write(1,'(2f10.4)') dreal(S12),dimag(S12)
write(1,'(a\)') '      S21      '
write(1,'(2f10.4)') dreal(S21),dimag(S21)
write(1,'(a\)') '      S22      '
write(1,'(2f10.4)') dreal(S22),dimag(S22)

S11=ptor(S11)
S12=ptor(S12)
S21=ptor(S21)
S22=ptor(S22)

DEL=S11*S22-S12*S21
K=1+DEL*DCONJG(DEL)-S11*DCONJG(S11)-S22*DCONJG(S22)
K=K/(2*CDSQRT((S12*S21)*DCONJG(S12*S21)))
S10=(S11-DEL*DCONJG(S22))
S10=S10/((1.0,0.0)-(DCONJG(S22))*S22)
K1=(S12*S21)/((1.0,0.0)-(DCONJG(S22))*S22)
K1=K1*((1.0,0.0)-DCONJG(S22))/((1.0,0.0)-S22)
U10=S10/CDABS(S10)
U12=(S12*S21)/CDABS(S21*S12)

if (cdabs(S22).gt.1.0) then
  T20=((1,0)-DCONJG(S22)*(U12/U10))/(S22-(U12/U10))
else
  T20=((1,0)+DCONJG(S22)*(U12/U10))/((U12/U10)+S22)
endif

Z20=(1+T20)/(1-T20)*50.0
S1MAX=S10+CDABS(K1)*U10
Z10=(1+S1MAX)/(1-S1MAX)

K=recp(K)
S10=recp(S10)
K1 =recp(K1)
U10=recp(U10)
U12=recp(U12)
S1MAX=recp(S1MAX)
T20=recp(T20)
Z20=recp(Z20)
Z10=recp(Z10)

 WRITE(*,'(A\)') '   K         '
 write(*,101) dreal(K),dimag(K)
 WRITE(*,'(A\)') '   S10       '
 write(*,101) dreal(S10),dimag(S10)
 WRITE(*,'(A\)') '   K1        '
 write(*,101) dreal(K1),dimag(K1)
 WRITE(*,'(A\)') '   U10       '
 write(*,101) dreal(u10),dimag(u10)
 WRITE(*,'(A\)') '   U12       '
 write(*,101) dreal(u12),dimag(u12)
```

```
      WRITE(*,'(A\)') '   S1MAX     '
      write(*,101) dreal(S1MAX),dimag(S1MAX)
      WRITE(*,'(A\)') '   T20       '
      write(*,101) dreal(T20),dimag(T20)
      WRITE(*,'(A\)') '   Z20       '
      write(*,101) dreal(Z20),dimag(Z20)
      WRITE(*,'(A\)') '   Z10       '
      write(*,101) dreal(Z10),dimag(Z10)

      write(1,104)
104   format(1h ,//,'        Results  ',//)
      WRITE(1,'(A\)') '   K         '
      write(1,101) dreal(K),dimag(K)
      WRITE(1,'(A\)') '   S10       '
      write(1,101) dreal(S10),dimag(S10)
      WRITE(1,'(A\)') '   K1        '
      write(1,101) dreal(K1),dimag(K1)
      WRITE(1,'(A\)') '   U10       '
      write(1,101) dreal(u10),dimag(u10)
      WRITE(1,'(A\)') '   U12       '
      write(1,101) dreal(u12),dimag(u12)
      WRITE(1,'(A\)') '   S1MAX     '
      write(1,101) dreal(S1MAX),dimag(S1MAX)
      WRITE(1,'(A\)') '   T20       '
      write(1,101) dreal(T20),dimag(T20)
      WRITE(1,'(A\)') '   Z20       '
      write(1,101) dreal(Z20),dimag(Z20)
      WRITE(1,'(A\)') '   Z10       '
      write(1,101) dreal(Z10),dimag(Z10)

      write(1,105)
105   format(1h ,//////)

101   format(1h,'              ',f10.4,' ',f10.4)

      stop
      end

c*************************************************************************
c
c Functions ptor and recp included in Appendix K
c
c *************************************************************************
```